

SYNTHESIS OF NANOFLUIDS CONTAINING ECO-
FRIENDLY FUNCTIONALIZED CARBON
NANOMATERIALS FOR IMPROVING HEAT DISSIPATION

RAD SADRI

FACULTY OF ENGINEERING
UNIVERSITY OF MALAYA
KUALA LUMPUR

2018

**SYNTHESIS OF NANOFLUIDS CONTAINING ECO-
FRIENDLY FUNCTIONALIZED CARBON
NANOMATERIALS FOR IMPROVING HEAT
DISSIPATION**

RAD SADRI

**THESIS SUBMITTED IN FULFILMENT OF THE
REQUIREMENTS FOR THE DEGREE OF DOCTOR OF
PHILOSOPHY**

**FACULTY OF ENGINEERING
UNIVERSITY OF MALAYA
KUALA LUMPUR**

2018

UNIVERSITY OF MALAYA
ORIGINAL LITERARY WORK DECLARATION

Name of Candidate: **RAD SADRI**

Matric No: **KHA130082**

Name of Degree: **PH.D. OF MECHANICAL ENGINEERING**

Title of Project Paper/Research Report/Dissertation/Thesis (“this Work”):

**SYNTHESIS OF NANOFLUIDS CONTAINING ECO-FRIENDLY
FUNCTIONALIZED CARBON NANOMATERIALS FOR IMPROVING HEAT
DISSIPATION**

Field of Study: **Heat transfer**

I do solemnly and sincerely declare that:

- (1) I am the sole author/writer of this Work;
- (2) This Work is original;
- (3) Any use of any work in which copyright exists was done by way of fair dealing and for permitted purposes and any excerpt or extract from, or reference to or reproduction of any copyright work has been disclosed expressly and sufficiently and the title of the Work and its authorship have been acknowledged in this Work;
- (4) I do not have any actual knowledge nor do I ought reasonably to know that the making of this work constitutes an infringement of any copyright work;
- (5) I hereby assign all and every rights in the copyright to this Work to the University of Malaya (“UM”), who henceforth shall be owner of the copyright in this Work and that any reproduction or use in any form or by any means whatsoever is prohibited without the written consent of UM having been first had and obtained;
- (6) I am fully aware that if in the course of making this Work I have infringed any copyright whether intentionally or otherwise, I may be subject to legal action or any other action as may be determined by UM.

Candidate’s Signature

Date:

Subscribed and solemnly declared before,

Witness’s Signature

Date:

Name:

Designation:

**SYNTHESIS OF NANOFLUIDS CONTAINING ECO-FRIENDLY
FUNCTIONALIZED CARBON NANOMATERIALS FOR IMPROVING HEAT
DISSIPATION**

ABSTRACT

Conventional working fluids used in high heat flux systems such as heat exchangers and solar collectors typically have low thermal conductivities which provides low heat transfer efficiency. Many studies have been performed to improve the heat transfer of the conventional working fluids by dispersing higher thermally conductive particles into them. In this study, highly conductive carbon nanostructures are dispersed in distilled (DI) water, and the thermal properties are significantly enhanced at the lowest particle concentration. This study is focused on the development of eco-friendly, facile, functionalization technique to synthesize a new generation of water-based carbon nanostructure nanofluids for use as coolants in order to improve the convective heat transfer and hydrodynamic properties of a single-tube heat exchanger. The approach is green since it does not involve the use of toxic, corrosive acids. The graphene nanoplatelets (GNPs) and multi-walled carbon nanotubes (MWCNTs) were covalently functionalized using clove buds and gallic acid, respectively, using the one-pot method. Next, the functionalized GNPs and MWCNTs were dispersed in DI water to synthesize the clove-treated GNP, gallic acid-treated GNP, gallic acid-treated MWCNT nanofluids. Moreover, graphene oxide was reduced using saffron in one pot to synthesize water-based saffron-reduced graphene oxide (SrGO). The nanofluids were produced at various particle concentrations (0.025, 0.075, and 0.1 wt %). The effectiveness of the covalent treatment and reduction method were evaluated using Fourier transform infrared spectroscopy, Raman spectroscopy, thermogravimetric analysis, X-ray photoelectron spectroscopy, transmission electron microscopy, and ultraviolet-visible spectroscopy.

Ultraviolet-visible spectroscopy and zeta potential measurements were also conducted to verify the colloidal stability and the presence of hydrophilic groups on the surface of the functionalized nanoparticles. The thermo-physical characteristics of the nanofluids were investigated experimentally and the results indicate there is significant thermal conductivity enhancement (up to 29.2%) for the water-based SrGO at 45°C. The turbulent convective heat transfer was studied using a heat exchanger subjected to constant heat flux (12,752 W/m²) within a Reynolds number range of 6,371–15,927. Preliminary experiments were conducted with DI water and the results were compared with those determined from empirical correlations. The results indicate good reliability and accuracy of the set-up. Experiments were conducted for the nanofluids flowing through the loop under fully-developed turbulent condition and the results show that the addition of a low fraction of green-functionalized carbon nanostructures into DI water significantly enhances the Nusselt number and convective heat transfer coefficient (up to 40% for water-based SrGO). The increase in friction factor and relative pumping power (<1.21) is negligible. The remarkable enhancement of the performance index (>1) indicates that these nanofluids have great potential for use as heat transfer fluids considering the overall thermal performance and energy savings. The computational fluid dynamics (CFD) simulation are performed using shear stress transport $k-\omega$ turbulence model to predict the heat transfer performance of water-based CGNPs nanofluids in three-dimensional heated tube. The results conform well to those from experiments with an average relative deviation of ± 10 . The experimental results confirm the applicability of the numerical model to simulate heat transfer performance of nanofluids in turbulent flow conditions.

Keywords: Convective heat transfer, eco-friendly functionalization, turbulent, nanofluids, carbon nanostructures

**SYNTHESIS OF NANOFUIDS CONTAINING ECO-FRIENDLY
FUNCTIONALIZED CARBON NANOMATERIALS FOR IMPROVING HEAT
DISSIPATION**

ABSTRAK

Cecair kerja konvensional yang digunakan dalam sistem fluks haba tinggi seperti penukar haba dan pengumpul suria biasanya mempunyai konduktiviti haba rendah yang mengurangkan kecekapan pemindahan haba secara ketara. Banyak kajian telah dijalankan untuk meningkatkan pemindahan haba bagi cecair kerja dengan menyebarkan zarah berkonduktif termal ke dalam cecair ini. Dalam kajian ini, struktur nanostruktur karbon yang sangat konduktif telah disebarkan ke dalam air suling (DI), dan sifat-sifat terma telah dipertingkatkan dengan ketara pada kepekatan zarah terendah. Kajian ini memberi tumpuan kepada pembangunan teknik pemungsaan yang mesra alam dan mudah bagi mensintesis nanofluid nanostruktur karbon berasaskan air generasi baru untuk digunakan sebagai penyejuk bagi meningkatkan perpindahan haba konvensional dan sifat-sifat hidrodinamik bagi penukar haba berasaskan tiub keluli tahan karat lurus. Pendekatannya ini adalah bersifat 'hijau' dan ia tidak melibatkan penggunaan toksik dan asid penghakis. Nanoplatlet graphene (GNP) dan nanotiub karbon berbilang dinding (MWCNTs) telah difungsikan secara kovalen menggunakan tunas cengkih dan asid gallic, masing-masing menggunakan kaedah pot tunggal. Seterusnya, GNP dan MWCNT yang difungsikan telah disebarkan di dalam air DI untuk mensintesis nanofluid GNP yang dirawat cengkih, GNP yang dirawat asid gallic dan MWCNT yang dirawat asid gallic. Di samping itu, graphene oksida telah dikurangkan dengan menggunakan saffron dalam pot tunggal untuk mensintesis oksida graphene yang dikurangkan saffron (SrGO) berasaskan air. Nanofluid telah disediakan pada kepekatan zarah yang berlainan (0.025, 0.075, dan 0.1 wt%). Keberkesanan kaedah pengurangan dan rawatan kovalen telah dinilai dengan menggunakan spektroskopi inframerah

transformasi Fourier, spektroskopi Raman, analisis termogravimetrik, spektroskopi fotoelektron X-ray, mikroskopi elektron penghantaran, dan spektroskopi boleh lihat-ultraviolet. Pengukuran potensi zeta dan spektroskopi boleh lihat-ultraviolet juga digunakan untuk mengesahkan kestabilan koloid dan untuk membuktikan kehadiran kumpulan hidrofilik pada permukaan nanopartikel yang berfungsi. Ciri-ciri thermo-fizikal dari nanofluids telah disiasat secara eksperimen dan hasilnya menunjukkan terdapat peningkatan kekonduksian terma yang ketara (sehingga 29.2%) untuk SrGO berasaskan air pada suhu 45 ° C. Pemindahan haba konveksi gelora telah dikaji menggunakan penukar haba yang diberikan fluks haba tetap (12,752 W/m²) dalam julat nombor Reynolds 6,371-15,927. Eksperimen awal dilakukan dengan air DI dan hasilnya dibandingkan dengan keputusan yang ditentukan dari korelasi empirikal. Hasil menunjukkan kebolehpercayaan dan ketepatan yang baik bagi set-up. Eksperimen telah dijalankan untuk nanofluid yang mengalir melalui gelung di bawah keadaan gelora terbina lengkap dan keputusan menunjukkan bahawa penambahan pecahan rendah karbon berstruktur nano berfungsi ke dalam DI air meningkatkan nombor Nusselt dan pemalar pemindahan haba konveksi dengan ketara (sehingga 40 % untuk SrGO berasaskan air). Peningkatan faktor geseran dan kuasa pam relatif (<1.21) boleh diabaikan. Peningkatan prestasi indeks luar biasa (> 1) menunjukkan bahawa nanofluid ini mempunyai potensi besar untuk digunakan sebagai cecair pemindahan haba dengan mengambilkira prestasi haba keseluruhan dan penjimatan tenaga. Simulasi dinamik bendalir berkomputer (CFD) telah dilakukan dengan menggunakan model gelora pengangkutan ricih k- ω untuk meramalkan prestasi pemindahan haba CGNPs nanofluid berasaskan air dalam tiub tiga dimensi yang dipanaskan. Keputusan menuruti dengan baik terhadap eksperimen dengan sisihan relatif purata ± 10 . Keputusan eksperimen mengesahkan kebolehgunaan model berangka untuk mensimulasikan prestasi pemindahan haba nanofluid dalam keadaan aliran gelora.

Kata kunci: pemindahan haba konvensional, pemfungsian yang mesra alam, turbulen, nanofluid, struktur nano karbon

University of Malaya

ACKNOWLEDGEMENTS

In the name of GOD, the most Gracious, the most Compassionate. First and foremost, I would like to express my deepest appreciation to my supervisor Assoc. Prof. Dr. Kazi Md. Salim Newaz, who was not only a tremendous mentor for me, but also an ethical teacher and a supportive person during difficult times. I would like to offer my sincerest appreciation to my supervisors Prof. Dr. Mahidzal Dahari and Dr. Ahmad Badarudin Badry. I would also like to thank my mentor Distinguished Prof. Goodarz Ahmadi for his priceless comments and suggestions on my articles, and his valuable recommendations on my career path as a research scientist. My deepest thanks to all of my colleagues in university of Malaya; especially to Maryam Hosseini who was my main project partner, and together we co-authored several articles, for her unforgettable helps and supports during my PhD; to Dr. Nashrul Zubir and Dr. Samira Bagheri who provided me continuous hints and financial supports; to Abdolrahman Mallah, PhD student, for his impotently, valuable and freely helps. Heartfelt and very special thanks are extended to my lovely parents for their support, faith, Sacrifice and encouragement during the hardship to achieve the best. Words cannot express how deeply grateful I am for them. The writing of this thesis had been the most challenging undertaking of my life to date. I could not have completed this work without the support and help of many people. I would also like to convey thanks to the Faculty of Engineering, University of Malaya and High Impact Research (MOHE-HIR) grant for providing the financial support and laboratory facilities.

Rad Sadri
Kuala Lumpur, August 2018

TABLE OF CONTENTS

Abstract	iii
Abstrak	iii
Acknowledgements	viii
Table of Contents	ix
List of Figures	xiv
List of Tables.....	xxii
List of Symbols and Abbreviations.....	xxiv
CHAPTER 1: INTRODUCTION.....	1
1.1 Scope of study.....	6
1.2 Objectives of the current research	8
CHAPTER 2: LITERATURE REVIEW.....	9
2.1 Background.....	9
2.2 Nanofluids.....	10
2.3 Carbon-based nanomaterials (carbon allotropes)	11
2.3.1 Carbon nanotube.....	13
2.3.2 Graphene nanoplatelets	14
2.4 Preparation of nanofluids.....	21
2.4.1 One-step method.....	22
2.4.2 Two-step method	24
2.5 Stability of nanofluids.....	26
2.5.1 pH control.....	28
2.5.2 Ultrasonic agitation (vibration)	30
2.6 Physical and chemical functionalization methods.....	31

2.6.1	Chemical functionalization methods: Covalent functionalization	32
2.6.2	Physical functionalization methods: Non-covalent functionalization.....	43
2.7	Green methods	50
2.8	Thermo physical properties of nanofluid.....	63
2.8.1	Thermal conductivity	64
2.8.2	Density.....	81
2.8.3	Viscosity.....	83
2.9	Heat transfer and friction factor of nanofluids	90
2.9.1	Forced convection heat transfer in a tube.....	90
2.9.2	Force convection and friction factor in turbulent flow conditions.....	91
2.10	Simulation.....	102
2.10.1	Governing equations.....	102
2.10.1.1	Single-phase models.....	102
2.10.1.2	Two-phase models.....	108
2.10.1.3	Eulerian-Eulerian model	112
2.10.1.4	Mixture model	112
2.10.2	Turbulence modeling.....	113
2.10.2.1	$k - \epsilon$ model.....	113
2.10.2.2	Standard $k - \omega$ model	114
CHAPTER 3: METHODOLOGY.....		116
3.1	Materials	116
3.1.1	Clove treated GNPs	116
3.1.2	Gallic acid treated GNPs and MWCNTs	116
3.1.3	Graphene oxide and reduced graphene oxide.....	116
3.2	Preparation of nano-coolants	117

3.2.1	Synthesis of Clove-treated GNPs aqueous suspensions.....	117
3.2.2	Synthesis of GA-treated GNPs aqueous suspensions.....	119
3.2.3	Graphene oxide and Reduced graphene oxide	124
3.3	Experimental procedure.....	130
3.4	Data Processing	134
3.5	Analysis methods.....	138
3.5.1	FT-IR.....	138
3.5.2	Raman.....	138
3.5.3	TGA.....	139
3.5.4	XPS.....	140
3.5.5	TEM.....	141
3.5.6	Zeta potential.....	142
3.5.7	UV-Vis	143
3.5.8	KD2-PRO	144
3.5.9	Rheometer	145
3.5.10	Density.....	146
3.5.11	DSC	147

CHAPTER 4: SYNTHESIS, CHARACTERIZATION, THERMO-PHYSICAL PROPERTIES, CONVECTIVE HEAT TRANSFER AND HYDRODYNAMIC PROPERTIES OF WATER-BASED GALLIC ACID-TREATED GRAPHENE NANOPLATELET NANO-COOLANT 148

4.1	Characterization of GA-functionalized GNPs.....	148
4.2	Thermo-physical properties of GAGNPs nanofluids	156
4.3	Heat transfer and hydrodynamic properties.....	163
4.3.1	Validation of the experimental results.....	163
4.3.2	GA-treated GNPs aqueous suspensions	165

CHAPTER 5: CHARACTERIZATION, THERMO-PHYSICAL PROPERTIES, CONVECTIVE HEAT TRANSFER AND HYDRODYNAMIC PROPERTIES OF WATER-BASED CLOVE-TREATED GRAPHENE NANOPATELET NANO-COOLANT.....	170
5.1 Characterization of Clove functionalized GNPs.....	170
5.2 Thermo-physical properties of water-based CGNPs nano-coolants.....	179
5.3 Heat transfer and hydrodynamic properties.....	184
CHAPTER 6: CHARACTERIZATION, THERMO-PHYSICAL PROPERTIES, CONVECTIVE HEAT TRANSFER AND HYDRODYNAMIC PROPERTIES OF WATER-BASED SRGO NANO-COOLANTS	189
6.1 Characterization of SrGO	189
6.2 Thermo-physical properties of SrGOs nanofluids	198
6.3 Heat Transfer and hydrodynamic properties	205
CHAPTER 7: CHARACTERIZATION, THERMO-PHYSICAL PROPERTIES, CONVECTIVE HEAT TRANSFER AND HYDRODYNAMIC PROPERTIES OF WATER-BASED GAMWCNT NANO-COOLANT	210
7.1 Characterization of GAMWCNT	210
7.2 Thermo-physical properties of GAMWCNTs nanofluids	218
7.3 Heat Transfer and hydrodynamic properties	224
CHAPTER 8: MODELING OF TURBULENT CONVECTIVE HEAT TRANSFER OF NANOFUIDS CONTAINING GREEN COVALENTLY FUNCTIONALIZED GRAPHENE NANOPATELETS IN A HORIZONTAL CIRCULAR HEATED TUBE.....	230
8.1 Validation of simulation results.....	237

CHAPTER 9: CONCLUSIONS.....	244
References.....	247
List of Publications	280
Appendix A.....	282

University of Malaya

LIST OF FIGURES

Figure 1.1: Research Process Flowchart	7
Figure 2.1: Growing trend of published papers related to nanofluids ("Web of Science," 2017).....	10
Figure 2.2: Various types of carbon nanostructures ("Carbon Nanotube TEM Image," 2017; Ksenevich et al., 2016).....	12
Figure 2.3: Different types of CNTs and their corresponding TEM images (Hanelt et al., 2011; Center; Center; Microphase Co.)	14
Figure 2.4: Structure of graphene nanoplatelets and their corresponding TEM image ..	15
Figure 2.5: Schematic of the modified magnetron sputtering system used to prepare nanofluids (Yujin Hwang et al., 2008).....	23
Figure 2.6: Schematic of the high-pressure homogenizer used to produce nanofluids (Yujin Hwang et al., 2008).....	25
Figure 2.7: (A) Transmission Electron microscope images of the agglomerated CNTs (Pawel Koblinski, Eastman, & Cahill, 2005) and (B) graphene sheets (Hiemenz, 1986).....	26
Figure 2.8: Primary CNT functionalization methods (J. Chen et al., 1998).....	32
Figure 2.9: Schematic showing modification of a SWCNT tip by coupling amine (RNH ₂) to a terminal (–COOH) and the application of this probe to sense specific interactions between the functional group (R) and surface –OH groups (Wong et al., 1998).....	33
Figure 2.10: Schematic showing the oxidation of covalently functionalized: (A) GNPs (Yarmand et al., 2016) and (B, C) CNTs (Weydemeyer, Sawdon, & Peng, 2015).....	34
Figure 2.11: Amidation reaction of CNTs (Y.-P. Sun et al., 2002)	36
Figure 2.12: Experimental procedure for chemical-assisted functionalization of GNP with PEG and Azo (Amiri, Shanbedi, et al., 2015).....	37
Figure 2.13: (A) Chemical esterification of modified carbon nanotubes and (B) synthesis procedure for chemical grafting of CH ₂ OH-terminated P3HT chains onto graphene (D. Yu et al., 2010).....	38

Figure 2.14: Covalent functionalization of SWCNTs by alkylhalides (Y. Xu et al., 2008)	39
Figure 2.15: (A) Experimental procedure for chemical-assisted functionalization of GNP with ethylene glycol (Amiri, Sadri, Shanbedi, Ahmadi, Kazi, et al., 2015) and (B) electrophilic addition reaction of GNP with TEA (Sarsam, Amiri, Zubir, et al., 2016)	40
Figure 2.16: Schematic representation of the “grafting to” approach for functionalization of nanotubes with polymers (Homenick, Lawson, & Adronov, 2007)	42
Figure 2.17: Schematic diagram of the complete functionalization strategy, where the first step involves radical addition to the sidewalls of CNTs and the second step involves redox radical grafting of polyacrylamide chains (Tasis et al., 2007)	42
Figure 2.18: Schematic representation of the “grafting from” approach used to functionalize nanotubes with polymers (Homenick et al., 2007)	43
Figure 2.19: Dispersant-CNT interactions (Fujigaya & Nakashima, 2015)	44
Figure 2.20: Schematic diagram showing the dynamic (upper) and static (lower) dispersion of CNTs (Fujigaya & Nakashima, 2015)	46
Figure 2.21: Schematic showing the procedure of the filtration process (Fujigaya & Nakashima, 2015)	47
Figure 2.22: Schematic showing the preparation and functionalization of graphene (C.-C. Teng et al., 2011)	49
Figure 2.23: Endohedral polymerization of C ₆₀ O inside the CNT (Britz & Khlobystov, 2006)	49
Figure 2.24: Schematic of the interactions between the CNTs and tannic acid: (A) The adsorbed TA monolayer sorbs more of the dissolved tannic acid molecules; (B) The thick lines in the figure represent the chemical bond linking to pyrogallol which interacts with the back side of the CNTs (Lin & Xing, 2008)	53
Figure 2.25: Schematic showing the Brownian motion of nanoparticles	76
Figure 2.26: Illustration of a nanofluid, which is a heterogeneous mixture of solid and liquid materials	81
Figure 2.27: Laminar shear flow in a straight pipe where the shear stress is proportional to the velocity gradient	84

Figure 3.1: Schematic diagram of the preparation procedure of the clove extract solution	118
Figure 3.2: Schematic diagram of (a) initiation reaction for free radical grafting, (b) Formation of CGNPs by free radical grafting technique	119
Figure 3.3: Synthesis of Gallic acid-treated GNPs	120
Figure 3.4: Synthesis of Gallic acid-treated GNPs and MWCNTs.....	121
Figure 3.5: Schematic diagram of the covalent functionalization process of GNPs (A) and MWCNTs with gallic acid(B)	123
Figure 3.6: Schematic diagram of preparation and oxidation of graphite.....	125
Figure 3.7: Schematic diagram of chemical composition of saffron	126
Figure 3.8: Procedure used to prepare the saffron reduced graphene oxide	128
Figure 3.9: Schematic diagram of reduction reaction of graphene oxide by saffron	129
Figure 3.10: (a) Schematic diagram and (b) Image of the experimental set-up for the measurement of convective heat transfer	133
Figure 3.11: Sectional view of the experimental test section.....	133
Figure 3.12: FT-IR spectroscopy (Bruker, IFS-66/S, Germany)	138
Figure 3.13: Raman spectra (Renishaw in Via)	139
Figure 3.14: Thermogravimetric analysis (TGA-50, Shimadzu, Japan).....	140
Figure 3.15: Axis Ultra-DLD system, Kratos Analytical X-ray photoemission spectrometer (XPS)	141
Figure 3.16: Hitachi HT7700 transmission electron microscope	142
Figure 3.17: Malvern Instruments Ltd Zeta sizer.....	143
Figure 3.18: Shimadzu UV-1800 spectrophotometer	144
Figure 3.19: Thermal conductivity measurements set up	145
Figure 3.20: Anton Paar rheometer	146
Figure 3.21: DE-40 density meter, Mettler Toledo.....	146

Figure 4.1: (A) FTIR spectra, (B) thermogravimetric analysis of the pristine and GA-treated GNPs nanoparticles	149
Figure 4.2: (A) Raman spectra and (B) wide-scan O1s and C1s XPS spectra for pristine GNPs and GAGNPs	150
Figure 4.3: C1s XPS spectra for (A) pristine GNP and (B) GAGNP, and O1s XPS spectra for (C) pristine GNP and (D) GAGNP	152
Figure 4.4: TEM images of (A) pristine and, (B) GA-treated GNPs nanoparticles and (C) zeta potential values of GAGNP-water nanofluid as a function of pH	153
Figure 4.5: (a)UV-vis spectroscopy analyses of water-based GAGNPs nanofluids at different concentrations and wavelengths, (b) absorption values of GAGNPs dispersed in DI water at different concentrations.....	155
Figure 4.6: (A)The colloidal stability of GA-functionalized GNPs dispersed in water, (B) photograph of GA-treated GNPs dispersed in water after 3 months ...	156
Figure 4.7: Thermal conductivity of GA-treated GNPs aqueous suspensions and DI water	157
Figure 4.8: Dynamic viscosity of GA-treated GNPs nanofluids and DI water as a function of temperature and weight concentration for shear rate of 150 s^{-1}	158
Figure 4.9: Dynamic Viscosity of water-based GAGNPs nanofluids in comparison with those calculated with Batchelor and Einstein model as functions of concentration and temperature	160
Figure 4.10: Plots of the measured values of dynamic viscosity versus shear rate for GAGNPs aqueous nanofluids at various weight concentrations ((A) DI water,(B) 0.025 wt%,(C) 0.075 wt% and (D) 0.1 wt %) and temperatures	161
Figure 4.11: Variation of Specific heat capacity of Gallic acid-treated GNPs aqueous suspensions versus temperature at different weight concentrations.....	162
Figure 4.12: (a) Variation of local Nusselt number versus the conduit axial distance for DI water. (b) Comparison of measured Nusselt number of DI water with the empirical correlations. (c) Comparison of the measured friction factors for DI water with the empirical.....	165
Figure 4.13: Variations of (A) average heat transfer coefficient and (B) Nusselt number of GA-treated GNPs aqueous suspensions as a function of Reynolds number at various concentrations	166

Figure 4.14: Variation of pressure drop (A) and friction factor of GA-treated GNPs(B) as a function of Reynolds number for various concentrations	167
Figure 4.15: Relative pumping power of the GAGNP-water nanofluids and distilled water	168
Figure 4.16: The performance index of the GA-treated GNPs versus Reynolds number at different concentrations	169
Figure 5.1: (A) FTIR spectra of pristine GNPs and C-GNPs, (B) TGA curves, and (C) Raman spectra of pristine GNPs and CGNPs	171
Figure 5.2: (a) Wide-scan XPS spectra for the GNPs and CGNPs; High-resolution XPS spectra of the deconvoluted peak components for C1s: (b) GNPs, (c) CGNPs; High-resolution XPS spectra of the deconvoluted peak components for O1s: (d) GNPs, (e) CGNPs.....	174
Figure 5.3: (a) TEM image of (a) pristine GNPs , (b) Clove-functionalized GNPs and (c) zeta potential values of the CGNP nanofluid as a function of Ph.....	176
Figure 5.4: (a) UV–vis spectroscopy analyses of water-based CGNPs nanofluids at different concentrations and wavelengths, (b) absorption values of CGNPs dispersed in DI water at different concentrations and (c) colloidal stability of Clove-treated GNPs dispersed in DI water	178
Figure 5.5: Variation of (a) thermal conductivity, (b) dynamic viscosity and (c) specific heat capacity of CGNP-water nano-coolants at different temperature and particle concentration	181
Figure 5.6: Plots of the measured values of dynamic viscosity versus shear rate for CGNPs aqueous nanofluids at various weight concentrations ((A) DI water,(B) 0.025 wt%,(C) 0.075 wt% and (D) 0.1 wt %) and temperatures	182
Figure 5.7: Dynamic Viscosity variation of water-based CGNPs nanofluids in comparison with those calculated with Batchelor and Einstein model as functions of concentration and temperature	183
Figure 5.8: (a) average heat transfer coefficient and (b) average Nusselt number of the CGNP-water nano-coolants and distilled water at various Reynolds number	185
Figure 5.9: Variation of (a) pressure drop and (b) friction factor as a function of Re for the CGNP-water nanofluids in the test section	186
Figure 5.10: Relative pumping power of the CGNP-water nanofluids and distilled water	187

Figure 5.11: Performance index of CGNP-water aqueous suspensions as a function of Reynolds number.....	188
Figure 6.1: (A) FTIR spectra of graphene oxide(GO) and SrGO, (B) TGA curves of GO and SrGO.....	190
Figure 6.2: (A) Raman spectra and (B) wide-scan O1s and C1s XPS spectra for Graphene oxide and SrGOs.....	192
Figure 6.3: C1s XPS spectra for (A) graphene oxide and (B) saffron reduced graphene oxides, O1s XPS spectra for (C) GO and (D) SrGO, and N1s XPS spectra for (E) SrGO.....	193
Figure 6.4: (A) TEM images of SrGO and (B) Zeta potential values of the SrGO nanofluid as a function of pH.....	196
Figure 6.5: (A) UV-vis spectroscopy analyses of water-based SrGO nanofluids at different concentrations and wavelengths, (B) absorption values of SrGO dispersed in DI water at different concentrations and (C) colloidal stability of SrGO dispersed in DI water.....	198
Figure 6.6: Thermal conductivity variation of water-based SrGO nano-coolants and DI water as a function of temperature and weight concentration.....	200
Figure 6.7: Dynamic viscosity of water-based SrGO nanofluids and DI water as a function of temperature and weight concentration at shear rate of 150 s^{-1}	201
Figure 6.8: Viscosity of water-based SrGO nanofluids compared with those calculated by theoretical models as function of concentration and temperature at the shear rate of 150 s^{-1}	202
Figure 6.9: Plots of the measured values of dynamic viscosity versus shear rate for SrGO aqueous nanofluids at various weight concentrations((A) DI water,(B) 0.025 wt%,(C) 0.075 wt% and (D) 0.1 wt %) and temperatures.....	203
Figure 6.10: Variation of specific heat capacity of water-based SrGO nano-coolants at different temperature and particle concentration.....	204
Figure 6.11: (A) Average Nusselt number of the water-based SrGO nanofluid and distilled water at various Reynolds number and (B)Average heat transfer coefficient of the water-based SrGO nanofluid and distilled water at various Reynolds number.....	206
Figure 6.12: Variation of (a) Pressure drop and (b) friction factor of water-based SrGO nano-coolants as a function of Reynolds number for various concentrations.....	207

Figure 6.13: Relative pumping power of the water-based SrGO nano-coolants and distilled water	208
Figure 6.14: Performance index Variation of the water-based SrGO nanofluids versus Reynolds number at different concentrations.....	209
Figure 7.1: (A) FTIR spectra of pristine MWCNTs and GAMWCNTs, and (B) TGA curves of pristine MWCNTs and GAMWCNTs.....	211
Figure 7.2: (A) Raman spectra and (B) wide-scan O1s and C1s XPS spectra for pristine MWCNTs and GAMWCNTs.....	212
Figure 7.3: C1s XPS spectra for (a) pristine MWCNTs and (b) GAMWCNTs, and O1s XPS spectra for (c) pristine MWCNTs and (d) GAMWCNTs.....	213
Figure 7.4: (A, B) TEM images of pristine MWCNTs and GAMWCNTs, and (C) zeta potential values of GAMWCNT-water nanofluid as a function of Ph.....	216
Figure 7.5: (A) UV-vis spectroscopy analyses of water-based GAMWCNTs nanofluids at different concentrations and wavelengths, (B) absorption values of GAMWCNTs dispersed in DI water at different concentrations and (C) colloidal stability of GAMWCNTs dispersed in DI	217
Figure 7.6: Dynamic viscosity of water-based GAMWCNT nanofluids as a function of temperature at various concentrations.....	219
Figure 7.7: Viscosity of water-based GAMWCNTs nanofluids compared with those calculated by theoretical models as function of concentration and temperature at the shear rate of 150 s^{-1}	220
Figure 7.8: Plots of the measured values of dynamic viscosity versus shear rate for GAMWCNTs aqueous nanofluids at various weight concentrations((A) DI water,(B) 0.025 wt%,(C) 0.075 wt% and (D) 0.1 wt %) and temperatures.....	221
Figure 7.9: Effective thermal conductivity of water-based GAMWCNT nanofluids as a function of temperature at various concentrations	222
Figure 7.10: Specific heat capacity variation of water-based GAMWCNT nanofluids as a function of temperature at various concentrations	223
Figure 7.11: (A) average heat transfer coefficient and (B) average Nusselt number of the GAMWCNT-water nano-coolants and distilled water at various Reynolds number.....	226
Figure 7.12: Variation of (a) pressure drop and (b) friction factor as a function of Re for the GAMWCNT-water nanofluids in the test section.....	227

Figure 7.13: Relative pumping power of the GAMWCNT -water nanofluids and distilled water	228
Figure 7.14: Performance index Variation of the water-based GAMWCNT nanofluids versus Reynolds number at different concentrations	229
Figure 8.1: Geometry of the three-dimensional horizontal circular heated tube	231
Figure 8.2: Grid of the solution domain.....	231
Figure 8.3: Grid independence test for the (a) Nu number and (b) pressure drop as a function of the Re number.....	235
Figure 8.4: Comparison of the (a) average Nu number and (b) friction factor between simulation, experiment, and empirical correlations for DI water	239
Figure 8.5: Variation of local Nusselt number along the horizontal tube for DI water in the turbulent flow regime at different Re numbers	240
Figure 8.6: Comparison of the (a) average heat transfer coefficient and (b) pressure drop of the CGNP-water nanofluids between simulations and experiments.....	241
Figure 8.7: Temperature distribution contours of the horizontal tube for (a) DI water and (b) CGNP nanofluid at $Re = 6,371$ and uniform heat flux of $12,752 \text{ W/m}^2$	243

LIST OF TABLES

Table 2.1: Various methods of synthesizing graphene sheets.....	19
Table 2.2: Summary of green methods used for reduction of GO	58
Table 2.3: Theoretical and empirical equations used to predict the effective thermal conductivity of nanofluids.....	67
Table 2.4: Literature review on the experimental study of effective thermal conductivity of carbon allotropes-based aqueous nanofluid	78
Table 2.5: Summary of models used to predict the effective dynamic viscosity.....	86
Table 2.6: Summary of the empirical correlations developed to determine the Nu number of flows through ducts.....	96
Table 2.7: Literature review on the experimental study of forced convective heat transfer of carbon allotropes-based nanofluid	101
Table 3.1: Specifications and errors of the measuring instruments and sensors used in the present experiment	134
Table 4.1: Raman spectra analysis results for pristine GNPs and GAGNPs	150
Table 4.2: XPS analysis results for pristine GNPs and GAGNPs.....	152
Table 4.3: Density of GA-treated GNPs and DI water as a function of temperature and concentration	162
Table 5.1: Raman spectra analysis results for pristine and clove-treated GNPs.....	172
Table 5.2: XPS analysis results for GNPs and CGNPs.....	175
Table 5.3: Density of CGNP-water nano-coolants and DI water as a function of temperature and particle concentration	184
Table 6.1: XPS analysis results for GO and SrGO	194
Table 6.2: Density of water-based SrGO nanofluid and DI water as a function of temperature and concentration	204
Table 7.1: Raman spectra analysis results for pristine MWCNTs and GAMWCNTs..	212
Table 7.2: XPS analysis results for pristine and GAMWCNTs.....	214

Table 7.3: Density of water-based GAMWCNT nano-coolants and DI water as a function of temperature and concentration.....	224
Table 8.1: Thermo-physical properties of the CGNP nanofluid at an inlet temperature of 30°C.....	232
Table 8.2: Effect of grid size on the Nu number for DI water.....	235
Table 8.3: Effect of grid size on the pressure drop for DI water.....	236
Table A.1: Rang of uncertainty for instrument used in the present investigation.....	282
Table A.2: Uncertainty ranges.....	283

University of Malaya

LIST OF SYMBOLS AND ABBREVIATIONS

P	: Power, Watts
Pr	: Prandtl number
Q	: Heat flow, Watts
\dot{q}	: Heat flux, W/m ²
Nu	: Nusselt number
h	: heat transfer coefficient
Re	: Reynolds number
Pr	: Prandtl number
T	: Temperature, °C
u	: Velocity, m/s
x	: Axial distance
GNP	: Graphene nanoplatelet
MWCNT	: Multi-walled carbon nanotube
GAGNP	: Gallic acid-treated graphene nanoplatelet
GAMWCNT	: Gallic acid-treated multi-walled carbon nanotube
CGNP	: Clove-treated graphene nanoplatelet
GO	: Graphene oxide
SrGO	: Saffron-reduced graphene oxide
wt%	: weight percentage
W	: Watt
TEM	: transmission electron microscopy
XPS	: X-ray photoelectron spectroscopy
FTIR	: Fourier transform infrared spectroscopy
TGA	: thermogravimetric analysis

Uv-vis	:	ultraviolet-visible spectroscopy
SDBS	:	Sodium dodecyl benzene sulfonate
SDS	:	Sodium dodecyl sulfonate

Greek symbols

Δp	:	Pressure drop
ε	:	Performance Index
λ	:	Wall thermal conductivity
μ	:	Dynamic viscosity, kg/m ² .s
ρ	:	Density, kg/m ³
τ	:	Shear stress, Pa
ω	:	Fiber coarseness, kg/m
K	:	Thermal conductivity, W/m.K
φ	:	Mass fraction

Subscripts

b	:	bulk
i	:	inlet
m	:	mass
o	:	outlet
t	:	Thermocouple
w	:	wall
bf	:	base fluid
nf	:	nanofluid
avg	:	average

CHAPTER 1: INTRODUCTION

Due to rapid development in industry and transportation followed by fast increment in energy consumption, saving energy is a vital issue; further, managing high thermal loads has become critical. Heat transfer is a significant key in many sectors such as air conditioning, power generation, and microelectronics due to having the heating and cooling systems. It is favorable to improve the Heat transfer efficiency of systems employed in these sectors; such this development can make it possible to minimize the size of heat transfer equipment and reduce the operating costs of the corresponding processes. Thus, several efforts have been performed to increase the heat transfer properties in this equipment. One important factor in heat transfer is the thermal conductivity of the working liquids. Generally, the conventional fluids such as engine oil, ethylene glycol and water used in heat transfer application possess very low thermal conductivity. Therefore, the scientists made efforts to discover a method in order to modify the thermal conductivity of such these liquids. One of the techniques to reach this goal is to produce mixtures by adding solid particles (millimeter or micrometer sized) especially metals which have higher thermal conductivity compared to the base fluids. Over the years the metals and metal oxides had been employed for enhancement of thermal conductivity of the conventional liquids (Ahuja, 1975a, 1975b; Hetsroni & Rozenblit, 1994; S. Lee, S. U. Choi, S. Li, and, & J. Eastman, 1999; Sohn & Chen, 1981; Xuan & Li, 2000). However, these mixtures cannot be utilized in practical applications due to creating problems such as erosion, fouling, sedimentation, channel clogging and enhanced pressure drop of the flow which elevates the needed pumping power and related operating costs. (Kebinski et al. 2002; Wanget al. 2003). Accordingly, due to these critical drawbacks, utilization of millimeter or micrometer sized particles has not been feasible.

The latest development in nanotechnology made it feasible to develop solid particles with a diameter smaller than 100 nm. As a consequence, an innovative idea of preparing liquid suspensions by dispersing these nanoparticles instead of millimeter- or micrometer-sized particles in a base fluid and utilizing them for heat transfer enhancement was proposed (S. U. Choi & Eastman, 1995; Masuda, Ebata, & Teramae, 1993). These liquid suspensions are called nanofluids. An important feature of nanofluids is that since nanoparticles are very small, they behave like fluid molecules and the better stability of nanofluids will prevent fast sedimentation and decline clogging in heat transfer devices.

It is even possible to use nanofluids in small passages such as microchannels (Chein and Chuang 2007; Lee and Mudawar 2007). It was also shown that by the use of proper activators and dispersants, it is possible to obtain stable suspensions. The high thermal conductivity of nanofluids translates into higher energy efficiency, better performance, and lower operating costs. They can reduce energy consumption for pumping heat transfer fluids. Miniaturized systems require smaller inventories of fluids where nanofluids can be used. Thermal systems can be smaller and lighter. In vehicles, smaller components result in better gasoline mileage, fuel savings, lower emissions, and a cleaner environment.

This new generation of conductive fluids with nanoparticles are referred to as nanofluids (Choi, 1995; Mohd Zubir et al., 2016). Various nanoparticles, such as carbon base nanomaterials and metal-oxides (copper oxide (CuO), aluminum oxide (Al₂O₃), Fe₂O₃ and silicon dioxide (SiO₂)) have been used to produce nanofluids with enhanced thermal conductivity. Recently, remarkable enhancement in thermo-physical, rheological and heat transfer properties of carbon based nanofluids was reported in the literature (Yulong Ding, Alias, Wen, & Williams, 2006; V. Singh & Gupta, 2016;

Zubir, Badarudin, Kazi, Huang, Misran, Sadeghinezhad, Mehrali, Syuhada, et al., 2015). Wang et al.(X. Wang, Xu, & S. Choi, 1999) estimated the viscosity of Al₂O₃ and CuO nanoparticles dispersed in water, vacuum pump fluid, engine oil and ethylene glycol and found 30% enhancement with Al₂O₃/water nanofluid at 3% volume concentration. Suresh et al.(Suresh, Chandrasekar, Selvakumar, & Page, 2012) experimentally investigated the convective heat transfer and friction factor characteristics in the plain and spiraled rod inserts in a plain tube under laminar flow with constant heat flux is carried out with Al₂O₃-water nanofluids. The experimental results of Nusselt number for 0.5% nanofluid with spiralled rod inserts under laminar flow showed a maximum of 24% higher than the plain tube and the isothermal pressure drop of nanofluids with spiraled rod inserts were about 5% to 15% higher than the plain tube. Syam Sundar et al.(Sundar, Singh, & Sousa, 2013) studied the experimental and theoretical determination of effective thermal conductivity and viscosity of magnetic Fe₃O₄/water nanofluid. The thermal conductivity and viscosity of the nanofluid suspensions were increased with an increase in the particle volume concentration. Viscosity enhancement was greater compared to thermal conductivity enhancement under the same volume concentration and temperature. Among different nanoparticles, carbon nanotubes (CNTs) in single, double, or multi-walled types as one dimensional carbon nanostructures and graphene nanoplatelets as two dimensional carbon nanostructures have attracted special interest due to unique thermal, mechanical and electrical properties which make them suitable candidate for heat transfer issues. Choi et al. (S. U. Choi & Eastman, 2001) observed 160% thermal conductivity enhancement with CNTs dispersed in synthetic poly (α -olefin) oil at 1.0% volume concentration. Bobbo et al.(Bobbo et al., 2012) investigated the viscosity of SWCNT/DI water and TiO₂/DI water nanofluids and found 12.9% and 6.8% enhancement at 1.0% volume concentration respectively. Sadri et al. (Sadri et al., 2014b)

studied the sonication time effect on the dynamic viscosity, thermal conductivity and dispersion of MWCNT aqueous suspensions. The results represented that the viscosity decreases, whereas the thermal conductivity of the nanofluids increases with an increase in temperature and sonication time. The maximum thermal conductivity enhancement was found to be 22.31% (ratio of 1.22) at a temperature and sonication time of 45°C and 40 min, respectively. The heat transfer and friction factor characteristics of multi-walled carbon nanotubes-Fe₃O₄ (MWCNT-Fe₃O₄) nanocomposite nanofluids flow in a tube with longitudinal strip inserts were studied by Syam Sundar and his coworkers (Sundar, Otero-Irurueta, Singh, & Sousa, 2016). From the results, the Nusselt number enhancement for 0.3% nanofluid flow in a tube without inserts is 32.72% and with inserts of aspect ratio 1 is 50.99% at a Reynolds number of 22,000. Graphene nanoplatelets, a two-dimensional atomic sp² carbon layer, by representing outstanding properties such as high specific surface area and excellent thermal conductivity have attracted researchers in the last few years (Loh, Bao, Ang, & Yang, 2010). These unique properties make it a promising additive for many applications such as inkjet printing, conductive thin films, solar cells, polymer composites, aerogels and heat exchangers (Allen, Tung, & Kaner, 2009; Worsley et al., 2010). Nevertheless, the peculiar characteristics of a nanofluid cannot be achieved simply by mixing the pure fluid with nanoparticles. In fact, to high specific surface area, graphene presents tendency to agglomerate by strong π - π stacking interaction, while the dispersibility of graphene in aqueous media is considered as one of the most important factor in heat transfer equipment, films and composites (Mohd Zubir et al., 2016; Y. Yang, Qiu, Xie, Wang, & Li, 2010). Hence several methods were employed to improve stability of graphene in aqueous and organic media by chemical and physical methods containing covalent and non-covalent functionalization of graphene (Q. Yang, Pan, Huang, & Li, 2010). To achieve highly disperses carbon nanomaterials in aqueous media, researchers commonly

select covalent functionalization in which, the hydrophilic functional groups like carboxyl acid, amine esters, alkalis group are attached on the surface of GNP by employing oxidizing, radical addition and alkali metal reduction (An et al., 2010; Y.-P. Sun, Fu, Lin, & Huang, 2002). Among them the free radical coupling is a promising method of functionalization carbon nanostructure has depicted facile way of covalent functionalization. In this method peroxides and substituted anilines (Tasis, Papagelis, Prato, Kallitsis, & Galiotis, 2007), were utilized as starting materials.

Even though these chemical routes are generally reliable to synthesize functionalized CNTs, these techniques are not environmentally friendly because the reagents used for synthesis are toxic and harmful to the environment. More importantly, some of these chemical routes may cause defects in the lattice which will degrade the inherent characteristics of CNTs.(Y. Yang, S. Qiu, X. Xie, et al., 2010) also their corresponding nanofluids (coolants) cause problems like equipment corrosion, environmental problems and cost of materials. Hence, there is a critical need to develop a simple, efficient, environmentally friendly technique for the dispersion of CNTs, which will be greatly beneficial in the long term since it helps reduce pollution resulting from the use of toxic reagents during syntheses.(Loh et al., 2010)

In addition, Since the Fluids flow in the heat exchangers and their convective heat transfer and hydrodynamic properties are significant phenomena in the engineering systems and widely used in key applications such as nuclear reactors, cooling of electronic devices, boilers, solar energy systems, and thermal storage systems, as a result studies on synthesis of an appropriate working fluids (nano-coolants) and their impact on environment and heat transfer enhancement in heat exchangers are essential.

1.1 Scope of study

The main focus of this work is concerned with the development of environmentally friendly, cost-effective and innovative functionalization techniques for synthesizing new generations of water-based carbon nanostructures nanofluids to use as coolants in order to improve thermal performance and hydrodynamic properties of a single tube heat exchanger. Graphene nanoplatelets (GNPs), multiwalled carbon nanotubes (MWCNTs) were separately functionalized covalently using a green method with clove buds and gallic acid. In a separate experiment, the graphene oxide was reduced using saffron in a one-pot method, followed by dispersing the corresponding treated nanoparticles in distilled water. Then they were characterized via FTIR, Raman, XPS, TGA, TEM and uv-vis. A zeta potential measurement was performed to validate the presence of hydrophilic groups in the nanoparticles. The thermo-physical properties, convective heat transfer and friction loss of nanofluids were experimentally evaluated in a flow loop with a horizontal heated tube test section subjected to a constant heat flux at a various Reynolds number range and weight concentrations. The corresponding pumping power and performance index were also calculated using experimental data for nanofluids. ANSYS–Fluent CFD software was used to predict the performance of the heat exchanger with water-based CGNP nanofluids as the working fluid in single-phase turbulent flow. The following flowchart (Figure 1.1) summarized the present research procedures.

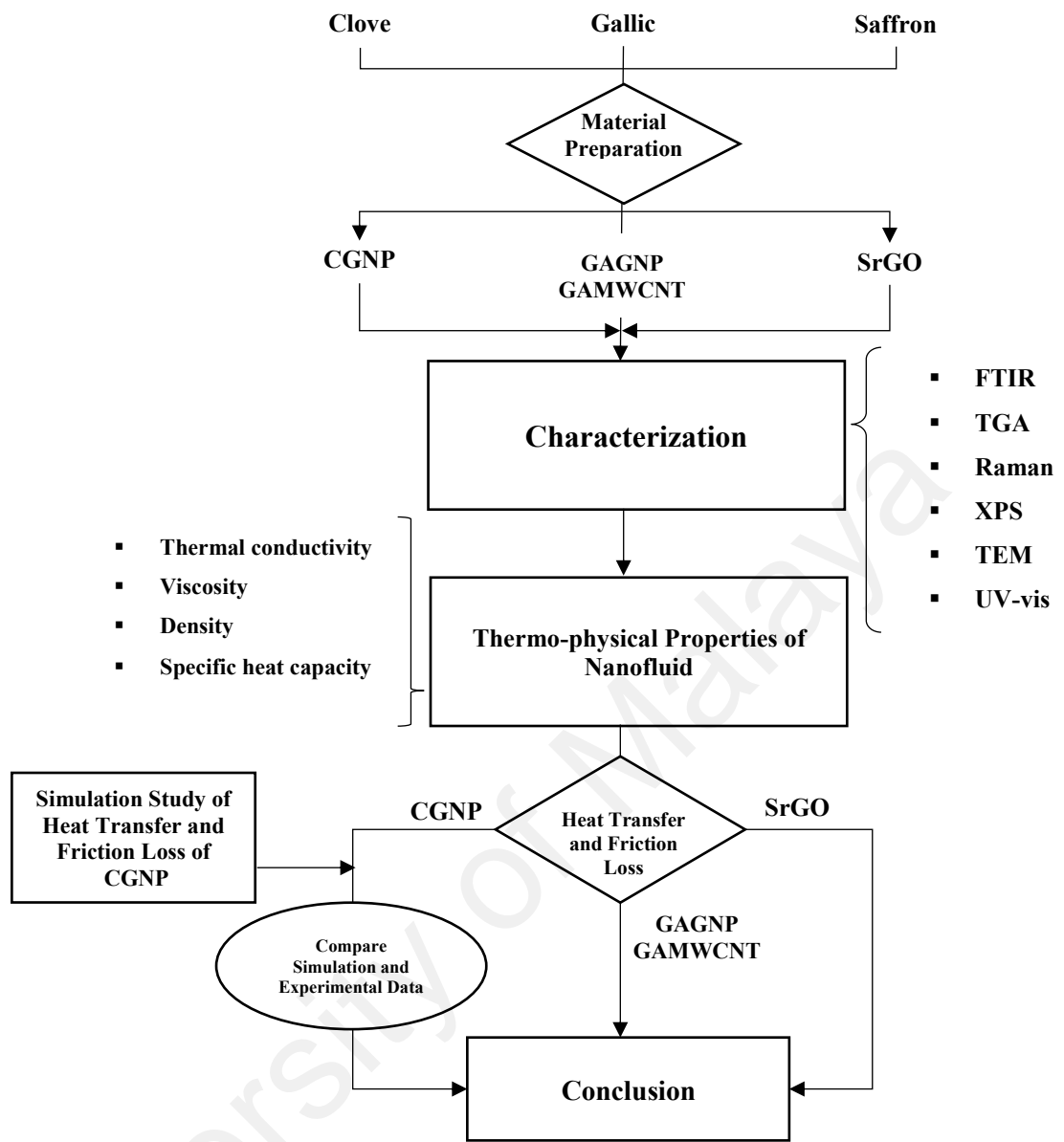


Figure 1.1: Research Process Flowchart

Main aim

Development of environmentally friendly, cost-effective, innovative, covalent functionalization techniques for synthesizing new generations of carbon nanostructures nanofluids to use as coolants to improve the convective heat transfer and hydrodynamic properties of heat exchangers.

1.2 Objectives of the current research

The overall goals of this study are summarized as follows:

1. To develop environmentally friendly, innovative, covalent functionalization techniques for synthesizing water-based carbon nanostructures aqueous suspensions (Nanofluids).
2. To investigate the effectiveness of the covalent functionalization procedure on functionalized carbon nanostructures via material characterization tests.
3. To investigate the thermophysical properties, Analyse the heat transfer and hydrodynamic characteristics of the developed nanofluids flowing in a single tube heat exchanger.
4. To simulate (CFD modeling) turbulent heat transfer to nanofluid flowing in heat exchanger and compare the experimental data with the numerically obtained results.

1.3 Problem statement

1. Low thermal conductivity of conventional working fluids such as Water, Ethylene glycol and Engine Oil.
2. Toxic and hazardous acids are typically used in common carbon nanomaterial functionalization procedures and cause equipment corrosion, environmental problems and cost of materials for synthesis of carbon based nano-coolants.
3. The low stability of Carbon nanomaterials in Base fluids leads to increase the pumping power, energy consumption, and higher operating costs, moreover, decrease the thermal conductivity of nanofluids and heat transfer efficiency.

CHAPTER 2: LITERATURE REVIEW

2.1 Background

Energy optimization is one of the critical issues in various industrial sectors, including building and construction, transportation, and defense. Convective heat transfer plays an important role in minimizing energy consumption of thermal systems such as cooling devices, solar collectors, and heat exchangers, where water, propylene glycol, ethylene glycol, and oil are typically used as coolants. All of these fluids have low thermal conductivities and it is known that thermal conductivity influences the thermal transfer efficiency of thermal systems. In recent years, much effort has been made to disperse nanoparticles with high thermal conductivity into the base fluid in order to solve the aforementioned problem (S. J. Aravind et al., 2011). Studies pertaining to the development of advanced heat transfer fluids began in 1985 at Argon National Laboratory (ANL). Masuda et al. (Masuda, Ebata, Teramae, & Hishinuma, 1993) studied the effect of thermal conductivity and viscosity of ultra-fine alumina, titanium dioxide, and silicon dioxide in Japan. Following Masuda, Choi (S. U. Choi & Eastman, 1995) succeeded in formulating colloidal dispersions containing high thermal conductivity nanoparticles and the term “nanofluids” was coined. Indeed, studies in ANL are the first coherent studies in nanofluids and thermal conductivity enhancement of these fluids. Some of these studies are similar to Masuda’s work while others are different. Previous researchers have reported that nanofluids result in dramatic thermal conductivity enhancement and this has led scientists and researchers from both the academic and industry to explore the properties and applications of nanofluids. The significance of nanofluids is apparent from the increasing number of studies available in the literature related to the subject, as shown in Figure 2.1.

Many scientists and researchers have synthesized nanoparticles and prepared nanofluids for laboratory experiments and industrial applications. They have also

investigated the effect of nanoparticle size, volume fraction of nanoparticles, and fluid temperature.

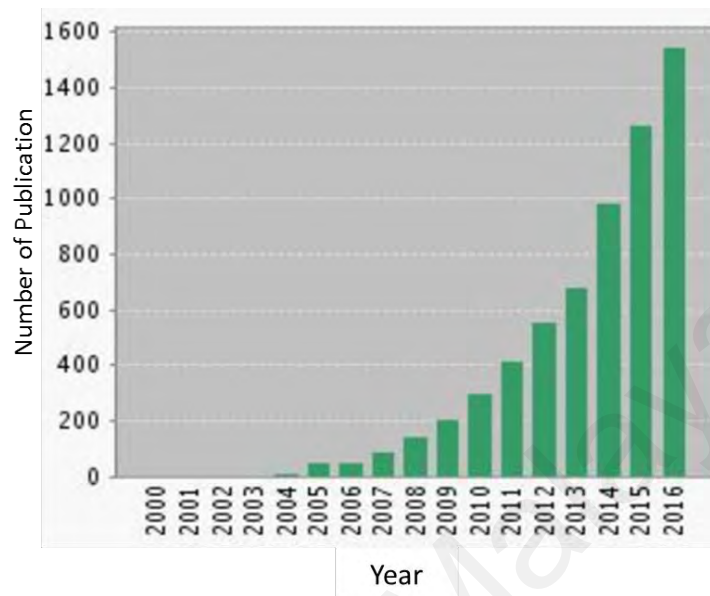


Figure 2.1: Growing trend of published papers related to nanofluids("Web of Science," 2017)

In this chapter, experimental, numerical, and theoretical studies pertaining to the synthesis, thermophysical properties, rheological properties, and heat transfer of nanofluids are reviewed and discussed.

2.2 Nanofluids

Nanofluids are solid-liquid composite materials consisting of nanosized solid particles, fibers, rods, or tubes suspended in different types of base fluids (Chol, 1995). These materials are promising fluids for heat transfer enhancement because of their wide range of benefits including high thermal conductivity. Nanofluids have higher colloidal stability compared with conventional fluids added with micrometer or millimeter-sized solid particles because of the minute size of the nanoparticles and Brownian motion of the nanoparticles in liquids (Baby & Sundara, 2011).

The surface to volume ratio of nanoparticles is higher than that for microparticles by three orders of magnitude. The high surface area of nanoparticles enhances heat conduction of nanofluids and therefore, more of the solid surface takes part in the heat exchange (Saini, Kaur, Sharma, & Gangacharyulu, 2016).

Various nanoparticles such as carbon-based nanomaterials and metal-oxides (e.g., copper oxide (CuO), aluminum oxide (Al₂O₃), iron oxide (Fe₂O₃) and silicon dioxide (SiO₂)) have been used to produce nanofluids with enhanced thermal conductivities. Carbon-based nanofluids have been proven to give remarkable enhancement in thermophysical, rheological, and heat transfer properties (Yulong Ding et al., 2006; V. Singh & Gupta, 2016; Zubir, Badarudin, Kazi, Huang, Misran, Sadeghinezhad, Mehrali, Syuhada, et al., 2015).

2.3 Carbon-based nanomaterials (carbon allotropes)

Carbon nanostructures are carbon allotropes with at least one dimension within the nanometer range. It has been proven that carbon nanomaterials are superior in terms of hardness, optical properties, heat resistance, radiation characteristics, chemical resistance, electrical insulation, electrical conductivity, thermal conductivity, and surface and interfacial properties, compared with other nanomaterials. It is also typically perceived that carbon materials encompass the whole spectrum of characteristics of all substances on the planet from the “the hardest to the softest”, “insulator to semiconductor to superconductor”, “thermal insulator to thermal conductor” and “fully light-absorbing to completely transparent”. For this reason, these materials can be used in a wide range of applications. Carbon nanomaterials have garnered much attention from the scientific community in recent years because of the possibilities to synthesize nanocarbon crystals in various shapes such as sheets, tubes, spheres, and many other morphologies (Yan, Gozin, Zhao, Cohen, & Pang, 2016). The most notable and

extensively studied members of this family are fullerenes, carbon nanotubes (CNTs), and graphene. These carbon nanomaterials are composed of sp^2 hybridized carbon atoms, which create conjugated polycyclic structures of different sizes and shapes. Fullerenes are closed carbon cages with spherical shape (with C60 being the most abundant) or elliptical shape (C70 and other giant fullerenes). For this reason, fullerenes are regarded as zero-dimensional (0D). Single-walled carbon nanotubes (SWCNTs) are rolled-up, seamless graphene cylinders, which are approximately one-dimensional (1D). Graphene, on the other hand, is strictly two-dimensional (2D) because it is formed by flat sheets of carbon with a thickness of one atom (Figure 2.2). It is interesting to note that the following carbon nanoforms can transform into one another under certain conditions. For instance, graphene nanoribbons have been prepared by longitudinal unzipping of CNTs under harsh chemical conditions (Jiao, Zhang, Wang, Diankov, & Dai, 2009; Kosynkin et al., 2009). Fullerenes can be converted into CNT) when these materials are encapsulated within other nanotubes. With the right stimulations, these materials can even be made into double-walled nanotubes (Bandow, Takizawa, Hirahara, Yudasaka, & Iijima, 2001; Pérez & Martín, 2015).

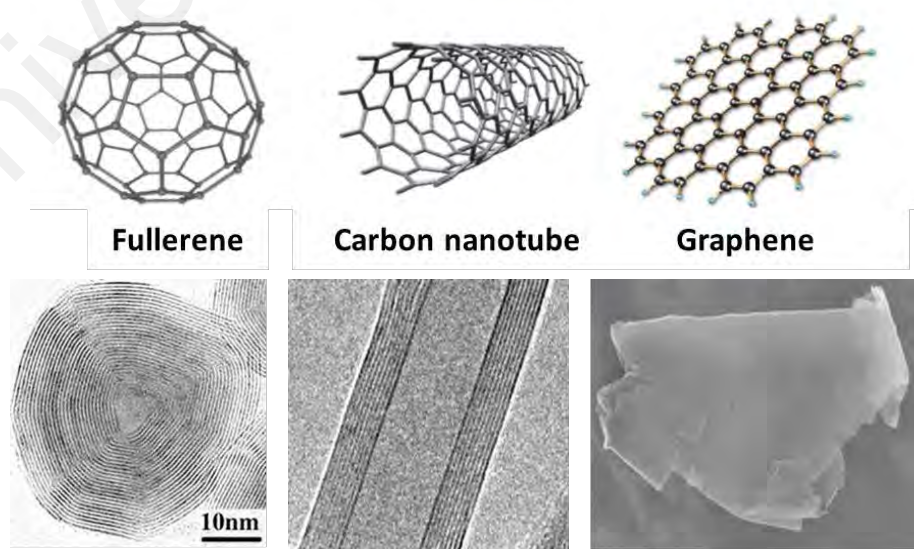


Figure 2.2: Various types of carbon nanostructures("Carbon Nanotube TEM Image," 2017; Ksenevich et al., 2016)

2.3.1 Carbon nanotube

CNTs are pure carbon macromolecules consisting of sheets of carbon atoms covalently bonded in hexagonal arrays that are seamlessly rolled into a hollow cylindrical shape. CNTs typically have an outer diameter within a range of ~1–100 nm and length up to several tens of micrometers. Since the discovery of CNTs in 1991 (Iijima, 1991; Lin & Xing, 2008), these nanomaterials have gained considerable interest among the scientific community because of their unique and outstanding electronic, mechanical, thermal, and chemical properties as well as their potential applications such as energy conversion, quantum nanowires, catalyst supports, and biomedicine. Researchers have also expressed interest on the environmental behavior and ecological risk of CNTs, considering the mass production and wide applications of CNTs (Lam, James, McCluskey, Arepalli, & Hunter, 2006; Lin & Xing, 2008).

There are two types of CNTs, depending on the process used to fabricate the CNTs: (1) single-walled CNTs (SWCNTs) and (2) multiwalled CNTs (MWCNTs). SWCNTs consist of a single graphene layer (Figure 2.3) rolled up into a seamless cylinder whereas MWCNTs consist of two or more concentric cylindrical shells of graphene sheets (Figure 2.3) coaxially arranged around a central hollow core with van der Waals forces between the adjacent layers. Based on a qualitative perspective, the structures of SWCNTs are very similar to those of fullerenes. Thus, it can be reasonably assumed that the same main principles apply, and most supramolecular complexes are based on optimizing the dispersibility of CNTs. The primary difference between fullerenes and SWCNTs is that SWCNTs have significantly higher aspect ratios, which increases interactions within these materials, resulting in the formation of insoluble aggregates.

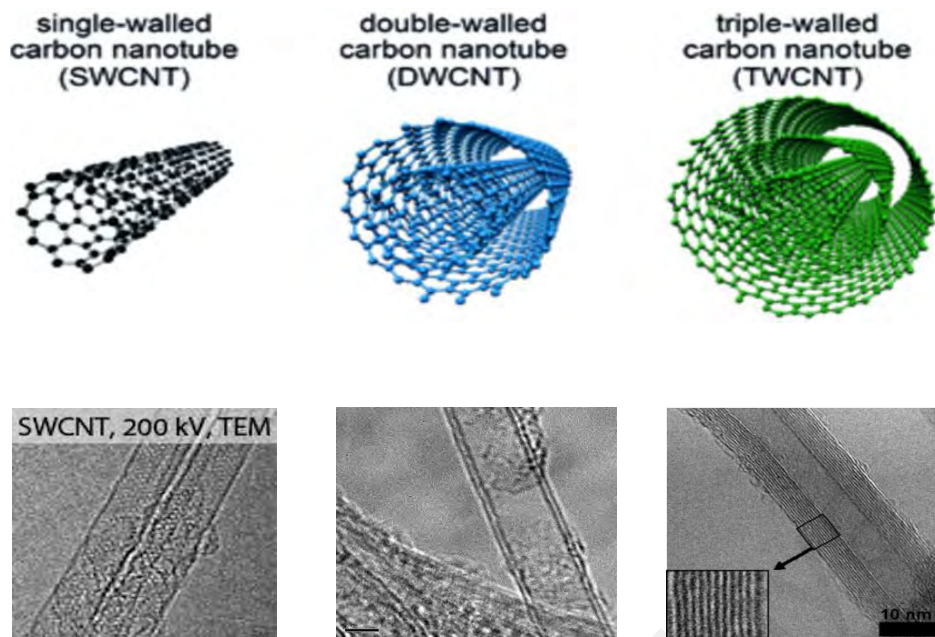


Figure 2.3: Different types of CNTs and their corresponding TEM images(Hanelt et al., 2011; Center; Center; Microphase Co.)

2.3.2 Graphene nanoplatelets

Graphene is composed of an atomically thin, 2D lattice of sp^2 -hybridized carbon (Figure 2.4). This material has demonstrated tremendous potential for a wide range of applications because of its thermal, mechanical, and electrical properties, as proven by analytical and experimental studies (Loh et al., 2010). The remarkable properties of graphene render this material a promising additive for several applications such as inkjet printing, conductive thin films, solar cells, polymer composites, aerogels, and heat exchangers (Allen et al., 2009; Worsley et al., 2010).

The chemical structure of graphene is very similar to that of SWCNTs, although the lack of curvature makes it less reactive in terms of covalent chemistry. In addition, graphene is prone to establish strong van der Waals forces and π - π interactions (Pérez & Martín, 2015).

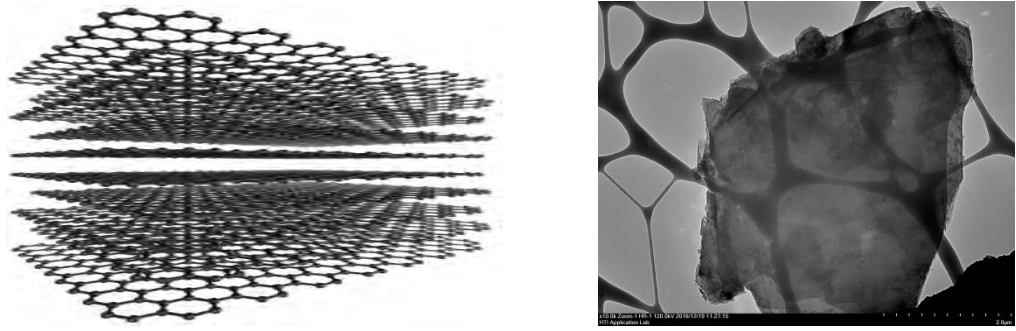


Figure 2.4: Structure of graphene nanoplatelets and their corresponding TEM image

Various methods have been developed to synthesize graphene including one-step and two-step methods. In the former method, graphite is directly converted into graphene. In the latter method, graphite is converted into graphite oxide and the products are then converted into graphene by a reduction process such as solar exfoliation technique (Eswaraiah, Aravind, & Ramaprabhu, 2011; Eswaraiah, Sankaranarayanan, & Ramaprabhu, 2011), mechanical exfoliation of graphite (Hernandez et al., 2008), chemical vapor deposition (CVD) (Bo et al., 2011; Reina et al., 2008), arc discharge process (Zhengzong et al., 2010), unzipping of CNTs (Tanaka et al., 2015), and chemical and thermal reduction of GO (graphene oxide) (Sadri, Zangeneh Kamali, et al., 2017).

Del Rio-Castillo et al. (Del Rio-Castillo, Merino, Díez-Barra, & Vázquez, 2014) synthesized single-layer graphene using the ball-milling exfoliation method, which is a simple, inexpensive, and eco-friendly way to produce high-quality graphene layers (Table 2.1(A)). On the other hand, they used melamine (2,4,6-triamine-1,3,5-triazine) as the exfoliating agent and carbon fibers as the carbon precursor material. The addition of a small amount of solvent during the ball-milling process of carbon fibers significantly improves the exfoliation process, which allows dispersion of single-layer graphene. They also demonstrated the use of Hansen solubility parameters to differentiate between

single-layer graphene and poorly exfoliated fibers. Overall, their method is a facile, inexpensive, and expandable method to synthesize monolayer graphene.

Liu et al. (C. Liu, Hu, & Gao, 2012) successfully synthesized high-quality graphene nanosheets on a large scale through a liquid-phase exfoliation method, otherwise known as electrochemical exfoliation. Few-layer graphene (FG) was produced in supercritical N,N-dimethylformamide (DMF) using expandable graphite (EG) as the starting material in less than 15 min. Monolayer graphene was produced by exfoliation of FG in supercritical DMF (Table 2.1(B)).

Yu et al. (L. Yu, Yasuda, & Murakoshi, 2012) used highly oriented pyrolytic graphite (HOPG) as a carbon source to exfoliate graphene from HOPG with a size of about 510 nm² using electrochemical exfoliation. Table 2.1(C) shows the schematic of the circuit connection of HOPG. Here, HOPG was attached to a tungsten wire by a silver pad and then it was inserted into the electrolyte as the anode of the circuit. A platinum (Pt) sheet was used as the cathode of the circuit in parallel with the HOPG. The results showed that the electrochemical exfoliation method is able to produce high-quality single-layer graphene within the nanometer range. The method is a promising method to realize conductive films for fuel cell applications.

Electrochemical intercalation of sodium dodecyl sulfate (SDS) into graphite and electrochemical exfoliation of the SDS-intercalated graphite are shown in Table 2.1(D). The features of the produced graphene sheets are greatly affected by the value of the electrode potential used for electrochemical intercalation of SDS into the graphite layers (e.g., the number of graphene layers, dimension, and structural order). The intercalation process can only take place when the electrode potential is higher than 1.4 V while a strong intercalation potential is used to produce monolayer graphene films. The intercalation method is advantageous compared with the exfoliation process because it

can prevent the individual exfoliated graphene sheets from restacking in the solution by having the surfactants adsorbed onto the surface of the graphene films. The successful large-scale production of reduced graphene films is a new avenue of research to be explored by scientists for various applications (Alanyalıoğlu, Segura, Oró-Solè, & Casañ-Pastor, 2012).

Another technique that can be used to synthesize graphene layer is to unzip SWCNTs (Table 2.1(E)). CNT is essentially a rolled-up graphene layer and therefore, unzipping a CNT can yield a thin elongated strip of graphene, which is known as “graphene nanoribbon”. Recently, Tanaka et al. (Tanaka et al., 2015) fabricated single-layer graphene nanoribbons (sGNRs) using double-walled carbon nanotubes (DWCNTs). The defects were initially induced in the DWCNTs by annealing them in the air at 500°C, followed by dispersing them in an organic solution. The DWCNTs were subjected to sonication treatment prior to unzipping in order to produce high-quality double-layer graphene nanoribbons (dGNRs). Following this, the dGNRs were further sonicated in order to form individual sGNRs.

The CVD technique involves decomposition of the carbon source molecules in the presence of a precursor in order to synthesize graphene films. Various precursors have been used in the past, comprising solid, liquid, and gas precursors. Gan et al. (Gan et al., 2012) developed a simple, low-temperature method to grow graphene on Cu foils using the CVD technique. Hexachlorobenzene (HCB) was used as the carbon source. In this method, the Cu foil serves as a catalytic substrate and reductant, and reacts with HCB to form the intermediate product C₆. The intermediate product serves as the building block for self-assembly of graphene. Indeed, they obtained high-quality graphene flakes at 360°C (Table 2.1(F)).

The exfoliation of graphite oxide (GO) using focused solar electromagnetic radiation has been discussed by Aravind et al. (Aravind, Eswaraiyah, & Ramaprabhu, 2011). The GO was irradiated with focused sunlight using a convex lens with a diameter of 90 mm. The temperature increased abruptly to 150–200°C within 1–2 s, resulting in exfoliation of GO into graphene. Exposure to the focused sunlight leads to decomposition of the insulating functional groups over the basal planes of GO. This mechanism is known as deflagration of GO. The photoacoustic effect results in a popping sound due to the high-temperature chemical reaction between the surface carbon and surrounding water. The solar exfoliation of GO produced well-separated ultra-thin graphene sheets. Next, the GO was substituted with metal salt-GO composites and the experiment was carried out using a convex lens having a diameter of 100 mm (Table 2.1(G)).

Hydrothermal treatment is a preferable technique in recent years because it is an eco-friendly technique to synthesize reduced graphite oxide (rGO) aqueous suspensions. This technique offers several advantages compared with other chemical reduction processes: (1) it only requires a very simple setup (i.e., an autoclave), (2) it has great scalability and therefore, it is suitable for batch processing, and (3) it retains the purity of the products since it only involves the use of water. Furthermore, this technique is capable of controlling the degree of the reduction process by adjusting the pressure and temperature (Table 2.1(I)) (J. Ding et al., 2012; Sadri, Zangeneh Kamali, et al., 2017).

The schematic of photoreduction of GO is shown in Table 2.1(H). Here, GO is dispersed in water (0.1 mg/mL) by magnetic stirring for 30 min followed by sonication for 1 h. Following this, a few milliliters of GO-water dispersion is degassed under nitrogen atmosphere and the dispersion is placed into an ultraviolet (UV) oven (3D systems, 50/60 Hz) for 48 h under nitrogen atmosphere (Rella et al., 2015).

Table 2.1: Various methods of synthesizing graphene sheets

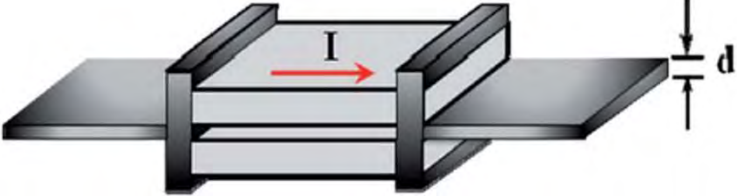
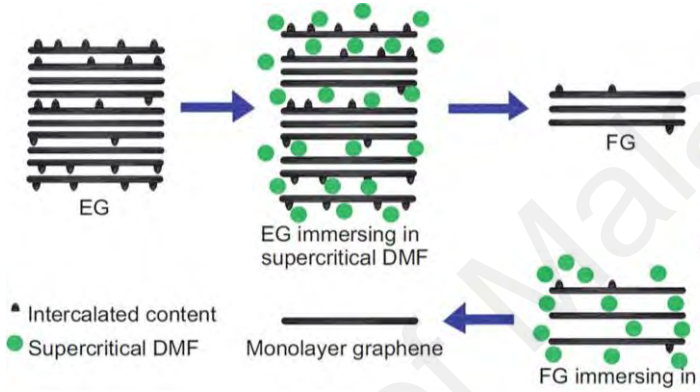
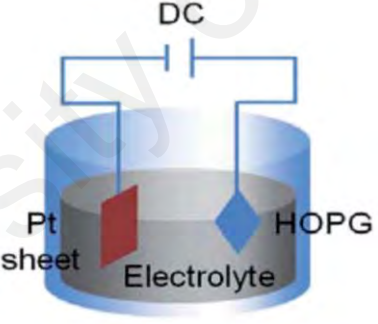
	Schematic of the synthesis method	Name of synthesis method
A		Ball-milling exfoliation (X. Yu et al., 2011)(Single-step method)
B		Electrochemical (C. Liu et al., 2012) (Single-step method)
C		Electrochemical exfoliation (L. Yu et al., 2012) (Single-step method)

Table 2.1, continued

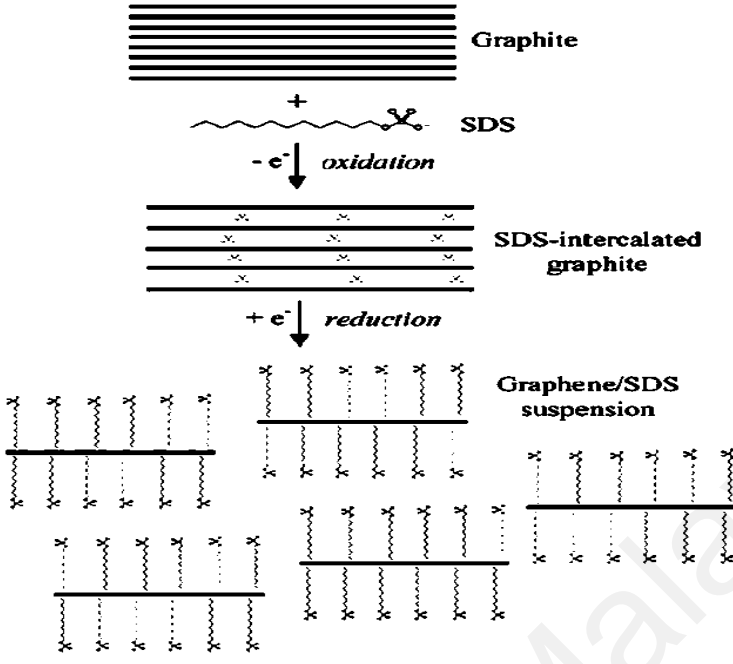
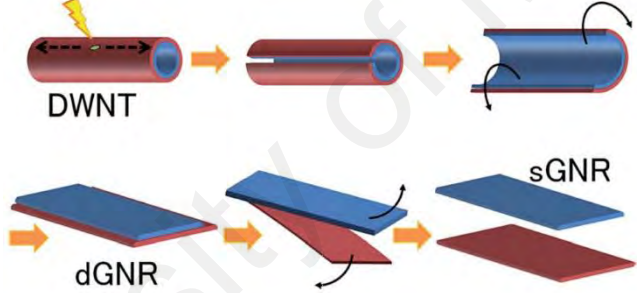
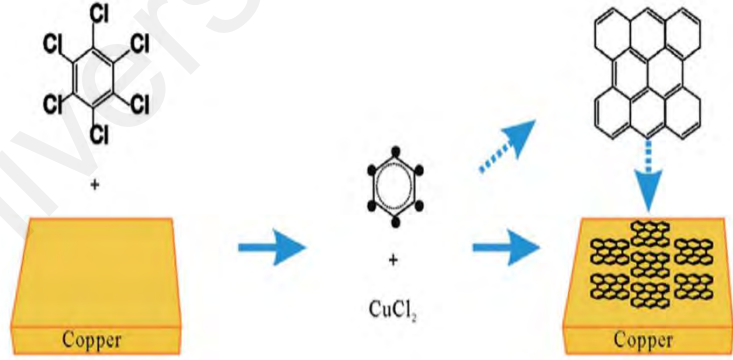
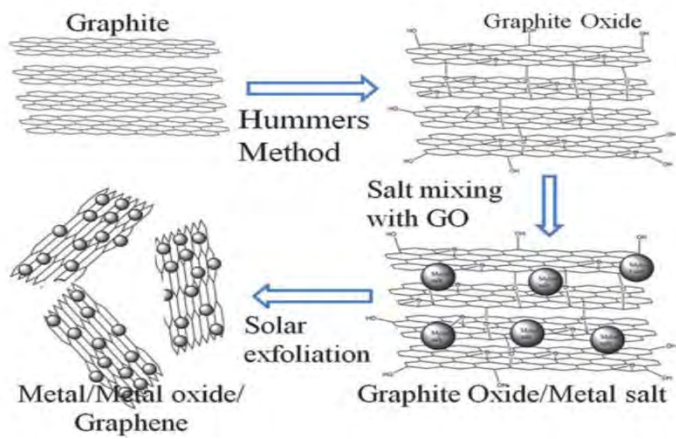
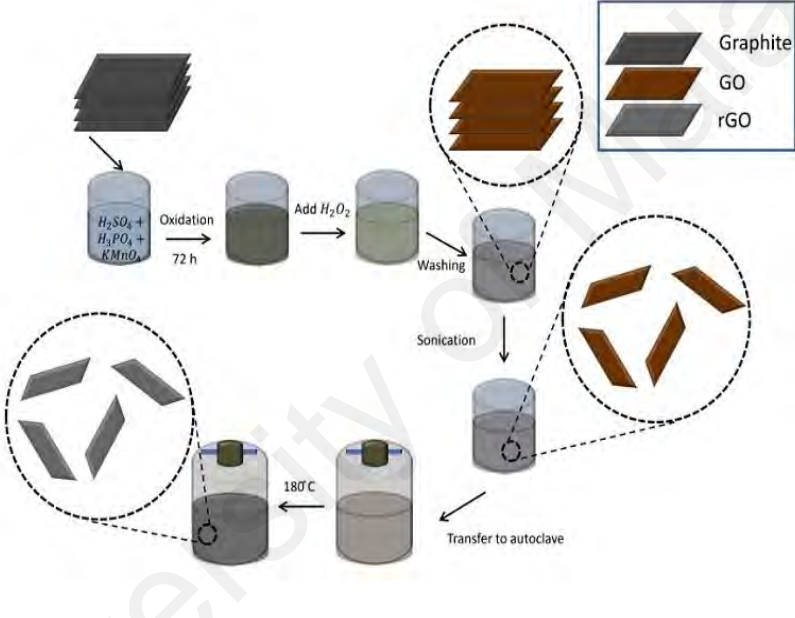
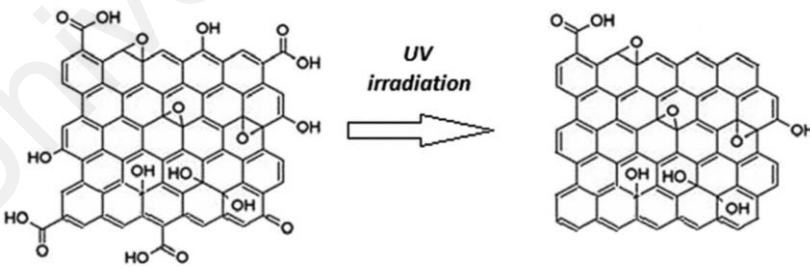
<p>D</p>	 <p>Graphite</p> <p>+ SDS</p> <p>$-e^-$ oxidation</p> <p>SDS-intercalated graphite</p> <p>$+e^-$ reduction</p> <p>Graphene/SDS suspension</p>	<p>Chemical exfoliation (Alanyalıoğlu et al., 2012)</p> <p>(Single-step method)</p>
<p>E</p>	 <p>DWNT</p> <p>dGNR</p> <p>sGNR</p>	<p>Unzipping of CNTs (Tanaka et al., 2015)</p> <p>(Single-step method)</p>
<p>F</p>	 <p>Copper</p> <p><chem>C6H2Cl6</chem></p> <p><chem>CuCl2</chem></p> <p>Copper</p>	<p>Chemical vapor deposition (Gan et al., 2012)</p> <p>(Single-step method)</p>

Table 2.1, continued

<p>G</p>	 <p>Graphite</p> <p>Hummers Method</p> <p>Graphite Oxide</p> <p>Salt mixing with GO</p> <p>Solar exfoliation</p> <p>Metal/Metal oxide/Graphene</p> <p>Graphite Oxide/Metal salt</p>	<p>Solar exfoliation (S. S. J. Aravind et al., 2011)</p> <p>(Two-step method)</p>
<p>H</p>	 <p>Graphite</p> <p>GO</p> <p>rGO</p> <p>Oxidation</p> <p>72 h</p> <p>Add H_2O_2</p> <p>Washing</p> <p>Sonication</p> <p>180°C</p> <p>Transfer to autoclave</p>	<p>Thermal reduction or hydrothermal treatment</p> <p>(Sadri, Zangeneh Kamali, et al., 2017)</p> <p>(Two-step method)</p>
<p>I</p>	 <p>UV irradiation</p>	<p>UV irradiation (Rella et al., 2015)</p> <p>(Two-step method)</p>

2.4 Preparation of nanofluids

Nanofluids are nanoscale colloidal suspensions containing condensed nanomaterials. Nanofluids are essentially two-phase systems where the nanoparticles (solid phase) are dispersed in the base fluid (liquid phase). There are several issues which need to be

considered when preparing two-phase systems such as nanofluids. One of the critical issues is the nanofluid stability, which remains a big challenge to this day.

As mentioned previously, there are two types of methods used to synthesize nanofluids: (1) one-step method and (2) two-step method (A Ghadimi, Saidur, & Metselaar, 2011).

2.4.1 One-step method

In the one-step method, the nanoparticles are synthesized simultaneously with the preparation of nanofluids. The nanoparticles are prepared directly using physical vapor deposition (PVD) or liquid chemical method. In this method, the processes of drying, storage, transportation, and dispersion of nanoparticles are avoided, which in turn, minimizes the agglomeration of nanoparticles and increases the stability of the nanofluid. However, the main disadvantage of the one-step method is that only fluids with low vapor pressures are compatible with the process, which limits the application of the method. Eastman et al. (Eastman, Choi, Li, Yu, & Thompson, 2001) implemented the one-step physical method to prepare nanofluids, where Cu vapor was directly condensed into nanoparticles by contact with flowing ethylene glycol, which is a liquid with low vapor pressure. Liu (M.-S. Liu, Lin, Tsai, & Wang, 2006) synthesized nanofluids containing Cu nanoparticles in water through chemical reduction method for the first time. Lo et al. (Lo, Tsung, & Chen, 2005; Lo, Tsung, Chen, Su, & Lin, 2005) prepared CuO nanofluids using a one-step method, which they called SANSS. They found that the SANSS method is effective in preventing particle aggregation, resulting in well-dispersed CuO nanoparticles with uniform size distribution in the deionized water suspension. Zhu (Wu, Zhu, Wang, & Liu, 2009) presented a novel one-step chemical method to prepare Cu nanofluids by reducing $\text{CuSO}_4 \cdot 5\text{H}_2\text{O}$ with $\text{NaH}_2\text{PO}_2 \cdot \text{H}_2\text{O}$ in ethylene glycol under microwave irradiation. They obtained stable Cu

nanofluids without agglomeration of Cu nanoparticles (A Ghadimi et al., 2011; Y. Li, Tung, Schneider, & Xi, 2009).

The modified “vacuum evaporation on running liquids” (VERL) process has been developed to prepare carrier liquids of low vapor pressures. The method involves the use of high-pressure magnetron sputtering (Wagener & Günther, 1999). Figure 2.5 shows the schematic of the magnetron sputtering system used to prepare the nanofluids. The vacuum in the chamber is pumped down to $1(10^{-6})$ torr using a diffusion pump. Once the chamber is filled with argon gas up to the desired gas pressure, the argon gas flow rate is adjusted to $15\text{--}50\text{ cm}^3/\text{min}$. The sputtering argon gas pressure is fixed at $1(10^{-2})$ torr in order to produce Ag nanoparticles. The target substrate is a rotating drum dipped into a reservoir filled with silicon oil. The rotational speed is varied from 0 to 10 rpm whereas the distance between the Ag sputter target and drum is fixed at 8 cm. The Ag particles, directly sputtered into the thin film of silicon oil, form on the rotating drum. Oleic acid (1 wt%) was dissolved in the base fluid prior to the sputtering process in order to prevent agglomeration of the Ag nanoparticles (Yujin Hwang et al., 2008).

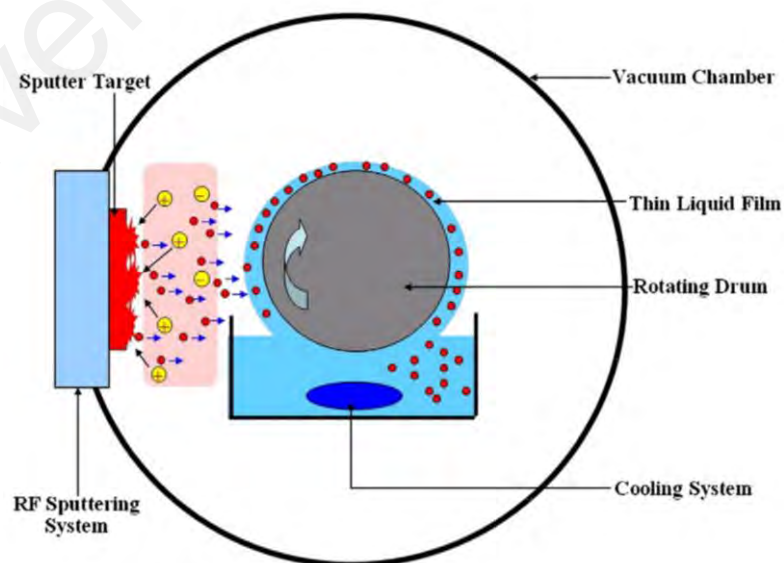


Figure 2.5: Schematic of the modified magnetron sputtering system used to prepare nanofluids(Yujin Hwang et al., 2008)

2.4.2 Two-step method

In the two-step method, the nanofluids are prepared by dispersing nanoparticles into the base liquids. The nanoparticles, nanofibers, or nanotubes are first prepared into dry powders by inert gas condensation, CVD, mechanical alloying, or other suitable techniques, and the nanopowders are then dispersed into the base fluids. In this method, the preparation of nanofluids is isolated from the preparation of nanoparticles. Consequently, the nanoparticles may agglomerate in both steps, especially during drying, storage, and transportation of nanoparticles. Agglomeration is undesirable because this will lead to settlement of the nanoparticles and clogging of microchannels, as well as decrease in the thermal conductivity. Simple techniques such as ultrasonic agitation or the addition of surfactants to the fluids are often used to minimize particle aggregation and improve dispersion behavior. Since nanopowder synthesis techniques have already been upscaled to commercial production, there are potential economic advantages in using two-step synthesis methods which rely on the use of such powders. However, the stability of the suspensions is of primary concern with two-step methods (Y. Li et al., 2009).

Hong (K. Hong, Hong, & Yang, 2006; T.-K. Hong, Yang, & Choi, 2005) prepared Fe nanofluids by dispersing Fe nanocrystalline powder in ethylene glycol using the two-step method. The Fe nanoparticles (mean size: 10 nm) were synthesized using a chemical vapor condensation process. To prevent the nanoparticles from aggregating in the nanofluids, they used an ultrasonic cell disrupter, which generates ultrasonic pulses of 700 W at 20 kHz. Xuan (Xuan & Li, 2000) prepared Cu/H₂O and Cu/oil nanofluids using the two-step method. They used surfactants and ultrasonic agitation to prevent nanoparticle aggregation. Murshed (Murshed, Leong, & Yang, 2005b) prepared TiO₂ suspensions in water using two-step method. Xie (H. Xie et al., 2002) prepared Al₂O₃/H₂O, Al₂O₃/EG, and Al₂O₃/PO nanofluids using the two-step method, and they

used intensive ultrasonication and magnetic force agitation to avoid nanoparticle aggregation.

A high-pressure homogenizer (e.g., Model no.: M-110LCE, Microfluidics, Inc.) can also be used in conjunction with the two-step method in order to produce nanofluids. Figure 2.6 shows the schematic of the high-pressure homogenizer, consisting of two micro-channels, dividing the liquid stream into two streams. Both of the streams are then merged in a reacting chamber. It is found that the velocity of the pressurized liquid streams in the microchannels increases, which leads to cavitation of the liquid (Yujin Hwang et al., 2008; Shaw & Costello, 1993).

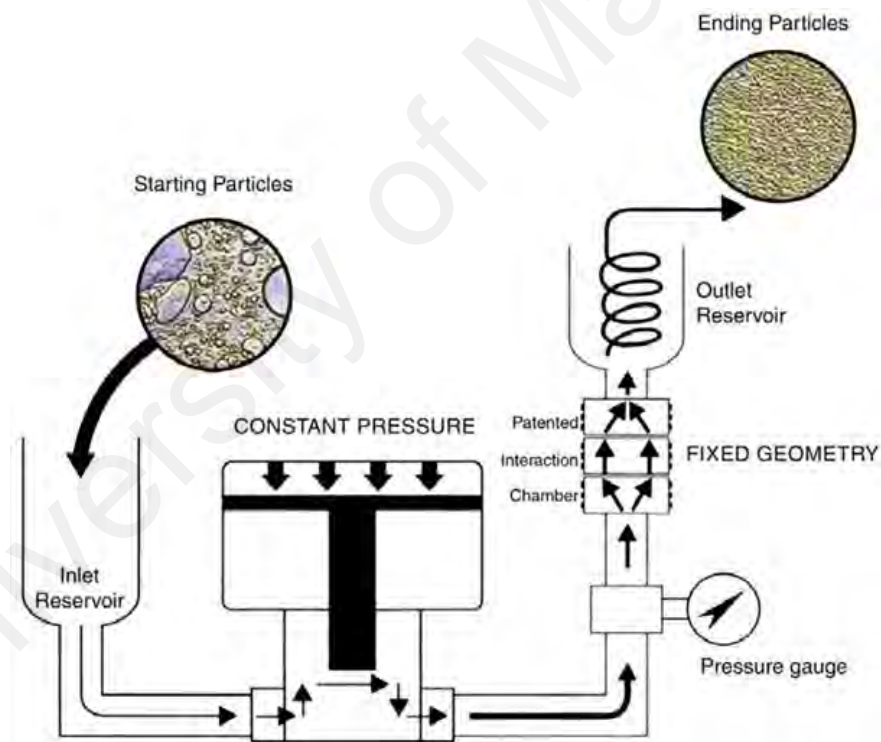


Figure 2.6: Schematic of the high-pressure homogenizer used to produce nanofluids(Yujin Hwang et al., 2008)

2.5 Stability of nanofluids

The main challenge in preparing carbon-based nanofluids is their poor colloidal stability due to the formation of agglomerates (Figure 2.7) resulting from the large surface area of the nanoparticles and strong forces of van der Waals between the nanoparticles. The stability of nanofluids is essential in practical applications owing to the fact that the thermophysical properties of unstable colloidal dispersions will vary significantly with time (Bianco, Manca, & Nardini, 2014).

In order to achieve a highly stable suspension, it is necessary to attain uniformly dispersed nanoparticles in the base fluid. The thermal and electrical properties of nanofluids are enhanced when the nanofluids are stable (Philip & Shima, 2012). The agglomeration of nanoparticles will not only lead to sedimentation and clogging of the microchannels, but also decreases the thermal conductivity of nanofluids (Beck, Yuan, Warriar, & Teja, 2010b). Hence, several methods have been devised over the years to improve stability of nanoparticles in aqueous and organic media by chemical and physical methods, which comprise physical and chemical functionalization methods, pH control, and ultrasonication.

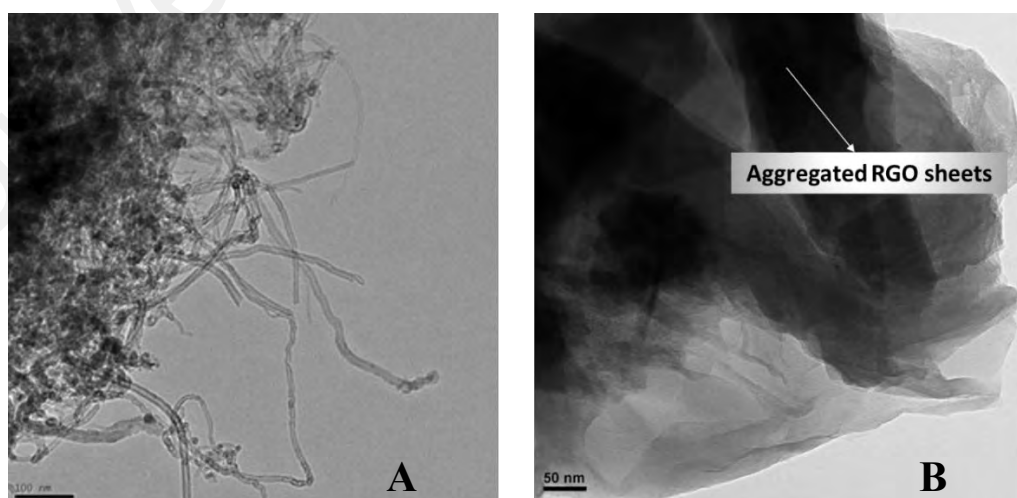


Figure 2.7: (A) Transmission Electron microscope images of the agglomerated CNTs (Pawel Keblinski, Eastman, & Cahill, 2005) and (B) graphene sheets (Hiemenz, 1986)

Preparing stable nanofluids is a prerequisite to optimize the thermal properties of the nanofluids. Various combinations of materials may be used depending on the application such as nanoparticles of metals, oxides, nitrides, and metal carbides, as well as carbon nanomaterials with or without surfactants, which are dispersed into the base fluid such as water, ethylene glycol, or oils (Pawel Keblinski et al., 2005).

In the stationary state, the sedimentation velocity of small spherical particles in liquid follows the Stokes law (Hiemenz, 1986):

$$V = \frac{2R^2}{9\mu} (\rho_p - \rho_l) \cdot g \quad (2.1)$$

Where V is the sedimentation velocity of the particle, R is the radius of the spherical particle, μ is the viscosity of the liquid medium, ρ_p and ρ_l are the density of the solid particle and liquid medium, respectively, and g is the acceleration due to gravity. This equation reflects the gravitational force, buoyancy force, and viscous drag that are acting on the nanoparticles suspended in the base fluid. Based on Eq. (2.1), the following measures can be taken to reduce the sedimentation velocity of the nanoparticles, which in turn, improves the stability of the nanofluid: (1) reducing the size of the nanoparticles, R , (2) increasing the viscosity of the base fluid, μ , and (3) reducing the difference in density between the nanoparticles and base fluid, $(\rho_p - \rho_l)$. It is evident that reducing the particle size will reduce the sedimentation velocity of the nanoparticles and improve the stability of nanofluids, considering that V is directly proportional to the square of R . According to the theory of colloidal chemistry, when the size of the particles decreases to a critical size, R_c , sedimentation does not occur because of the Brownian motion of nanoparticles (diffusion). However, smaller nanoparticles will have higher surface energy, increasing the likelihood of aggregation.

Thus, it is crucial to prepare stable nanofluids when smaller sized nanoparticles are used in order to prevent aggregation of the nanoparticles (Wu et al., 2009).

2.5.1 pH control

There is a direct relationship between the stability of aqueous nanofluid and its electrokinetic properties. Through the high surface charge density, the strong repulsive forces can facilitate stability of a well-dispersed suspension (D. Zhu et al., 2009). Xie et al. (H. Xie, Lee, Youn, & Choi, 2003) found that with simple acid treatment, the CNTs attain good stability in water. This is due to the hydrophobic-to-hydrophilic conversion of the surface nature due to the generation of hydroxyl groups. The isoelectric point (IEP) is the concentration of potential controlling ions at which the zeta potential is zero. Thus, at this point, the surface charge density is equal to the charge density, which is the starting point of the diffuse layer. Hence, the charge density in the diffuse layer is zero. It shall be noted that the repulsive energy must be smaller for smaller sized particles in order to ensure nucleation and stabilization of the nanoparticles in the solution and for this reason, a higher zeta potential is required to ensure stability of the suspension (H. Chang, Jwo, Fan, & Pai, 2007). As the pH of the solution departs from the IEP of the particles, the stability of the colloidal particles increases, which alters the thermal conductivity of the fluid. The state of surface charge is the fundamental characteristic that is primarily responsible to increase the thermal conductivity of the nanofluids (D. Lee, Kim, & Kim, 2006). In addition, it is found that the particle shape conversion is related to variations in pH (Hadjov, 2009). In a liquid suspension, the particles may either attract or repel each other. This interaction depends on the distance between the particles and the total interface energy, E_{tot} , which is the sum of the van der Waals attraction, E_A , and the electrostatic repulsion, E_{el} , between them. The E_{el} between the two charged particles and the surface potentials (φ_{d1} and φ_{d2}) is approximated by the DLVO theory (A Ghadimi et al., 2011):

$$E_{el} = \frac{\epsilon_0 \epsilon_1 r_1 r_2}{r_1 + r_2} \left\{ 2\varphi_{d1} \varphi_{d2} \ln \left[\frac{1 + \exp(-kx)}{1 - \exp(-kx)} \right] + (\varphi_{d1}^2 + \varphi_{d2}^2) \ln[1 - \exp(-2kx)] \right\} \quad (2.2)$$

Where r is the radius of the particles, x is the interparticle surface-to-surface distance, and the other symbols have their conventional meanings. It shall be noted that that higher potentials (φ_d or f) will create a larger potential barrier for agglomeration. In an aqueous nanofluid containing 0.3 vol% of CuO and ~8.5–9.5 of PZC, the interparticle distance is ~100 nm for mobility-equivalent spherical particles.

It is imperative to quantify the stability of the suspension in terms of the collision efficiency, α , which is responsible for growth of the colloidal particles. Here, α is reciprocal of the stability coefficient, W , which is associated with the rate constant of aggregation, $k = \alpha k_{diff} = k_{diff}/W$. It shall be noted that k_{diff} represents the rate constant of coagulation between the uncharged particles. Hence, the stability coefficient, W , can be expressed in terms of the total interaction energy, E_{tot} , as (D. Lee et al., 2006):

$$W = 2r \int_0^\infty \exp\left(\frac{E_{tot}}{k_b T}\right) \frac{dx}{(2r + x)^2} \quad (2.3)$$

For example, if the pH of the nanofluid deviates far from the IEP, the surface charge increases with the addition of sodium dodecylbenzene sulfonate (SDBS) surfactant in the Cu/H₂O nanofluid. Since more frequent attacks occur to the surface hydroxyl and phenyl sulfonic groups by potential-determining ions (H⁺, OH, and phenyl sulfonic groups), this increases the zeta potential of the colloidal particles. Thus, the stability of the suspension increases, which alters the thermal conductivity of the nanofluid (X. Li et al., 2008). Lee (K. Lee et al., 2009) also studied the effect of pH on Al₂O₃ nanofluids. The results showed that when the pH of the nanofluid is 1.7, the agglomerated particle size decreases by 18% whereas when the pH of the nanofluid is 7.66, the agglomerated particle size increases by 51%. The significant increase in the agglomerated particle size is due to reduction in electric repulsion force. When the Al₂O₃ particles are immersed in

water, hydroxyl groups ($-OH$) are produced at the surface of the Al_2O_3 particles. The relevant reactions depend on the pH of the solution. When the pH of the solution is lower than the PZC, the hydroxyl groups react with the H^+ ions from water, which leads to a positively charged surface. However, when the pH of the solution is higher than the PZC, the hydroxyl groups react with $-OH$ from the water, producing a negatively charged surface (A Ghadimi et al., 2011).

2.5.2 Ultrasonic agitation (vibration)

Ultrasonic baths, processors, and homogenizers are all powerful tools used to break down particle agglomerations compared with magnetic and high-shear stirrers (Yujin Hwang et al., 2008). However, occasionally, after the optimum duration of the process, all of these tools will further aggravate agglomeration and speeds up sedimentation of the particles.

Sadri et al. (Sadri et al., 2014a) experimentally studied the effects of ultrasonication, temperature, and type of surfactant on the thermophysical properties of MWCNT nanofluids. Three types of surfactants were used in the experiments, namely, gum arabic (GA), sodium dodecylbenzene sulfonate (SDBS), and sodium dodecyl sulfate (SDS). They measured the thermal conductivity and viscosity of the nanofluids at various temperatures. The results showed that the use of GA in the nanofluid leads to superior thermal conductivity compared with SDBS and SDS. Using distilled water as the base liquid, the samples were prepared with 0.5 wt% MWCNTs and 0.25% GA and sonicated at different sonication times. The results showed that the sonication time influences the thermal conductivity, viscosity, and dispersion of the nanofluids. The thermal conductivity of the nanofluids enhances with an increase in temperature and sonication time. The maximum thermal conductivity enhancement is 22.31% (ratio of 1.22) at a temperature of $45^\circ C$ and sonication time of 40 min. The viscosity of the

nanofluids show non-Newtonian shear-thinning behavior. In addition, the viscosity of the MWCNT nanofluids increases to a maximum value at a sonication time of 7 min and subsequently decreases with a further increase in the sonication time. The results indicate that the viscosity and thermal conductivity of nanofluids are influenced by the sonication time. In addition, the CNT agglomerates break up with an increase in sonication time. At high sonication times, all of the agglomerates disappear and the CNTs are fragmented and the mean length of the CNTs decreases.

2.6 Physical and chemical functionalization methods

Carbon allotropes tend to agglomerate due to strong π - π stacking interactions. The dispersibility of carbon nanostructures in aqueous media is one of the most important criteria in thermal systems and synthesis of films and composites (Y. Yang, S. Qiu, X. Xie, et al., 2010). The tendency of carbon allotropes to agglomerate hinders the processability of CNTs in industrial applications (Sadri et al., 2014a). Hence, several methods have been developed to improve the stability of carbon allotropes in aqueous and organic media by chemical and physical methods containing covalent and non-covalent functionalization of graphene, as shown in Figure 2.8.

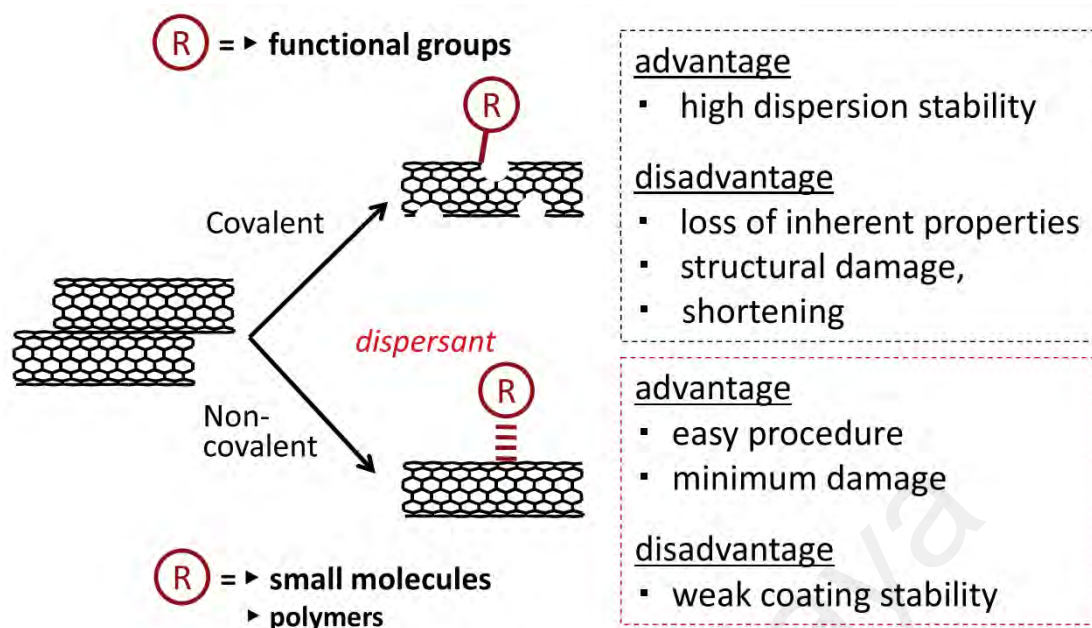


Figure 2.8: Primary CNT functionalization methods(J. Chen et al., 1998)

2.6.1 Chemical functionalization methods: Covalent functionalization

Recently, chemical functionalization has gained popularity because this method has great potential to improve the stability of nanoparticles in aqueous media. Chemical functionalization involves rehybridization of one or more sp^2 carbon atoms of the carbon network into the sp^3 configuration, which facilitates attachment of the hydrophilic organic groups such as carboxyl, esters, alkalis, and amine groups onto the surface of carbon nanomaterials. The bundles of nanostructures are broken up into smaller bundles during the functionalization process.

A common method for this oxidation process involves refluxing the CNTs or graphene nanoplatelets (GNPs) in a mixture of concentrated nitric and sulfuric acids under prolonged sonication treatment (S. J. Aravind et al., 2011; J. Chen et al., 1998; Kuznetsova et al., 2000; Yarmand et al., 2016). Wong et al. (Wong, Woolley, Joselevich, Cheung, & Lieber, 1998) reported the first covalent modification of SWCNTs in order to create high-resolution, chemically-sensitive microscopy probe tips (Figure 2.9). The carboxylic acid groups at the open ends of SWCNTs were coupled to

amines in order to create additional probes with basic or hydrophobic functionality. Force titrations recorded between the ends of the SWCNT tips and hydroxy-terminated self-assembled monolayers (SAMs) confirmed the chemical sensitivity and robustness of the SWCNT tips (Wong et al., 1998).

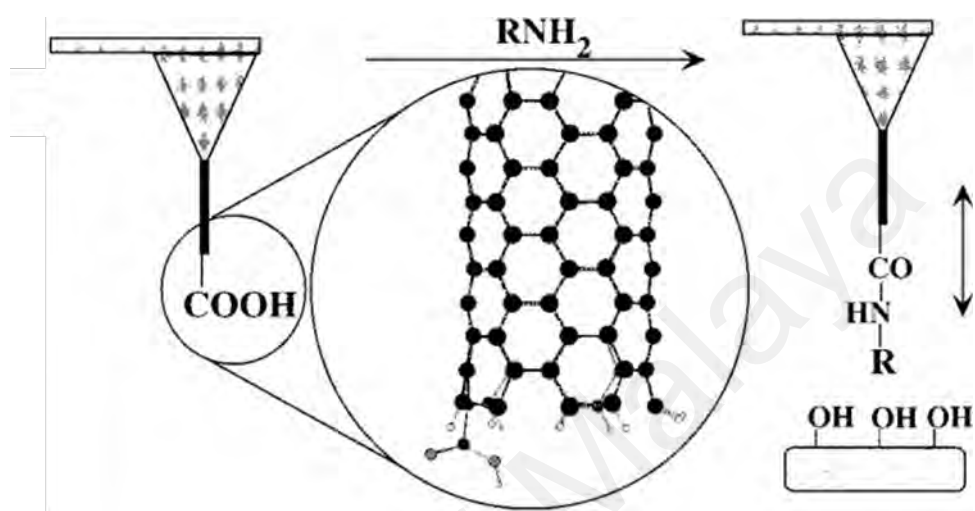


Figure 2.9: Schematic showing modification of a SWCNT tip by coupling amine (RNH_2) to a terminal ($-\text{COOH}$) and the application of this probe to sense specific interactions between the functional group (R) and surface $-\text{OH}$ groups (Wong et al., 1998)

Other oxidizing agents include HCl , KMnO_4 , H_2O_2 , O_3 , OSO_4 , HClO_4 , and low concentrations of nitric acid (Byl, Liu, & Yates, 2005; J. Chen et al., 1998; Jin Zhang et al., 2003) (Figure 2.10). The chemical reaction between the oxidant and carbon nanomaterials results in opening of the trigonal bond, which creates favorable sites for covalent reaction with dissociated ions. This leads to the formation of oxygen-based moieties that mostly consist of hydroxyl, carboxyl, ether, and other groups (Ajayan et al., 1993; Tsang, Chen, Harris, & Green, 1994). The attachment of various oxygenated groups on the surface of carbon nanomaterials (CNTs and GNPs) does not only improve the solubility of these materials in dipolar solvents but also serves as the foundation for solution-based chemistry through ionic and covalent functionalization (Hamon et al., 1999; Shiral Fernando, Lin, & Sun, 2004; Vigolo et al., 2000).

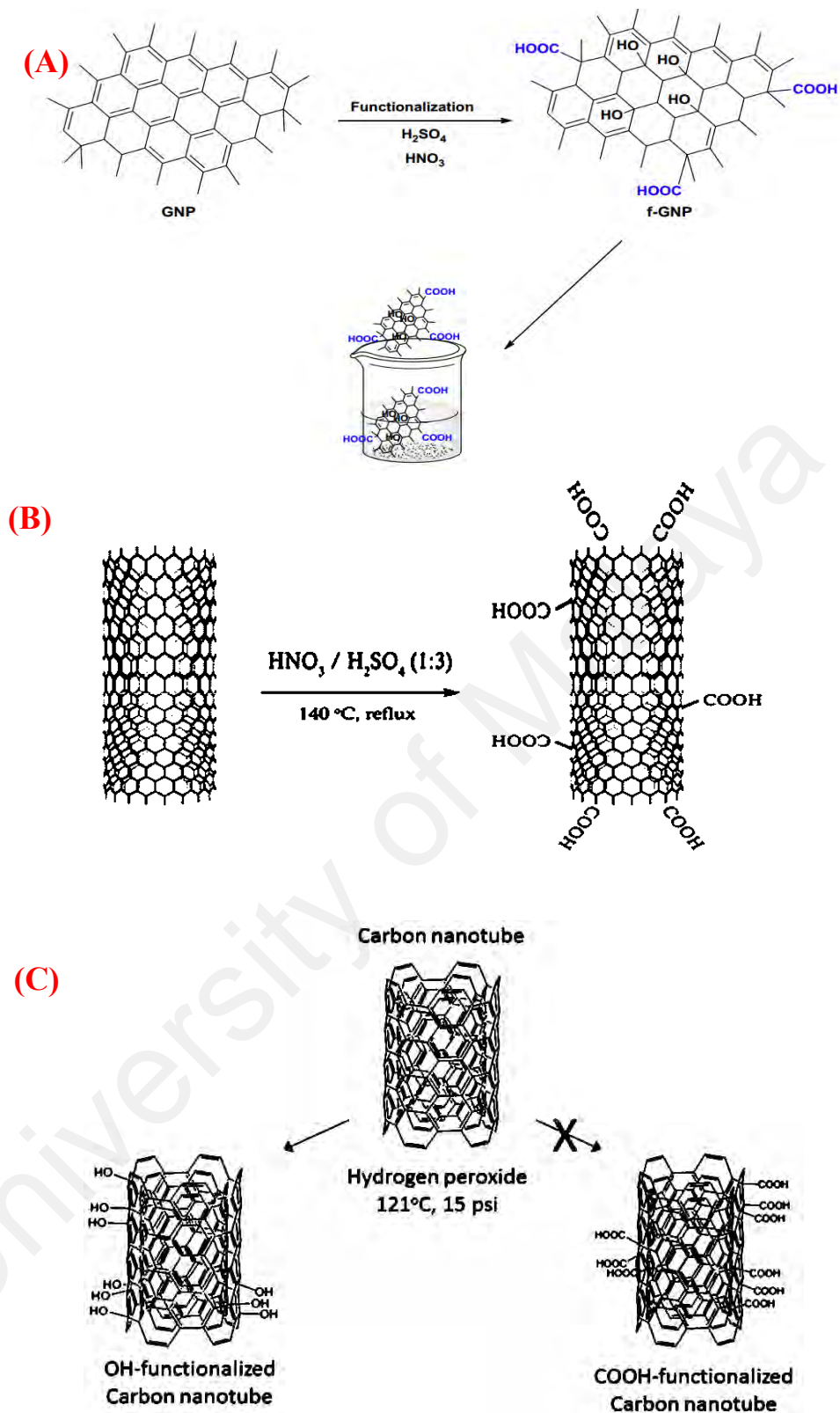


Figure 2.10: Schematic showing the oxidation of covalently functionalized: (A) GNPs(Yarmand et al., 2016) and (B, C) CNTs (Weydemeyer, Sawdon, & Peng, 2015)

It can be seen from Figures 2.10(B) and (C) that autoclaving in hydrogen peroxide may lead to two types of functionalization on the CNT surface, hydroxyl groups, and carboxylic acid groups. When the temperature is increased to 110–120°C, the hydrogen peroxide becomes unstable and decomposes spontaneously into hydroxyl radicals (Eq. (2.4)) and perhydroxyl radicals (Eq. (2.5)) (Weydemeyer et al., 2015).



However, since the reaction given by Eq. (2.4) is a kinetically dominant reaction, it is expected that most of the hydroxyl radicals generated will attack the CNTs, leading to the formation of hydroxyl groups on the CNT surface. An *ab initio* computational quantum mechanical study supports functionalization of CNTs by hydroxyl radical adduct. Besides the addition of OH radicals to the CNTs, it is also anticipated that some of the highly active hydroxyl radicals produced from the reaction (Eq. (2.4)) may trigger the following reaction (Eq. (2.6)) in aqueous H₂O₂ as the more dominant pathway than (Eq. (2.5)) in order to produce perhydroxyl radicals.



The calculated barrier energies indicate that the OOH radical is much less reactive than the OH radical with regards to the additional reactions with CNTs, cytosine, and thymine in both gaseous and aqueous media. It is hypothesized that the functionalization of CNTs in hydrogen peroxide through autoclaving is primarily driven by the addition of hydroxyl radicals (Weydemeyer et al., 2015).

Other covalent reactions of carbon-based nanomaterials include amidation and esterification, radical addition, alkali metal reduction, Bingel cyclopropanation, nitrene cycloaddition, 1,3-dipolar cycloaddition, electrophilic addition, nucleophilic addition,

carbene addition and Diels-Alder cycloaddition (Y.-P. Sun et al., 2002; Tasis, Tagmatarchis, Bianco, & Prato, 2006).

2.6.1.1 Amidation and esterification reaction

In amidation with the amino-containing functional group (Figure 2.11), the acyl chloride route generally produces samples that are more soluble than those from the diimide-activated coupling reactions. The samples produced from diimide-activated coupling reactions contain more bundled carbon nanomaterials in the soluble fraction such that the resulting solution exhibits a higher level of light scattering (Y.-P. Sun et al., 2002).

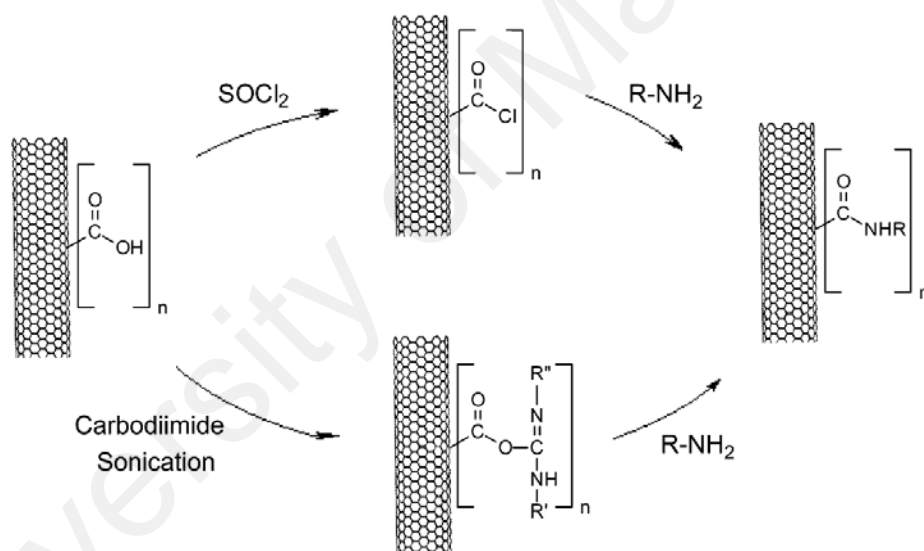


Figure 2.11: Amidation reaction of CNTs(Y.-P. Sun et al., 2002)

Amiri et al. (Amiri, Shanbedi, et al., 2015) used microwave-assisted direct coupling of GNPs with polymers including hydroxyl (-OH) groups such as polyethylene glycol (PEG) and bio-molecules such as 4-phenylazophenol (Azo). The addition of Lewis acid results an electrophilic addition reaction within a short period (30 min). Hence, this method is less time-consuming compared with multiple-step approaches. The colloidal stability was investigated using particle absorbance measurements and the results showed that the nanofluid has good stability with very low sedimentation. Figure 2.12

shows the experimental procedure for chemical-assisted functionalization of GNP with PEG and Azo.



Figure 2.12: Experimental procedure for chemical-assisted functionalization of GNP with PEG and Azo (Amiri, Shanbedi, et al., 2015)

Haddon and co-workers first reported the use of acid groups to attach long alkyl chains to SWCNTs via amide linkages (J. Chen et al., 1998) or carboxylate-ammonium salt ionic interactions (J. Chen et al., 2001). Abuilawi et al. (Abuilawi, Laoui, Al-Harhi, & Atieh, 2010) showed that esterification of carboxylic acids can also be used to functionalize and solubilize nanotubes. Figure 2.13(A) shows the mechanism of esterification. Yu et al. (D. Yu, Yang, Durstock, Baek, & Dai, 2010) reported functionalization of GO with $-\text{CH}_2\text{OH}$ terminated regioregular poly(3-hexylthiophene) (P_3HT) through the formation of ester bonds with the carboxyl groups of GO nanoplatelets (Figure 2.13(B)). Due to the large amounts of hydroxyl groups in the added polymer, the P_3HT -functionalized GO is soluble in common organic solvents, which facilitates its characterization and fabrication by solution processing.

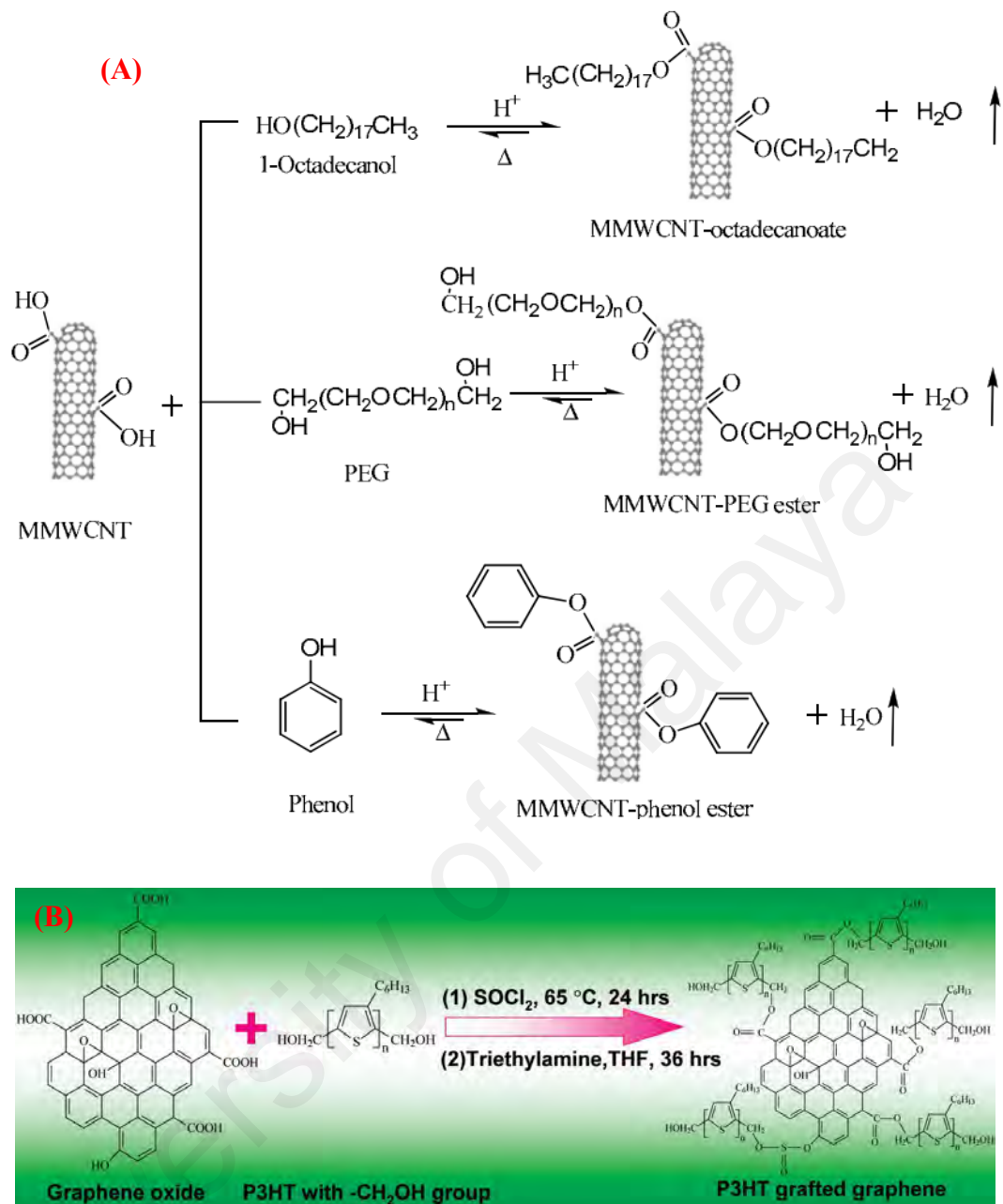


Figure 2.13: (A) Chemical esterification of modified carbon nanotubes and (B) synthesis procedure for chemical grafting of CH₂OH-terminated P3HT chains onto graphene (D. Yu et al., 2010)

2.6.1.2 Electrophilic addition reaction

It is known that functionalization under microwave radiation is somewhat different, faster and more efficient than conventional chemical functionalization methods (W. Zhang, Chen, Lu, & Nagashima, 2004). Microwave-induced method has been used in some reactions of CNTs with remarkable effects such as carboxylation (Yubing Wang,

Iqbal, & Mitra, 2006), 1,3-dipolar cycloaddition (Junxin Li & Grennberg, 2006; Yubing Wang, Iqbal, & Mitra, 2005) ,and radical functionalization with 4-methoxyphenylhydrazine (J. Liu et al., 2007). Yang et al. (Y. Xu et al., 2008) conducted microwave-induced electrophilic addition of SWCNTs with alkylhalides using Lewis acid as the catalyst, followed by hydrolysis. The reaction results in the attachment of alkyl and hydroxyl groups to the surface of the nanotubes. The rapid, high-energy microwave radiation is found to be highly efficient for this reaction, and the whole process takes place within several minutes (Y. Xu et al., 2008), as shown in Figure 2.14.

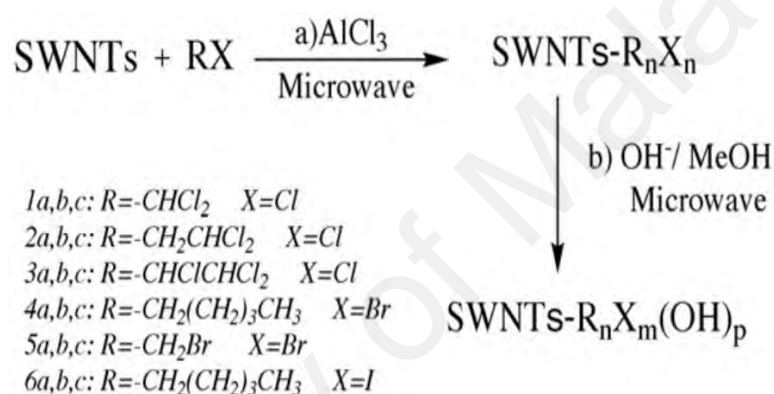


Figure 2.14: Covalent functionalization of SWCNTs by alkylhalides(Y. Xu et al., 2008)

Amiri et al. (Amiri, Sadri, Shanbedi, Ahmadi, Kazi, et al., 2015) synthesized triethanolamine-treated graphene nanoplatelets (TEA-GNPs) using electrophilic addition reaction functionalization with molecules including hydroxyl (–OH) groups. The synthesis procedure was quick and the nanofluids obtained were of high stability. They prepared highly-dispersed GNPs decorated with non-corrosive hydrophilic groups in water in order to produce the nanofluid, as shown in Figure 2.15(A). Sarsam et al. (Sarsam, Amiri, Zubir, et al., 2016) used electrophilic addition reaction under microwave irradiation, which is found to be a promising, quick, and cost-effective approach to functionalize GNPs with ethylene glycol. The alkyl and hydroxyl groups

were successfully attached to the GNPs through electrophilic addition reaction under microwave irradiation (Figure 2.15(B)).

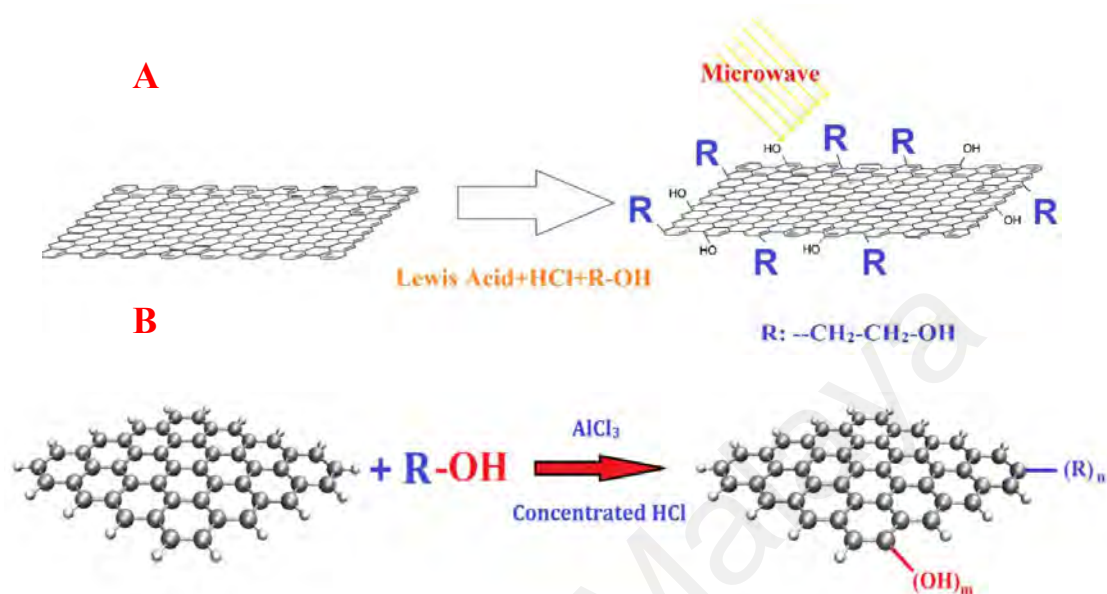


Figure 2.15: (A) Experimental procedure for chemical-assisted functionalization of GNPs with ethylene glycol(Amiri, Sadri, Shanbedi, Ahmadi, Kazi, et al., 2015) and (B) electrophilic addition reaction of GNPs with TEA(Sarsam, Amiri, Zubir, et al., 2016)

2.6.1.3 Free radical grafting method

Free radical coupling is a promising method to functionalize carbon nanostructures and it is a facile way of covalent functionalization. In this method, peroxides, aryl diazonium salts, substituted anilines, and benzophenone are used as starting materials (X. Peng & Wong, 2009). The radical coupling to CNTs or GNPs is an emerging field where aryl diazonium salts(Doyle, Rocha, Weisman, & Tour, 2008), substituted anilines, alkyl or aryl peroxides (Hudson, Casavant, & Tour, 2004), and benzophenone are used as the starting materials. Among this rich group of reactions, the coupling of diazonium to CNTs or GNPs has become the dominant route to functionalize CNTs and GNPs due to its simplicity, scalability, and versatility(Y. Yang, S. Qiu, X. Xie, et al., 2010).

There are two techniques used to graft carbon nanomaterials, depending on the building of polymer chains. The “grafting to” approach involves synthesizing a polymer with a specific molecular weight terminated with reactive groups or radical precursor (Figure 2.16). In a subsequent reaction, the polymer chain is attached to the surface of the carbon nanostructure by addition reactions. This method is disadvantageous because the grafted polymer content is limited, which is due to the relatively low reactivity and high steric hindrance of macromolecules. The “grafting from” approach, however, involves growing polymers from the surface of the carbon nanostructure through in situ polymerization of monomers initiated by chemical species immobilized on the CNT sidewalls or surface and edges of the GNPs (Spitalsky, Tasis, Papagelis, & Galiotis, 2010). In general, the “grafting to” approach involves preformed polymer chains reacting with the surface of either pristine, oxidized, or pre-functionalized CNTs and GO or rGO. The “grafting to” techniques include direct covalent linkage of the functional polymers on the GO or pre-functionalized CNT surface using esterification, amidation, click chemistry, nitrene chemistry, and radical addition (Layek & Nandi, 2013). The main approaches exploited in this functionalization strategy are radical or carbanion additions as well as cycloaddition reactions to the CNT or GNP double bonds. Since the curvature of the carbon nanostructures imparts a significant strain upon the sp^2 hybridized carbon atoms that constitute their framework and the energy barrier required to convert these atoms to sp^3 hybridization is lower than that of the flat graphene sheets, these materials are susceptible to various addition reactions (Spitalsky et al., 2010).

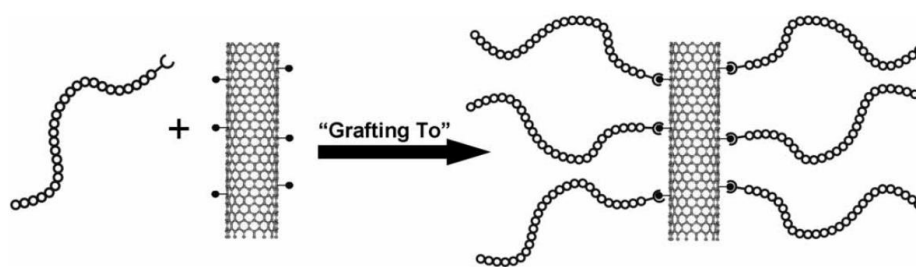


Figure 2.16: Schematic representation of the “grafting to” approach for functionalization of nanotubes with polymers(Homenick, Lawson, & Adronov, 2007)

Tasis et al. (Tasis et al., 2007) described a process to graft water-soluble polymer chains from the surface of CNTs. In the first step, they covalently attached organic radicals thermally produced from organic peroxides. In the second step, they prepared polyacrylamide-coated SWCNTs and MWCNTs by carrying out ceric ion-induced redox process. The main advantage of this grafting step is that it can be done in aqueous media and at room temperature. These reactions are summarized in Figure 2.17 (Tasis et al., 2007).

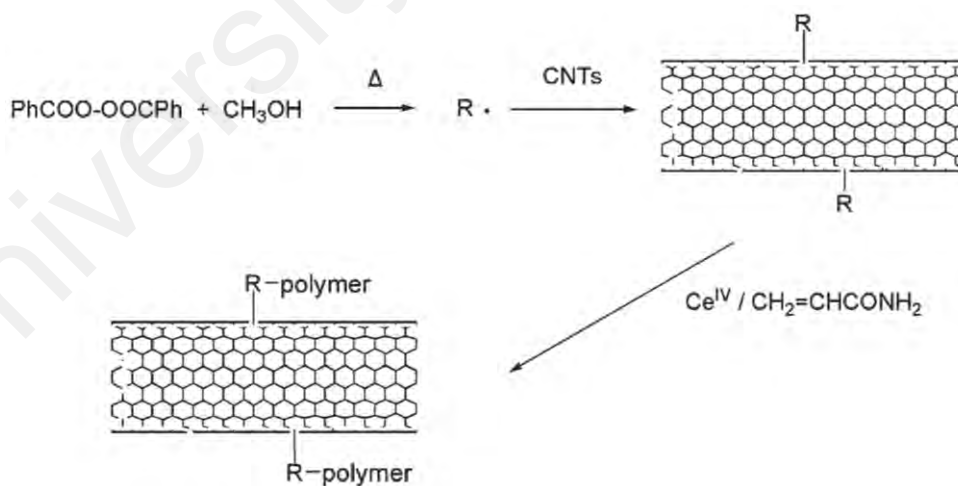


Figure 2.17: Schematic diagram of the complete functionalization strategy, where the first step involves radical addition to the sidewalls of CNTs and the second step involves redox radical grafting of polyacrylamide chains(Tasis et al., 2007)

In general, the “grafting from” approach involves polymerization of monomers from surface-derived initiators on either MWCNTs or GNPs (Figure 2.18). These initiators are covalently attached using various functionalization reactions developed for small molecules, including acid defect group chemistry and sidewall functionalization of CNTs. The advantage of the “grafting from” approach is that the polymer growth is not limited by steric hindrance, allowing high molecular weight polymers to be efficiently grafted. In addition, this method enables preparation of carbon nanostructure-polymer composites with high grafting density (Spitalsky et al., 2010).

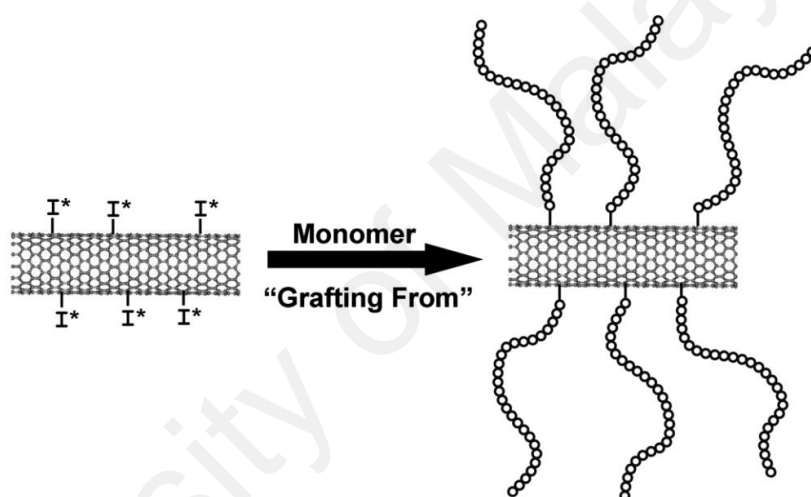


Figure 2.18: Schematic representation of the “grafting from” approach used to functionalize nanotubes with polymers(Homenick et al., 2007)

2.6.2 Physical functionalization methods: Non-covalent functionalization

It is known that the chemical groups attached to nanomaterials can significantly enhance the solubility of the nanomaterials (Hirsch, 2002). However, the attachment of these chemical groups can also create defects, which will alter the functional properties of the carbon allotropes (CNTs or GNPs). An alternative non-destructive method that can be used to improve the solubility of carbon allotropes is to promote non-covalent interactions of amphiphilic molecules (surfactants) with the surface of the nanoparticles. Here, the hydrophilic parts of the molecules interact with water whereas the hydrophobic parts are adsorbed onto the nanotube surface, which solubilizes the carbon

allotropes and prevents them from aggregating into bundles and ropes. The structures of the hydrophilic groups of surfactants are very diverse and their nature defines the efficiency of the dispersion of carbon allotropes in solutions (Britz & Khlobystov, 2006).

The attachment of different molecules to the basic structure of carbon nanomaterials through physical interactions is the fundamental mechanism of non-covalent functionalization. The adsorption is mediated by different types of forces such as van der Waals forces, electrostatic forces, π - π stacking interactions and hydrogen bonds. These forces form the basis of non-covalent functionalization which is mainly based on the formation of supramolecular complexes (C. Zhu, Guo, Fang, & Dong, 2010). Non-covalent functionalization is realized via (1) enthalpy-driven interactions, such as π - π , CH- π , and NH- π between the surface of CNTs or GNPs and the dispersants and/or (2) entropy-driven interaction, which is a hydrophobic interaction in the presence of surfactants (Figure 2.19) (Fujigaya & Nakashima, 2015).



Figure 2.19: Dispersant-CNT interactions(Fujigaya & Nakashima, 2015)

Some of the common surfactants that have been used in other studies are sodium dodecylsulfate (SDS) (Bostwick, Ohta, Seyller, Horn, & Rotenberg, 2007; Q. H. Wang & Hersam, 2009), SDBS (Si & Samulski, 2008; Van Noorden, 2011), salt and oleic acid

(N. Liu et al., 2013), cetyltrimethylammoniumbromide (CTAB) (Huh, Park, Kim, Hong, & Kim, 2011), dodecyl trimethylammonium bromide (DTAB), sodium octanoate (SOCT), hexadecyltrimethylammoniumbromide (HCTAB), polyvinylpyrrolidone (PVP) (Kosynkin et al., 2009), and gum arabic (Si & Samulski, 2008).

It is worth mentioning that the surfactant molecules on the surface of the carbon nanomaterials are in a dynamic equilibrium between the surfactants in the bulk solution (Figure 2.20 (A)). Therefore, the dispersants can be easily removed by filtration or dialysis, which leads to aggregation of the CNTs (Figure 2.20(B)) (Noguchi, Fujigaya, Niidome, & Nakashima, 2008). Similar dynamic dispersions also take place in the case of enthalpy-driven functionalization using small molecules as the dispersant. On the other hand, when polymer is used in enthalpy-driven functionalization, this often results in static dispersion due to multi-point interactions between the polymers and surface of the CNTs (Noguchi et al., 2008). In this case, the non-covalently surrounded polymers are retained even after the washing process such as filtration, which results in polymer-wrapped CNTs. In some applications, these wrapped dispersants serve as a contaminant. However, in some cases, the wrapped CNTs synergistically improve the performance of the CNTs if the polymers are strategically designed (Fujigaya & Nakashima, 2015).

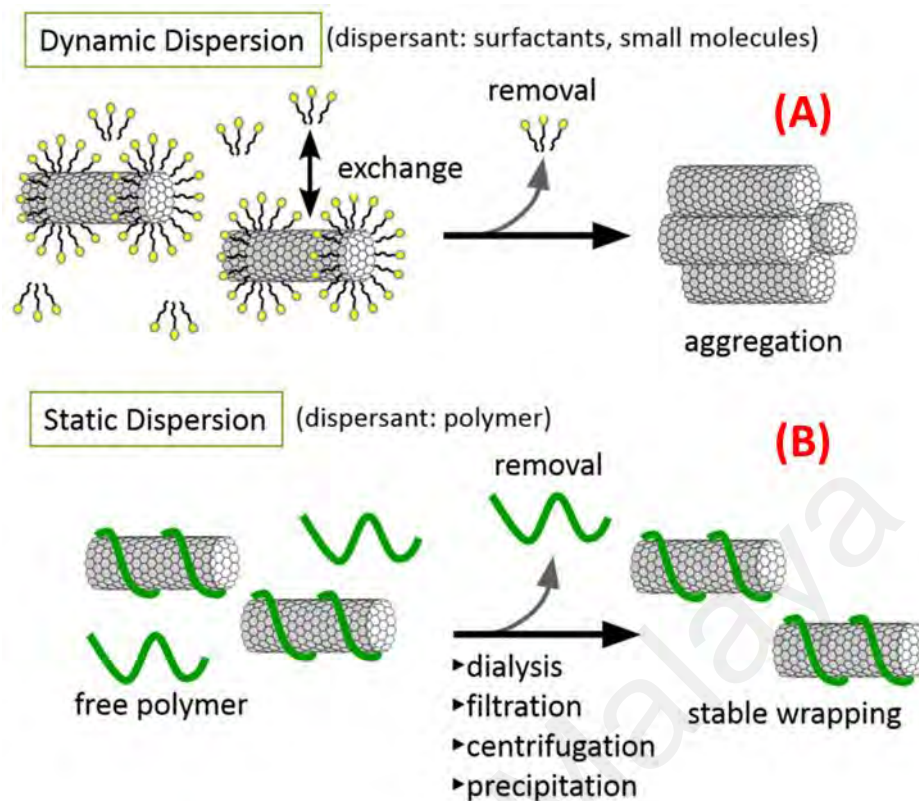


Figure 2.20: Schematic diagram showing the dynamic (upper) and static (lower) dispersion of CNTs(Fujigaya & Nakashima, 2015)

One of the advantages of polymer wrapping is that this approach provides a thermodynamically stable coating on the surface of the CNTs. In addition, this approach makes it possible to remove the unbound (free) polymer and leave the wrapping polymer on the CNT surface (Figure 2.20). The unbound polymer in the bulk solution can be removed by either one of the following methods: (1) dialysis (Jeng, Moll, Roy, Gastala, & Strano, 2006), (2) precipitation/decantation cycle (Stranks, Habisreutinger, Dirks, & Nicholas, 2013), (3) filtration/washing process (Izard et al., 2008; Okamoto, Fujigaya, & Nakashima, 2009), (4) ultracentrifugation/decantation process (Stranks et al., 2013), and (5) chromatographic separation (Fujigaya & Nakashima, 2015). In the filtration process, it is quite easy to distinguish a stable dispersion since a good dispersion is achieved from the washed materials after stable wrapping has taken place (Figure 2.21).

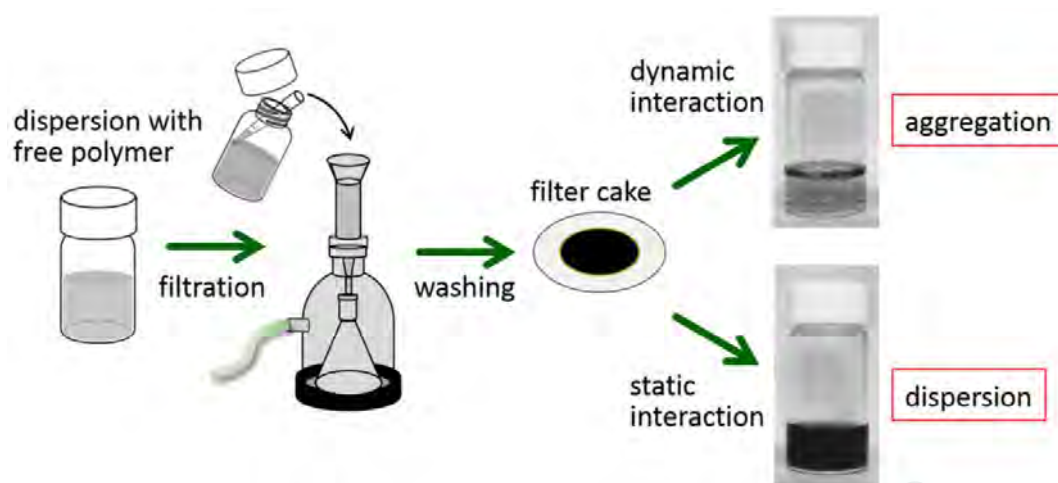


Figure 2.21: Schematic showing the procedure of the filtration process(Fujigaya & Nakashima, 2015)

For charged surfactants such as sodium dodecylsulfate (SDS) or tetraalkylammonium bromide, the nanotube dispersions are stabilized by electrostatic repulsion between the micelles. However, for charge-neutral surfactants such as polyvinylpyrrolidone (PVP), the nanotube dispersions are stabilized due to the large solvation shells created by hydrophilic moieties of surfactants assembled around the nanotubes (Moore et al., 2003). The hydrophobic parts of the surfactants are interacted directly with the surface of the nanotubes. These interactions can potentially alter properties of the nanotubes (Britz & Khlobystov, 2006). Non-covalent functionalization by π - π interactions is an appealing synthesis method because it offers the possibility of attaching functional groups to graphene without disturbing the electronic networks (Georgakilas et al., 2012).

Sarsam et al. (Sarsam, Amiri, Kazi, & Badarudin, 2016) investigated the effect of four types of surfactants (SDBS, SDS, CTAB, and gum arabic), each with three different concentrations, and five ultrasonication times (15, 30, 60, 90, and 120 min) on the stability of water-based GNP nanofluids. The viscosity and thermal conductivity of the sample with the highest stability were measured at different temperatures. The results showed that the water-based pristine GNP nanofluids are unstable and the

stability of the nanofluids improves upon the addition of surfactants. The presence of SDBS, SDS, and CTAB surfactants in the nanofluids results in excessive foam. The best water-based GNPs nanofluid was selected based on the following criteria: (1) highest colloidal stability, (2) highest thermal conductivity, and (3) lowest viscosity. They found that the (1-1) SDBS-GNP sample ultrasonicated for 60 min has the highest stability (relative concentration of particles: 82% after 60 days), second highest thermal conductivity (8.36%), and nearly the lowest viscosity (7.4% higher than that of distilled water).

In chemistry, π stacking (also called π - π stacking) refers to the attractive, non-covalent interactions between aromatic rings, because they contain π bonds. Zhu and Pignatello (Lin & Xing, 2008) reported that π - π interaction is the main mechanism regulating the adsorption of both π -acceptors and π -donors. It shall be noted that the combination of these two bonds is called sigma-donor/ π -acceptor on the graphene surface. With a rolled hollow cylindrical graphite-like structure, the CNTs act in an amphoteric role toward the adsorbates of both π -acceptors and π -donors through π - π interactions. In addition, the stacking of benzene rings onto the CNT surface significantly increases the surface coverage of surfactants and polymers (Lin & Xing, 2008).

Non-covalent functionalization has been used to functionalize graphene nanosheets (GNSs) through π - π stacking of pyrene molecules with a functional segmented polymer chain. This yields remarkable improvement in the thermal conductivity of GNS-filled polymer composites. The functional segmented poly(glycidyl methacrylate) containing localized pyrene groups (Py-PGMA) was prepared by atom transfer radical polymerization, and the Py-PGMA was characterized by nuclear magnetic resonance spectroscopy (C.-C. Teng et al., 2011), as shown in Figure 2.22.

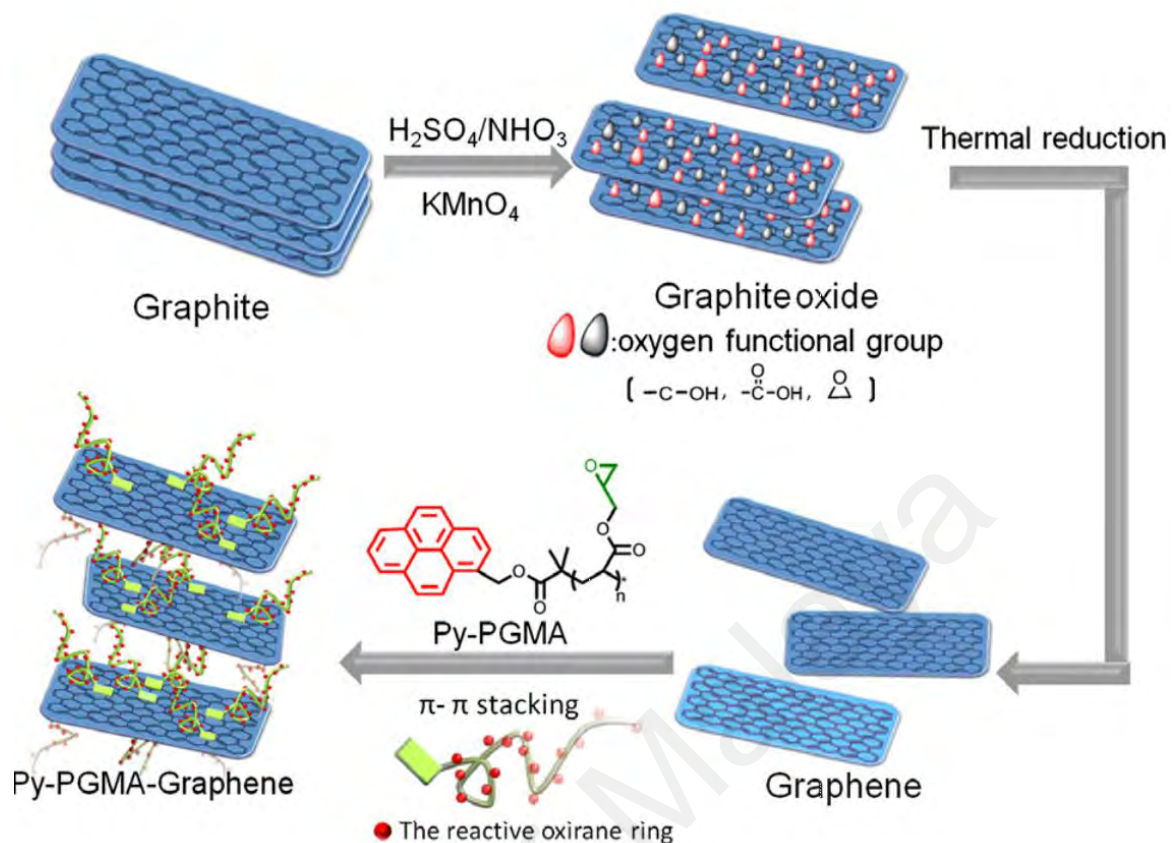


Figure 2.22: Schematic showing the preparation and functionalization of graphene(C.-C. Teng et al., 2011)

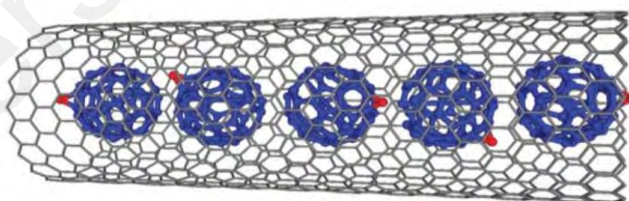


Figure 2.23: Endohedral polymerization of C60O inside the CNT(Britz & Khlobystov, 2006)

Endohedral functionalization involves the insertion of various nanoparticles into the inner walls. This can be done by (1) spontaneous penetration with colloidal nanoparticle suspensions filling the inner walls by evaporation of the carrier solvent or (2) by wet chemistry, where the compounds are introduced into the inner walls of the nanotubes

and transformed into nanoparticles while maintaining the predetermined thermal or chemical conditions (Hirsch, 2002), as shown in Figure 2.23.

The addition of surfactants is not suitable for high-temperature applications (Z. Sun et al., 2010). This is due to the fact that the bonding between the surfactant and nanoparticles can be damaged at temperatures more than 60°C (X. Huang, Qi, Boey, & Zhang, 2012). Therefore, the nanofluid will lose its stability, resulting in sedimentation of the nanoparticles (Basu, Basu, & Bhattacharyya, 2010). In addition, this approach restricts the viscosity of the nanofluid and it can be expected that there will be a significant increase in the pressure drop and pumping power especially if gum arabic is used as the surfactant in nanofluids. It has been proven that the addition of SDBS, SDS, and CTAB surfactants results in excessive amounts of foam. Thus, care should be taken when using these surfactants to prepare water-based GNP or CNT nanofluids for heat transfer applications because of the adverse effects of foam on the heat transfer efficiency and fluid flow characteristics (Sarsam, Amiri, Kazi, et al., 2016).

2.7 Green methods

With global warming being one of the major environmental concerns nowadays, much effort has been made to eliminate or reduce the amounts of hazardous materials in chemical reactions in order to reduce environmental hazards associated with these chemicals. This approach is known as green chemistry and it has been embraced by scientific communities all over the world. By preventing hazardous wastes, this reduces handling, transportation, and disposal of hazardous materials, and reduce costs associated with these activities.

According to chemists, green chemistry consists of 12 important principles: (1) eliminate chemical wastes, (2) reduce derivatives, (3) invent safer chemicals, (4) reduce hazardous chemical syntheses, (5) select safer auxiliaries and solvents, (6) design for

degradation, (7) catalysis, (8) time analysis to prevent pollution, (9) improve energy performance, (10) consideration of atom economy, (11) use renewable sources, and (12) practice safer chemistry for accident prevention.

Green chemical processes have gained much attention because these processes are environmentally benign and produce products that are comparable or better than conventional toxic processes (Anastas & Warner, 1998; Kumar et al., 2004). Conventional functionalization procedures involve the use of strong acids and inorganic solvents which leads to problems such as environmental pollution, equipment corrosion, and health hazards. Therefore, it is imperative to develop environmentally friendly methods to functionalize carbon-based nanostructures (Y. Yang, S. Qiu, C. He, et al., 2010).

A large number of plant-based extracts have been used as stabilizing and reducing agents for graphitic materials. Green tea, DNA, polysaccharides, tannic acid, humic acid, and fulvic acid have been successfully used to stabilize CNTs in aqueous-based systems (Lin & Xing, 2008). Much effort has also been made to understand the mechanisms that propel mutual interactions between phytochemicals and CNTs (Pan & Xing, 2008). Other researchers have extended the work by incorporating well-stabilized phytochemical-grafted CNTs as the precursor material for various engineering applications (Uddin, Watanabe, Gotoh, Saito, & Yumura, 2012). Based on spectroscopic and microscopic techniques, only a low concentration of phytochemical is required to isolate the CNTs, which reduces interference from the dispersant on the physicochemical properties. Nakamura et al. (Nakamura, Narimatsu, Niidome, & Nakashima, 2007) found that tea polyphenols contain different types of phenolic compounds (i.e., epicatechin (EC), epicatechin gallate (ECG), epigallocatechin (EGC), and epigallocatechin gallate (EGCG)) which are primarily responsible for stabilizing CNTs through π - π interactions, which are similar to the polycyclic aromatic

hydrocarbons (PAH)-based dissolution mechanism. Uddin et al. (Uddin et al., 2012) found that highly soluble green tea greatly facilitates the CNT solution to act as a precursor to reinforce the DMSO/PVA-based composite structure. The results showed that there is significant improvement in the strength, modulus, and toughness of the composite structure compared with those for the base material. On the other hand, Chen et al. (W. Chen & Yan, 2010) found that the well-dispersed CNTs along with the presence of polyphenol component in the CNT/green tea composite improves the sensitivity of the material toward reactive oxygen species resulting from oxidation of the phenolic group. In addition, there is electron transfer enhancement between the interacting species. They concluded that the composite may serve as the foundation to develop simple resistivity-based sensors. Fujitsuka and Oya (Fujitsuka & Oya, 2012) have experimentally proven that catechin (one of the constituents of tea extract) is certainly more effective in exfoliating CNT bundles compared with non-ionic surfactants. This leads to efficient response toward external alternating current, resulting in a well-aligned composite structure due to the highly discrete nature of catechin. Further investigation revealed that the well-aligned CNT-composite paper samples have higher electrical conductivity compared with the non-aligned samples. Figure 2.24 shows the schematic of the interactions between the CNTs and tannic acid. The tannic acid molecules anchored onto the tube wall with benzene rings bond themselves to the surface carbon rings through π - π interactions, forming a monolayer (Lin & Xing, 2008).

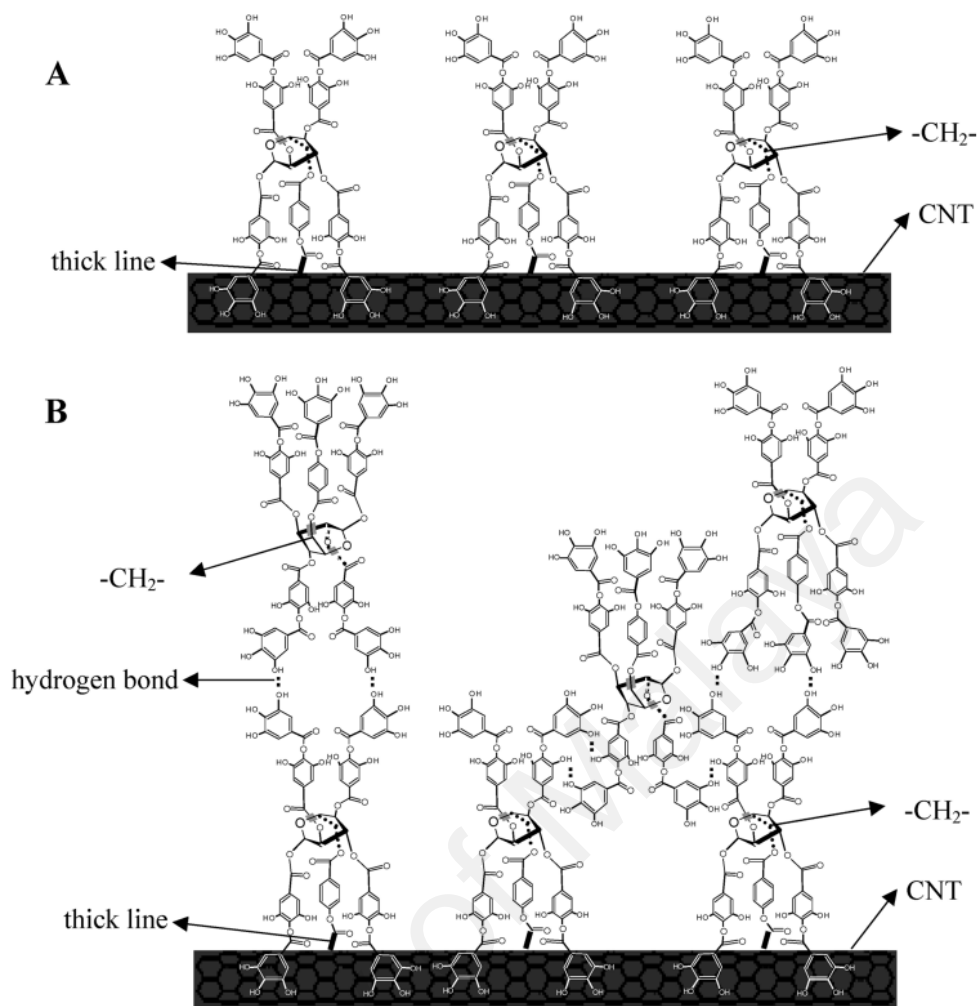


Figure 2.24: Schematic of the interactions between the CNTs and tannic acid: (A) The adsorbed TA monolayer sorbs more of the dissolved tannic acid molecules; (B) The thick lines in the figure represent the chemical bond linking to pyrogallol which interacts with the back side of the CNTs (Lin & Xing, 2008)

Nowadays, low-cost, environmentally friendly, and facile processing are the main criteria in selecting a suitable method to synthesize bulk graphene on an industrial scale. Green nanotechnologies have been widely explored in the synthesis of metal nanoparticles, where biomolecules, microbes and plant extracts are used as the reducing and capping agents. Here, the chemical components that are implicated in the bio-reduction process, formation, and stabilization of nanoparticles include bio-molecules such as proteins, amino acids, polysaccharides, alkaloids, alcoholic derivatives, polyphenolic compounds, enzymes, chelating agents, and vitamins (Iravani, 2011; Park, Hong, Weyers, Kim, & Linhardt, 2011). This principle has also been used for bio-

reduction of GO into graphene. In general, biological approaches used to synthesize graphene are considered facile, environmental friendly, inexpensive, and producing high product yields. More importantly, biological approaches do not involve the use of harsh and toxic chemicals (Agharkar, Kochrekar, Hidouri, & Azeez, 2014).

Nowadays, more focus is given on developing greener reducing agents in order to synthesize rGO. Some of the green reducing agents that have been used include phenols (e.g., tea polyphenol, tannic acid, and gallic acid) (Bo et al., 2014; Lei, Tang, Liao, & Guo, 2011; R. Liao, Tang, Lei, & Guo, 2011; Yan Wang, Shi, & Yin, 2011; L. Q. Xu, Yang, Neoh, Kang, & Fu, 2010; Zubir, Badarudin, Kazi, Huang, Misran, Sadeghinezhad, Mehrali, & Yusoff, 2015), metals (e.g., zinc, iron, and aluminum)(Bo et al., 2014; Z.-J. Fan et al., 2010; Z. Fan et al., 2010; S. Yang et al., 2012), alkaline solutions (e.g., sodium hydroxide and potassium hydroxide) (Fan et al., 2008), alcohols (e.g., ethyl alcohol, methyl alcohol, and isopropyl alcohol) (Dreyer, Murali, Zhu, Ruoff, & Bielawski, 2011), sugars (e.g., sucrose, glucose, and fructose)(Bo et al., 2014; H. Peng, Meng, Niu, & Lu, 2012), and other materials such as ammonia borane(Zhuo, Zhang, Du, & Yan, 2015), vitamin C, and glycine(Bose, Kuila, Mishra, Kim, & Lee, 2012; Fernández-Merino et al., 2010). However, there are some disadvantages with green reduction methods. For example, the low capabilities of tea polyphenol and methanol as reducing agents result in poor deoxygenation of GO(Bo et al., 2014; Dreyer et al., 2011; Y. Wang et al., 2011). On the other hand, the use of metals as reducing agents leaves impurities in the rGO (Z.-J. Fan et al., 2010; Z. Fan et al., 2010; S. Yang et al., 2012). Hence, hydrothermal treatment is a preferable method in recent years because it is an eco-friendly method to synthesize rGO aqueous suspensions.

Glucose is the mostly studied analyte because of its great biological importance. Glucose is typically used as a reducing agent owing to its mild reductive ability and

non-toxicity. Zhu et al. (C. Zhu et al., 2010) developed a green, facile approach to synthesize chemically converted graphene nanosheets (GNSs) using reducing sugars such as glucose, fructose, and sucrose, with exfoliated GO as the precursor.

A green and fast electrochemical approach has also been developed to synthesize GNSs using exfoliated GO as the precursor. The beauty of this method is that it does not lead to contamination of graphene. However, there are some defects in the electrochemically-reduced graphene because of the fast reduction rate. These defects can be eliminated by performing electrochemical reduction at elevated temperatures or by annealing the products (Guo, Wang, Qian, Wang, & Xia, 2009).

Liu et al. (K. Liu et al., 2011) developed a green, facile method to prepare gelatin-functionalized graphene nanosheets (gelatin-GNSs), where gelatin is used as the reducing agent. Meanwhile, the gelatin also serves as a functionalized reagent to prevent aggregation of the GNSs. They found that the biocompatible gelatin-GNS have excellent stability in water and various physiological fluids such as cellular growth media and serum. This is indeed an important pre-requisite for use of graphene in biomedicine. Wang et al. (Y. Wang et al., 2011) developed a green, facile strategy to fabricate soluble rGO. The proposed method is based on the reduction of exfoliated GO in green tea solution, which utilizes the reducing capability and aromatic rings of tea polyphenol found in the tea solution. Kumar et al. (Babu, Nahm, & Hwang, 2014) formulated a simple, environmentally benign, time-efficient, and cost-effective approach for reduction of GO and synthesis of rGO/mono and bimetallic composites using *Azadirachta indica* extract.

Ding et al. (YH Ding et al., 2011) presented a green approach to synthesize and stabilize aqueous graphene dispersions through ultraviolet-irradiated reduction of exfoliated GO. Polyvinyl pyrrolidone (PVP) was used to enhance the dispersibility of reduced graphene oxide by one-step functionalization. This method is simple and low-

cost because it does not involve the use of photocatalysts or reducing agents, and therefore, it is possible to produce stable reduced graphene oxide dispersions on a commercial scale using this approach. Sui et al. (Sui, Zhang, Lei, & Luo, 2011) reported an environmentally friendly, scalable route to synthesize rGO hydrogel by simple reduction of exfoliated GO with excess vitamin C.

Gurunathan et al. (Gurunathan, Han, Eppakayala, & Kim, 2013) demonstrated an environmentally friendly, cost-effective, and simple method to prepare water-soluble graphene using bacterial biomass. This reduction method avoids the use of toxic reagents such as hydrazine and hydrazine hydrate.

Haghighi et al. (Thakur & Karak, 2012) introduced the use of rose water as a reducing and stabilizing agent. The rose water was used for chemical reduction of exfoliated GO and synthesis of reduced graphene oxide nanosheets (RGONs). Thakur et al. (B. Haghighi & Tabrizi, 2013) conducted reduction of GO by phytochemicals using aqueous leaf extracts of *Colocasia esculenta* and *Mesua ferrea* Linn. and aqueous peel extract of orange (*Citrus sinensis*).

Gurunathan et al. (Gurunathan, Han, & Kim, 2013) developed a green, rapid, and simple method to synthesize graphene from GO, where mitochondrial polypeptide humanin is used as the reducing agent. Graphene was prepared via one-step reduction of GO under mild conditions in an aqueous solution. Tavakoli et al. (Tavakoli, Salavati-Niasari, & Mohandes, 2015) have successfully synthesized GNSs in the presence of pomegranate juice. In their approach, pomegranate juice serves not only as a reducing agent but also as a capping agent to produce the GNSs. Zheng et al. (Bo et al., 2014) reported a new, green, and efficient reducing agent (caffeic acid) for GO reduction. The results showed that the caffeic acid rGO has a high C/O ratio (7.15), which is among the best rGOs prepared with green reducing reagents. According to Sheng et al. (S. Zhang

et al., 2011), poly(diallyldimethylammonium chloride) (PDDA) serves as a reducing agent and stabilizer when they prepared soluble GNSs from GO.

Kartick et al. (Kartick & Srivastava, 2013) develop a green route to synthesize graphene by reduction of GO using *Cocos nucifera* L. (coconut water) as the reducing agent. Coconut water is desirable because it is naturally available, non-toxic, and environmental friendly. Wang et al. (G. Wang, Qian, Saltikov, Jiao, & Li, 2011) found that GO can be reduced to graphene using a normal aerobic setup under ambient conditions where the process is mediated by microbial respiration of *Shewanella* cells. The results showed that the microbially-reduced graphene (MRG) has excellent electrochemical properties. They systematically investigated extracellular electron transfer pathways at the cell/GO interface and the results suggest that both direct electron transfer and electron mediators are involved in the GO reduction.

Grape (*Vitis vinifera*) extract was also used as a green reducing agent to prepare rGO from GO. The effects of reduction time on the physical, chemical, and optical properties of the rGO were also investigated. The results showed that the synthesized rGO samples have excellent capability as an adsorbent to remove organic dye. The synthesis route is indeed environmentally friendly, cost-effective, with great potential for large-scale production of rGO (Upadhyay et al., 2015). Maddinedi et al. (Maddinedi et al., 2014) developed one-step biosynthesis of graphene from GO, where casein is used as the stabilizer, which is a naturally occurring milk protein. The synthesis of casein reduced graphene oxide (CRGO) is complete within 7 h under reflux at 90°C with the formation of a few layers of fine GNSs. The aspartic acid and glutamic acid residues present in the casein molecules are responsible for the reduction of GO. Some of the aforementioned methods are summarized in Table 2.2.

Table 2. 2: Summary of green methods used for reduction of GO

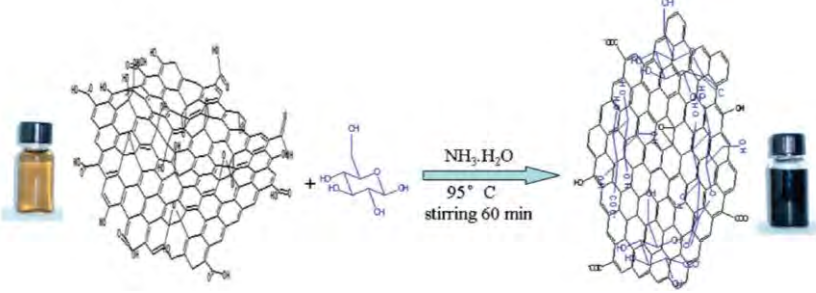
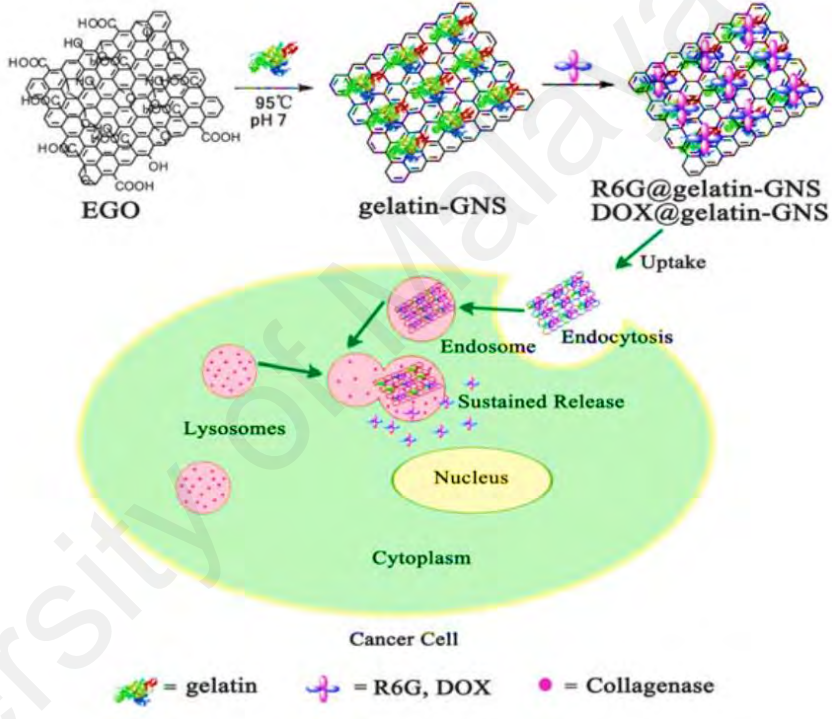
<p>Researchers / Remarks</p>	<p>Mechanism of preparation</p>
<p>Zhu et al. (C. Zhu et al., 2010) Glucose, 60 min at 95°C</p>	
<p>Liu et al. (K. Liu et al., 2011) Gelatin, 24 h, 95°C</p>	 <p style="text-align: center;">Cancer Cell</p> <p style="text-align: center;"> ■ = gelatin ■ = R6G, DOX ● = Collagenase </p>

Table 2.2, continued

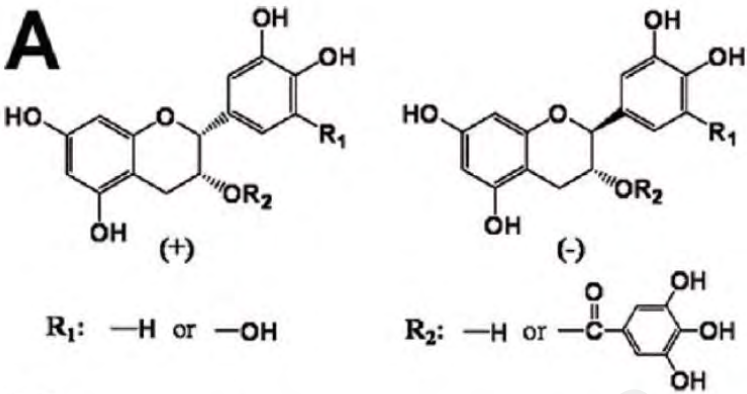
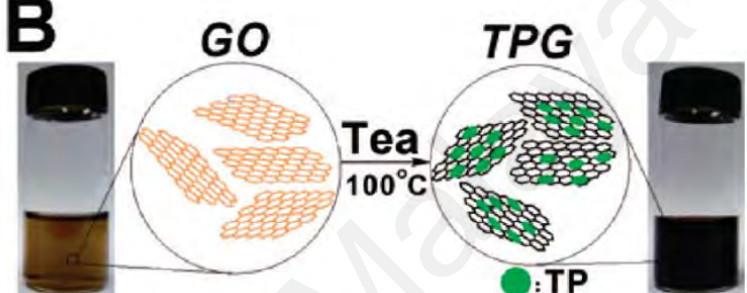
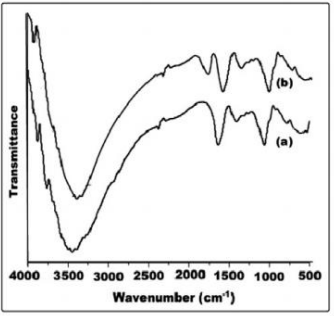
<p>Wang et al. (Y. Wang et al., 2011) Green tea solution</p>	<div style="text-align: center;"> <p>A</p>  <p>$R_1: -H \text{ or } -OH$ $R_2: -H \text{ or } -C(=O)-C_6H_2(OH)_3$</p> </div> <div style="text-align: center;"> <p>B</p>  </div>
<p>Thakur et al. (Thakur & Karak, 2012) Room temperature or refluxed</p>	<div style="text-align: center;"> <p>Phytochemicals \Rightarrow Apigenin, Luteolin, ascorbic acid</p> <p>Oxidising form \Rightarrow Apigenin, Luteolin, ascorbic acid</p> <p>GO (Epoxide) + HO-OH \rightarrow Intermediate 1 $\xrightarrow{-H_2O}$ GO (Hydroxyl)</p> <p>GO (Carbonyl) + HO-OH \rightleftharpoons GO (Hydroxyl)</p> <p>Intermediate 2 $\xrightarrow{-H_2O}$ RGO</p> </div> <div style="text-align: right;">  </div>

Table 2.2, continued

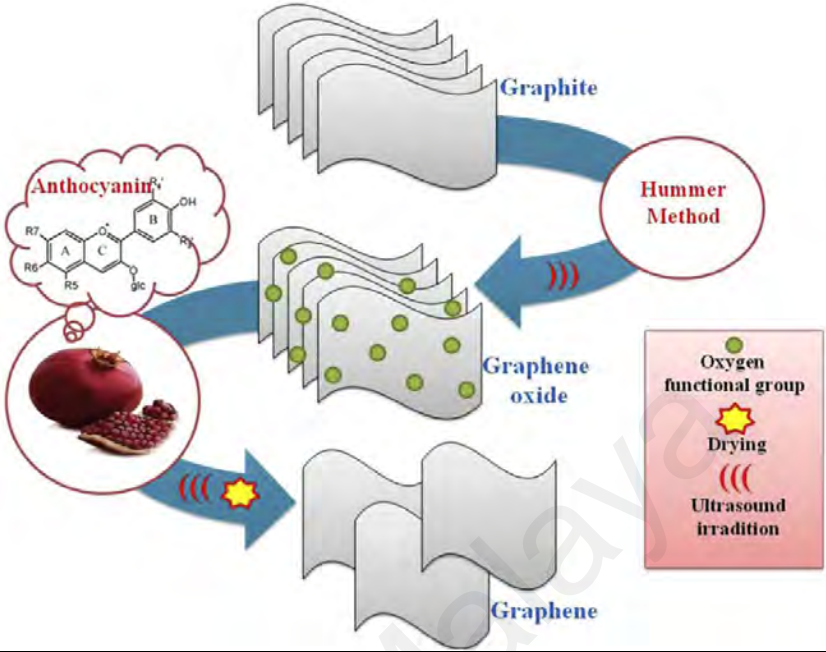
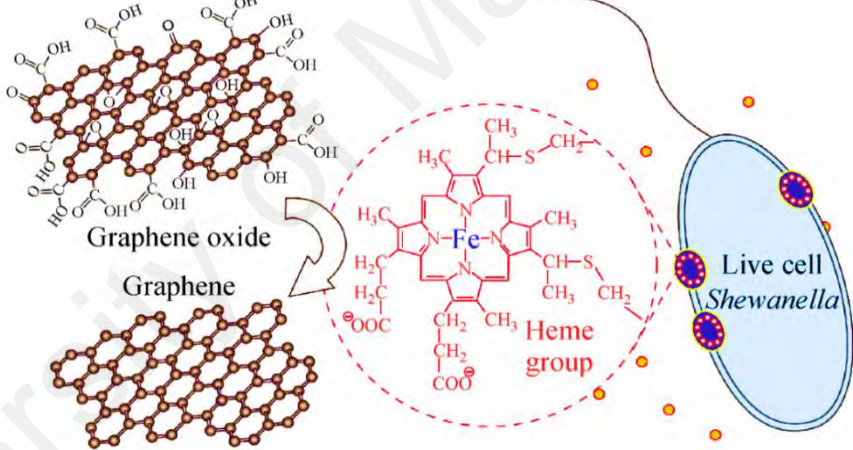
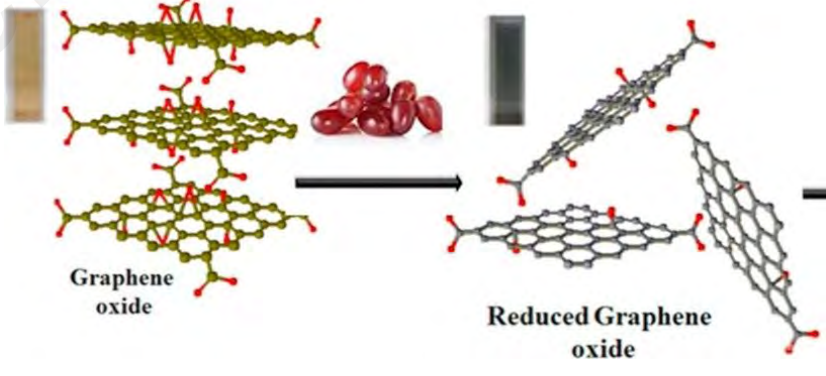
<p>Tavakoli et al. (Tavakoli et al., 2015) 12, 18, and 24 h</p>	 <p>The diagram illustrates the Hummer Method for the synthesis of graphene. It starts with graphite, which is converted to graphene oxide using the Hummer Method. Anthocyanin, a natural reducing agent, is used to reduce graphene oxide to graphene. The legend indicates that green dots represent oxygen functional groups, a yellow star represents drying, and red wavy lines represent ultrasound irradiation.</p>
<p>Wang et al. (G. Wang et al., 2011)</p>	 <p>The diagram shows the interaction of graphene oxide and graphene with a heme group and a live cell of <i>Shewanella</i>. The heme group is shown with its iron atom coordinated to four nitrogen atoms. The live cell is shown with a heme group on its surface.</p>
<p>Upadhyay et al. (Upadhyay et al., 2015) 95°C at different time intervals (1, 3 and 6 h) using water condenser</p>	 <p>The diagram shows the reduction of graphene oxide to reduced graphene oxide using water condenser. The diagram shows the chemical structure of graphene oxide and reduced graphene oxide.</p>

Table 2.2, continued

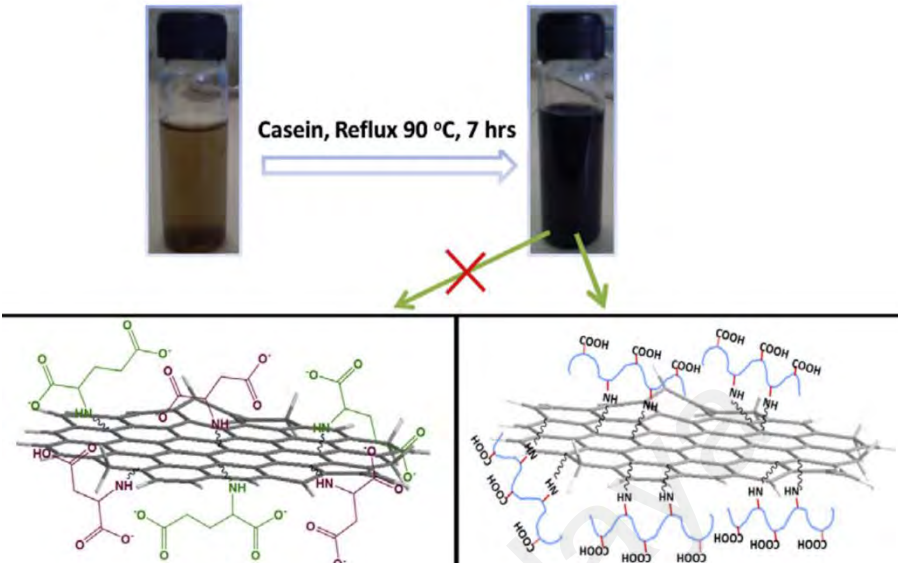

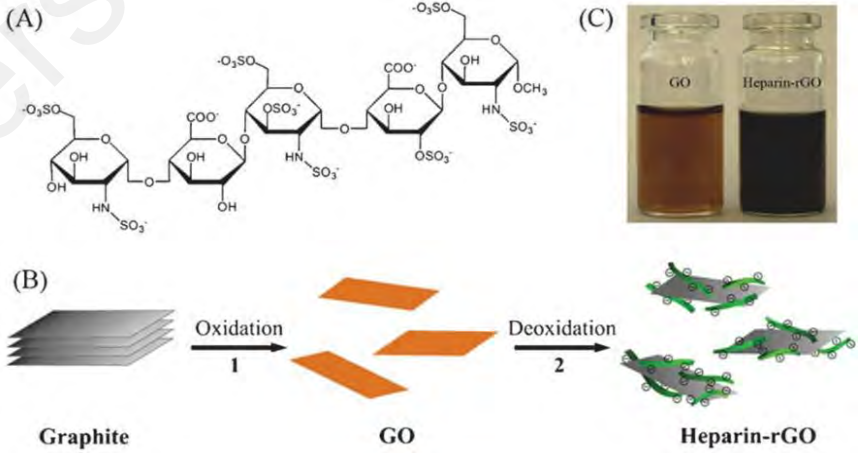
<p>Maddinedi et al. (Maddinedi et al., 2014)</p> <p>Casein (Milk protein)</p>	
<p>Liu (Y. Liu et al., 2011)</p> <p>Zn powder</p>	
<p>Wang et al. (Yi Wang et al., 2012)</p> <p>Heparin, 1 h, 95°C</p>	

Table 2.2, continued

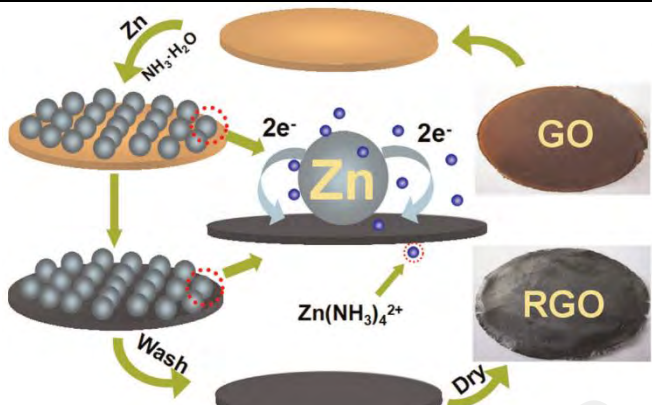
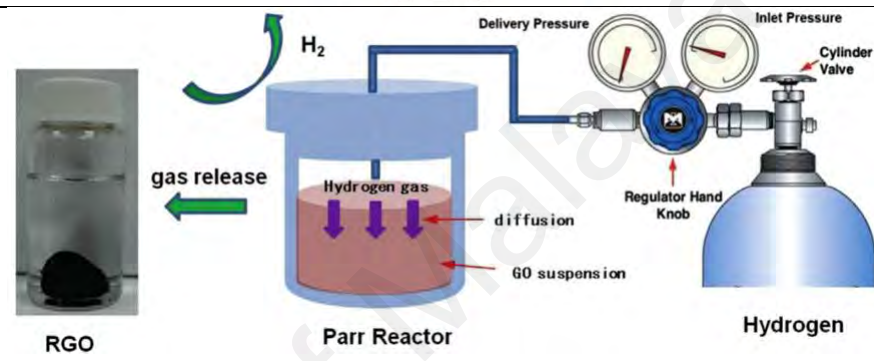
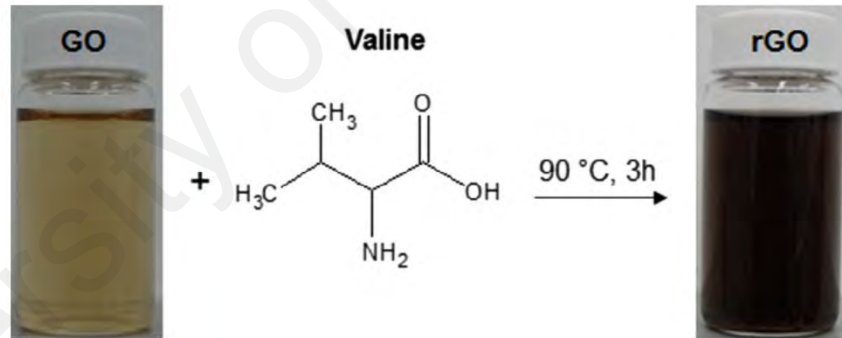

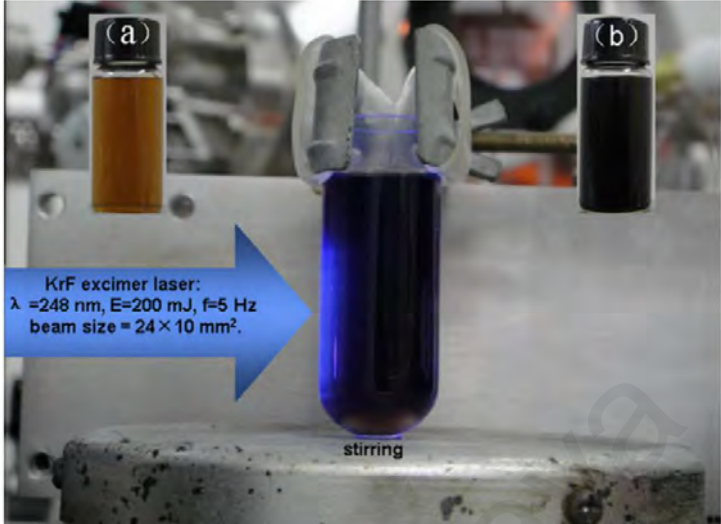
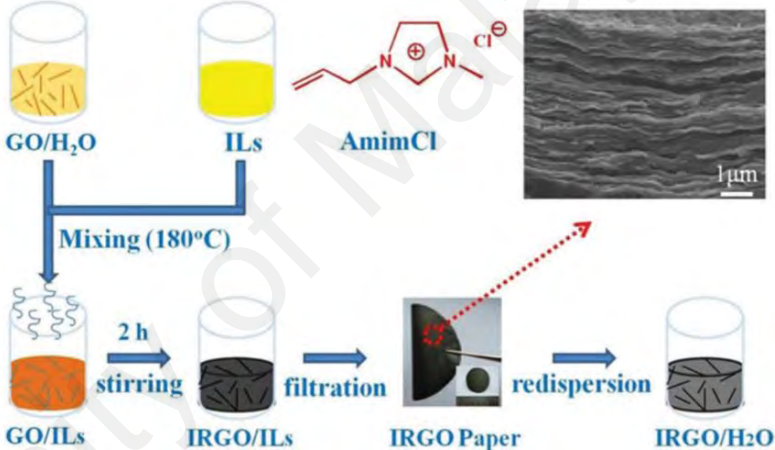
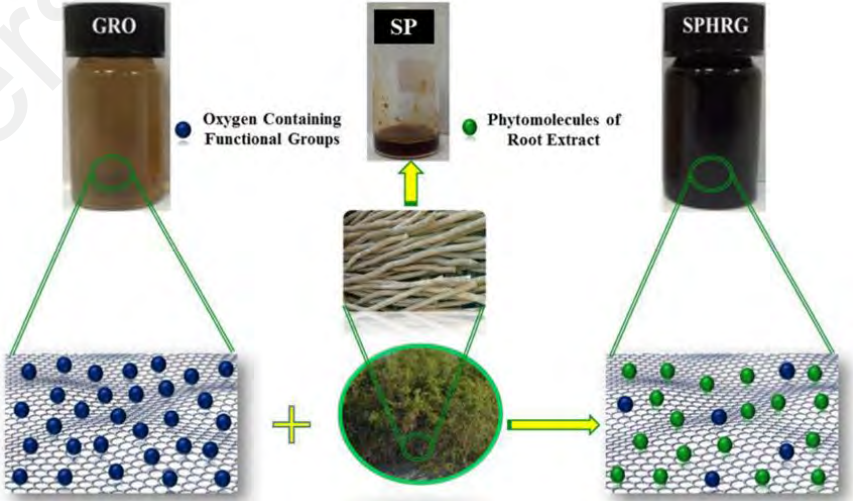
<p>Li et al. (Y.-F. Li, Liu, Zhang, Guo, & Chen, 2015)</p> <p>Zn powder, 1, 5, 10, 30, 60 min</p>	
<p>Li et al. (C. C. Li, Yu, Yan, & Hng, 2015)</p> <p>High-pressure hydrogen, 50 or 100°C for 24 h</p>	
<p>Tran et al. (Tran, Kabiri, & Losic, 2014)</p> <p>Valine, 90°C, 3, 6, and 12 h</p>	
<p>Vusa et al. (Vusa, Berchmans, & Alwarappan, 2014)</p> <p>Carrot, 1 h at 90°C</p>	

Table 2.2, continued

<p>Lei et al. (L. Huang et al., 2011)</p> <p>Pulsed laser</p>	
<p>Zhang et al. (T. Zhang, Liu, Sheng, Duan, & Zhang, 2014)</p> <p>Ionic liquid</p> <p>180°C</p>	
<p>Khan et al. (Khan et al., 2015)</p> <p><i>Salvadora persica</i> L. (<i>S. persica</i> L.) roots (miswak)</p> <p>24 h at 98°C</p>	

2.8 Thermophysical properties of nanofluid

The thermos-physical properties are essential parameters in order to understand the convective heat transfer behavior of nanofluids. The high thermal conductivity of

nanofluids aqueous suspensions is the property that is exploited to improve heat transfer of thermal systems. Thermal conductivity, in particular, is one of the most significant thermos-physical characteristics of nanofluids. On the other hand, it is challenging to predict the thermal conductivity of nanofluids because there are many parameters that will affect the thermal conductivity values such as temperature, type of base fluid, type of nanoparticles, size, shape, and volume fraction of the nanoparticles, as well as synthesis and mixing methods. Hence, one of key issues in nanofluid research is to accurately predict the thermal conductivity of nanofluids. In this section, a review on studies pertaining to the thermal conductivity of nanofluids is presented in order to shed some light on the factors that affect the thermal conductivity of nanofluids. Viscosity is also a crucial property of nanofluids because high viscosity will increase the usage of the nanofluid, which will increase the pumping power required to circulate the nanofluid. Predicting the viscosity of nanofluids is also challenging and it is one of the key issues in nanofluid research. The factors that affect the thermal conductivity of nanofluids will also affect the viscosity values. Estimating the viscosity is also important in order to determine the heat transfer coefficient, especially for turbulent flows, because viscosity is used to determine the Reynolds (Re) number.

The density and specific heat capacity also affect the heat transfer performance of nanofluids. Fortunately, it is easier to predict these thermophysical properties compared with other properties. The thermophysical properties of nanofluids are often compared with the properties of base fluids in order to reach a conclusion.

2.8.1 Thermal conductivity

Thermal conductivity is the ability of a material to transport energy in the form of energetic vibrations which manifest as heat. For solids, thermal conductivity is a measure of the direct exchange of energy through atomic level lattice vibrations and

free electron diffusion. In contrast, for fluids or gases, thermal conductivity is a measure of direct molecular contact and molecular diffusion. Thermal conductivity is a fundamental property of physical materials and it is defined as the power per unit temperature and per unit length over which conduction takes place. The thermal conductivity of a material is dependent on the physical structure of the material and its current state. Thermal conductivity is one of the important thermal transport characteristics of a material and it plays a vital role in numerous thermal design problems. Therefore, much effort has been made to measure the thermal conductivities of various materials over the last few centuries.

The physical mechanism underlying thermal conductivity enhancement of nanofluids is not well understood. Maxwell (Maxwell, 1904) was one of the pioneers to analyze thermal conduction through suspended particles analytically. Maxwell used a much diluted suspension of spherical particles and neglected the interactions between particles. The Maxwell equation can be obtained by solving the Laplace equation for the temperature field outside the particles using either one of the following methods. In the first approach, one can consider analyzing a large sphere containing all of the spherical particles with an effective thermal conductivity, k_e , embedded in a matrix with a thermal conductivity, k_m . Alternatively, one can consider analyzing all of the spherical particles with a thermal conductivity, k_p , embedded in a matrix with a thermal conductivity, k_m . The resulting equation is given by:

$$k_e = k_m + 3\vartheta_p \frac{k_p - k_m}{2k_m + k_p - \vartheta_p(k_p - k_m)} k_m \quad (2.7)$$

Where ϑ_p is the particle volume concentration. It is worth noting that the Maxwell equation is only a first-order approximation and therefore, it is only applicable to mixtures with low particle volume concentrations. Various modifications have been

made to the Maxwell equation, taking into account various factors that will affect the effective thermal conductivity such as the particle shape (Fricke, 1953; Granqvist & Hunderi, 1978), particle distribution (Rayleigh, 1892), high volume fraction (Böttcher, 1945), particle-shell structure (Qingzhong, 2000), and contact resistance (Benveniste, 1987). Even though these modified equations provide a reasonable prediction of the thermal conductivity for dilute mixtures containing relatively large particles in fluids, there is a lack of agreement between the experimental data and theoretical predictions for nanofluids. In general, these equations either underpredict the experimental data for nanofluids containing spherical particles or overpredict the experimental data for nanofluids containing prolate spheroids with semi-axes, i.e., $a \gg b = c$, such as nanotubes. In order to improve the predictions, various mechanisms have been proposed for nanoscale materials including the effects of nanoparticle-matrix interfacial layer (Prasher, Bhattacharya, & Phelan, 2006), Brownian motion of the nanoparticles (Prasher, Bhattacharya, et al., 2006), and nanoparticle clusters or aggregates. Each of the results from previous studies are applicable only for a limited range of data and to date, there are no accepted mechanisms or theories to predict the thermal conductivity enhancement of nanofluids. However, the situation is better in experimental research since a number of thermal conductivity enhancement results have been reported for a variety of nanofluids (Wenhua Yu, France, Routbort, & Choi, 2008). Some of the models used to predict thermal conductivity are summarized in Table 2.3.

Table 2. 3: Theoretical and empirical equations used to predict the effective thermal conductivity of nanofluids

Researchers	Empirical correlations	Remarks
Hamilton-Crosser (H-C) model (Hamilton & Crosser, 1962)	$\frac{k_{eff}}{k_f} = \frac{k_p + (n-1)k_f + (n-1)\varphi(k_p - k_f)}{k_p + (n-1)k_f - (n-1)\varphi(k_p - k_f)}$ <p>k_p and k_f are the thermal conductivity of the particles and base fluid, respectively, and n is the empirical shape factor</p> <p>$n=3$ for spheres and $n=6$ for cylinder</p>	The liquid phase is larger than 100. $n = \frac{3}{\psi}$, ψ is the particle sphericity, and φ is the nanoparticle concentration.
Yu and Choi correlation (W Yu & Choi, 2003)	$\frac{k_{eff}}{k_f} = \frac{k_p + 2k_f + 2\varphi(k_p - k_f)(1 + \beta)^3}{k_p + 2k_f - \varphi(k_p - k_f)(1 + \beta)^3}$	β is the ratio of the nanolayer thickness to the original particle radius and φ is the nanoparticle concentration.
Maxwell model (Maxwell, 1881)	$\frac{k_{nf}}{k_{bf}} = \frac{k_{np} + 2k_{bf} + 2\varphi(k_{np} - k_{bf})}{k_{np} + 2k_{bf} - \varphi(k_{np} - k_{bf})}$	φ is the volume concentration.
Yu and Choi correlation (W Yu & Choi, 2003)	$\frac{k_{nf}}{k_w} = \frac{k_s + 2k_w + 2(k_s - k_w)(1 + \beta)^3 v}{k_s + 2k_w - (k_s - k_w)(1 + \beta)^3 v}$ <p>v is the nanoparticle volume fraction.</p> <p>k_w is the thermal conductivity of water.</p> <p>k_s is the thermal conductivity of nanoparticles.</p>	β is the ratio of the nanolayer thickness to the original particle radius, where $\beta = 0.1$.
Pakdaman et al. (Pakdaman, Akhavan-Behabadi, & Razi, 2012)	$\frac{k_{eff}}{k_{bf}} = 1 + 304.47(1 + \varphi)^{136.35} \exp(-0.021T) \left(\frac{1}{d_{np}}\right)^{0.369} \left(\frac{T^{1.2321}}{10^{2.4642B/(T-C)}}\right)$ <p>d_{np} is the diameter of nanoparticles (nm) T is the temperature (K). $B = 247.8$ and $C = 140$</p>	
Maxwell model (Maxwell, 1881)	$\frac{k_{eff}}{k_{bf}} = 1 + \frac{3(\alpha - 1)\varphi}{(\alpha - 2) - (\alpha - 1)\varphi}$	$\alpha = \frac{k_{np}}{k_{nf}}$
Yu et al. (W Yu & Choi, 2003)	$\frac{k_{eff}}{k_{bf}} = 1 + \frac{3\varphi(\alpha - 1)(1 + \beta)^3}{1 + 2\alpha - \varphi(1 - \alpha)(1 + \beta)^3}$	$\alpha = \frac{k_{np}}{k_{nf}}$, $\beta = \frac{h}{r}$
Aberoumand (Aberoumand, Jafarimoghaddam, Moravej, Aberoumand, & Javaherdeh, 2016)	$k_{nf} = (3.9 \times 10^{-5}T - 0.0305)\varphi^2 + (0.086 - 1.6 \times 10^{-4}T)\varphi + 3.1 \times 10^{-4}T + 0.129 - 5.77 \times 10^{-6}k_{nf} - 40 \times 10^{-4}$	

Table 2.3, continued

Murshed et al. (Murshed, Leong, & Yang, 2005a)	$k_{eff} = 0.25[(3\varphi - 1)k_{np} + (2 - 3\varphi)k_{bf}] + \frac{k_{bf}}{4}\sqrt{\Delta}$ $\Delta = (3\varphi - 1)^2 \left(\frac{k_{np}}{k_{bf}}\right)^2 + (2 - 3\varphi)^2 + 2(2 + 9\varphi - 9\varphi^2)9\left(\frac{k_{np}}{k_{bf}}\right)$	
--	---	--

It is apparent that there are significant amounts of experimental data gathered by researchers upon examining the scientific literature. The data are presented in a variety of formats and categories such as morphology, clustering, type of base fluid, temperature, motion, and so on. Some of these are reviewed in this section.

2.8.1.1 Morphology

In materials science, morphology is defined as the shape, size, texture, and phase distribution of physical objects. Murshed et al. (Murshed et al., 2005b) measured the effective thermal conductivity of rod-shaped (diameter \times length: 10 nm \times 40 nm) and spherical-shaped (diameter: 15 nm) TiO₂ nanoparticles in deionized water. The results showed that the rod-shaped nanoparticles have higher thermal conductivity enhancement, which is consistent with the theoretical predictions using Hamilton-Crosser's model (Hamilton & Crosser, 1962). Evans et al. (Evans et al., 2008) investigated the effect of aspect ratio on the thermal conductivity enhancement of nanofluids. They compared the thermal conductivity enhancement of long fibers in flat plates at a specific concentration for different aspect ratios. The results suggest that the fibers with high aspect ratios (CNTs) lead to superior thermal conductivity enhancement compared with spherical or ellipsoidal particles.

Xie et al. (H.-q. Xie, Wang, Xi, & Liu, 2002) studied the effect of nanoparticle shape and the results revealed that the cylindrical-shaped nanoparticles have higher thermal conductivity enhancement compared with spherical-shaped ones for the same base fluid,

despite their larger average size. This conclusion was confirmed by other researchers (YJ Hwang et al., 2006; H. Xie et al., 2003). Moreover, the increase in length-to-diameter ratio of the dispersed nanotubes results in higher thermal conductivity enhancement (Assael, Metaxa, Arvanitidis, Christofilos, & Lioutas, 2005; Xing Zhang, Gu, & Fujii, 2007). Likewise, Choi et al. (S. Choi, Zhang, Yu, Lockwood, & Grulke, 2001) found that the MWCNTs yield an anomalously non-linear increase in the effective thermal conductivity, which contrasts the predicted effective thermal conductivity, which shows a linear behavior. On the other hand, fullerenes, which are carbon molecules in the form of hollow spheres, ellipsoids, tubes or other shapes (Kharisov, Kharissova, & Ortiz-Mendez, 2016), showed lower thermal conductivity enhancement. This result was also confirmed by Putnam et al. (Putnam, Cahill, Braun, Ge, & Shimmin, 2006) who dispersed C60–C70 fullerenes in toluene and compared their effect on the thermal conductivity enhancement against those of gold nanoparticles. The results showed that fullerenes have lower thermal conductivity enhancement compared with gold nanoparticles at low particle loadings (Tawfik, 2017).

Some researchers investigated the effect of nanoparticle size and in general, they found that nanoparticle size has a significant effect on the thermal conductivity of nanofluids. Another characteristic of nanoparticles is the specific surface area (SSA), which needs to be considered in the preparation of nanofluids because this parameter affects the effective thermal conductivity of nanofluids. The SSA is defined as:

$$SSA = \frac{\text{Particle surface area}}{\text{Particle volume}} \quad (2.8)$$

Lee et al. (S. Lee, S.-S. Choi, S. Li, and, & J. Eastman, 1999) suspended CuO and Al₂O₃ nanoparticles (CuO particle size: 18.6 and 23.6 nm, Al₂O₃ particle size: 24.4 and

38.4 nm) in different types of base fluids: water and ethylene glycol. They produced four types of nanofluids: CuO-water, CuO-ethylene glycol, Al₂O₃-water, and Al₂O₃-ethylene glycol nanofluids. The results showed that the thermal conductivity ratios increase almost linearly with the volume fraction of nanoparticles. The results indicate that the particle shape and size are the dominant factors that influence the thermal conductivity of nanofluids. Xie et al. (H. Xie et al., 2002) demonstrated the effect of nanoparticle size on the thermal conductivity enhancement and they measured the effective thermal conductivity of Al₂O₃-ethylene glycol nanofluids with different particle sizes. They reported that the thermal conductivity increases almost linearly with an increase in the volume fraction of nanoparticles. In addition, the rate of thermal conductivity enhancement ratio is dependent on the volume fraction of the dispersed nanoparticles. They found that the thermal conductivity enhancement is dependent SSA and the mean free path of the nanoparticles and base fluid. At small particle sizes, the Brownian motion of the nanoparticles increases, which dominates nano-convection. This in turn, increases the effective thermal conductivity of the nanofluids. Yoo et al. (Yoo, Hong, & Yang, 2007) investigated the thermal conductivities of TiO₂, Al₂O₃, Fe, and WO₃ nanofluids. They found that the surface-to-volume ratio of the nanoparticles is a key factor which influences the thermal conductivity of nanofluids.

2.8.1.2 Temperature

In conventional suspensions of solid particles (where the size of the particles is within the millimeter or micrometer range) in liquids, the thermal conductivity of the mixture is only dependent on temperature, which is due to the dependence of thermal conductivity of the base liquid and solid particles on temperature (Özerinç, Kakaç, & Yazıcıoğlu, 2010). However, for nanofluids, changes in temperature affects the Brownian motion and clustering of nanoparticles (C. H. Li, Williams, Buongiorno, Hu, & Peterson, 2008) which results in dramatic variations of the thermal conductivity of

nanofluids with temperature. Das et al. (Sarit Kumar Das, Putra, Thiesen, & Roetzel, 2003) discovered that the nanofluids have strong temperature-dependent thermal conductivity compared with the base fluid. They measured the effective thermal conductivities of Al_2O_3 and CuO nanoparticles in water when the temperature of the nanofluids was varied from 21 to 51°C. They observed that the thermal conductivity enhancement of the nanofluids increases by a factor of 2–4 within the range of temperatures investigated. Patel et al. (Patel et al., 2003) reported that there is a considerable increase in the thermal conductivity enhancement ratios of the Au nanofluids as the temperature is increased. Zhang et al. (X Zhang, Gu, & Fujii, 2006) measured the effective thermal conductivity of Al_2O_3 -distilled water nanofluids within a temperature range of 5–50°C and their results are in good agreement with those of Das et al. (Sarit Kumar Das et al., 2003). However, other experimental studies showed a different thermal conductivity enhancement behavior. Yu et al. (Wei Yu, Xie, & Chen, 2010) investigated the enhancement ratios of thermal conductivity of nanofluids including graphene oxide nanosheets (GONs) and they discovered that the thermal conductivity enhancement ratios are nearly invariant at different temperatures. This indicates that the thermal conductivity enhancement ratios are influenced by various factors. One of these factors is the viscosities of the base fluids. In their experiments, they used ethylene glycol as the base fluid, which has a high viscosity. However, since the size of the GONs was large, the effect of Brownian motion was not obvious.

2.8.1.3 Thermal conductivity of base-fluid

Different types of fluids (e.g., water, ethylene glycol, vacuum pump oil, and engine oil) have been used as the base fluids in preparation of nanofluids. One study showed that the thermal conductivity enhancement decreases with an increase in thermal conductivity of the base fluid, regardless of the type of nanoparticles (H. Xie, Yu, Li, & Chen, 2011). For nanofluids with the same nanoparticles, it is found that the thermal

conductivity enhancement is inversely proportional to the thermal conductivity of the base fluid, regardless of the shape of the nanoparticles (Kim, Choi, & Kim, 2007). This observation was confirmed by other studies, where it is found that the thermal conductivity enhancements for ethylene glycol-based nanofluids are higher compared with those for water-based nanofluids (Beck, Yuan, Warriar, & Teja, 2010a; H. Xie et al., 2003). In contrast, a couple of studies (Agarwal, Verma, Agrawal, Duchaniya, & Singh, 2016; M.-S. Liu, Lin, Huang, & Wang, 2005) have shown that the use of ethylene glycol results in higher thermal conductivity enhancement at the same volume fraction of nanoparticles. This finding was also confirmed by the following studies (Agarwal et al., 2016; Chopkar, Sudarshan, Das, & Manna, 2008), where water-based nanofluids have higher thermal conductivity enhancement compared with ethylene glycol-based ones at the same volume fraction of nanoparticles. A new research trend emerged beginning from the 2000s where mixtures of base fluids were used instead of conventional ones. For example, Beck et al. (Beck et al., 2010a) used a mixture of ethylene glycol and water (50:50 wt%) as the base fluid and the results showed that thermal conductivity enhancement is higher for this base fluid compared with conventional ones. The thermal conductivity enhancement increases upon the addition of nanoparticles. However, a more detailed investigation is needed when using mixed base fluids in order to select the appropriate mixing ratio because this will significantly affect the thermal conductivity of the resultant nanofluid. Abdolbaqi et al. (Abdolbaqi, Azmi, Mamat, Sharma, & Najafi, 2016) obtained a thermal conductivity enhancement of 24% by dispersing Al_2O_3 nanoparticles (diameter: 13 nm) into 2 vol% of ethylene glycol-water base fluid (40:60 wt%) at 80°C. The thermal conductivity enhancement dropped to 13% when the mixing ratio of the base fluid was 60:40 wt%. Their results are in good agreement with those of Usri et al. (Usri, Azmi, Mamat, Hamid, & Najafi, 2015), who dispersed Al_2O_3 nanoparticles (diameter: 13 nm) in ethylene glycol-water

base fluid and the results showed that the thermal conductivity decreases with an increase in the ethylene glycol concentration (Tawfik, 2017). Xie et al. (H. Xie et al., 2002) investigated the thermal conductivity of suspensions containing nanosized alumina particles. The results showed that at the same nanoparticle concentration, the thermal conductivity enhancement ratio decreases with an increase in the thermal conductivity of the base fluid. Liu et al. (M.-S. Liu et al., 2005) also investigated the effect of base fluid on the thermal conductivity enhancement of MWCNT nanofluids. Ethylene glycol and synthetic engine oil were used as the base fluids in their experiments. The thermal conductivity enhancement of the 1 vol% MWCNT-ethylene glycol nanofluid was 12.4% relative to that for the base fluid. In contrast, the thermal conductivity enhancement of the 2 vol% MWCNT-synthetic engine oil nanofluid was 30%. Hence, it is apparent here that the thermal conductivity enhancement is higher when synthetic engine oil is used as the base fluid.

2.8.1.4 Brownian motion

Brownian motion refers to the random movement of particles in the fluid, where the particles constantly colliding with one another. Brownian motion accounts for direct transport of heat from one solid to another which ultimately increases the thermal conductivity. Brownian motion is defined by the particle diffusion constant, D , which is given by the Stokes-Einstein formula:

$$D = \frac{k_B T}{3\pi\eta d} \quad (2.9)$$

where k_B is the Boltzmann constant, η is the fluid viscosity, and d is the particle diameter. This equation provides an estimation on the effect of Brownian motion on the thermal conductivity where the time scale of particle motion is compared with the time scale of heat diffusion in the liquid. By comparing the time required for a particle to move by a distance equal to its size with the time required for heat to move in the liquid

by the same distance, Keblinski's team demonstrated that the thermal diffusion is much faster than Brownian diffusion, even when nanoparticles were considered in the analysis. They concluded that the movement of nanoparticles due to Brownian motion is too slow to transport significant amounts of heat through the nanofluid. However, Brownian motion can have an important and indirect role in clustering of particles, which enhances thermal conductivity. Keblinski et al. (Phillpot Keblinski, Phillpot, Choi, & Eastman, 2002) and Koo and Kleinstreuer (Junemo Koo & Clement Kleinstreuer, 2005) suggested that the potential mechanism for thermal conductivity enhancement is the transfer of energy due to collision between the particles at higher temperatures with those at lower temperatures. The effectiveness of Brownian motion decreases with an increase in the bulk viscosity.

In conventional approaches, the effect of Brownian motion of particles is neglected due to the large particle size. As the particle size approaches the nanometer scale, the Brownian motion of the particles results in heat exchange between the particles and surrounding liquid. The contribution of Brownian motion of the nanoparticles in enhancing thermal conduction may be viewed in two different ways: (1) the thermal conduction is enhanced due to the movement of the nanoparticles which transfers heat and (2) the thermal conduction is enhanced due to microconvection of the fluid around the individual nanoparticles. The first one has been shown theoretically to be negligible (Phillpot Keblinski et al., 2002). On the other hand, microconvection also has a minor effect on the thermal conductivity based on theoretical analysis (Evans, Fish, & Keblinski, 2006). The random motion of the nanoparticles enhances the thermal conductivity of the nanofluid. Therefore, the effective thermal conductivity of the nanofluids is dependent on the nanostructures of the suspensions as well as the dynamics of the nanoparticles in the base fluid. Consequently, one needs to consider the movement of nanoparticles due to the interactions between the nanoparticles and base

liquid molecules when developing a prediction model (Sarit K Das, Choi, Yu, & Pradeep, 2007). Koblinski et al. (Koblinski et al., 2002) performed molecular dynamics (MD) simulations to calculate the thermal conductivity of a simple liquid and solid model by using Green-Kubo relationships. The results showed that the effect of collision between the nanoparticles due to Brownian motion is not significant because the ratio of thermal diffusion to Brownian motion is significantly higher. Furthermore, the Brownian motion may affect the formation of particle clusters which can improve the thermal conductivity of nanofluids.

Li and Peterson (C. Li & Peterson, 2007) analyzed the mixing effect of the base fluid in contact with the nanoparticles due to the Brownian motion of nanoparticles by using ANSYS CFX 5.5.1 software in order to simulate the temperature, pressure, and velocity fields. They investigated the effects of single, adjacent, and multiple nanoparticles. Their results imply that Brownian motion induces microconvection and the mixing significantly enhances heat transfer of the nanofluid on a macroscopic scale. Brownian motion is one of the important factors for the anomalous enhancement of the effective thermal conductivity of nanofluids. Sarkar and Selvam (Sarkar & Selvam, 2007) developed a nanofluid system comprising argon and copper nanoparticles dispersed in the base fluid at various particle concentrations. They used an equilibrium MD simulation to model the nanofluid system. They used the Green-Kubo relationship in order to determine the thermal conductivities of the base fluid and nanofluids. They found that the effective thermal conductivities of the copper-argon nanofluids are significantly higher than those predicted by the Hamilton-Crosser model at low volume fractions (up to 0.4%) and high volume fractions (up to 8%). They also found that the motion of the liquid atoms in the nanofluids increases considerably compared with the base fluid (by a factor of 1.41 for the nanofluid with 1% particle concentration). The movement of the nanoparticles is also 28 times slower than that of the base fluid for the

nanofluid with 1% particle concentration. This implies that the Brownian motion of the nanoparticles is too slow to transport heat. On the other hand, the localized fluid movement around the nanoparticles is induced by the liquid atoms travelling at higher speeds. They concluded that these phenomena are the main mechanisms underlying the thermal conductivity enhancement of nanofluids. However, they only considered single nanoparticles in their simulations and excluded the effects of aggregation (Aybar, Sharifpur, Azizian, Mehrabi, & Meyer, 2015), as shown in Figure 2.25.

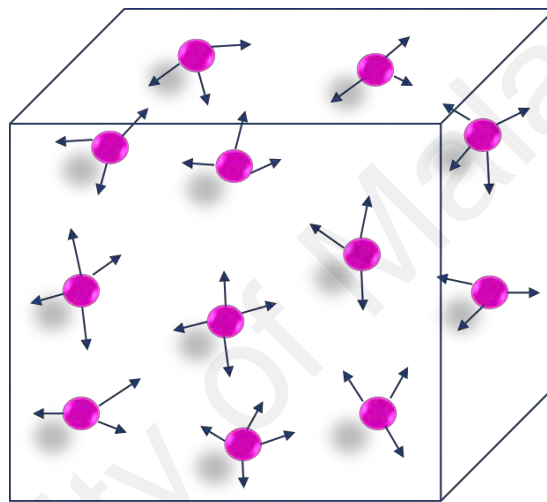


Figure 2.25: Schematic showing the Brownian motion of nanoparticles

2.8.1.5 Clustering

Clustering is the formation of larger particles through the aggregation of nanoparticles. Clustering effect is always present in nanofluids and it is factor that influences the thermal conductivity of nanofluids (Özerinç et al., 2010). The probability of aggregation increases as the particle size decreases at a constant volume fraction because the average interparticle distance decreases, which increases the van der Waals forces between the particles (Sarit K Das et al., 2007). Aggregation reduces the Brownian motion due to the increase in the mass of aggregates whereas it can increase the thermal conductivity due to percolation effects in the aggregates as the highly

conducting particles contact one another (Prasher, Phelan, & Bhattacharya, 2006). However, the larger clusters tend to settle down in the base fluid, which reduces thermal conductivity enhancement.

A number of researchers have strongly suggested that nanoparticle aggregation plays a significant role in heat transport of nanofluids. Using the effective medium theory, Prasher et al. (Prasher, Evans, et al., 2006) demonstrated that the thermal conductivity of nanofluids can be significantly enhanced by the aggregation of nanoparticles, resulting in the formation of clusters. Hong et al. (K. Hong et al., 2006) investigated the effect of nanoparticle clustering on the thermal conductivity of nanofluids. They found that there is significant thermal conductivity enhancement for the Fe nanofluids sonicated at high-powered pulses. They measured the average size of the nanoclusters and thermal conductivities of the sonicated nanofluids as a function of time after the sonication stopped. They found that the reduction of the nanofluid thermal conductivity is directly related to the agglomeration of nanoparticles. Kwak and Kim (Kwak & Kim, 2005) demonstrated that the significant thermal conductivity enhancement is accompanied by an abrupt increase in viscosity at low volume fractions of nanoparticles (<1%). This indicates that it is more effective to use small volume fractions of nanoparticles rather than large volume fractions in preparation of nanofluids. Lee et al. (D. Lee et al., 2006) demonstrated the critical importance of particle surface charge on the thermal conductivity of nanofluids. Surface charge is one of the primary factors that control nanoparticle aggregation. Furthermore, Putnam et al. (Putnam et al., 2006) and Zhang et al. (X Zhang et al., 2006) demonstrated that nanofluids with good dispersibility do not result in any unusual thermal conductivity enhancements (Evans et al., 2008). Table 2.4 summarized the results of effective thermal conductivity measurement from literature on nanofluids containing carbon allotropes.

Table 2. 4: Literature review on the experimental study of effective thermal conductivity of carbon allotropes-based aqueous nanofluid

Author(s)	Nanoparticle type	Base fluid	Size	nanoparticle Concentration	Thermal conductivity ratio/enhancement	Temperature range	Remarks
N.Singh et al. (2012)(N. Singh, Chand, & Kanagaraj, 2012)	Acid treated-MWCNT	EG+water	D 60-30 nm L 5-15µm	0.12-0.4 wt%	Up to 72%	-	-
T.X.Phuoc et al. (2011)(Phuoc, Massoudi, & Chen, 2011)	MWCNT	(+ Chitosan)-water	OD 20-30nm, ID 5-10nm L 10-30 µm	0.5-3 wt%	2.3%-13%	35°C	-
P. Garg et al. (2009) (Garg et al., 2009)	MWCNT	(+ gum arabic)-water	OD 10-20 nm, L 0.5-40µm	1 wt%	Up to 20%	15-35°C	Ultrasonication effect
Amiri et al. (Amiri, Shanbedi, Eshghi, Henis, & Baniadam, 2012)	Ag-decorated MWCNT	Water	D 10-20 nm, L 5-15 µm	0.5-1 wt%	25%-30%	30-80 °C	
Ruan and Jacobi.2012(Ruan & Jacobi, 2012)	Ruan and Jacobi.2012[9]	EG	OD 10-30, L 10-30, ID 5-10	0.5 wt%	23%	Room temperature	Ultrasonication effect 1355 mins
Shende and Sundara (Shende & Sundara, 2015)	Nitrogen doped graphene	EG Water		0.005-0.03 vol% 0.005-0.02 vol%	Up to 15.1% Up to 17.7%	25-50 °C 25-50 °C	

Table 2.4, continued

A.Amrollahi et al.2008(Amrollahi, Hamidi, & Rashidi, 2008)	MWCNT	EG	OD 1-4, ID 0.8-1.1	2.5 vol%	Up to 20 %	25-50 °C	Temperature Effect
Lee and Rhee (G.-J. Lee & Rhee, 2014)	Graphene nanoplatelets	EG	-	0.5-4 vol%	Up to 32%	10-90 °C	-
Sarsam et al. (Sarsam, Amiri, Kazi, et al., 2016)	GNP-GA GNP-SDBS GNP-CTAB	Water Water Water	SSA 300 m ² /g SSA 300 m ² /g SSA 300 m ² /g	0.1 wt% 0.1 wt% 0.1 wt%	6.519-10.80% 5.09-8.36% 4.07-5.80%	20-40 °C 20-40 °C 20-40 °C	Effect of different surfactant
Ghozatloo et al.(Ghozatloo, Shariaty-Niasar, & Rashidi, 2013)	Graphene nanosheets	Water	-	0.01-0.05 wt%	3.8%-17%	10-50 °C	CVD method
Liu et al. (Lomascolo, Colangelo, Milanese, & de Risi, 2015)	MWCNT	EG/EO	D 20-50	0.20-2.00 vol%	12/30%	Ambient temperature	-
Teng et al. (K. Teng, Amiri, Kazi, Bakar, & Chew, 2016)	EDTA-treated MWCNT	Water	OD 8-15 nm, L 30µm	0.015-0.045 wt%	16%-23%	20-50 °C	-
L.Chen, H. Xie 2010 (L. Chen & Xie, 2010)	MWCNT	(+Cationic gemini)-water	OD 30-50 nm, L ~ 20 µm	0.6 Vol%	5.6%-34%	5-65 °C	-
Marquis et al. (Lomascolo et al., 2015)	SWCNT	Diesel oil	10-50 nm, 0.3-10 µm	0.25-1 vol%	10/46	Ambient temperature	-
Xie et al. (H. Xie et al., 2003)	Acid-treated MWCNT	Decene/ethylene glycole/water	D 15nm, L 30 µm	1 Vol%	19.6%/12.7%/7%	-	-

Table 2.4, continued

Assael et al.(Assael, Chen, Metaxa, & Wakeham, 2004)	MWCNT	(+SDS)-Water	100nm, L 70µm	0.6 Vol%	38%	-	-
Yu et al.(Wei Yu, Xie, Wang, & Wang, 2011)	Graphene oxide	EG	-	2-5 wt%	Up to 86%	10-60 °C	-
Hosseini et al.(Hosseini et al., 2017)	Clove-treated MWCNT	Water	OD 20-40	0.075-0.175 wt%	Up to 20.15%	20-50 °C	Green method
Sadri et al. (Sadri et al., 2014a)	MWCNT	(+GA)-Water	OD 20-30, L 10-30	0.05 wt%	Up to 22.31%	20-45°C	Ultrasonication effect
Shanbedi et al. (Shanbedi et al., 2015)	MWCNT	(+GA)-Water	AD 30 nm, L 10-20 µm	0.05-0.2 wt%	5%-24%	20-80 °C	-
Present study(Sadri, Hosseini, Kazi, Bagheri, Ahmed, et al., 2017)	Acid treated-MWCNT	Water	AD 30 nm, L 10-20 µm	0.05-0.2 wt%	9-27.5%	20-80 °C	
Present study(Sadri, Hosseini, Kazi, Bagheri, Ahmed, et al., 2017)	gallic acid-treated GNP	Water	SSA 750 m2/g	0.025-0.1 wt%	Up to 24.18%	20-45 °C	Green method
Present study(Sadri et al., 2018)	clove-treated GNP	Water	SSA 750 m2/g	0.025-0.1 wt%	Up to 22.92%	20-45 °C	Green method

2.8.2 Density

In essence, nanofluids are heterogeneous mixtures of solid and liquid materials. In order to illustrate this concept, consider a nanofluid in which solid nanoparticles occupy volume V_s whereas the base fluid occupies volume V_f , as shown in Figure 2.26.

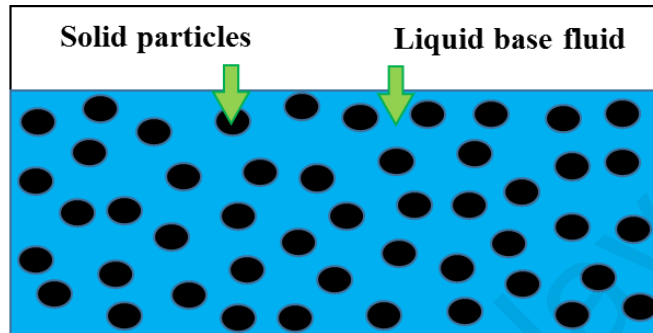


Figure 2.26: Illustration of a nanofluid, which is a heterogeneous mixture of solid and liquid materials

Nanofluid systems consist of solid nanoparticles that occupy volume V_s and liquid base fluid that occupies volume V_f . According to the conservation of volume of heterogeneous mixtures, the following expression is used for the nanofluid volume, V .

$$V = V_s + V_f \quad (2.10)$$

The volume fraction of the solid particles, φ , is defined as:

$$\frac{V_s}{V} = \varphi \quad (2.11)$$

Therefore, the volume fraction of the liquid base fluid is:

$$\frac{V_f}{V} = 1 - \varphi \quad (2.12)$$

The mass that is enclosed within the volumes V_f and V_s can be expressed in terms of the densities of the solid particles and base fluid ρ_s and ρ_f . Thus, the total mass m can be expressed as:

$$m = m_s + m_f = \rho_s \varphi V + \rho_f (1 - \varphi) V \quad (2.13)$$

The average density of heterogeneous mixture can be determined from the ratio of mass and volume.

$$\rho_{ave} = \frac{m}{V} = \rho_s \varphi + \rho_f (1 - \varphi) \quad (2.14)$$

It shall be noted that ρ_{ave} is the average density of the entire fluid. At any local point within the nanofluid, the density is either the density of the base fluid or the density of the nanoparticles, or it can be discontinuous at the particle surface. Similarly, the average density for a very small volume is not necessarily equal to the average density because the concentration of the solid particles may vary slightly locally (Mikkola, 2015).

Like viscosity, density also affects the pressure drop and pumping power, as it affects the Re number, Nusselt (Nu) number, thermal diffusivity, and heat transfer coefficient of the heat transfer fluid. However, only a limited number of studies have been carried out to investigate the effect of density of nanofluids. Sommers et al. (Sommers & Yerkes, 2010) obtained a linear relationship between density and particle concentration for Al_2O_3 -propanol nanofluids. Vajjah et al. (R. Vajjha, Das, & Mahagaonkar, 2009) also investigated the density of ethylene glycol-water based nanofluids with Al_2O_3 , ZnO_2 and $\text{Sb}_2\text{O}_4:\text{SnO}_2$ nanoparticles.

2.8.3 Viscosity

Viscosity is a measure of the fluid resistance to flow. This resistance arises from the attractive forces between the fluid molecules. Fluid will only flow when there is sufficient energy to overcome these forces. Isaac Newton was the first to give a scientific definition for viscosity. He derived a mathematical formula that relates viscosity with the resistive (drag) force experienced by a thin plate “shearing” through the fluid. The definition given by Isaac Newton is based on two quantities:

1. Shear rate: This refers to the speed of the thin plate divided by its distance from some reference surface such as the container wall.
2. Shear stress: This is the drag force experienced by the thin plate divided by its surface area.

In any flow, the fluid layers move at different velocities and the fluid viscosity stems from the shear stress between the layers that opposes the applied force. The relationship between the shear stress and velocity gradient can be obtained by considering two plates closely spaced at a distance y and separated by a homogeneous substance. It is assumed that each plate has large surface area, A , such that edge effects may be neglected. The lower plate is fixed and force, F , is applied to the upper plate. If this force causes the substance between the plates to undergo shear flow with a velocity gradient u (as opposed to just shearing elastically until the shear stress in the substance balances the applied force), the substance is called a fluid, as shown in Figure 2.27.

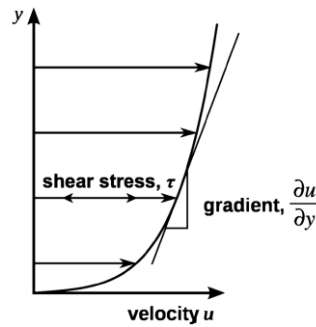


Figure 2.27: Laminar shear flow in a straight pipe where the shear stress is proportional to the velocity gradient

The applied force is proportional to the area and velocity gradient of the fluid. However, the applied force is inversely proportional to the distance between the plates. The applied force as a function of these terms is given by:

$$F = \mu A \frac{u}{y} \quad (2.15)$$

where μ is the proportionality factor called viscosity.

Equation (2.15) can be expressed in terms of the shear stress, $\tau = \frac{F}{A}$. For straight, parallel, uniform flows, the shear stress between the fluid layers is proportional to the velocity gradient in the direction perpendicular to the layers, as given by the following equation (Symon, 1971):

$$\tau = \mu \frac{\partial u}{\partial y} \quad (2.16)$$

The relationship between the shear stress and velocity gradient can be obtained with this method. Note that the rate of shear deformation is $\frac{u}{y}$, which can also be written as the shear velocity, $\frac{\partial u}{\partial y}$.

The rheological properties of colloids have been studied extensively over the past century. In fact, Einstein (1906) proposed a theoretical equation to predict the viscosity

of a very dilute colloidal system (less than 1% by volume) 100 years ago. Many researchers have attempted to improve the viscosity model of colloids. As the particle concentration increases, the hydrodynamic interaction between the particles becomes more pronounced because the disturbance of fluid around one particle will interact with that surrounding other particles. In 1977, Batchelor (1977) considered this factor and proposed an improved model to predict the viscosity of colloids at relatively higher concentrations of particles. The results showed that as the particle concentration increases, the interactions between the colloidal particles becomes significant. However, there is no rigorous analysis regarding this subject. In 1959, Krieger and Dougherty (1959) proposed a semi-empirical correlation for the shear viscosity which encompasses the entire range of particle concentrations. In addition, a large number of experiments have been conducted to understand the viscosity of colloids. Goodwin and Hughes (2008), Larson (2005) and Abdulagatov and Azizov (2006) experimentally investigated the rheological properties of colloids. C. Chang and Powell (1994) and (Luckham and Ukeje (1999)) have investigated the effects of particle size and particle distribution on the viscosity of colloids. The results showed that smaller particle size result in higher viscosity, whereas larger particle size distribution reduces the viscosity of colloids. However, studies on the rheological properties of nanofluids are still scarce.

Most flow applications require low-viscosity fluids because this will reduce the pumping power required to transport the fluid. In heat transfer applications, extra pumping power is required to transport fluid in active systems. In convective heat transfer systems where nanofluids are used as the working fluid, the viscosity of nanofluids may increase the required pumping power of the system while increasing heat transfer. This is one of the disadvantages of nanofluids, which needs to be overcome because the increase in fluid viscosity will negate thermal conductivity enhancement.

The viscosity of nanofluids is dependent on several factors such as the concentration, type, size and shape of the nanoparticles, the type of base fluid, and pH of the nanofluid. Similar to thermal conductivity enhancement, fluid viscosity increases with an increase in particle concentration and decrease in the size of particles. On the other hand, an increase in temperature will slightly decrease the relative viscosity of the nanofluid. Some of the common empirical correlations used to predict the dynamic viscosity of nanofluids are summarized in Table 2.5.

Table 2. 5: Summary of models used to predict the effective dynamic viscosity

Researchers	Empirical correlation
Einstein's equation (Einstein, 1956)	$\mu_{nf} = (1 + 2.5\varphi)\mu_{bf}$
Brinkman's model (Brinkman, 1952)	$\mu_{nf} = \frac{\mu_f}{(1 - \varphi)^{2.5}}$
Pak and Cho's correlation (Pak & Cho, 1998)	$\mu_{nf} = \mu_f(1 + 39.11\varphi + 533.9\varphi^2)$
Brownian model (Orozco, 2005)	$\mu_{nf} = \mu_f(1 + 2.5\varphi + 6.17\varphi^2)$
Gherasim et al.'s model (Gherasim, Roy, Nguyen, & Vo-Ngoc, 2009)	$\mu_{nf} = \mu_f(0.904e^{14.8\varphi})$
Maiga's model (Maiga, Palm, Nguyen, Roy, & Galanis, 2005)	$\mu_{nf} = \mu_f(1 + 7.3\varphi + 123\varphi^2)$
Nguyen's model (Nguyen et al., 2008)	$\mu_{nf} = \mu_f(1 + 0.025\varphi + 0.015\varphi^2)$
Batchelor's model (Sarsam, Amiri, Zubir, et al., 2016)	$\frac{\mu_{nf}}{\mu_{bf}} = 1 + 2.5\varphi_{\vartheta} + 6.5\varphi_{\vartheta}^2$
Sarsam et al.'s model (Sarsam, Amiri, Zubir, et al., 2016)	$\frac{\mu_{nf}}{\mu_{bf}} = 1 + 550\varphi_{\vartheta}$

Pak and Cho (Pak & Cho, 1998) measured the viscosity of Al₂O₃-water nanofluids as a function of the shear rate and particle concentration. The Al₂O₃ nanoparticles have an average diameter of 13 nm and the particle concentration was varied up to 10 vol%. In general, the nanofluids show Newtonian behavior, where the viscosity is independent of the shear rate and the maximum viscosity of nanofluids is up to 300 times higher than that of the base fluid. The measured viscosities of nanofluids are significantly higher than those predicted by Batchelor's equation. Wang et al. (X. Wang, Xu, & Choi, 1999) only observed a 90% increase in viscosity for Al₂O₃-water nanofluids with similar concentrations and particle dimensions. Even though they measured the viscosities of the Al₂O₃ nanofluids and did not find any non-Newtonian effect, many nanofluid systems show non-Newtonian behavior, unlike the corresponding base fluids. Das et al. (Sarit K Das, Putra, & Roetzel, 2003) measured the viscosity of Al₂O₃-water nanofluids and they observed that there is a slight change in the viscosity as the shear rate increases and the nanofluids behave as Newtonian fluids. They also investigated the variation of viscosity as a function of temperature and the results are similar to those for the base fluid. The maximum viscosity is obtained for the nanofluid with the highest particle loading at the lowest temperature. Kwak and Kim (Kwak & Kim, 2005) dispersed 12-nm CuO nanoparticles in ethylene glycol and measured the viscosity of the nanofluids. They observed that the viscosity of the nanofluids change from Newtonian to shear thinning as the particle concentration increases. For nanofluid with a CuO particle concentration of 1 vol%, the viscosity decreases by two orders of magnitude as the shear rate increases from 0.01 to 1000 1/s. Kulkarni et al. (Kulkarni, Das, & Chukwu, 2006) observed the same shear thinning behavior in CuO-water nanofluids. Ding et al. (Yulong Ding et al., 2006) dispersed MWCNTs in water and found that the results of these nanofluids are similar to those of spherical nanoparticle suspensions. In fact, the shear thinning behavior of CNT-water nanofluids is more apparent than that of

nanofluids with spherical nanoparticles. Davis et al. (Davis et al., 2004) observed similar shear thinning behavior in the viscosity of CNT nanofluids and they obtained a local maximum and a local minimum when they measured the viscosity of nanofluids as a function of the CNT concentration. This trend can be explained by the phase behavior of the Brownian rigid rods in nanofluids. At the beginning, as the volume fraction of the CNT increases, the nanofluids transit from a dilute regime (in which there is no interaction between the CNTs) to the liquid crystal phase. Stated differently, as the concentration of CNTs increases, the motion of the CNTs are restricted by interactions between the CNTs, which increases the viscosity. When the CNT concentration is increased further, this causes the nanofluid system to transit from a bi-phasic system to a solely liquid crystal system, and this occurs between the local maximum and local minimum of viscosities. However, if the concentration continues to increase, the viscosity will increase rapidly from the local minimum point.

Wang and Mujumdar (X.-Q. Wang & Mujumdar, 2007) reported that there are limited studies on the rheological behavior of nanofluids. The viscosities of CuO-water suspensions were measured by Li et al. (Junming Li, Li, & Wang, 2002) using a capillary viscometer. They observed that there is a decrease in the apparent viscosity of nanofluids. They also pointed out that the capillary tube diameter may influence the apparent viscosity at higher nanoparticle mass fractions, especially at lower temperatures. Das et al. (Sarit K Das et al., 2003) measured the viscosities of Al₂O₃-water nanofluids as a function of shear rate. They reported that the viscosity increases with an increase in the particle concentration and they stated that there is a strong possibility that the nanofluids may be non-Newtonian fluids, or even viscoelastic in some cases. However, they proposed that further experimental studies are needed in order to define the viscosity models of nanofluids and obtain simulation results with higher accuracy. Ding et al. (Yulong Ding et al., 2006) measured the viscosities of

CNT-water nanofluids as a function of shear rate. They observed that the viscosity of the nanofluid increases with an increase in CNT concentration and decrease in temperature. They also observed shear thinning behavior, which means that nanofluids can improve fluid flow performance due to higher shear rate at the wall, which results in low viscosity (H. Mohammed, Bhaskaran, Shuaib, & Saidur, 2011).

2.8.4 Specific heat capacity

The specific heat capacity of a pure substance or a mixture is defined as the heat required to raise the temperature of 1 mole of a substance under specified conditions. It is crucial to determine the specific heat accurately in order to evaluate the thermal performance of nanofluids. This property is required in thermal conductivity, thermal diffusivity, and spatial temperature measurements in free convection flows and it is one of the key parameters to describe convective flows of nanofluids. Some studies have shown that nanoparticles have a very small effect on the specific heat of nanofluid due to the low volume fraction of nanoparticles. However, in most cases, it is assumed that the specific heat is strongly dependent on the volume fraction of nanoparticles. In the absence of available experimental data, two models widely used in experimental and numerical studies of nanofluids. These models are described as follows.

Model I. This model is analogous to the mixing theory of ideal gas mixtures. The specific heat of a nanofluid is expressed as:

$$C_{p,nf} = \varphi C_{p,n} + (1 - \varphi)C_{p,nf} \quad (2.17)$$

where the subscripts nf , n , and f refer to the nanofluid, base fluid, and nanoparticle, respectively. Because of its simplicity, Equation (2.17) has been used to assess the heat transfer performance of nanofluids in numerous experiments and theoretical simulations.

Model II. This model is based on classical and statistical theories. Assuming that the base fluid and the nanoparticles are in thermal equilibrium, the specific heat of the nanofluid can be predicted using the following equation:

$$C_{p,nf} = \frac{\varphi(\rho C_p)_n + (1 - \varphi)(\rho C_p)_f}{\varphi\rho_n + (1 - \varphi)\rho_f} \quad (2.18)$$

Where ρ is density. In this model, the density variations of the nanofluid, nanoparticles, and base fluid are involved. Equation (2.18) has also been used as the basic formula in many nanofluid investigations, such as in the theoretical models of anomalous thermal conductivity (Xuan & Roetzel, 2000), thermal diffusivity measurements (Murshed, Leong, & Yang, 2006), and convective heat transfer (S. Zhou & Ni, 2008).

2.9 Heat transfer and friction factor of nanofluids

It is known that there are three modes of thermal energy transport, which are conduction, convection, and radiation. However, it is very rare that there is only one mode of heat transfer in thermal processes, though one of these three modes may dominate a particular process.

2.9.1 Forced convection heat transfer in a tube

In most industrial processes, heat is transferred by forced convection. Therefore, the performance of heat transfer fluids used in these systems has a remarkable impact on the energy efficiency of practical applications. Significant economic and environmental benefits can be gained by exploiting the use of effective heat transfer fluids. Several studies have shown anomalous enhancement in convective heat transfer of nanofluids (Gupta, Arora, Kumar, Kumar, & Dilbaghi, 2014; Kakac, Yener, & Pramuanjaroenkij, 2013; Michaelides, 2014). Hence, nanofluids have great potential to improve convective heat transfer processes.

Convection is one of the modes of heat transfer, in which thermal energy is transferred by fluid motion. In practice, forced convection systems include two mechanisms of heat transfer: thermal conduction and advection. Due to the presence of advection, convection heat transfer is a highly complex phenomenon compared with thermal conduction. Analytical solutions of convection problems require one to solve the governing equations of mass, momentum and energy.

Convection of laminar flows is quite well understood and there are analytical solutions for several geometries. However, there is no generic momentum equation for turbulent flows and thus, the heat transfer coefficients cannot be accurately determined analytically. Due to the lack of analytical solutions, the heat transfer coefficients of nanofluids in turbulent flow conditions are often determined using experimental correlations. However, the heat transfer coefficients obtained using these correlations are not accurate, with a large error range of ~5–15% (Kakac et al., 2013).

2.9.2 Force convection and friction factor in turbulent flow conditions

Heat transfer coefficient is a better indicator for nanofluids compared with the thermal conductivity enhancement when designing heat exchangers. Since nanofluids can improve the heat transfer coefficient of thermal energy systems, these fluids can facilitate in reducing the size of such systems which increase the energy and fuel efficiencies, reduce pollution, and improve reliability. It is essential to directly measure the heat transfer performance of nanofluids under turbulent flow conditions that are representative of those in the actual applications. While not as common as reports on thermal conductivity enhancement of nanofluids, there are still several significant studies on heat transfer coefficient enhancement of nanofluids under turbulent flow conditions. Most heat transfer studies involve the use of the Nu number, which is the ratio of convective to conductive heat transfer across the boundary.

Several mechanisms have been proposed to describe convective heat transfer enhancement and new correlations or numerical methods have been used to estimate convective heat transfer of nanofluids. Empirical correlations are usually of practical importance for engineering design purposes due to their simplicity. For fully-developed turbulent flows in a hydraulically smooth pipe, the correlations (Newaz, Duffy, & Chen, 1998) generally used to estimate the Fanning friction factor are given by the following equations:

$$f = 0.079Re^{-0.25}, Re \leq 2 \times 10^4 \quad (2.19)$$

and

$$f = 0.046Re^{-0.20}, Re \geq 2 \times 10^4 \quad (2.20)$$

In practice, the tubes used in industrial applications are not hydraulically smooth. The turbulent flow friction factor of real pipes is strongly dependent on the smoothness of the internal surface. J. Nikuradse (1933) experimentally investigated sand-grain roughened tubes to evaluate the effect of roughness (ε) on the friction and velocity distributions. However, there is a lack of emphasis on heat transfer measurements (Kazi, 2001).

J. Nikuradse (1933) identified the three regimes of flows in pipes, which depends on the values of f , Re_ε , and ε/r . These regimes are given by the following equations:

$$\text{Hydraulically smooth regime: } 0 \leq Re_\varepsilon \leq 5, \quad f = F(Re) \quad (2.21)$$

$$\text{Transition regime: } 5 \leq Re_\varepsilon \leq 70, \quad f = F(\varepsilon/r, Re) \quad (2.22)$$

$$\text{Completely rough regime: } Re_\varepsilon \geq 70, \quad f = F(\varepsilon/r) \quad (2.23)$$

In hydraulically smooth regimes, ε is very small such that the sand grains are contained within the laminar sub-layer. Hence f is not affected by ε and $f = F(Re)$. In the transition regime, the sand grains extend partly outside the laminar sublayer, which

imposes additional resistance to the flow in the form of profile drag. In this case, the friction coefficient is dependent on ε/r and Re . Thus, in the transition regime, the laminar sub-layer is completely disrupted. In this case, the friction coefficient is solely dependent on the size and shape of the sand grains, i.e., $f = F(\varepsilon/r)$.

Prandtl (1960), Von Karman (2012), and V. Nikuradse (1932) developed a correlation for $f = F(Re)$ on theoretical basis. This correlation is valid for an arbitrarily large Re and the values predicted by this equation are in good agreement with extensive experimental measurements within $\pm 2\%$. This correlation is recommended for a Re number range of $4 \times 10^3 - 1 \times 10^7$.

$$\frac{1}{\sqrt{f}} = 1.7372 \ln(Re\sqrt{f}) - 0.3946 \quad (2.24)$$

Later, Colebrook (1939) developed a correlation for flows in a smooth circular duct:

$$\frac{1}{\sqrt{f}} = 1.5635 \ln\left(\frac{Re}{7}\right) \quad (2.25)$$

This correlation is also valid within a Re range of $4 \times 10^3 - 1 \times 10^7$.

Colebrook (1939) developed an implicit formula which is applicable for $0 \leq Re_\varepsilon \leq 5$. This formula spans the entire transition, hydraulically smooth, and completely rough flow regimes.

$$\frac{1}{\sqrt{f}} = 3.48 - 1.7372 \ln\left(\frac{\varepsilon}{r} + \frac{9.35}{Re\sqrt{f}}\right) \quad (2.26)$$

Equation (2.26) is valid within the Re range of $4 \times 10^3 - 1 \times 10^7$.

For turbulent heat transfer in smooth pipes, Colburn (1933) equation can be used as a general approach to calculate the dimensionless Nu number. The Nu number is correlated with the Re number and Prandtl number (Pr) in an exponential function for

fully developed turbulent pipe flows. The Colburn empirical correlation has been widely used in practice.

$$\text{Nu} = C\text{Re}^m\text{Pr}^n \quad (2.27)$$

where C , m , and n are the constants which need to be determined from experimental data for a certain type of tube. Typically for smooth tubes, $C \approx 0.023$, $m \approx 0.8$, and $n \approx 0.3$. If these values are used, the equation is known as the Dittus-Boelter correlation (Dittus & Boelter, 1930) for the case where the fluid is heated.

$$\text{Nu} = 0.023 \text{Re}^{0.8} \text{Pr}^{0.3}, 0.7 < \text{Pr} < 160 \text{ and } \text{Re} \geq 10^4 \quad (2.28)$$

Equation (2.28) is recommended for general use; however, the standard deviation of error is ~13%.

Petukhov and Kirilov (1958) developed correlations (Equations (2.29) and (2.30)) to determine the Nu number for fully developed turbulent flows in a smooth circular duct for gases and liquids. These correlations are valid for $0.5 \leq \text{Pr} \leq 10^6$ and $4000 \leq \text{Re} \leq 5 \times 10^6$.

$$\text{Nu} = \frac{(f/2)\text{RePr}}{C + 12.7 \left(\frac{f}{2}\right)^{\frac{1}{2}} (\text{Pr}^{\frac{2}{3}} - 1)} \quad (2.29)$$

$$\text{where } C = 1.07 + \frac{900}{\text{Re}} - \left[\frac{0.63}{1+10\text{Pr}}\right]$$

$$\text{Nu} = \frac{(f/2)\text{RePr}}{1.07 + 12.7 \left(\frac{f}{2}\right)^{\frac{1}{2}} (\text{Pr}^{\frac{2}{3}} - 1)} \quad (2.30)$$

The first Petukhov correlation is in agreement with the most reliable experimental data on heat and mass transfer within an accuracy of $\pm 5\%$. This correlation is valid for $0.5 \leq \text{Pr} \leq 10^6$ and $400 \leq \text{Re} \leq 5 \times 10^6$. The second correlation is a simplified

version of the first one and it was modified by V1 Gnielinski (1976), resulting in the following correlation:

$$\text{Nu} = \frac{(f/2)(\text{Re} - 1000)\text{Pr}}{1 + 12.7\left(\frac{f}{2}\right)^{1/2}(\text{Pr}^{2/3} - 1)} \quad (2.31)$$

The Gnielinski correlation extends the Petukhov correlation to within the following range: $2300 \leq \text{Re} \leq 5 \times 10^6$. When $0.5 \leq \text{Pr} \leq 2000$ and $2300 \leq \text{Re} \leq 5 \times 10^6$, the Gnielinski correlation gives the best agreement with the experimental data and it agrees with the Petukhov correlation within -2 and 7.8% , respectively.

The effect of tube roughness on the turbulent flow friction factor leads to the development of correlations to determine the Nu number for rough tubes. The correlations for smooth tubes do not show good agreement with experimental data when these correlations are used for rough tubes. Thus, several correlations have been developed to determine the Nu number for fully developed turbulent flows in rough circular ducts (Kazi, 2001). The correlation developed by (Martinelli, 1947) for a fully rough flow regime is given by:

$$\text{Nu} = \frac{\text{RePr}\sqrt{f/2}}{5[\text{Pr} + \ln(1 + 5\text{Pr}) + 0.5 \ln(\text{Re}\sqrt{f/2} / 60)]} \quad (2.32)$$

Some of the correlations for convective heat transfer of flows through ducts are summarized in Table 2.6.

Table 2. 6: Summary of the empirical correlations developed to determine the Nu number of flows through ducts

Researcher(s)	Correlation	Medium	Flow conditions
Sieder and Tate (Sieder & Tate, 1936)	$Nu = 0.027Re^{0.8}Pr^{1/3}\left(\frac{\mu}{\mu_s}\right)^{0.14}$	Fully turbulent flows	$Re \geq 10^4$ $0.7 \leq Pr \leq 16,700$ $L/D \geq 10$
Hausen (Hausen, 1959)	$Nu = 0.037(Re^{0.75} - 180)Pr^{0.42}\left[1 + \left(\frac{D}{L}\right)^{2/3}\right]\left(\frac{\mu_b}{\mu_w}\right)^{0.14}$	Transitional and turbulent flows	$2300 < Re < 10^6$ $0.5 < Pr < 1000$
Maïga's equation	$Nu = 0.085Re^{0.71}Pr^{0.35}$		
Sundar et al. (Sundar, Naik, Sharma, Singh, & Reddy, 2012)	$Nu = 0.02172Re^{0.8}Pr^{0.5}(1 + \varphi)^{0.5181}$	Fe ₃ O ₄ nanofluid	$3000 < Re < 22000$ $3.72 < Pr < 6.5$ $0 < \varphi < 0.6\%$
Pak and Cho (Pak & Cho, 1998)	$Nu = 0.021Re^{0.8}Pr^{0.5}$	Al ₂ O ₃ and TiO ₂ nanofluids	$10^4 < Re < 10^5$ $6.54 < Pr < 12.33$ $0 < \varphi < 3.0\%$
Duangthongsuk and Wongwises (Duangthongsuk & Wongwises, 2010)	$Nu = 0.074Re^{0.707}Pr^{0.385}\varphi^{0.074}$	TiO ₂ nanofluid	$3000 < Re < 18000$ $0 < \varphi < 2.0\%$
Sundar (Sundar, Singh, & Sousa, 2014)	$Nu = 0.0215Re^{0.8}Pr^{0.5}(1 + \varphi)^{0.78}$	Hybrid MWCNT- Fe ₃ O ₄ /water nanofluids	$3000 < Re < 22000$ $3.72 < Pr < 6.37$ $0 < \varphi < 0.6\%$
Xuan and Li	$Nu_{nf} = 0.0059(1 + 7.6286\varphi^{0.6886}Pe_d^{0.001})Re_{nf}^{0.9238}Pr_{nf}^{0.4}$		
Vajjha et al. (R. S. Vajjha, Das, & Kulkarni, 2010)	$Nu = 0.065(Re^{0.65} - 60.22)(1 + 0.0169\varphi^{0.15})Pr^{0.542}$		$0 < \varphi < 6.0$ CuO, SiO ₂ $0 < \varphi < 10.0$ Al ₂ O ₃ $3000 < Re$ $< 1.6 \times 10^4$
Sajadi and Kazemi (Sajadi & Kazemi, 2011)	$Nu = 0.067Rr^{0.71}Pr^{0.35} + 0.0005Re$	TiO ₂ /water nanofluids	$0.2 < \varphi < 0.25$ vol% $5000 < Re < 3 \times 10^4$
Dittus-Boelter correlation [36]	$Nu = 0.023Re^{0.8}Pr^{0.4}$		$Re \geq 10^4$ $0.6 \leq Pr \leq 160$

Researchers have conducted experimental investigations to improve the heat transfer performance and pressure drop of nanofluids with various nanoparticle concentrations in laminar and turbulent flow regimes (Youssef, Aly, & Zeidan, 2012).

There are many experimental studies available in the literature concerning nanofluids in the laminar flow regime. Most of the results confirm that the heat transfer enhancement increases with an increase in particle concentration and thermal conductivity for almost all types of nanofluids. The convective heat transfer characteristics of copper-water nanofluids in a horizontal straight tube with constant heat flux and different flow rates have also been experimentally investigated in (Xuan &

Li, 2003). The results revealed that the presence of the copper nanoparticles has a promising effect on the heat transfer performance of the base fluid, and the friction factor values of the nanofluids are at par with those of water. Based on their findings, the copper-water nanofluids have superior convective heat transfer coefficient compared with the base fluid, with a value of ~60% at a particle concentration of 2 vol%. In addition, they proposed a new correlation to predict the heat transfer coefficient of the nanofluids for both laminar and turbulent flow conditions. They also conducted pressure drop studies at different flow rates to justify the use of copper-water nanofluids due to the fact that a higher pressure drop results in higher pumping power. However, they found that there is no significant increase in the pressure drop, which indicates that the nanofluids do not impose any extra penalty in the pumping power.

Faulkner et al. (Faulkner, Rector, Davidson, & Shekarriz, 2004) was the first to conduct convective heat transfer experiments of aqueous CNT nanofluids in a microchannel with hydraulic diameter of 355 μm within a Re number range of 2–17. They observed that there is considerable enhancement in heat transfer coefficient when the CNT concentration is 4.4%. Ding et al. (Yulong Ding et al., 2006) studied the heat transfer characteristics of aqueous suspensions of MWCNT nanofluids flowing through a horizontal tube. They observed that there is significant convective heat transfer enhancement of the nanofluids, which are dependent on the Re number, MWCNT concentration, and pH, where the pH has the lowest effect on the heat transfer enhancement. The results showed that the maximum convective heat transfer enhancement of the nanofluid containing 0.5 wt% of MWCNTs is more than 350% at Re = 800, which is not solely due to enhanced thermal conduction. They proposed that particle rearrangement, shear-induced thermal conduction enhancement, reduction of thermal boundary due to the presence of nanoparticles, and the significantly high aspect ratio of MWCNTs are possible mechanisms that lead to the high convective heat

transfer enhancement. Mehrali et al. (Mehrli et al., 2015) investigated the heat transfer characteristics and thermal conductivity of GNP nanofluids (where the GNPs have an SSA of $750 \text{ m}^2/\text{g}$) inside a circular stainless steel tube subjected to constant wall heat flux. The experiments were carried out under laminar forced convection conditions. The flow velocity was kept constant and the GNP concentration was varied from 0.025 to 0.1 wt%. They obtained thermal conductivity enhancement of 12–28% relative to that for the base fluid. The convective heat transfer coefficient for the GNP nanofluid is found to be up to 15% higher than that for the base fluid. The heat transfer rate and thermal performance for the nanofluid containing 0.1 wt% of GNPs are higher by a factor of up to 1.15.

Kumaresan et al. (Kumaresan, Khader, Karthikeyan, & Velraj, 2013) studied the heat transfer characteristics of CNT nanofluids in a tubular heat exchanger of various lengths for cooling/heating applications. The nanofluids were prepared by dispersing MWCNTs in water-ethylene glycol mixture (70:30 by volume). The results showed that the Pr number increases by 115.8 and 180.2% at 0 and 40°C , respectively, for the nanofluid containing 0.45 vol% of MWCNTs. In contrast to the conventional heat transfer concept, the Nu number of the nanofluids increases with a decrease in the Re number as the MWCNT concentration increases. The results showed that there is significant enhancement in the convective heat transfer coefficient in the entrance region. The possible reason for the abnormal enhancement in the heat transfer coefficient for the test section with the shorter length is the migration of the MWCNTs, which hinders rapid development of the thermal boundary layer.

Sunder et al. (Sundar et al., 2014) experimentally investigated the convective heat transfer coefficient and friction factor for fully developed turbulent flow of MWCNT- Fe_3O_4 /water nanofluids flowing through a circular tube uniformly heated at a constant

heat flux. The results indicate that the maximum enhancement in Nu number is 31.10%; however, this comes at the expense of increased pumping power by a factor of 1.18 for a particle loading of 0.3%. The Re number was 22,000.

Akhavan-Zanjani et al. (Akhavan-Zanjani, Saffar-Avval, Mansourkiaei, Ahadi, & Sharif, 2014) experimentally studied the thermal conductivity and turbulent convective heat transfer of graphene/water nanofluids (with various concentrations of graphene) inside a uniformly heated circular tube. The results showed that there is enhancement in the thermal conductivity with a moderate increment of viscosity at low volume fractions of nanoparticles. Moreover, there is a significant increment in the heat transfer coefficient while the pressure loss remains unchanged. The maximum thermal conductivity, viscosity, and heat transfer coefficient enhancements are 10.30, 4.95, and 6.04%, respectively.

Amrollahi et al. (Amrollahi, Rashidi, Lotfi, Meibodi, & Kashefi, 2010) investigated convective heat transfer of water-based FMWNT nanofluid under both laminar and turbulent regimes flowing through a uniformly heated horizontal tube in entrance region. The nanoparticles functionalized by acid treatment. The experimental results indicated that the convective heat transfer coefficient of these nanofluids increases by up to 33–40% at a concentration of 0.25 wt.% compared with that of the pure water in laminar and turbulent flows respectively and 20 °C.

In another interesting study, Cárdenas Gómez et al. (Gómez, Hoffmann, & Bandarra Filho, 2015) compared the thermal performance of CNT nanofluids with different CNT aspect ratios (0.24 vol% of MWCNT with aspect ratios of 100 and 2400). They tested the CNT nanofluids flowing in a horizontal pipe under the following test conditions: (1) Re number range: 3,000–20,000, (2) inlet temperature: 10, 15, and 20°C, (3) heat flux in the test section: 10–18 kW/m², and (4) mass flow rate: 20–100 g/s. They concluded that

the sample with the higher CNT aspect ratio has superior thermal performance because the heat transfer coefficient increases by 15% (relative to that of the base fluid) while increase in pumping power insignificant (<10%). Table 2.7 summarized the results of experimental study of forced convective heat transfer from literature on carbon allotropes-based nanofluid.

University of Malaya

Table 2. 7: Literature review on the experimental study of forced convective heat transfer of carbon allotropes-based nanofluid

Author(s)	Nanoparticle/Bas e fluid	Particle Size	Particle Concentration	Re	Boundary condition	Geometry/flow nature	Enhancement of h
Amrollahi et al. (Amrollahi et al., 2010)	MWCNT/Water	150–200 nm	0.1-0.25 wt.%	1592-4778	$q'' = \text{Const.}$	Tube/laminar and turbulent	Up to 33-40%
Ding et al. (Yulong Ding et al., 2006)	MWCNT/Water	-	0.5 wt.%	800	$q'' = \text{Const.}$	Tube/laminar	Up to 350%
Wang et al. (J. Wang, Zhu, Zhang, & Chen, 2013)	MWCNT/Water	D 20–30 nm L 5–30 μm	0.05–0.24 vol. %	120	$q'' = \text{Const.}$	Tube/laminar	Up to 70-190%
Garg et al. (Garg et al., 2009)	MWCNT/Water	D 10–20 nm, L 0.5–40 μm	1 wt%	600-1200	$q'' = \text{Const.}$	Tube/Laminar	Up to 32%
Liao and Liu(L. Liao & Liu, 2009)	MWCNT/Water	D 10–20 nm L 1–2 μm	0.5–2 wt.%	500-10000	$q'' = \text{Const.}$	Tube/laminar to turbulent	Up to 18-56%
Yarmand et al.(Yarmand et al., 2016)	Acid-treated GNP/Water	SSA 500 m2/g	0.02-0.1 wt%	5000-17500	$q'' = \text{Const.}$	Tube/Turbulent	Up to 17.72-32.68%
Hosseini et al.(Hosseini et al., 2017)	MWCNT/Water	OD 20-40	0.075-0.175 wt%	3055-7944	$q'' = \text{Const.}$	Annular/turbulent	12.38-35.89%
Present study (Sadri et al., 2018)	Clove-treated GNP/Water	SSA 750 m2/g	0.025-0.1 wt%	6371–15,927	$q'' = \text{Const.}$	Circular Tube/turbulent	9.26-37.54%
Present study (Sadri, Hosseini, Kazi, Bagheri, Ahmed, et al., 2017)	GA-treated GNP/Water	SSA 750 m2/g	0.025-0.1 wt%		$q'' = \text{Const.}$	Circular Tube/turbulent	9.89-38.58%

2.10 Simulation

There are a number of studies focused on modeling convective flows where nanofluids are used as the working fluids. Several methods have been used by researchers to perform the simulations. These methods can be generally classified as single-phase and two-phase models, which are reviewed and presented in the following sub-sections. As a matter of fact, most researchers used numerical methods to determine the effective thermal parameters such as convective heat transfer coefficient and thermal conductivity of nanofluid flows because these methods are more cost-effective than traditional experimentation.

2.10.1 Governing equations

2.10.1.1 Single-phase models

Single phase (homogeneous) models are very popular for numerical studies involving nanofluids due to the simplicity of these models. In this approach, the nanoparticles are assumed to be uniformly distributed in the base fluid (Niu, Fu, & Tan, 2012). Moreover, the effective thermophysical properties, including conductivity, viscosity, heat capacity and density, are based on the mixture of nanoparticles and base fluid. Furthermore, in single-phase modelling, both the liquid and solid particle phases are in chemical and thermal equilibrium, and the relative velocity between the phases is equal to zero (Corcione, Cianfrini, & Quintino, 2012; Q. Li, Xuan, & Wang, 2003; Namburu, Das, Tanguturi, & Vajjha, 2009). This assumption may be realistic because the relative velocity decreases with a decrease in particle size and the nanoparticles are more minute in size compared with microparticles (Namburu et al., 2009). In this approach, it is also assumed that there is ease of fluidization of nanoparticles in the base fluid and therefore, the effective mixture has similar behavior as that for single-phase fluids (Q. Li et al., 2003; Namburu et al., 2009). The accuracy of the numerical results

for single-phase models is strongly dependent on proper selection of the effective thermophysical properties.

The governing equations for steady-state nanofluids using single-phase modelling are as follows (Vanaki, Ganesan, & Mohammed, 2016):

Conservation of mass:

$$\nabla \cdot (\rho_{nf} \vec{V} g) = 0 \quad (2.33)$$

Conservation of momentum:

$$\nabla \cdot (\rho_{nf} \vec{V} \vec{V}) = -\nabla P + \mu_{nf} \nabla^2 \vec{V} - \rho_{nf} \nabla \cdot (\overline{VV}) - (\rho\beta)_{nf} (T - T_0) g \quad (2.34)$$

The third and fourth terms on the right side of Eq. (2.34) indicate the effect of turbulent flow and natural convection, respectively. For laminar forced convection flows, these terms are considered zero.

Conservation of energy:

$$\nabla \cdot ((\rho C p)_{nf} \vec{V} T) = \nabla \cdot (k_{nf} \nabla T - (\rho C p)_{nf} \overline{Vt}) \quad (2.35)$$

where $(\rho C p)_{nf} \overline{Vt}$ is used for turbulent flow regime (Vanaki et al., 2016).

Maïga et al. (Maïga, Nguyen, Galanis, & Roy, 2004) modeled the forced convection flow of a nanofluid (gAl_2O_3 dispersed in water and ethylene glycol) in a straight tube with circular cross-section. They assumed that the flow is single phase in order to derive the governing equations and calculate the heat transfer enhancement of nanofluids in laminar and turbulent flow conditions. The nanoparticle concentration was varied from 0 to 10%. For laminar flow conditions, the results showed that there is an increase in the heat transfer rate (particularly at the walls) with variation of w . When $w = 10\%$, the

product rc_p and thermal conductivity, k , increases by 18 and 33%, respectively. In addition, the heat transfer coefficient ratio, hr , increases by almost 60% with an increase in particle concentration, particularly at the tube end. Furthermore, the average heat transfer enhancement is more pronounced for the gAl_2O_3 /ethylene glycol nanofluid compared with that for the gAl_2O_3 /water nanofluid for $w > 3\%$ (identical otherwise). The wall shear stress increases considerably with an increase in the particle volume fraction and along the tube length. For the turbulent flow regime, there is a sharp increase in the heat transfer coefficient within a very short distance from the inlet section. The variations of hr and tr are similar to those in the previous case. Palm et al. (Palm, Roy, & Nguyen, 2006) numerically investigated the enhanced heat transfer capabilities of Al_2O_3 /water nanofluids ($g = 38$ nm; $w = 1\text{--}4\%$) in a radial laminar flow cooling system. They used temperature-dependent nanofluid properties in their simulations. The experimental results obtained using the single-phase approach showed that there are noticeable fluctuations in the properties near the injection inlet. The viscosities are lower at higher temperatures, the wall shear stress decreases with an increase in the wall heat flux, and the heat transfer rates are higher compared with predictions obtained using constant properties. Hwang et al. (K. S. Hwang, Jang, & Choi, 2009) performed a study on Al_2O_3 /water nanofluids in fully developed laminar flow regime. They found that the nanofluid friction factor can accurately be predicted using the classical Darcy equation for single phase flows. On the contrary, there is anomalous enhancement in the heat transfer coefficient, which cannot be predicted using classical equations. Namburu et al. (Namburu et al., 2009) developed a single-phase model to study turbulent flow and heat transfer characteristics of nanofluids in a circular tube. The results showed that the nanofluids containing smaller diameter nanoparticles have higher viscosities and Nu numbers. Akbarinia and Behzadmehr (Akbarinia & Behzadmehr, 2007) developed a single-phase CFD model to investigate

laminar convection of Al_2O_3 /water nanofluid in a horizontal curved tube. The effects of buoyancy force, centrifugal force, and nanoparticle concentration were discussed in their work. Zeinali et al. (S. Z. Heris, M. N. Esfahany, & G. Etemad, 2007a) proposed a dispersion model to account for the presence of nanoparticles in nanofluids. They showed that the dispersion and random movement of nanoparticles inside the fluid alters the structure of the flow field, which leads to heat transfer enhancement. Behzadmehr et al and Mirmasoumi et al. (Behzadmehr, Saffar-Avval, & Galanis, 2007; Mirmasoumi & Behzadmehr, 2008) used two-phase models to predict turbulent forced convection of nanofluids in a tube with uniform heat flux. They used a mixed model based on a two-phase model for a single fluid in their CFD simulations.

(a) ***Brownian motion and dispersion model***

The increase in Brownian motion (microconvection effect) is supposed to be one of the main reasons for the thermal conductivity enhancement of nanofluids. This has led to the development of several new theoretical models (Jang & Choi, 2004) (which are temperature-dependent) in order to evaluate the effective thermal conductivity of nanofluids. These single-phase CFD models with temperature-dependent effective thermal conductivity were already used in (Akbari, Galanis, & Behzadmehr, 2012; Namburu et al., 2009) to investigate the turbulent forced convection of three types of nanofluids (Al_2O_3 , CuO and SiO_2 in ethylene glycol-water mixtures). The results showed that there is good agreement between the predicted Nu numbers and those determined from the Gnielinski correlation for the nanofluids. It shall be noted that the chaotic movement of nanoparticles also causes thermal dispersion in the nanofluid and this may be one of the reasons that led to the thermal conductivity enhancement of nanofluids. A few researchers have used the dispersion model and they found that this model gives a more reliable prediction of the heat transfer behavior of nanofluids when the results were validated against experimental data. Heris et al. (Heris et al., 2007a)

numerically investigated laminar flow convective heat transfer of nanofluids in a circular tube using a constant wall temperature boundary condition. They concluded that dispersion and random movement of nanoparticles inside the fluid alter the structure of the flow field, which leads to heat transfer enhancement. The numerical and experimental results for $\text{Al}_2\text{O}_3/\text{water}$, CuO/water , and Cu/water nanofluids were compared to assess the accuracy of the dispersion model in predicting the heat transfer coefficient of nanofluids, and the results showed that there is good agreement between the numerical predictions and experimental data. Mokmeli and Saffar-Avval (Mokmeli & Saffar-Avval, 2010) introduced a new thermal conductivity relationship in the radial direction based on the dispersion model in order to study the laminar convective heat transfer behavior of nanofluids in straight pipes. They observed that the dispersion model gives a more reliable prediction of the heat transfer behavior of nanofluids. The discrepancies in the results in response to changes in the volume fraction of nanoparticles and Re number are less than 2.5 and 4%, respectively. In contrast, the discrepancies in the results for the homogeneous model are within a range of 14–30%. Mojarrad et al. (Mojarrad, Keshavarz, & Shokouhi, 2013) conducted experimental and numerical studies to analyze the heat transfer performance of $\text{Al}_2\text{O}_3/\text{water}$ nanofluids flowing in the entrance region of a circular tube with constant wall surface temperature. The diameter of the Al_2O_3 nanoparticles is 30 nm. They proposed a new correlation to determine the thermal conductivity in the radial direction. They reported that the new dispersion model gives accurate prediction of the experimental data.

(b) *Newtonian and non-Newtonian rheology*

One simplified view which has been considered in many works (J Koo & C Kleinstreuer, 2005; Moraveji & Ardehali, 2013) is to treat nanofluid as a Newtonian fluid with modified properties (Niu et al., 2012). For example, Maïga et al. (Maïga et al., 2004) numerically investigated laminar and turbulent forced convective heat transfer

of Al_2O_3 /water and Al_2O_3 /ethylene glycol nanofluids inside a heated tube. They used the single-phase model with constant dynamic viscosity (i.e., Newtonian fluid behavior) and constant thermal conductivity which were selected from the experimental data for each nanoparticle volume fraction. They found that there is good agreement between the predicted heat transfer coefficient and experimental data with a maximum error of 10%. Moraveji et al. (Moraveji, Darabi, Haddad, & Davarnejad, 2011) used a similar model to investigate the heat transfer enhancement of Al_2O_3 /water nanofluid under laminar forced convection. They reported that the predicted values approximate those from experiments with an increase in the Re number and decrease in the size of particles. The maximum deviation in the Nu number between the predicted and experimental data is 10%. On the contrary, some researchers suggested that the rheological behavior of nanofluid is more likely shear-thinning rather than Newtonian. For example, Chang et al. (H. Chang et al., 2005) found that the CuO/water nanofluid behaves as a non-Newtonian fluid in their experimental study. The non-Newtonian rheological behavior can be described by the power law model with a flow index of less than 1 (Niu et al., 2012). Putra et al. (Putra, Roetzel, & Das, 2003) conducted an experimental study to examine the relationship between shear stress and shear strain of Al_2O_3 /water nanofluids. According to the data given by Putra et al. (Putra et al., 2003), the constants of power-law model have been extracted by several researchers for use in numerical studies. Santra et al. (Santra, Sen, & Chakraborty, 2009) numerically investigated laminar forced convection of Cu/water nanofluids through two isothermally heated parallel plates using the Newtonian and power law rheology models. They found that the difference in the predicted Nu number between the two models becomes significant as the Re number increases. Hence, it is imperative to consider the non-Newtonian effect of nanofluids.

2.10.1.2 Two-phase models

Nanofluids are essentially two-phase fluids and therefore, it is expected that nanofluids share the same features inherent of solid-liquid mixtures. For this reason, the classical theory for two-phase flows is used for nanofluids. In two-phase modelling, the nanoparticles and base fluid are considered as two different phases with different velocities and temperatures. Hence, the assumption of zero slip velocity between the fluid and particles is no longer valid (Xuan & Roetzel, 2000) because the effects of gravity, friction between the fluid and solid particles, Brownian motion, Brownian diffusion, sedimentation, and dispersion need to be considered. The results obtained from two-phase modelling are more realistic because this approach accounts for the movement between the solid and fluid molecules. Although this modelling approach offers insight into the functions of both liquid and solid phases in the heat transfer process, this approach results in long computational time, and a high-performance computer is needed for the simulations. There are two types of models used for two-phase modelling (Vanaki et al., 2016).

According to the findings of Ding and Wen (Yulong Ding & Wen, 2005), if the nanoparticle concentration is lower near the wall region compared with the core region, the assumption that the distribution of nanoparticles is homogeneous in the base fluid may not always hold true for a nanofluid (Kamyar, Saidur, & Hasanuzzaman, 2012). In addition, factors such as gravity, Brownian motion, Brownian diffusion, friction force between the fluid and nanoparticles, sedimentation, dispersion, layering at the solid-liquid interface, ballistic phonon transport, and thermophoresis, may affect nanofluid flows (Bahiraei, 2014; Moghari, Akbarinia, Shariat, Talebi, & Laur, 2011). These factors may be attributed to nanoparticle migration, slip velocity between nanoparticles and base fluid, as well as non-homogeneous distribution of nanoparticles in the base fluid (Aminfar & Motallebzadeh, 2011; Moraveji & Ardehali, 2013). These findings

have motivated researchers to use two-phase models in numerical studies of nanofluids. In two-phase modelling, the nanoparticles and base fluid are distinguished as two separate phases with distinctive thermophysical properties. The multiphase flows are solved using Eulerian or Lagrangian frameworks. In the Eulerian-Eulerian framework, each phase is treated as a continuum with separate transport equations. In contrast, in the Eulerian-Lagrangian framework, the particle phase is traced as a discrete phase. The interphase interactions between the particles and fluid are accounted for in both of these frameworks (Fluent, 2009). There are two types of Eulerian two-phase models commonly used to simulate nanofluid flows: (1) mixture model and (2) Eulerian-Eulerian (two-fluid) model. The mixture model only solves the governing equations for the mixture phase and uses the relative velocities to describe the dispersed phases, whereas the Eulerian-Eulerian model solves the equations for each phase. For this reason, the Eulerian-Eulerian model results in higher computational time and cost compared with the mixture model (Fluent, 2009). Akbari et al. (Akbari et al., 2012) conducted a numerical study to investigate turbulent forced convection of $\text{Al}_2\text{O}_3/\text{water}$ and Cu/water nanofluid in a straight pipe with constant wall heat flux. They used the single-phase model (with temperature-dependent properties) and three different two-phase models (volume of fluid (VOF), mixture, and Eulerian-Eulerian models). The results showed that all of the two-phase models result in similar predictions in the thermal field properties. However, interestingly, there is a significant deviation between the results predicted by the two-phase models and experimental data, compared with the results predicted by the single-phase model. The deviation between the results predicted by the two-phase models and experimental data increases with an increase in the nanoparticle volume fraction. However, the results predicted by the single-phase model show good agreement with the experimental data in almost all flow conditions. The results also showed that the Nu number predicted using CFD methods are less

dependent on the Re number compared with those obtained from experiments. They believed that this is due to the clustering phenomena and the effect of Re number, which alters the thermal and hydrodynamic properties of nanofluids. Behzadmehr et al. (Behzadmehr et al., 2007) used a two-phase mixture model to investigate turbulent forced convection of nanofluids inside a pipe. They assumed that both nanoparticles and base fluid are at the same temperature (i.e., the phases are in thermal equilibrium). The results of the two-phase model are found to be closer to the experimental data than those of the single-phase homogeneous model.

Nevertheless, many researchers have performed numerical simulations using the single-phase assumption and have reported acceptable results for heat transfer and hydrodynamic properties of the flow (Rashidi, Nasiri, Khezerloo, & Laraqi, 2016). Several numerical and semi-analytical methods have been used by several researchers in order to simulate heat transfer and flow characteristics of nanofluids (Rashidi et al., 2016). Xuan and Li (Q. Li et al., 2003) studied the single-phase flow and heat transfer performance of nanofluids in tubes in turbulent flow conditions. Their experimental results showed that the convective heat transfer coefficient and Nu number of nanofluids increase with an increase in the Re number and volume fraction of nanoparticles under turbulent flow conditions. Compared with that for water, the Nu number of the nanofluid containing 2.0 vol% of Cu nanoparticles increases by more than 39% (Vanaki et al., 2016). Sheikholeslami et al. (M Sheikholeslami, Gorji-Bandpy, & Soleimani, 2013) used heatline analysis for two-phase simulation in order to investigate the flow and heat transfer characteristics of nanofluids. The results showed that the average Nu decreases as the buoyancy ratio number increases until it reaches a minimum value, followed by an increase thereafter (Mohsen Sheikholeslami, Abelman, & Ganji, 2014). Namburu et al. (Namburu et al., 2009) simulated turbulent flow and heat transfer enhancement of nanofluids flowing through a circular pipe. The nanofluids

comprise three types of nanoparticles dispersed in ethylene glycol-water mixtures. They used the $k-\varepsilon$ turbulence model proposed by Launder and Spalding (Launder & Spalding, 1974) and the results showed that the average Nu increases with an increase in the nanoparticle concentration. Akbari et al. (Akbari et al., 2012) compared numerical predictions of a single-phase model with those of three two-phase models (VOF, mixture, and Eulerian) models for nanofluids flowing in a horizontal tube with uniform heat flux in turbulent forced convection conditions. They compared with results with two sets of experimental data. The results showed that the single-phase model coupled with the best property correlations gives better predictions compared with the two-phase models with the best outlet condition. They concluded that the single-phase model is more appropriate for their investigation considering that this model is easier to implement and requires less computer memory and computational processing time. Malvandi and Ganji (Malvandi & Ganji, 2014) studied the effects of Brownian motion and thermophoresis on slip flow of alumina/water nanofluid inside a circular microchannel in the presence of a magnetic field. Moshizi et al. (Moshizi, Malvandi, Ganji, & Pop, 2014) conducted a two-phase theoretical study of nanofluids flowing inside a concentric pipe with heat generation/absorption. In the case of heat absorption, they found that the dimensional temperature profile becomes more uniform by imposing heat flux at both walls. Malvandi and Ganji (Malvandi & Ganji, 2015b) investigated the effects of magnetic field and slip on free convection inside a vertical enclosure filled with alumina/water nanofluid. In another study, Malvandi and Ganji (Malvandi & Ganji, 2015a) analyzed the effects of nanoparticle migration on hydromagnetic mixed convection of alumina/water nanofluid in vertical channels with asymmetric heating. They observed that the nanoparticles eject themselves from the heated walls, producing a depleted region, and accumulate in the core region. However, they noted that the nanoparticles are more likely to accumulate toward the wall with lower heat flux.

Malvandi et al. (Malvandi, Ganji, & Kaffash, 2015) studied the effects of magnetic field on the nanoparticle migration and heat transfer of alumina/water nanofluid in a parallel-plate channel with asymmetric heating. Malvandi et al. (Malvandi, Safaei, Kaffash, & Ganji, 2015) also studied MHD mixed convection in a vertical annulus filled with Al_2O_3 /water nanofluid taking into account the migration of nanoparticles. Ashorynejad et al. (Ashorynejad, Sheikholeslami, Pop, & Ganji, 2013) studied the flow and heat transfer characteristics of nanofluids in a stretching cylinder in the presence of a magnetic field. They showed that selecting copper (for small values of the magnetic parameter) and alumina (for large values of the magnetic parameter) leads to the highest cooling performance for their problem. Sheikholeslami and Ganji (M Sheikholeslami & Ganji, 2014) studied heated permeable stretching surface in a porous medium.

2.10.1.3 Eulerian-Eulerian model

The Eulerian-Eulerian model is recommended for two-phase mixtures containing large amounts of solid particles. For simulation purposes, it is perceived that the Eulerian-Eulerian model is a suitable model for nanofluids with large amounts of nanoparticles, even at low volume fractions. The three common Eulerian-Eulerian models are volume of fluid (VOF), mixture, and Eulerian models (Vanaki et al., 2016).

2.10.1.4 Mixture model

One of the most common approaches in modeling two-phase slurries is the mixture theory, which is also known as the theory of interacting continua (Ishii, 1975; J. Xu et al., 2004). The popularity of this approach in multi-phase applications can be attributed to the following features of this model. For instance, the mixture model is simple in theory and implementation, which reduces run time and central processing unit usage. It is straightforward to introduce turbulence model into the mixture model. The mixture model is also reasonably accurate for a wide range of two-phase flows. The mixture

model is based on the following assumptions (Moraveji & Ardehali, 2013): (1) there is strong coupling between the phases and the particles closely follow the flow; (2) all of the phases share a single pressure and the interactions between different dispersed phases are neglected; (3) each phase has its own velocity vector field and there is a certain fraction of each phase within a given control volume. In addition, it is assumed that the secondary disperse phase consists of spherical particles having a uniform particle size. This is specified during the calculations. The concentration of the secondary disperse phase is solved using scalar equations taking into account corrections due to phase slip. However, the mixture model has the following limitations (Moraveji & Ardehali, 2013): (1) there is no possibility for phase change and the flow compressibility is not accounted for; and (2) the pressure boundary condition cannot be specified because the ideal gas law is not applicable. In addition, the turbulence generation in the secondary phase is not accounted for as well as the turbulence of the primary phase which is directly affected by the presence of the secondary phase (El-Batsh, Doheim, & Hassan, 2012).

2.10.2 Turbulence modeling

In order to solve the governing equations of fluid dynamics for turbulent flows, experimental data or approximate models are necessary to account for turbulence phenomena.

2.10.2.1 $k - \varepsilon$ model

Namburu et al. (Namburu et al., 2009) recommended the use of the $k - \varepsilon$ model proposed by Launder and Spalding (Launder & Spalding, 1972). Two new equations were introduced in the $k - \varepsilon$ model equations; one for the turbulent kinetic energy whereas the other for the rate of dissipation. These equations are given by:

$$\nabla \cdot (\rho_m \vec{V}_m k) = \nabla \cdot \left(\frac{\mu_{t,m}}{\sigma_k} \nabla k \right) + G_{k,m} - \rho_m \varepsilon \quad (2.36)$$

$$\nabla \cdot (\rho_m \vec{V}_m \varepsilon) = \nabla \cdot \left(\frac{\mu_{t,m}}{\sigma_k} \nabla \varepsilon \right) + \frac{\varepsilon}{k} (C_1 G_{k,m} - C_2 \rho_m \varepsilon) \quad (2.37)$$

Where

$$\mu_{t,m} = \rho_m C_\mu \frac{k^2}{\varepsilon} \quad (2.38)$$

$$G_{k,m} = \mu_{t,m} (\nabla \vec{V}_m + (\nabla \vec{V}_m)^T) \quad (2.39)$$

With $C_1 = 1.44$, $C_2 = 1.92$, $C_\mu = 0.09$, $\sigma_k = 1$, $\sigma_\varepsilon = 1.3$.

Various damping functions have been developed over the years for the $k - \varepsilon$ model, which improves the agreement between the data obtained from this model and those obtained from direct numerical simulations (Menter, 1994).

2.10.2.2 Standard $k - \omega$ model

The $k-\omega$ model is the model of choice to solve for the sublayer of the boundary layer. Unlike any other two-equation models, the $k-\omega$ model does not involve damping functions. Thus, simple Dirichlet boundary conditions can be specified using this model. The $k-\omega$ model is superior to other models because of its simplicity, especially with regards to the numerical stability. Furthermore, this model provides good accuracy in predicting the mean flow profiles. Wilcox (WILCOX, 1988) made modifications to the $k-\omega$ model which accounts for rough walls and surface mass injection (Menter, 1994). The turbulent kinetic energy, k , for the $k-\omega$ model is given by:

$$\frac{\partial}{\partial t} (\rho k) + \frac{\partial}{\partial x_i} (\rho k u_i) = \frac{\partial}{\partial x_j} \left[\left(\mu + \frac{\mu_t}{\sigma_k} \right) \frac{\partial k}{\partial x_j} \right] + G_k - Y_k + S_k \quad (2.40)$$

where Y_k is the dissipation rate of kinetic energy due to turbulence, σ_k is the turbulent Prandtl number for kinetic energy, and $\mu_t = \alpha^* \rho k / \omega$. It shall be noted that α^* is the viscosity damping coefficient, which equals to unity. The specific rate of dissipation for kinetic energy, ω , for the $k-\omega$ model is given by:

$$\frac{\partial}{\partial t}(\rho\omega) + \frac{\partial}{\partial x_i}(\rho\omega u_i) = \frac{\partial}{\partial x_j} \left[\left(\mu + \frac{\mu_t}{\sigma_\omega} \right) \frac{\partial \varepsilon}{\partial x_j} \right] + G_\omega - Y_\omega + S_\omega \quad (2.41)$$

where Y_ω and σ_ω represent the turbulence dissipation rate and Prandtl number due to ω , respectively. Here, $\sigma_{\omega,1} = 2.0$, $\sigma_{k,1} = 1.176$, $\sigma_{\omega,2} = 1.168$, and $\sigma_{k,2} = 1.0$.

2.11 Summary

To achieve highly dispersed carbon nanomaterials in aqueous media, researchers commonly select covalent functionalization in which, the hydrophilic functional groups are attached on the surface of carbon nanostructures by employing oxidizing, radical addition and alkali metal reduction. Among them the free radical coupling is a promising method of functionalization of carbon nanostructures has depicted facile way of covalent functionalization. In this method peroxides and substituted anilines were utilized as starting materials. Even though these chemical routes are generally reliable to synthesize functionalized carbon nanostructures, these techniques are not eco-friendly because the reagents used for synthesis are toxic and harmful to the environment. More importantly, some of these chemical routes may cause defects in the lattice which will degrade the inherent characteristics of carbon nanostructures. Also their corresponding nanofluids cause problems like equipment corrosion, environmental problems and cost of materials. Hence, there is a critical need to develop a simple, efficient, eco-friendly technique for the dispersion of carbon nanostructures, which will be greatly beneficial in the long term since it helps reduce pollution resulting from the use of toxic reagents during syntheses. Moreover, Since the Fluids flow in the heat exchangers and their convective heat transfer and hydrodynamic properties are significant phenomena and widely used in key applications such as cooling of electronic devices, boilers, solar energy systems, and thermal storage systems, as a result studies on synthesis of an appropriate nanofluids and their impact on environment and heat transfer enhancement in heat exchangers are essential.

CHAPTER 3: METHODOLOGY

3.1 Materials

3.1.1 Clove treated GNPs

Pristine Graphene nanoplatelets (GNPs) with thickness and lateral size of about 2 nm and 2 μm , specific surface area 750 m^2/g and purity 99.5% were purchased from, XG Sciences, Lansing, MI, USA. Hydrogen peroxide (H_2O_2 , 30%) and Gallic acid (3, 4, 5-trihydroxybenzoic acid) were purchased from Sigma-Aldrich (M) Sdn. Bhd., Selangor, Malaysia and dried clove buds, as a source of Eugenol, Vitamin C (ascorbic acid), Eugenyl acetate and β -caryophyllene, obtained from grocery store in Iran.

3.1.2 Gallic acid treated GNPs and MWCNTs

Pristine Graphene nanoplatelets (GNPs) with maximum particle diameter of 2 μm , specific surface area 750 m^2/g and purity 99.5%, and Pristine multiwalled carbon nanotubes (MWCNTs) with a diameter less than 8 nm a purity of more than 95% and specific surface area more than 500 m^2/g were obtained from, XG Sciences, Lansing, MI, USA and Nanostructured & Amorphous Materials Inc. (Houston, TX, USA). Rest of the chemical materials were of analytical grade such as Gallic acid (3,4,5-trihydroxybenzoic acid) and hydrogen peroxide (H_2O_2 , 30%) were procured from Sigma-Aldrich.

3.1.3 Graphene oxide and reduced graphene oxide

Graphite flakes (code no 3061) were purchased from Asbury Graphite Mills, Inc. Sulfuric acid (H_2SO_4 , 98%), phosphoric acid (H_3PO_4 , 85%), potassium permanganate (KMnO_4 , 99.9%), ammonia (NH_3 , 30%), and hydrogen peroxide (H_2O_2 , 30%) were purchased from Merck. Hydrogen chloride (HCl , 37%) was purchased from Sigma-Aldrich. Saffron, as a source of Carbohydrate, Protein, Vitamin, Fat and Mineral, obtained from grocery store in Iran.

3.2 Preparation of nano-coolants

3.2.1 Synthesis of Clove-treated GNPs aqueous suspensions

In this study, an eco-friendly method for covalent functionalization of GNPs has been proposed in order to improve its stability in polar Solvents by employing dried clove buds. In this technique, Eugenol, Eugenyl acetate and β -caryophyllene as a main components of cloves (Parthasarathy, Chempakam, & Zachariah, 2008)) was grafted onto the GNPs by employing hydrogen peroxide(a free-radical oxidizer that generates non-toxic by-products and leaves no chemical residue) and ascorbic acid as the redox initiator (K. A. K. Mohammed, Abdulkadhim, & Noori, 2016). This method includes two stages: 1. Preparation of clove extract 2. Functionalization procedure. As can be seen in scheme 3.1, in the first stage, 15 g of ground cloves were added into a 1000 ml of distilled water preheated at 80°C. The solution was then homogenized (at 1200 rpm) and heated (at 80°C) for 30 min. Lastly, extract solution was filtered utilizing a 45 μ m polytetrafluoroethylene (PTFE) membrane, using Vacuum Filtration System (Vilkhu, Mawson, Simons, & Bates, 2008; Zubir et al., 2016) (Figure 3.1). In second stage, pristine GNPs (5 g) were poured into a beaker filled with 1000 ml of clove extract solution, followed by continuous stirring for 15 min order to achieve a homogeneous black suspension. Following this, 25 ml of hydrogen peroxide was added dropwise into the reaction mixture during the sonication time. The mixture was ultra-sonicated (10 min) and heated to 80°C under reflux for 14 h respectively. The resultant suspension was centrifuged (at 14000 rpm) and washed with abundant distilled water repeatedly until the suspension attained a neutral ph. The functionalized sample was dried overnight in a vacuum oven set at 60°C. It was observed that the CGNPs are highly stable in aqueous medium. To synthesize the clove-treated GNPs nanofluid, the CGNPs were ultra-sonicated with distilled (DI) water as the base fluid for 10 min. The nanofluids were prepared for three different concentrations of CGNPs: 0.025, 0.075 and

0.1 wt.%. Here, the free radical grafting pathway is employed for functionalization purpose.

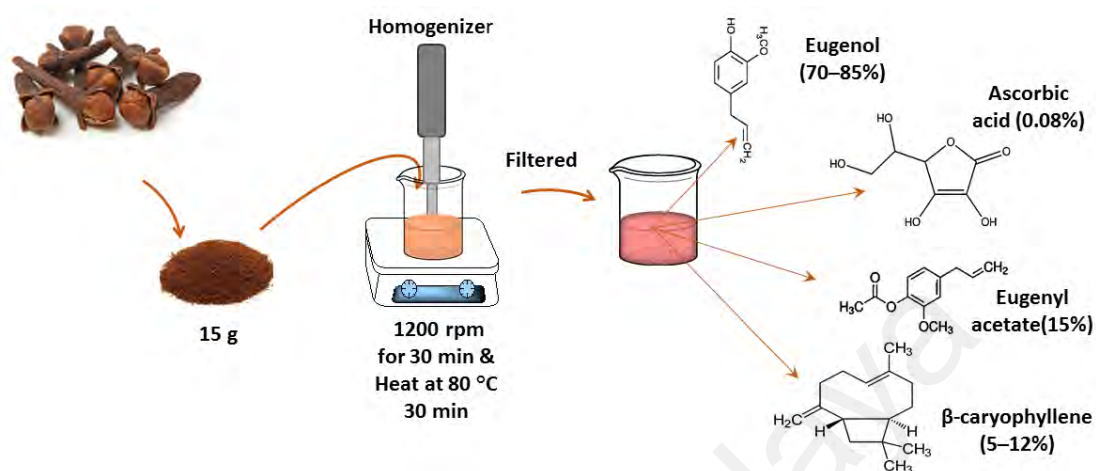


Figure 3.1: Schematic diagram of the preparation procedure of the clove extract solution

Figure 3. 2 (a) illustrates the initiation reaction. In this step, the vitamin C reacts with hydrogen peroxide producing hydroxyl radicals.(Kitagawa & Tokiwa, 2006; Weydemeyer et al., 2015) Also at high temperatures(at 80 °C), the hydrogen peroxide becomes unstable and decomposes spontaneously into hydroxyl radicals(Baskaran, Mays, & Bratcher, 2004). Figure 3. 2 (b) shows that the hydroxyl radicals will attack Eugenol and Eugenyl acetate to produce free radicals on their structures, which leads to linkage of the activated component onto the surface of GNPs. In addition, the hydroxyl radicals can attack the GNPs directly, leading to formation of hydroxyl groups on the surface of GNPs.

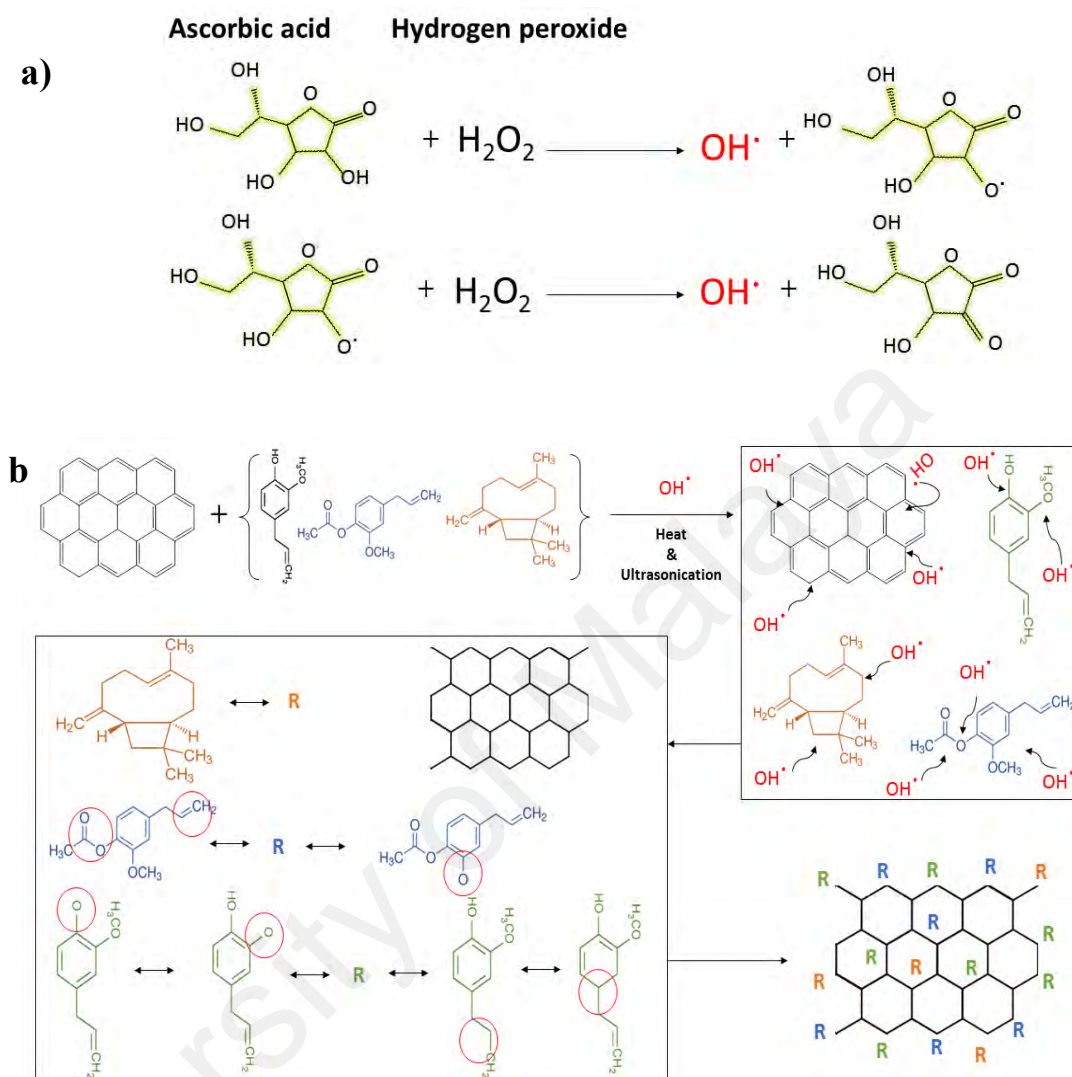


Figure 3.2: Schematic diagram of (a) initiation reaction for free radical grafting, (b) Formation of CGNPs by free radical grafting technique

3.2.2 Synthesis of GA-treated GNPs aqueous suspensions

In order to synthesize the covalently functionalized GNPs, 5 g of pristine GNPs (XG Sciences Inc., Lansing, Minnesota, USA) and 15 g of gallic acid (3, 4, 5-trihydroxybenzoic acid) (Sigma-Aldrich (M) Sdn. Bhd., Selangor, Malaysia) were poured into a vessel filled with 1000 ml of distilled (DI) water and then stirred for 15 min at 80°C to attain a homogeneous black suspension. Following this, 25 ml of concentrated hydrogen peroxide (30%) (Sigma-Aldrich (M) Sdn. Bhd., Selangor,

Malaysia) was poured dropwise into the vessel as an initiator throughout the sonication time. The mixture was then ultrasonicated with a probe sonicator for 15 min. After sonication, the reaction mixture was heated at 80°C under reflux condition for 14 h. The oxidized GNPs were centrifuged and washed several times with large amounts of DI water until the pH was neutral (Figure 3.3). The covalently functionalized sample (GAGNPs) was dried overnight in a vacuum oven set at 60°C. The nanofluids were prepared for three different concentrations of GAGNPs: 0.025, 0.075 and 0.1 wt.%. The GAGNPs were much more soluble in water compared to the pristine GNPs, which was due to strong covalent functionalization.

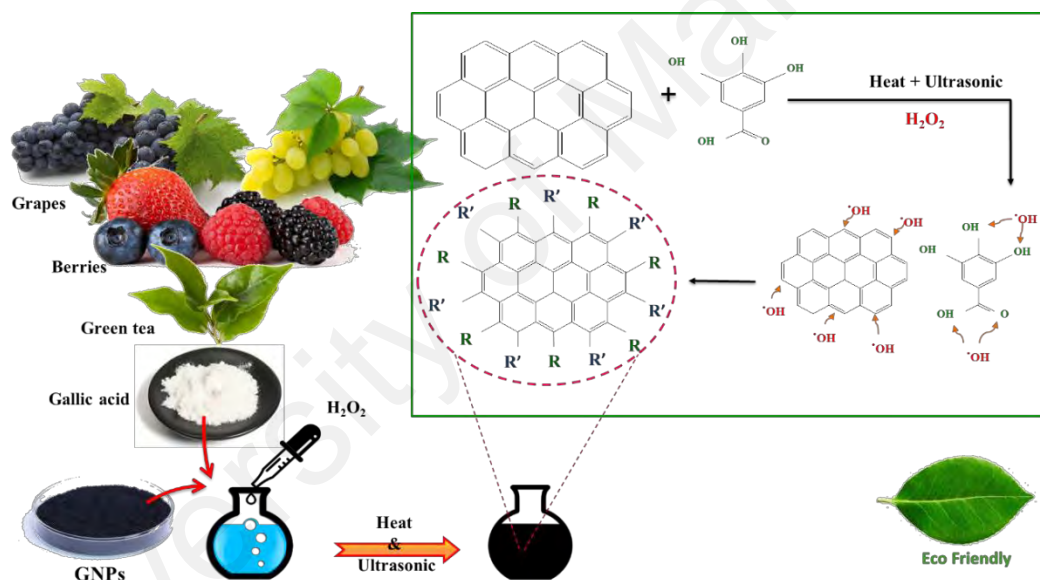


Figure 3.3: Synthesis of Gallic acid-treated GNPs

In order to synthesize the covalently functionalized MWCNTs, 5 g of pristine MWCNTs and 15 g of gallic acid (3,4,5-trihydroxybenzoic acid) were poured into a vessel filled with 1000 ml of distilled (DI) water and then stirred for 15 min at 80 °C to attain a homogeneous black suspension. Following this, 25 ml of concentrated hydrogen peroxide (30%) was poured dropwise into the vessel as an initiator throughout the

sonication time. The mixture was then ultrasonicated with a probe sonicator for 20 min. After sonication, the reaction mixture was heated at 80 °C under reflux condition for 14 h. The oxidized MWCNTs were centrifuged and washed several times with large amounts of DI water until the pH was neutral. The covalently functionalized sample (GAMWCNTs) was dried overnight in a vacuum oven set at 60 °C. The GAMWCNTs were much more soluble in water compared to the pristine MWCNTs, which was due to strong covalent functionalization. Figure 3.4 shows the schematic diagram of the covalent functionalization of MWCNTs with GA. The significant enhancement in dispersion of the GAMWCNTs in water can be attributed to the miscibility of GA. The GAMWCNTs (0.025, 0.075 and 0.1 wt.%) were sonicated in DI water for 10 min in order to synthesize the GAMWCNT-water nanofluid.

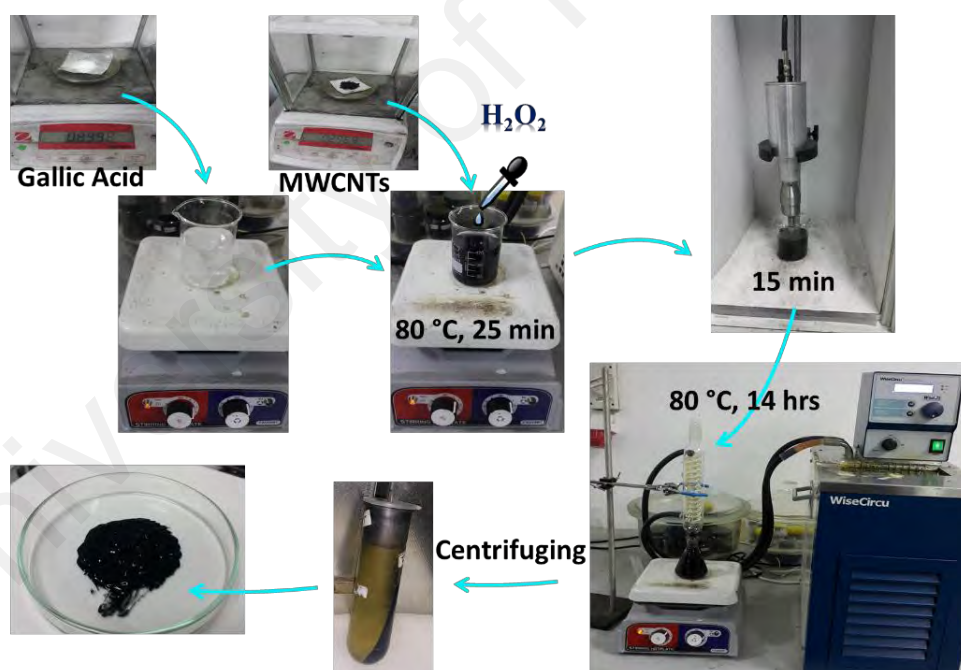


Figure 3.4: Synthesis of Gallic acid-treated GNPs and MWCNTs

Figure 3.5 shows the schematic diagram of the covalent functionalization of GNPs and MWCNTs with GA. The significant enhancement in dispersion of the GAGNPs and GAMWCNTs in water can be attributed to the miscibility of Gallic acid(GA). The GAGNPs and GAMWCNTs were sonicated in DI water for 10 min in order to synthesize the GAGNP-water and GAMWCNTs-water nanofluid. Figure 3.5 shows the proposed free radical grafting reaction of graphene nanoplatelet and multi walled carbon nanotube in aqueous media. In the initiation step, hydrogen peroxide (as a free-radical oxidizer that generates non-toxic by-products and leaves no chemical residue) at high temperatures becomes unstable and decomposes spontaneously into hydroxyl radicals (Weydemeyer et al., 2015). These producing hydroxyl radicals will attack Gallic acid to produce free radicals on the Gallic acid structure, which leads to linkage of the activated molecules onto the surface and edges of GNPs. In addition, the hydroxyl radicals can attack the GNPs directly, leading to formation of hydroxyl groups on the surface of GNPs(Y. Yang, S. Qiu, X. Xie, et al., 2010).

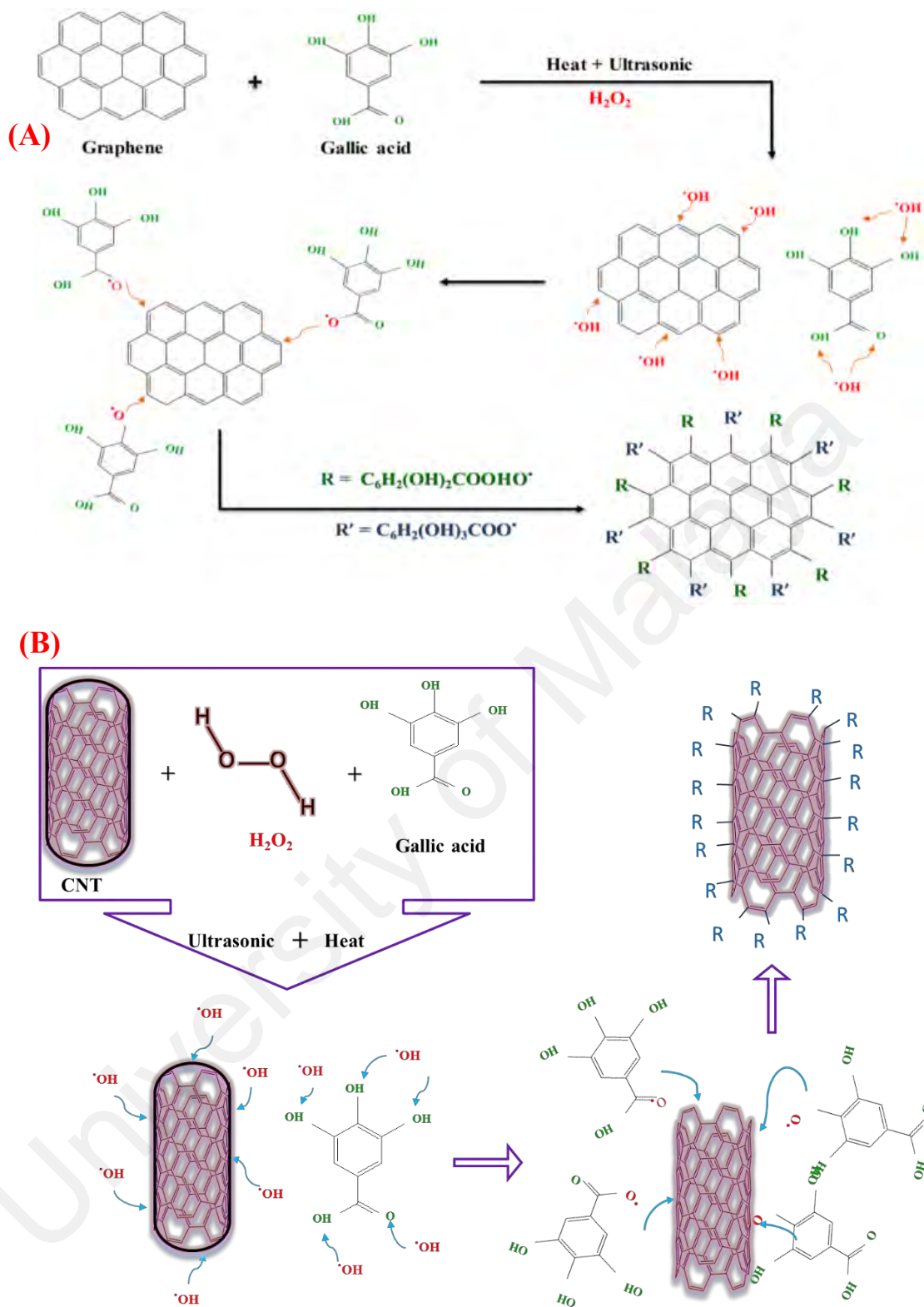


Figure 3.5: Schematic diagram of the covalent functionalization process of GNPs(A) and MWCNTs with gallic acid(B)

3.2.3 Graphene oxide and reduced graphene oxide

There are three stages involved in this technique: (1) preparation of the graphene oxide (2) preparation of saffron extract and (3) Reduction and functionalization procedure. In the first step, Graphite oxide was prepared by the established simplified Hummer's method.(Hummers Jr & Offeman, 1958). Figure 3.6 presents the preparation procedure of graphene oxide. Oxidation of graphite was carried out by mixing highly concentrated H_2SO_4 and H_3PO_4 with the ratio of 320:80 mL in a 2 L beaker initially, which was followed by addition of graphite flakes, and 18 g $KMnO_4$. The one-pot mixture was left for stirring for 3 days to allow the oxidation of graphite. The color of the mixture changed from dark purplish green to dark brown. Then, for the termination of the oxidation process, sufficient amount of DI water iced cubes added to the mixture (oxidized graphite), after that 27 ml H_2O_2 solution was slowly poured into the solution under the stirring mode. Exothermic condition controlled by the ice cubes. When the color of the mixture changed to bright yellow, it was the indicative of a high oxidation level of graphite. The graphite oxide formed was washed three times with 1 M of HCl aqueous solution and repeatedly centrifuged with deionized water at 11,500 rpm until a pH of 4–5 was achieved. The washing process was carried out using simple decantation of supernatant via a centrifugation technique with a centrifugation force of 10,000g. During the washing process with deionized water, the graphite oxide experienced exfoliation, which resulted in the thickening of the graphene solution, forming a GO gel.

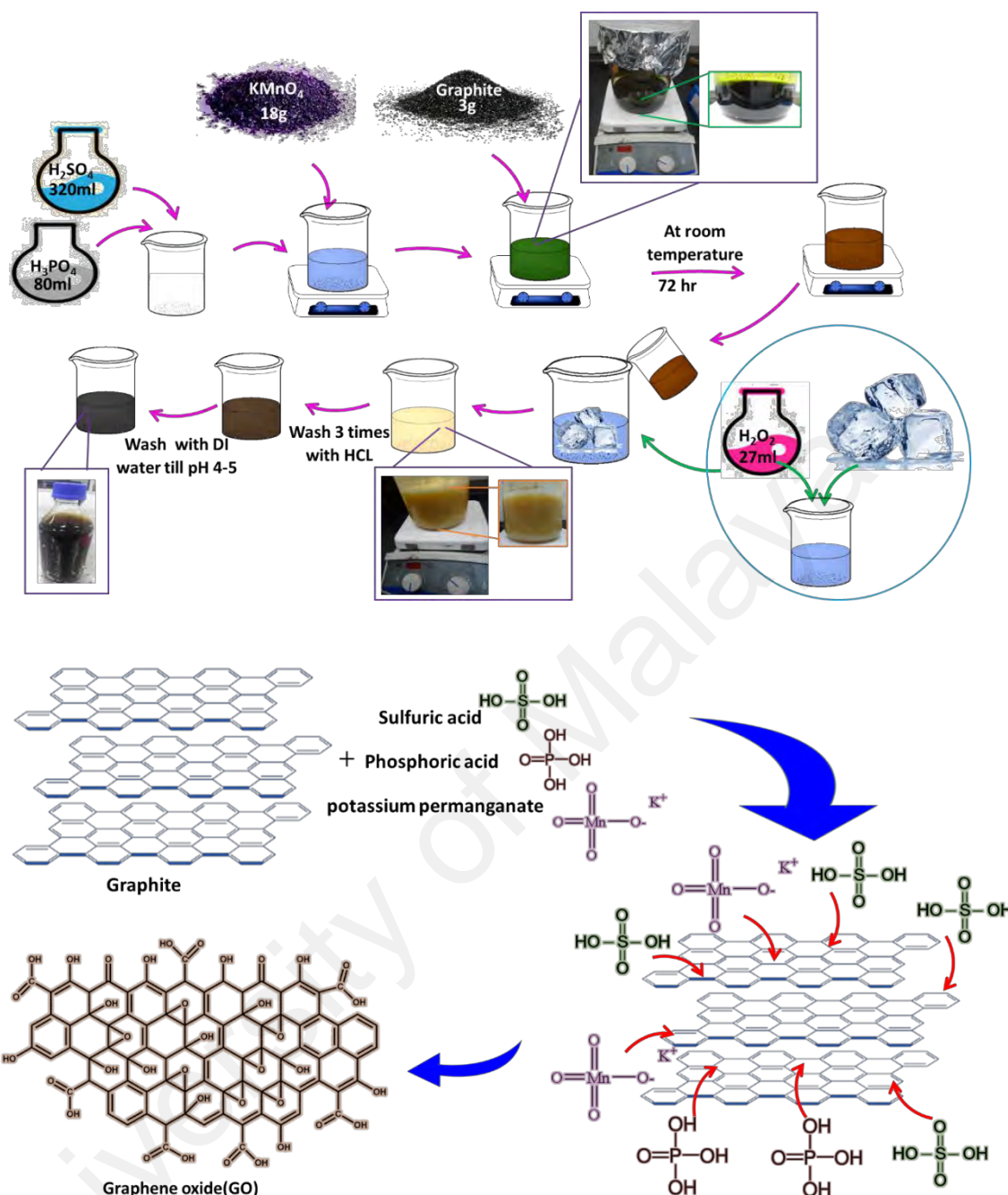


Figure 3.6: Schematic diagram of preparation and oxidation of graphite

Graphite oxide consists of layered GO sheets that contain many oxygen functional groups (e.g. hydroxyl, epoxide, carbonyl, and carboxyl groups). These functional groups significantly alter van der Waals interactions between the layers and endow GO with strong hydrophilicity. Based on the models proposed in this research, GO contains oxygen functionalities on the basal planes and edges of sheets. The presence of these functional

groups destroys the planar sp^2 carbons of graphite and converts them to sp^3 carbons. Therefore, the π - π electronic conjugation of graphite is destroyed in GO. (Kuila, Mishra, Khanra, Kim, & Lee, 2013) This research proposed an eco-friendly method for covalent functionalization and reduction of graphene oxide by employing saffron, in order to improve its electrical and thermal conductivity beside its stability in polar Solvents. Saffron spice is made up of 65.37/100 g carbohydrate, 11.43/100 g protein, 2.54/100 g minerals, 5.85/100 g fat and 81/100 mg vitamins. Figure 3.7 shows component list of saffron which is reported by National Nutrient Database.

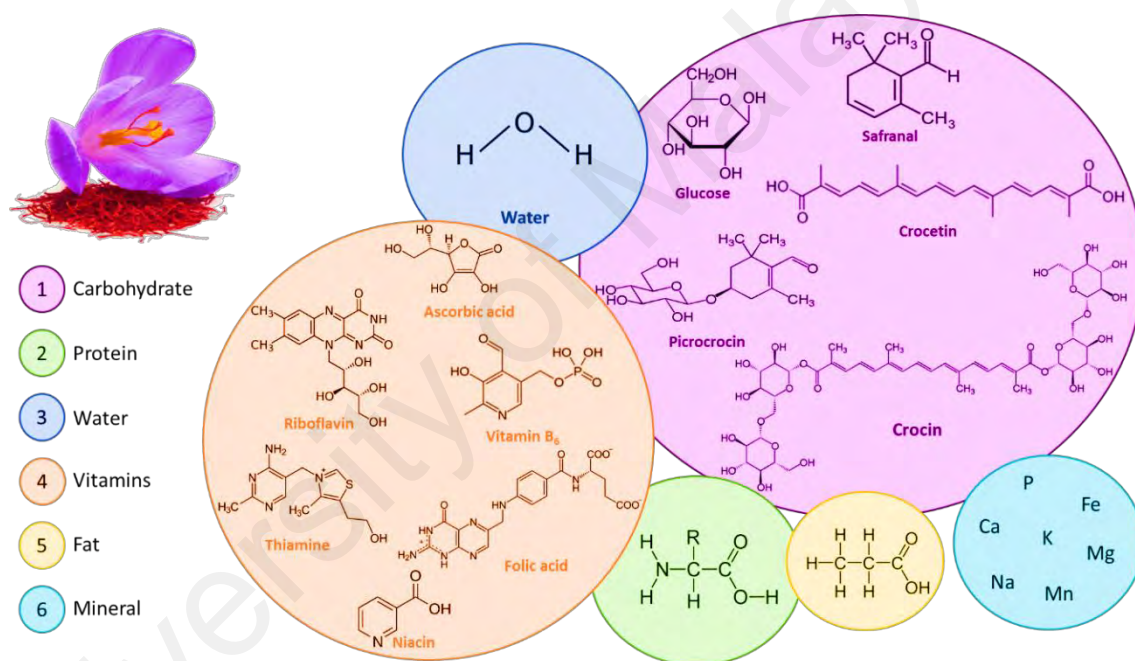


Figure 3.7: Schematic diagram of chemical composition of saffron

Synthetic routes used to prepare the saffron extract solution, oxygen reduction reaction, and functionalized precursors material are presented in Figure 3.8 (a) and (b), respectively. Firstly, 0.8 g of saffron added into 100 ml of distilled (DI) water that was preheated at 80 °C. This solution was stirred continuously for 30 min in heating mood (80°C) in order to achieve reddish colour solution. Lastly, extract solution was filtered utilizing a 45 μ m polytetrafluoroethylene (PTFE) membrane, using Vacuum Filtration

System (Vilkhu et al., 2008; Zubir et al., 2016). In second step, 20 ml of GO ($1 \frac{mg}{ml}$) aqueous solution was transferred to beaker contains 100 ml saffron extract solution, which was followed by the addition of some drops of ammonia solution (25%) to adjust pH at 10.5 and enhance stability of graphene oxide. The reaction mixture was ultrasonicated for 40 min and then heated it to 90 °C under reflux for 6 h (change in color from brown to black). The resultant suspension was centrifuged at 14,000 rpm and washed the suspension with a significant amount of DI water repeatedly until a neutral pH is obtained for the suspension. The stable saffron reduced graphene oxide was collected after cooling at room temperature and the concentrations of nanofluids were maintained at 0.025, 0.075 and 0.1 wt.%. Figure 3.8 depicts proposed reaction of graphene oxide with ammonia and different component of saffron. As can be seen from Figure 3.8, Oxygen-containing functional groups are removed during reduction, and Thiamine was covalently functionalized over GO using nucleophilic ring opening of epoxide functional groups by amine group in the presence of ammonia (Vij, Tiwari, & Kim, 2016). Also, Graphene oxide probably interacts with ammonia and rest of saffron component at high temperature and produce amine group over graphene oxide. The reduced GO may also have some residual oxygen and amine functionalities, such as the carboxylic groups and thiamine as shown in Figure 3.9. Thus, vitamins, proteins and fats (saffron components) might form hydrogen bonds with the residual oxygen and nitrogen (amine group) functionalities on the reduced GO surfaces. Such interactions can disrupt the π - π stacking between the reduced GO sheets, and further prevent the formation of the agglomerates (Jiali Zhang et al., 2010).

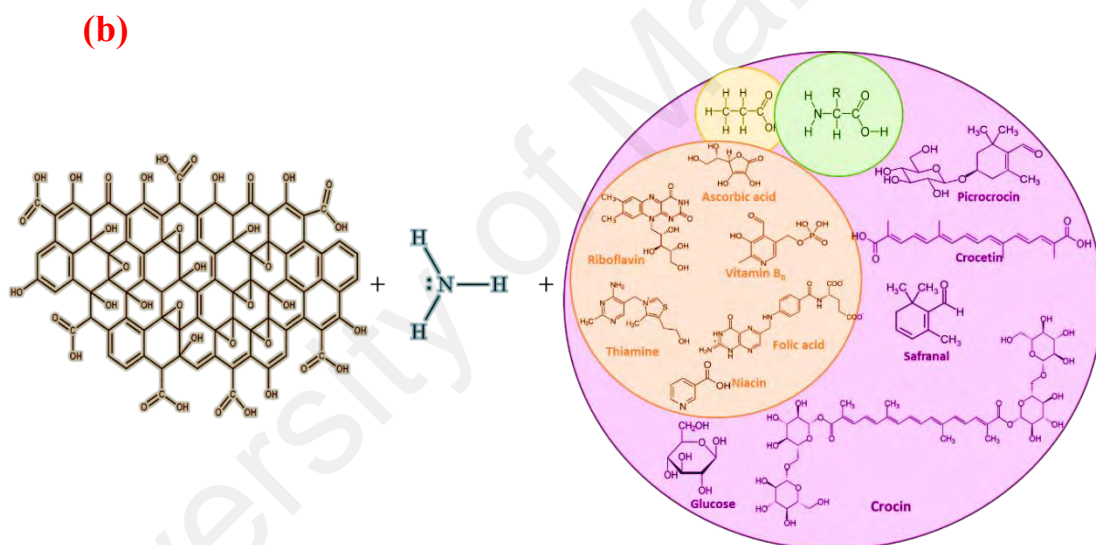
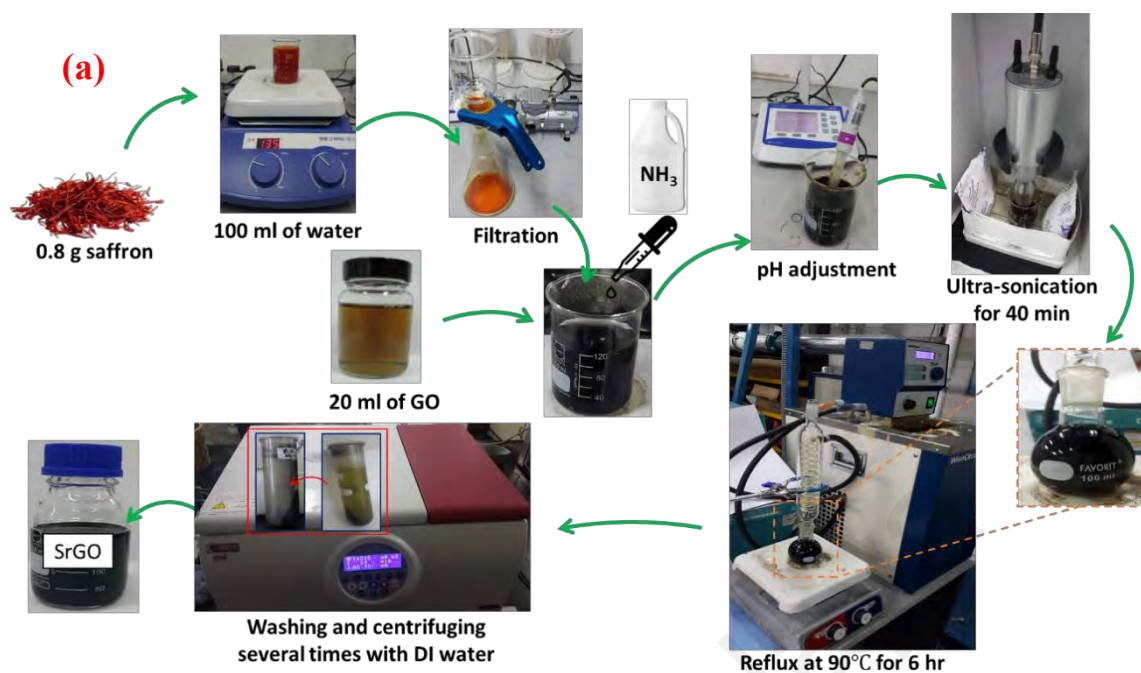


Figure 3.8: Procedure used to prepare the saffron reduced graphene oxide

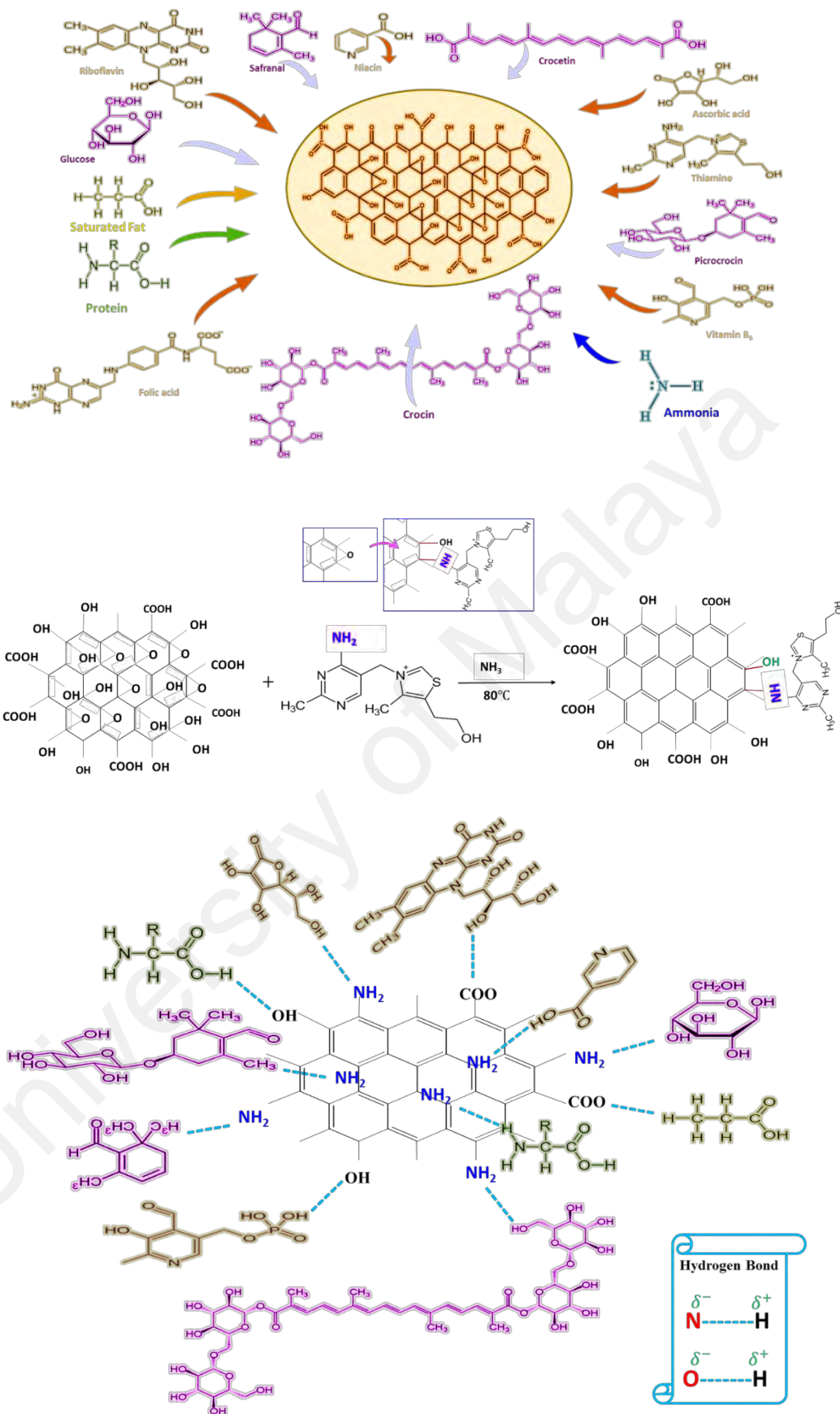


Figure 3.9: Schematic diagram of reduction reaction of graphene oxide by saffron

3.3 Experimental procedure

Experimental were performed in several steps. First the nanofluids were synthesized, and their thermos-physical properties of base and synthesized nanofluids were evaluated. Nanomaterials and fluids were characterized using different analytical equipment and finally the heat transfer and frictional properties of nanofluids flowing in a closed conduit were evaluated. Ultrasonication was conducted via ultrasonic liquid processor (Misonix Inc., Farmingdale, New York, NY, USA) having an output of 600 W. Hitachi HT7700 transmission electron microscope (high-resolution digital TEM) was used to examine the morphological characteristics of the samples. For the TEM analysis, the samples were prepared by ultrasonically dispersing the nanoparticles in ethanol prior to collection on Lacey carbon grids.

The Raman spectra were recorded using Renishaw in Via Raman with laser excitation at 514 nm. Zeta sizer Nano ZS two-angle particle and molecular size analyser (Malvern Instruments Ltd., Malvern, UK) was used to measure the zeta potential of the nanofluid samples. An X-ray photoemission spectrometer (XPS, Axis Ultra DLD system, Kratos Analytical, UK) equipped with a 150 W monochromatic Al K α X-ray source (1486.8 eV) was used to identify the functional groups in treated nanoparticles. The CASA XPS program with a Gaussian–Lorentzian mix function and Shirley background subtraction was used for the deconvolution of the XPS spectra. The UV Spectrophotometer (UV-1800, Shimadzu Corporation, Kyoto, Japan) was used to evaluate the dispersibility of nanofluids. To permit for detectable wavelengths for the UV–vis spectrometer to pass through the samples, a dilution ratio of 1:20 with distilled water was used. Using special quartz cuvettes suitable for UV region, light absorbance of all samples was measured at different time intervals for 63 days. Thermal conductivities of the nanofluids were measured by the KD-2 pro device (Decagon, USA) where the KS-1 probe sensors were used was 6 cm long and had a diameter of 1.3

mm. The accuracy of the measured thermal conductivity was about 5%. To ensure the equilibrium of the nanofluids, an average of 16 measurements were recorded during 4h for each temperature and weight concentrations. Calibration of instrument with DI water was performed before the measurements of nanofluids. The thermal conductivity of DI water at 30 °C was measured and a value of 0.609 W/mK was found, which is in agreement with the previous investigations (Duangthongsuk & Wongwises, 2009) and (X Zhang et al., 2006). The viscosity of the nanofluids was measured using Physica MCR rheometer (Anton Paar, Austria). The rotational rheometer consists of a moving cylindrical plate and a stationary cylindrical surface placed in parallel with a small gap between them. The density of the samples was measured using DE-40 density meter (Mettler Toledo, Switzerland), with an accuracy of 10^{-4} g/cm³.

The overall experimental set-up for convective heat transfer includes the horizontal pipe as a test section, a reservoir tank, a pump, a data acquisition system, a cooling unit, a heated test section, and measuring instruments including a differential pressure transmitter (DPT) and a flow meter. The experimental set-up is shown in Figure 3.10 (a-b). The aqueous suspensions were pumped using Araki EX-70 R magnet pump from a 10 L stainless steel jacketed tank at a flow rate of 0–14 L/min. The pressure loss and flow rate were measured using a Foxboro™ differential pressure transmitter and SE 32 inline paddle wheel transmitter with display (Bürkert Contromatic Corp., USA), respectively. The pump flow was regulated using Hoffman Muller inverter. A straight seamless tube (stainless steel) with a 12 ± 0.1 mm outer diameter, 10 mm inner diameter and length of 1400 mm, was used as the test section. An ultra-high-temperature flexible tape heater (with a 12.5 mm width and 3.6 m length dimension) was carefully wrapped surrounding the test section at a maximum power of 940 W to prepare the final heated section of 1.2 m. The heater was linked to a QPS VT2-1 variable voltage transformer (Success Electronics & Transformer Manufacturer Sdn. Bhd., Malaysia) and, voltage

and current were measured to set the desired heating power. Five K-type thermocouples were inserted into stainless steel thermocouple sleeves, which were installed on the upper surface of the test section employing high temperature epoxy glue (Figure. 3.10). The axial distances of the thermocouples from test tube inlet are 20, 40, 60, 80, and 100 cm as it can be seen in Figure 3.11. The bulk temperature of the flow was measured using two platinum resistance temperature detectors (Pt-100 RTDs) which were placed inside the pipe at the outlet and inlet of the test section. The maximum error for thermocouples was $\pm 0.2^{\circ}\text{C}$. The thermocouples were connected to a GL220 10-channel multi logger (Graphtec Corporation, Japan) in order to monitor and record the temperature data. The test section was wrapped with thick fibreglass wool in order to reduce heat loss to the surroundings, as well, as achieving steady state temperature at the inlet and outlet of the test section.

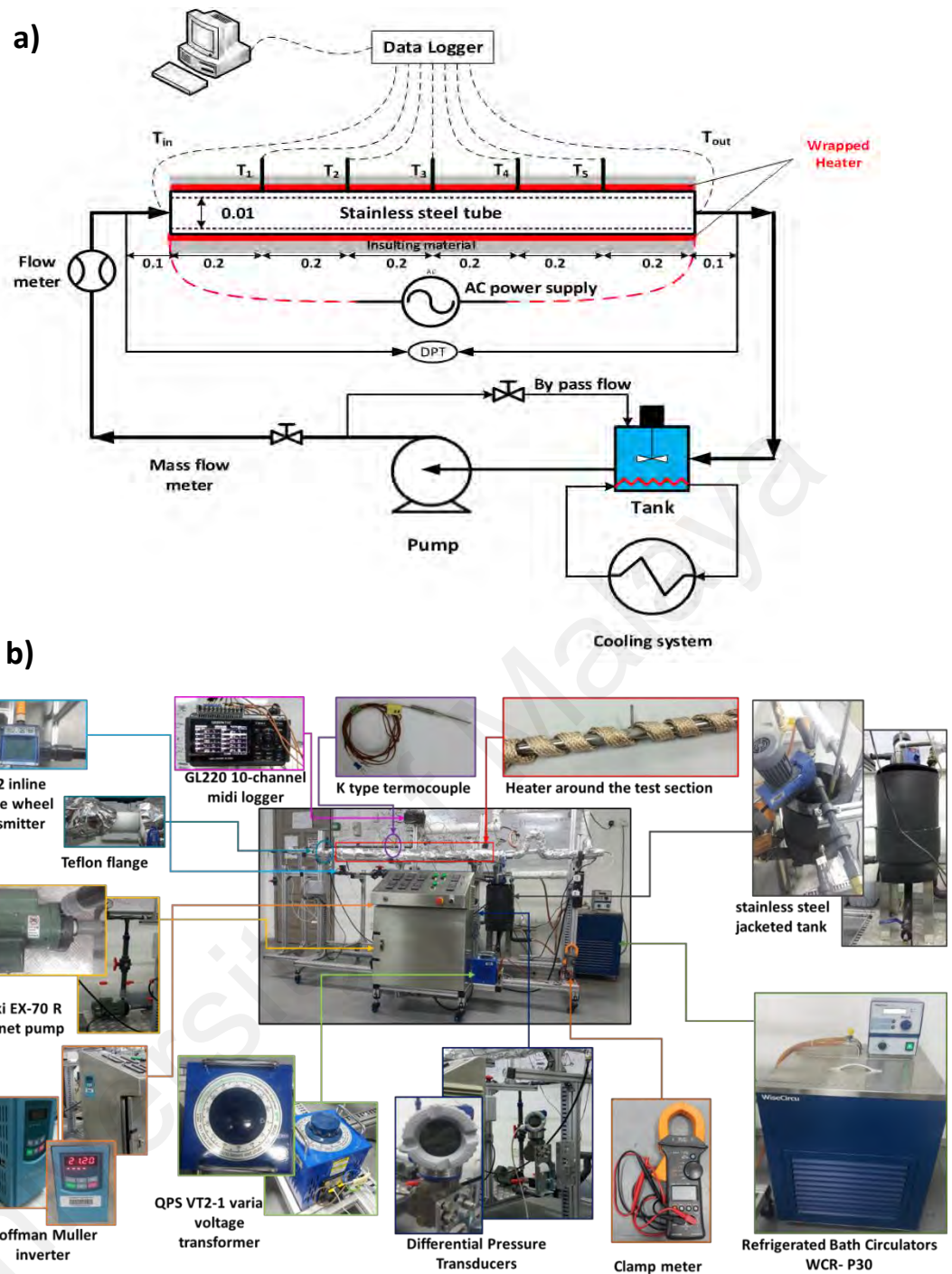


Figure 3.10: (a) Schematic diagram and (b) Image of the experimental set-up for the measurement of convective heat transfer

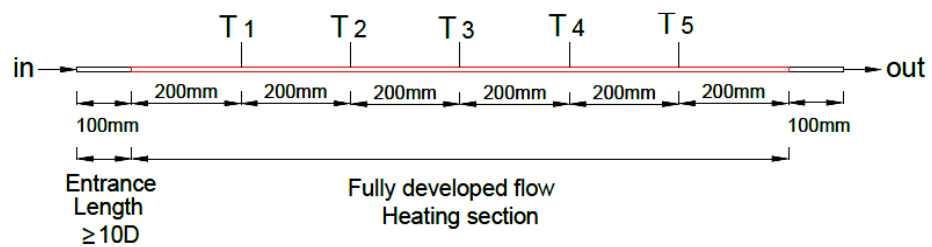


Figure 3.11: Sectional view of the experimental test section

The specifications and the accuracy of the measuring instruments and sensors used in the present experimental setup are presented in Table 3.1.

Table 3.1: Specifications and errors of the measuring instruments and sensors used in the present experiment

Measured parameter	Instrument and sensor type	Operating	Error
Surface temperature	Type K thermocouple	0-300°C	±0.1°C
Bulk Temperature	RTD (PT-100) sensor	0-200°C	±0.1°C
Fluid flow meter	Bürkert, Ceramic paddle wheel	0.03-12 m/s	±0.5%
Fluid pressure drop	ALIADP, Differential Pressure Transmitter (DPT)	0-25 kPa	±0.075%
Cooling unit	WiseCircu, DAIHAN Scientific, Refrigerated circulating bath	2.2 kW	±0.1°C

3.4 Data Processing

The experimental values were processed to assess the heat transfer performance and hydrodynamic behaviour of a novel eco-friendly synthesized GNPs coolant in a closed conduit system. By considering the conduction in the tube wall and convection heat transfer with the fluid at the test section, a calibration is essential to measure the temperatures at the internal surface of the tube. accordingly, a Wilson plot technique (Fernandez-Seara, Uhía, Sieres, & Campo, 2007) was performed which acts According to the equating the resistance between various sections of the heat transfer direction and measuring the internal surface temperatures of the horizontal pipe via mathematical manipulation. To study the effect of the CGNPs aqueous suspensions on thermal properties of DI water, the significant parameters, namely convective heat transfer coefficient (h), Nusselt number (Nu) and pressure drop (DP) are required to be evaluated. The convective heat transfer coefficient was evaluated from the experimental values including the measured bulk, surface, inlet and outlet temperatures via the Newton's cooling law.

That is,

$$h = \frac{q''}{(T_w - T_b)} \quad (3.1)$$

Where, T_w , T_b and q'' represents the wall temperature, bulk temperature and heat flux, respectively. T_b is defined as $\frac{T_o + T_i}{2}$, where T_o and T_i is the outlet and inlet temperature of the flow, respectively. The heat flux can be calculated using Eq. (3.2),

$$q'' = \frac{Q}{A} \quad (3.2)$$

Where, Q is the input power (VI) provided by the power supply and A is the internal heated surface area of the tube. Note that $A = \pi DL$.

The input power (VI) of 600 W was used in this experimental study. The Nusselt number is given as,

$$Nu = \frac{h \times D}{K} \quad (3.3)$$

Where, K , h and D are, respectively, the thermal conductivity, the heat transfer coefficient and the tube inner diameter, respectively. The Reynolds number (Re) was evaluated using the following equation:

$$Re = \frac{\rho v D}{\mu} \quad (3.4)$$

Where, v , ρ and μ are the velocity, density and the dynamic viscosity of the working fluid, respectively.

For single-phase fluids, the empirical correlations for Nusselt number were suggested by Gnielinski (Volker Gnielinski, 1975), Petukhov (Petukhov, 1970) and Dittuse Boelter (Duangthongsuk & Wongwises, 2008), respectively, as

$$Nu = \frac{\left(\frac{f}{8}\right)(Re - 1000)Pr}{1 + 12.7\left(\frac{f}{8}\right)^{0.5}\left(Pr^{\frac{2}{3}} - 1\right)} \quad (3.5)$$

Here Re is the Reynolds number, Pr is the Prandlt number and f is the friction factor.

Eq. (3.4) is used in the range of $3 \times 10^3 < Re < 5 \times 10^6$ and $0.5 < Pr < 2000$.

$$Nu = \frac{\left(\frac{f}{8}\right)RePr}{1.07 + 12.7\left(\frac{f}{8}\right)^{0.5}\left(Pr^{2/3} - 1\right)} \quad (3.6)$$

Eq. (3.5) applicable for the range of $3000 < Re < 5 \times 10^6$ and $0.5 < Pr < 2000$.

$$Nu = 0.023Re^{0.8}Pr^{0.4} \quad (3.7)$$

Eq. (3.6) is used in the range of $Re > 10^4$ and $0.6 < Pr < 200$.

The friction factor(f), in Equations (3.4) and (3.5) is given as Petukhov (Petukhov, 1970).

$$f = (0.79 \ln Re - 1.64)^{-2} \quad (3.8)$$

For $2300 < Re < 5 \times 10^6$

The friction factor (f) of the DI water and CGNPs aqueous suspensions was determined from the pressure drop across the test section measured from experiments using the following equation (Eq.3.9):

$$f = \frac{\Delta P}{\left(\frac{L}{D}\right)\left(\frac{\rho v^2}{2}\right)} \quad (3.9)$$

Where, ΔP and v are the pressure drop and flow velocity, respectively.

The empirical correlations suggested by Petukhov (Petukhov, 1970) and Blasius (Blasius, 1907) for the friction factor of the base fluid is given by Eqs. (3.8) and (3.10), respectively.

$$f = 0.3164 Re^{-0.25} \quad (3.10)$$

For the range of Reynolds numbers, $3000 < Re < 10^5$.

University of Malaya

3.5 Analysis methods

3.5.1 FT-IR

Fourier Transformation Infrared Spectrometer (Bruker, IFS-66/S, Germany) at the wave ranges of 4000-400 cm^{-1} was employed to analyse functional groups on the surface of the carbon nanostructures. Fourier transform infrared spectroscopy (FT-IR) samples were prepared by grinding a very low proportion of dry material with potassium bromide (KBr) to form a very fine powder. This powder was then compressed into a thin pellet for analysis. Figure 3.12 shows Fourier Transformation Infrared Spectrometer (Bruker, IFS-66/S, Germany).

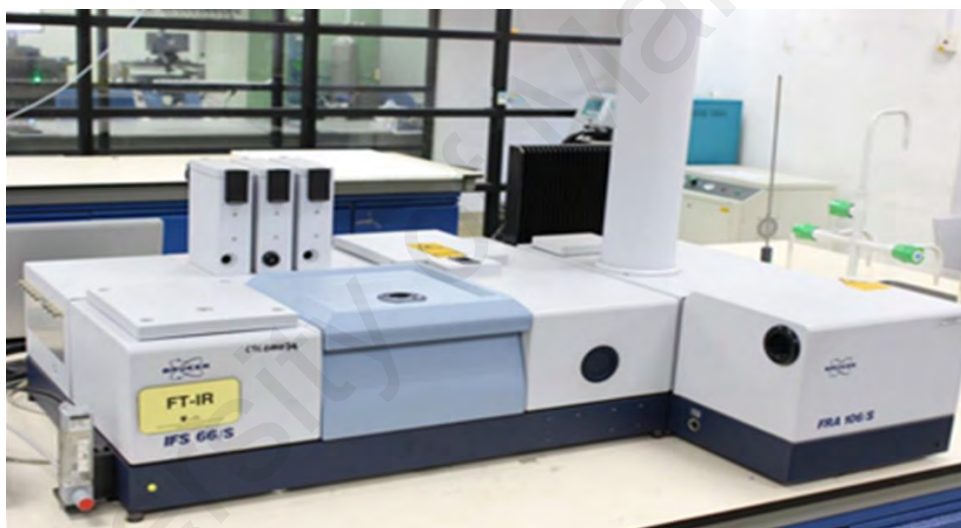


Figure 3.12: FT-IR spectroscopy (Bruker, IFS-66/S, Germany)

3.5.2 Raman

Raman spectroscopy is becoming a technique of increasing relevance for the characterization of carbon materials. Apart from being non-destructive, it is simple and rather sensitive not only to the crystal structure (the long range order), but also to structural changes occurred at the molecular level (the short range order). Therefore, Raman spectroscopy has the high potential to access the chemical functionalization status.

Raman scattering of monochromatic light usually from a laser in the visible near infrared or near ultraviolet range. The laser light interacts with molecular vibrations, phonons or other excitations in the system, resulting in the energy of the laser photons being shifted up or down. The shift in energy provides information about the vibrational modes in the system. Raman spectra were collected using a Renishaw in Via Raman spectrometer equipped with laser excitation at 514nm. (Figure 3.13)



Figure 3.13: Raman spectra (Renishaw in Via)

3.5.3 TGA

TGA is a thermal analysis technique, whereby modifications in the structure of materials are evaluated with varying temperature in a controlled atmosphere. The TGA instrument (TGA-50, Shimadzu, Japan) continuously weighs a sample as it is heated to temperatures of up to 1000 °C for coupling with Mass spectrometry gas analysis. As the temperature increases, various components of the sample are decomposed and the weight percentage of each resulting mass change can be measured. (Figure 3.14)

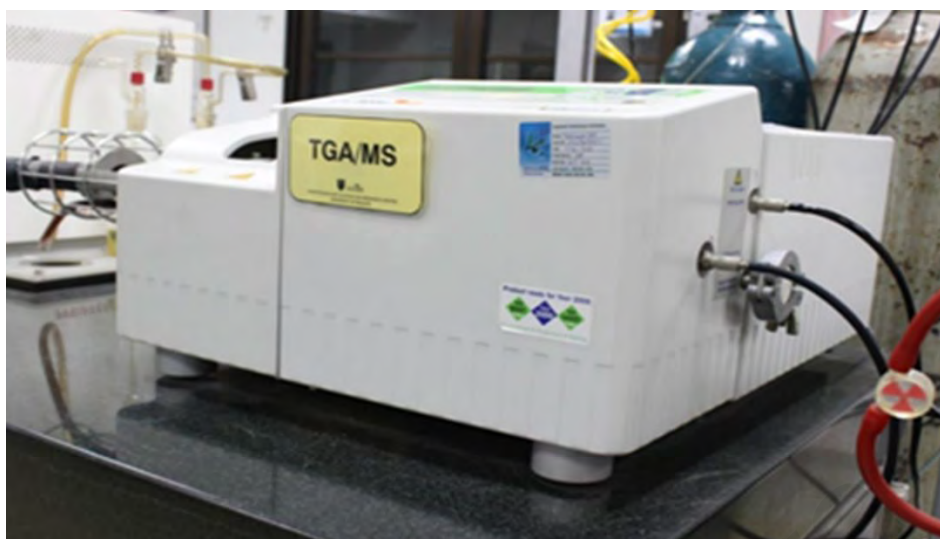


Figure 3.14: Thermogravimetric analysis (TGA-50, Shimadzu, Japan)

3.5.4 XPS

X-ray photoelectron spectroscopy (XPS) is a surface-sensitive quantitative spectroscopic technique that measures the elemental composition at the parts per thousand range, empirical formula, chemical state and electronic state of the elements that exist within a material. XPS spectra are obtained by irradiating a material with a beam of X-rays while simultaneously measuring the kinetic energy and number of electrons that escape from the top 0 to 10 nm of the material being analyzed. Axis Ultra-DLD system, Kratos Analytical X-ray photoemission spectrometer (XPS) with Al K α X-ray source ($h\nu = 1486.8$ eV) was used to recognize the functional groups in carbon nanostructures. CASA XPS programme with Gaussian-Lorentzian mix function and Shirley background subtraction were used for deconvolution of the XPS spectra (Figure 3.15).



Figure 3.15: Axis Ultra-DLD system, Kratos Analytical X-ray photoemission spectrometer (XPS)

3.5.5 TEM

Transmission electron microscopy (TEM) is the primary technique to verify single particle dimensions and to identify agglomerations of the particles. The electron beam can be used to see features on the nanometer level. A major drawback to the use of TEM is that samples must be dried out of solution in order to be attached to the carbon matrix and placed in the vacuum chamber of the TEM; therefore, the particles are not exactly in the colloid state and agglomeration might occur during drying. However, TEM can be used in combination with dynamic light scattering to acquire exact sizing in nanofluid form. Hitachi HT7700 transmission electron microscope (Figure 3.16) was conducted to examine the morphological characteristics of the samples. For the TEM analysis, the samples were prepared by ultrasonically dispersing the nanoparticles in ethanol prior to collection on Lacey carbon grids.



Figure 3.16: Hitachi HT7700 transmission electron microscope

3.5.6 Zeta potential

It is worth noting here that the stability of nanofluid is closely linked with its electrokinetic properties. The high surface charge density of nanoparticles will generate strong repulsive forces, which helps in the attainment of well-dispersed, stable carbon nanoparticles suspensions. (L. Chen & Xie, 2010) Hence, zeta potential measurements were taken to investigate the electrophoretic behavior and further understand the dispersion behavior of MWCNTs and GNPs in water. (Bala et al., 2005; Mayer, Neveu, Secheresse, & Cabuil, 2004) Zeta potential values that are more negative than -30 mV or more positive than $+30$ mV are generally considered to represent sufficient mutual repulsion to ensure stability of the dispersion. The particles can no longer be strongly repelled close to the isoelectric point (i.e. point of zero charge) and therefore, they begin to aggregate and sediment over time (Ko et al., 2007). Zeta sizer Nano ZS two-angle particle and molecular size analyser (Malvern Instruments Ltd., Malvern, UK) was used to measure the zeta potential of the nanofluid samples (Figure 3.17).

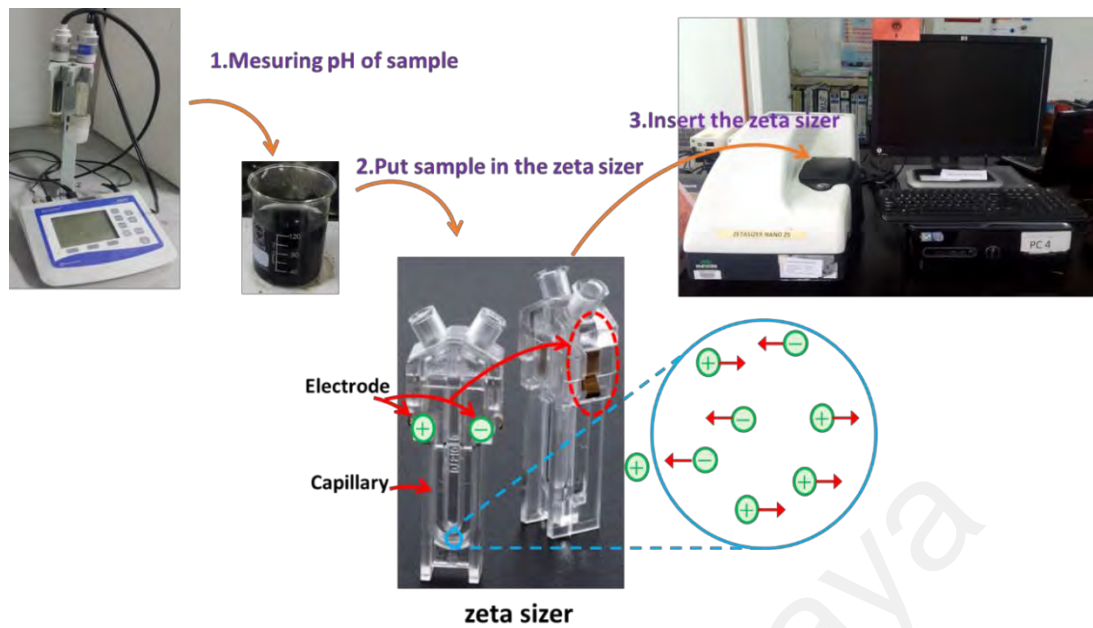


Figure 3.17: Malvern Instruments Ltd Zeta sizer

3.5.7 UV-Vis

The solubility and stability of nanoparticles in the base fluids is very significant for practical application, the data from this instrument is limited on evaluating of the dispersibility of nanofluids. Shimadzu UV-1800 spectrophotometer (Figure 3.18) was used to determine the dispersibility of Clove treated carbon nanostructure-water nanofluids. For the UV-vis analysis, the sample nanofluids were diluted with DI water at a dilution ratio of 1:20 in order to ensure that the detectable wavelengths of the UV-vis spectrometer were able to pass through the samples. Following that the samples were poured into quartz cuvettes specialized for transmission of UV wavelengths and the absorbance of the samples were measured at pre-defined time intervals over the course of 63 days.

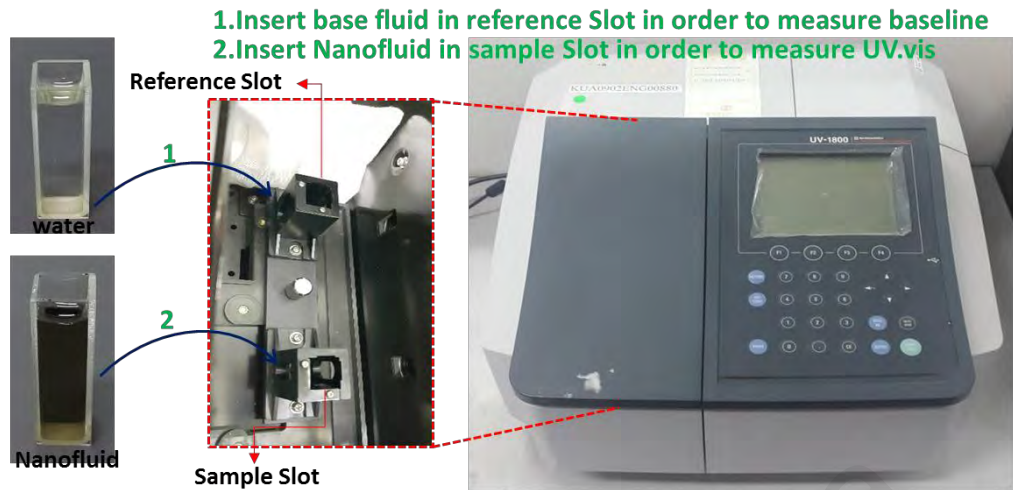


Figure 3.18: Shimadzu UV-1800 spectrophotometer

3.5.8 KD2-PRO

The effective thermal conductivity of the samples was evaluated via KD-2 PRO portable field and laboratory thermal property analyser (Decagon Devices, USA). The KS-1 probe has a length and diameter of 60 and 1.3 mm, respectively. The accuracy of the thermal conductivity measurements is around 5%. In order to ensure equilibrium of the nanofluids, an average of 20 measurements were recorded over a 5-hrs period for each nanoparticle concentration and temperature. Calibration of the instrument was also done with DI water prior to collecting the measurements using nanofluids. Figure 3.19 shows thermal conductivity setup.

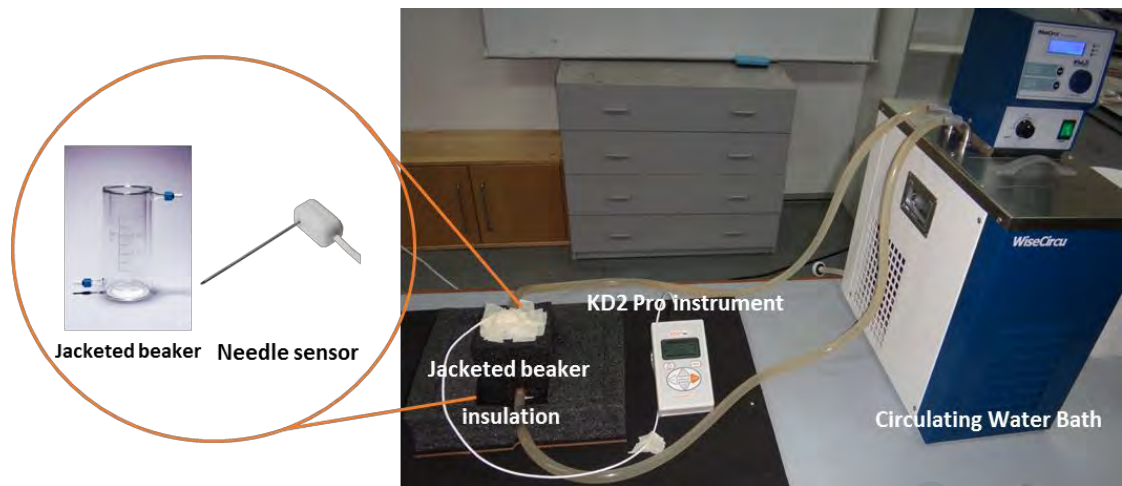


Figure 3.19: Thermal conductivity measurements set up

3.5.9 Rheometer

Viscosity of nanofluids (suspensions contained nanoparticles) is one of the most important parameters, which determines the quality of the heat transfer liquid. As in the case of simple fluids, the viscosity of a nanofluid depends largely on the temperature (Mehrali et al., 2014). Moreover, the viscosity of nanofluids is measured at different rotor RPMs to investigate if the nanofluids are Newtonian or non-Newtonian fluids. The viscosity of the nanofluid suspensions was evaluated via Physica MCR rheometer (Anton Paar, Austria). The rotational rheometer consists of a moving cylindrical plate and a stationary cylindrical surface placed in parallel with a small gap between them (Figure 3.20).



Figure 3.20: Anton Paar rheometer

3.5.10 Density

The density of the samples was evaluated via DE-40 density meter (Mettler Toledo, Switzerland), with an accuracy of 10^{-4} g/cm³. The measurements were made in triplicate for each sample and temperature. Figure 3.21 depicts density meter setup.



Figure 3.21: DE-40 density meter, Mettler Toledo

3.5.11 DSC

Differential scanning calorimetry (DSC) is a powerful tool to measure the heat capacity of the nanofluids. The difference in the amount of heat flow required for heating up a sample pan and reference pan are measured as a function of temperature. During the whole process, the sample and reference pans are maintained at nearly the same temperature throughout the experiment. The heat capacity of the reference pan is already known. By measuring the difference in heat flow, the heat capacity of the sample is obtained. If there are phase transitions happened in the sample pan, more or less heat will need to flow out of it than the reference to maintain both at the same temperature, so endothermic or exothermic peaks are shown on the DSC curves, corresponding to melting or freezing, respectively. The phase transition temperatures and latent heats are determined according to the DSC curves. The heat capacities of the nanofluids and DI water were obtained from a differential scanning calorimeter (Perkin Elmer DSC 800 differential scanning calorimeter with an accuracy of $\pm 1.0\%$).

CHAPTER 4: SYNTHESIS, CHARACTERIZATION, THERMO-PHYSICAL PROPERTIES, CONVECTIVE HEAT TRANSFER AND HYDRODYNAMIC PROPERTIES OF WATER-BASED GALLIC ACID-TREATED GRAPHENE NANOPATELET NANO-COOLANT

4.1 Characterization of GA-functionalized GNPs

To analyze the GAGNPs, the FTIR spectroscopy was employed to investigate chemical groups that are attached to the GNPs. The FTIR spectra of the pristine GNPs and GAGNPs are shown in Figure 4.1(A). In contrast to the pristine GNPs, it is seen that the GAGNPs sample provides some cues of the GA molecules. The spectrum of GAGNPs indicates a broad peak at 3448 cm^{-1} , which could be ascribed to the O-H stretching vibration. This peak could be because of the reaction of one of the hydroxyl groups of the GA with GNPs and/or the attached hydroxyl groups on the GNPs. The symmetric and antisymmetric fundamental vibrations of CH bonds are observed at $2920\text{--}2980\text{ cm}^{-1}$ for the GAGNPs. The peaks in the range of $1579\text{--}1639\text{ cm}^{-1}$ are attributed to C=C graphitic stretching mode of GNP, which is infrared-activated by functionalization. Moreover, GNPs functionalization via GA was confirmed by the appearance of the peaks at 1451 cm^{-1} , 1388 cm^{-1} and $1056\text{--}1189\text{ cm}^{-1}$, respectively, for the CH_2 bending vibration, out of plane CH vibration and C-O stretching vibrations. The peaks at 1014 and 877 conform to the stretching vibration of C-C and COH out of plane deformation. TGA provides information about the quantitative amount of functional groups on GNPs surface by thermal analysis of samples. Figure 4.1 (B) shows evidence of the functionalization of GNPs with GA. According to the figure, there is no significant weight loss in the pristine GNPs; however, a steady weight loss between 150 and $400\text{ }^\circ\text{C}$ is seen in the GAGNPs, which confirms the decomposition of the functional groups. Also, the second mass loss after $500\text{ }^\circ\text{C}$ is associated with the

degradation temperature of the main graphitic structures in the air. Furthermore, the results show that the functionalization of GNPs with GA is successful, since a steady weight loss of GAGNPs with increase of temperature is observed. GA as a functional group can provide suitable dispersibility, and also does not have any corrosive effects for different metals.

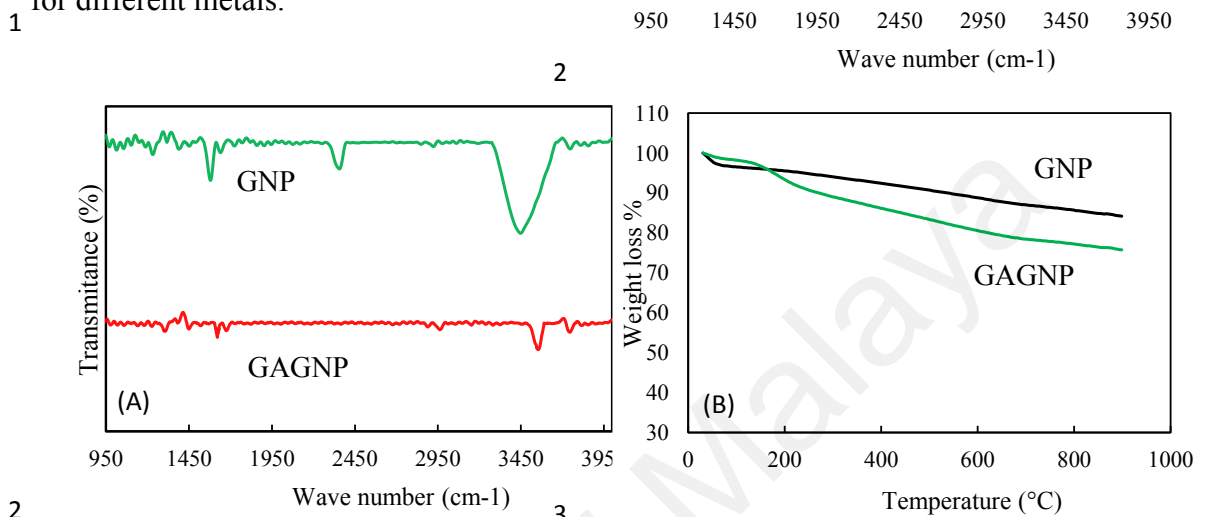


Figure 4.1: (A) FTIR spectra, (B) thermogravimetric analysis of the pristine and GA-treated GNPs nanoparticles

Raman spectroscopy was used to provide insight on the covalent functionalization of GNPs with GA and the results are shown in Figure 4.2(A). It can be observed from the Raman spectra that both pristine GNPs and GAGNPs have D, G and 2D band at a wavenumber of 1342, 1574 and 2713 cm^{-1} respectively. The blue shift in G and 2D band of GAGNPs is related to a sufficient concentration of defects (Kudin et al., 2008). The G band is associated with graphitic carbon (sp^2) whereas the D band is associated with amorphous or disordered carbon (sp^3). The increase in the Raman intensity ratio (I_D/I_G) is due to changes in the hybridized carbon from sp^2 to sp^3 as a consequence of covalent functionalization. The I_D/I_G ratio is found to be 0.64 and 0.74 for the pristine GNPs and GAGNPs, respectively. The higher I_D/I_G ratio obtained for the GAGNPs is attributed to the higher number of sp^3 carbons present and the occurrence of electrophilic addition reaction. The Raman spectra can be considered as one of the solid proofs in examining

the covalent functionalization of GNPs. Raman spectroscopy can distinguish a single layer from a few layers by focusing on the intensity, size and shape of the 2D bands, as the number of the layers in graphene increased, the 2D band becomes much smaller and broader. A single, sharp 2D peaks of GAGNPs compare with GNPs can verify the presence of single layered- or few layered- graphene (Ferrari et al., 2006). Full Raman spectra analysis data is given in Table 4.1.

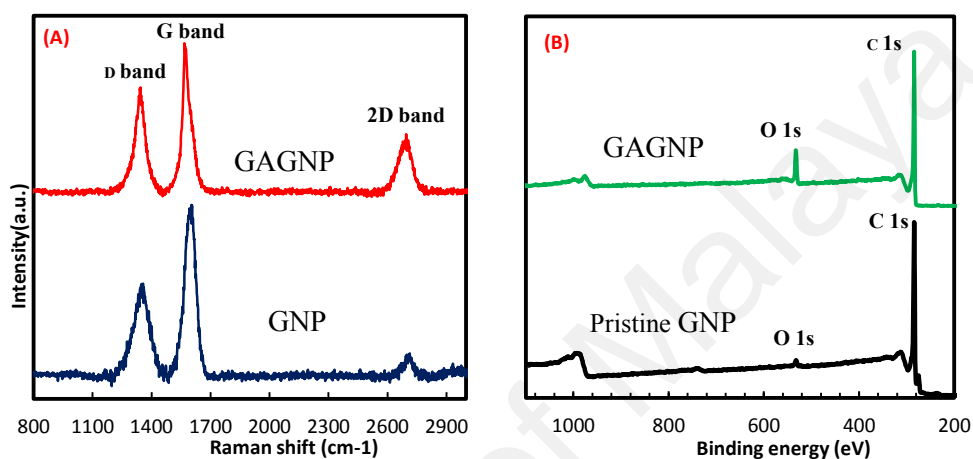


Figure 4.2: (A) Raman spectra and (B) wide-scan O1s and C1s XPS spectra for pristine GNPs and GAGNPs

Table 4.1: Raman spectra analysis results for pristine GNPs and GAGNPs

Sample	Peaks	Centre (cm ⁻¹)	Intensity(a.u.)	I _D /I _G
GNPs	D bond	1341.824	503.376	0.64
	G bond	1572.288	785.834	
	2D bond	2713.13	297.565	
GAGNPs	D bond	1341.824	832.443	0.74
	G bond	1566.247	1120.019	
	2D bond	2695.02	527.102	

X-ray photoelectron spectroscopy (XPS) was used to examine the surface of the graphene sheets before and after covalent functionalization with GA. The wide-scan O1s and C1s XPS spectra for GNPs and GAGNPs are shown in Figure 4.2(B). The peaks at a binding energy of 284.6 and 533 eV were generated by photoelectrons emitted from the C1s and O1s core level, respectively. The oxygen-to-carbon (O/C) ratio increases from 0.04 (pristine GNPs) to 0.14 (GAGNPs) (Felten, Bittencourt, & Pireaux, 2006), indicating that the free radical grafting of GNPs was successful in oxidizing amorphous carbon impurities and grafting different oxygen functional groups onto the GAGNPs. Figure 4.3 (A–D) show the high-resolution XPS spectra of the C1s and O1s deconvoluted peak components for pristine GNPs and GAGNPs. The peaks at 284.6, 285.4, 286.4, 287.9, 289.4 and 291 eV are assigned to the C=C (aromatic), C–C (aliphatic), C–O (hydroxyl and epoxy), C=O (carbonyl), O–C=O and π - π interaction bonds, respectively (Kuila et al., 2011; T. Zhou et al., 2010). Figure 4.3(A) and (B) shows the three main oxygen peaks that arise from the C–O (hydroxyl and epoxy \sim 286.4 eV), C=O (carbonyl \sim 287.9 eV) and O–C=O (\sim 289.4 eV) functional groups for pristine GNPs and GAGNPs, respectively. After covalent functionalization, these three peaks (associated with the C–O, C=O and O–C=O bonds, respectively) increases from 5.70, 4.00 and 1.61% (GNPs) to 11.37, 4.61 and 3.28% (GAGNPs), which confirms the presence of large fractions of oxygen atoms as C–O and C=O functional groups in the GAGNPs. The higher peak intensities at 531 and 533 eV in the O1s spectrum confirms the presence of large fractions of oxygen atoms in the form of O–C=O and C–O functional groups in the GAGNPs. The oxygen atoms in the C–O functional group (O1s spectrum) were generated from O–C=O linked to the aromatic rings in the GAGNPs. In contrast, the pristine GNPs show the presence of generic functional groups such as C–O–C and O–C=O (C1s spectrum) and C–OH and C=O (O1s spectrum), as shown in Figure 4.3(A) and (C). These functional groups were generated unintentionally when

the GNPs were exposed to the environment containing natural oxidizing agents such as ozone and hydroxyl radicals (R. Das et al., 2015). Full XPS analysis data is given in Table 4.2.

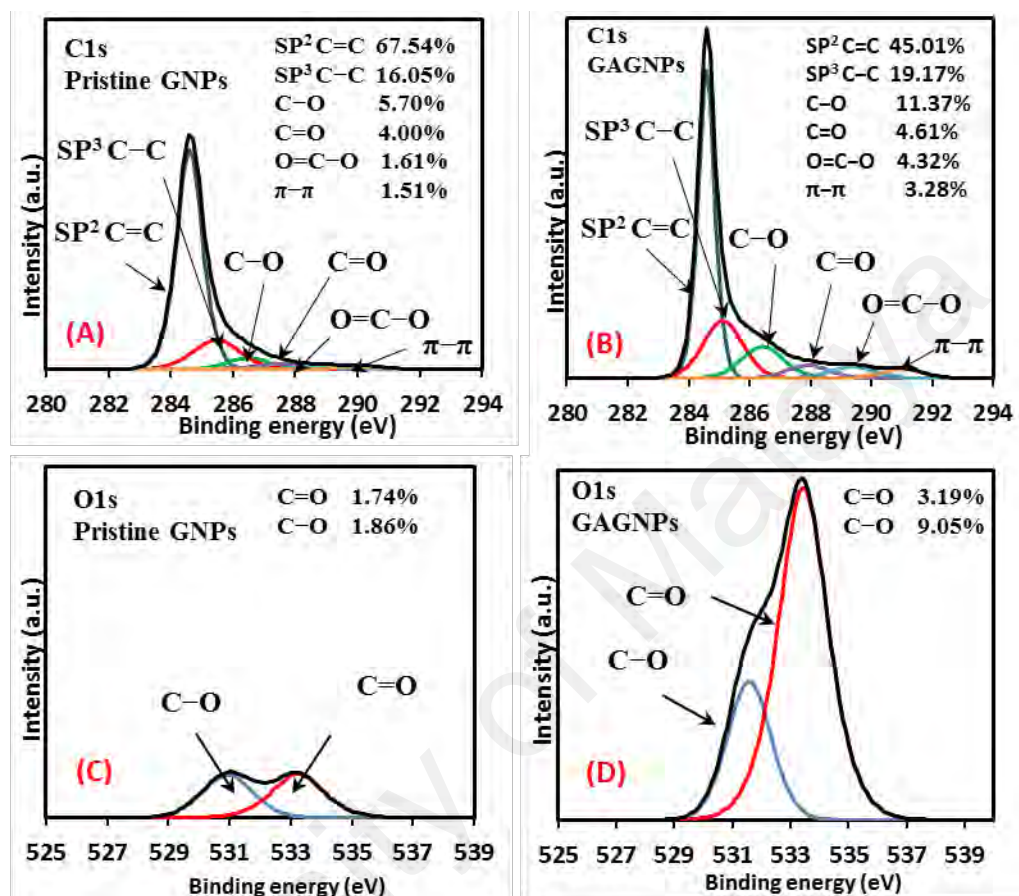


Figure 4.3: C1s XPS spectra for (A) pristine GNP and (B) GAGNP, and O1s XPS spectra for (C) pristine GNP and (D) GAGNP

Table 4.2: XPS analysis results for pristine GNPs and GAGNPs

Sample	Elemental composition (atom %)										
	Overall Percentage (atom %)		C1s							O1s	
	C1s	O1s	C=C	C-C	C-O	C=O	O-C=O	π-π	C-O	C=O	
GNPs	96.09	3.91	67.54	16.05	5.70	4.00	1.61	1.51	1.74	1.86	
GAGNPs	86.09	13.97	45.01	19.17	11.37	4.61	4.32	3.28	3.19	9.05	

The TEM images of the GAGNPs and pristine sample are shown in Figure 4.4, Fig. 4(a) is the pristine GNPs, which show flakes with fairly smooth surface and layer edge. The TEM image for the GAGNPs shown in Figure 4.4(b) shows surface deterioration and wrinkles of the GNPs that formed as a result of functionalization with GA. As it is clear from TEM images, the GAGNPs flakes preserved their size and shape compared with GNPs. The presence of wrinkles within the GAGNPs flakes can be ascribed to the inherent instability of the 2D structures and the improved flexibility of GNPs flakes after functionalization.

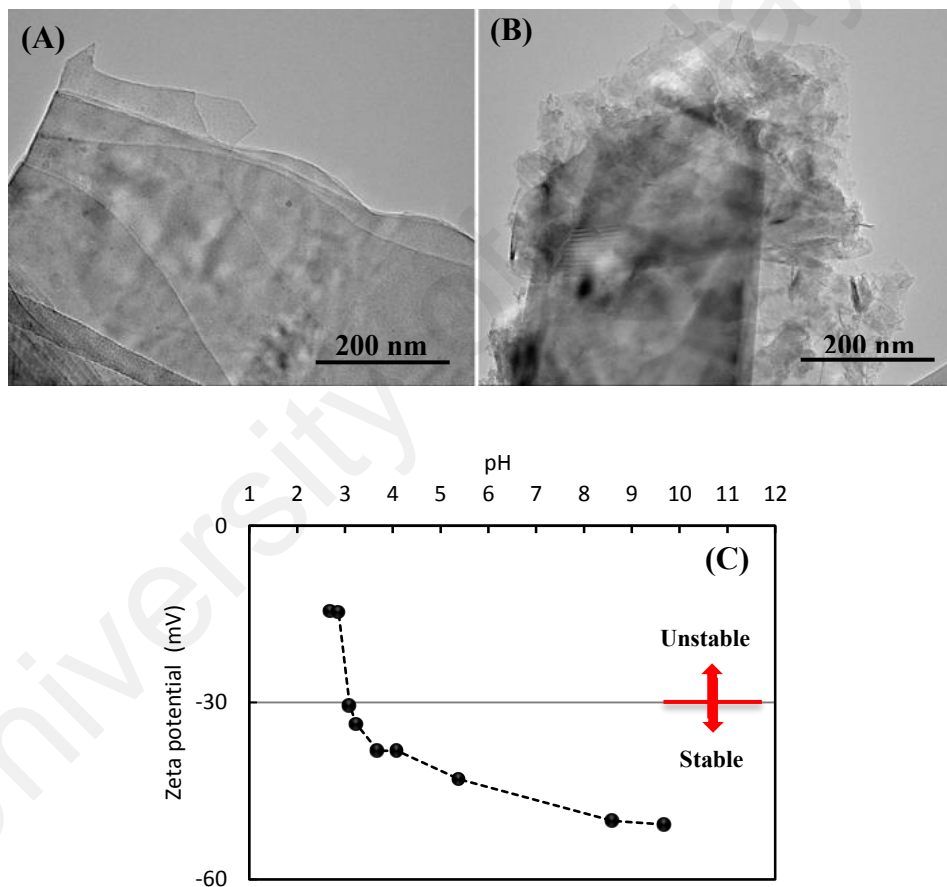


Figure 4.4: TEM images of (A) pristine and, (B) GA-treated GNPs nanoparticles and (C) zeta potential values of GAGNP-water nanofluid as a function of pH

Figure 4.4(C) shows the measured zeta potential values of the GAGNP-water nanofluid as a function of pH. It can be seen that the GAGNP-water nanofluid has high negative zeta potential values (-30.6 to -50.7 mV) within a pH of 3.10–9.69, which are far from the isoelectric point (*i.e.* point of zero charge). This indicates that the GAGNP-water nanofluid has strong electrostatic repulsion forces within this pH range and resists aggregation *via* non-covalent interactions such as π - π interactions or H-bonding. This property can be attributed to the oxygen functionalities at the surface of the GNPs. The GAGNP-water nanofluid is stable when the pH is more than 3.1. The zeta potential value of the nanofluid is around -30.6 mV at this pH. The results indicate that the GAGNP-water nanofluid is stable even in slightly acidic conditions. In highly acidic solutions (pH < 3.1), the GAGNP-water nanofluid tends to agglomerate and undergoes intermolecular dehydration catalyzed by H^+ , which leads to the coupling of GNPs *via* ether linkages. It can be clearly seen from Figure 4.4(C) that the GAGNP-water nanofluid becomes more stable upon the addition of alkali, which leads to the generation of additional negative charges in the nanoparticles.

UV-vis spectra analysis is a typical procedure used for investigating stability of nanoparticles aqueous suspensions. In accordance with the Beer–Lambert's law, there is a direct connection between the absorbance of a colloidal suspensions and the concentration of the absorbing species such as nanoparticles in the colloidal suspensions. Based on this Law, the absorption spectrum of the prepared nanofluids indicated a maximum peak at around 265 nm corresponding to $\pi - \pi$ transition of conjugation system in the polyaromatic structures.

The UV–vis spectroscopy analysis for the DI water-based GAGNPs nanofluids with different weight fractions were evaluated and the photometric analysis of the UV–vis spectroscopy was employed to pursue the variation of relative weight fraction of the samples versus times (day). The UV–vis spectrum for the water-based GAGNP

nanofluids with different weight concentrations are presented in Figure 4.5 (a). It shows that the peak values of absorbance for all the samples were located in the wavelength of 265 nm that is due to the presence of GAGNPs. Also it can be seen that the absorbance of GAGNPs nanofluids reduces from 0.1 to 0.025 wt.% that shows the enhancing amount of dispersed GAGNPs will increase the value of absorbance. As shown in Figure 4.5(b), there is a good linear relationship between the absorbance and the concentration of GNPs, which conforms to the Beer's law and shows that graphene sheets were dispersed well into the base fluid.

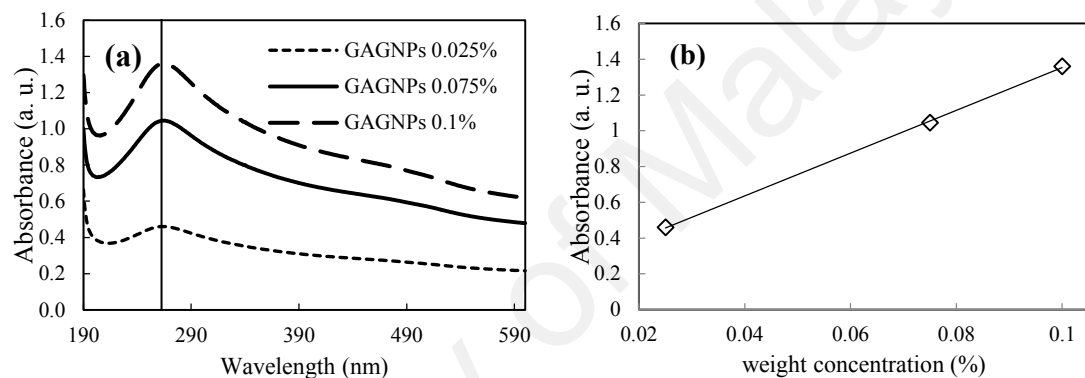


Figure 4.5: (a) UV-vis spectroscopy analyses of water-based GAGNPs aqueous nanofluids at various concentrations and wavelengths, (b) absorption values of GAGNPs dispersed in DI water at different concentrations

Figure 4.6 (A) illustrates the variation of stability of water-based GAGNPs nanofluids as a function of the number of the days after preparation. It is seen that the relative concentration of GAGNPs suspensions decreases with the number of days after sample preparation. However, the relative concentration of the nanofluids is almost constant after Day 50 for all samples. The highest sedimentation magnitude of 8, 9.47 and 10.7% are found, respectively, for the weight concentration of 0.025, 0.075 and 0.1%. This verifies the stability of the GAGNPs-water nano-coolants. Digital image of gallic acid-functionalized GNPs (GAGNPs) dispersed in DI water after 90 days, is represented in Figure 4.6(B).

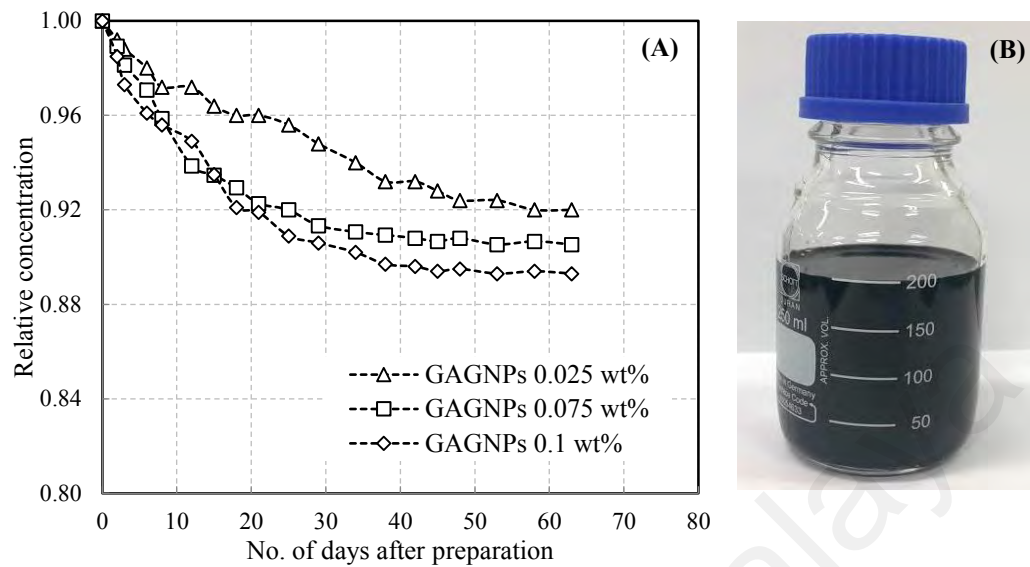


Figure 4.6: (A) The colloidal stability of GA-functionalized GNPs dispersed in water, (B) photograph of GA-treated GNPs dispersed in water after 3 months

4.2 Thermo-physical properties of GAGNPs nanofluids

The thermal conductivity of gallic acid-treated graphene nanoplatelets (GAGNPs) nanofluids was measured experimentally and the results are presented in Figure 4.7. Three different concentrations of 0.025, 0.075 and 0.1 wt%, and a range of temperatures from 20 to 45 °C are considered and variations of thermal conductivity with temperature and concentration are studied. To prevent a drastic increase in viscosity, nanofluids with low concentrations of GA-GNPs are selected. The thermal conductivity of the base fluid is also shown in the Figure 4.7 for comparison. It is seen that the experimental values of thermal conductivity for DI water shows good agreement with the NIST database (Ramires et al., 1995) with an error less than 1%. Moreover, the thermal conductivity of the GAGNPs-water nanofluids is markedly higher than that of the DI water. In addition, Figure 4.7 clearly shows that the thermal conductivity of GAGNPs nanofluids as well as DI water increases with the fluid temperature. However, the rate of increase is noticeably higher for the GAGNPs nanofluids at higher solid concentrations. The main

mechanism for the enhancement of thermal conductivity with increase of temperature is attributed to the Brownian motion of the nanoparticles suspended in the base-fluid (S. J. Aravind et al., 2011). In addition, the formation of nanolayers in nanofluids is a significant mechanism for enhancing the thermal conductivity of GAGNPs nanofluids. These layers are generated around the GAGNPs by liquid molecules and the local ordering of the liquid layers increases at the interface region. These liquid layers have greater thermal conductivity than the base fluid (S. J. Aravind et al., 2011). The higher slope in thermal conductivity of GAGNPs nanofluids with concentrations of 0.1 and 0.075 wt% reveals the greater rate of generation of the nanolayers.

The percentage of thermal conductivity enhancement was computed using $[(k_{nf} - k_{bf}) * 100]/k_{bf}$, where “ k_{nf} ” corresponds to thermal conductivity of nanofluids and “ k_{bf} ” that of base fluid. Over the range of temperatures tested, the maximum enhancement in thermal conductivity for concentrations of 0.025, 0.075 and 0.1 wt.% are, respectively, about 6.28, 16.64, and 24.18% at 45 °C.

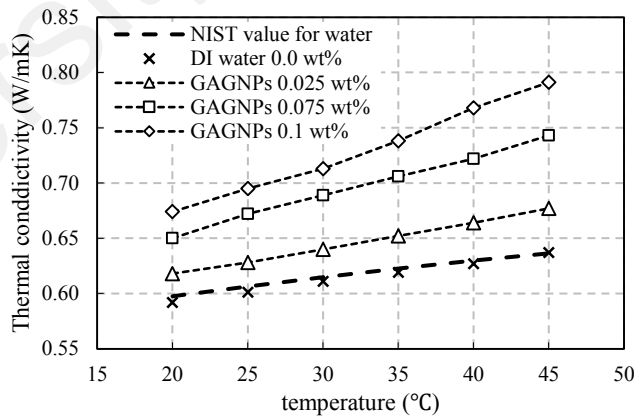


Figure 4.7: Thermal conductivity of GA-treated GNPs aqueous suspensions and DI water

The effective viscosity of gallic acid-functionalized graphene nanoplatelets (GAGNPs) aqueous suspensions and DI water was experimentally measured at a shear rate of 150 s^{-1} and the results are shown in Figure 4.8 for temperature range of 20–50°C.

This figure shows rather small increment in the measured viscosity of nanofluid with an increase in concentration of GAGNPs compared to that of the DI water. This is indeed expected since a low concentration of GAGNPs is used in our samples. This also shows the benefit of covalent functionalization using Gallic acid since the GAGNPs remain suspended in the DI water. In agreement with the earlier studies of Sadri et al. (Sadri, Hosseini, Kazi, Bagheri, Zubir, Solangi, et al., 2017) and Aravind et al. (S. J. Aravind et al., 2011), Figure 4.8 shows that the viscosity of nanofluids and DI water decreases with an increase in temperature, which is due to the weakening of the intermolecular forces. The rather mild increase in the effective viscosity with nanoparticle concentration is an important advantage, since a high increase in viscosity could undermine the overall positive impact of enhanced heat transfer due to the pumping fluid penalty (Timofeeva, Routbort, & Singh, 2009; W Yu, France, Timofeeva, Singh, & Routbort, 2010).

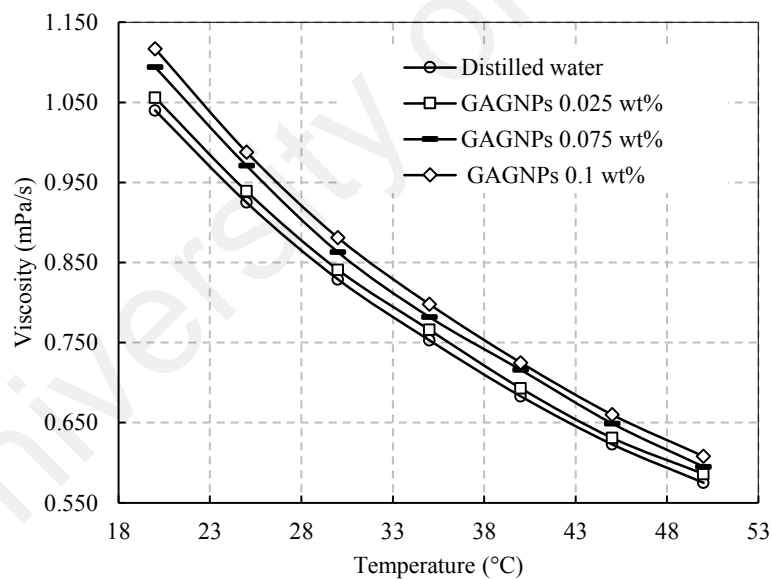


Figure 4.8: Dynamic viscosity of GA-treated GNPs nanofluids and DI water as a function of temperature and weight concentration for shear rate of 150 s^{-1}

The experimentally measured values of dynamic viscosity for the water-based GAGNPs suspension were compared with those calculated with the empirical correlations of Batchelor (Khanafer & Vafai, 2011) and Einstein (J.-H. Lee et al., 2008) using Equations (4.1) and (4.2), respectively, and the results are depicted in the Figure

4.9. This indicates that the values calculated from experimental data are in good agreement with those determined from empirical correlations for water-based GAGNPs nanofluid with a maximum error of ~7%.

$$\text{Batchelor model, } \frac{\mu_{nf}}{\mu_{bf}} = 1 + 2.5\varphi + 6.5\varphi^2 \quad (4.1)$$

$$\text{Einstein model, } \frac{\mu_{nf}}{\mu_{bf}} = 1 + 2.5\varphi \quad (4.2)$$

Where μ_{nf} is the viscosity of the nanofluid, μ_{bf} is the viscosity of the base fluid and φ is the volume fraction of the nanoparticles.

It is crucial to keep down the increment in viscosity of the heat transfer working fluids by using an appropriate synthesis method and considering low weight concentrations for the nano-coolants, particularly in heat transfer systems, in where the overall positive impact in heat transfer is being undermined by pumping fluid penalty occurs with an increase in viscosity (Timofeeva et al., 2009; W Yu et al., 2010). Hence, in order to maximize the heat transfer performance of closed-loop systems in which nanofluids are used as the working fluids, it is imperative to maintain the resultant colloidal mixtures in Newtonian behavior since this will reduce the pumping power compared to non-Newtonian fluids.

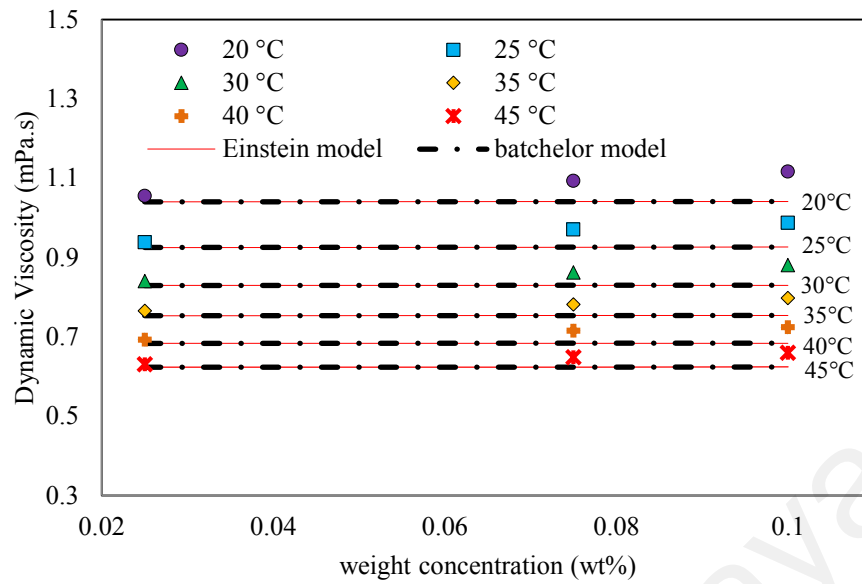


Figure 4.9: Dynamic Viscosity of water-based GAGNPs nanofluids in comparison with those calculated with Batchelor and Einstein model as functions of concentration and temperature

The Figure 4.10 represented the dynamic viscosity of nano-coolants as functions of shear rate, temperature and weight concentration. As shown in Figures 6(c–e), the behavior of synthesized water-based GAGNPs nanofluids in this research are quite Newtonian, whereby the viscosity of the nanofluids remains constant with an increase in the shear rate. The amount of variation in dynamic viscosity with increasing the weight concentration is insignificant and negligible. From a thermal transport perspective, this material is deemed suitable as an additive to enhance heat transfer performance.

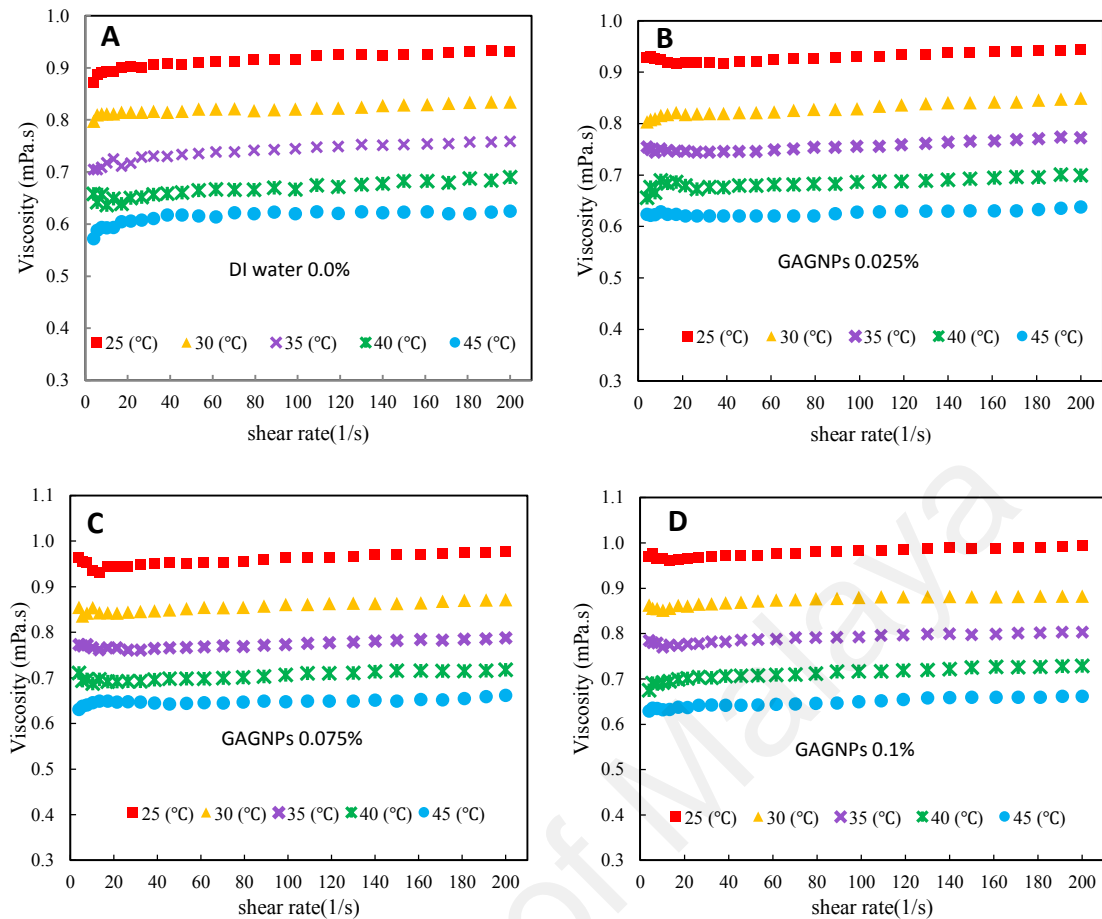


Figure 4.10: Plots of the measured values of dynamic viscosity versus shear rate for GAGNPs aqueous nanofluids at various temperatures and weight concentrations ((A) DI water,(B) 0.025 wt%,(C) 0.075 wt% and (D) 0.1 wt %)

The density of the GA-treated GNPs aqueous suspensions and the DI water as the base fluid is also measured experimentally as a function of mass fraction and temperature and the results are listed in Table 4.3. It can be seen that the density of GAGNPs nanofluids as well as the base fluid reduces with an increase in temperature, which is related to the thermal expansion of liquid. For example, the density of the DI-water and GAGNPs aqueous suspensions at mass concentration of 0.1% decreases by 0.6%, when the temperature increases from 20 to 40 °C, respectively.

There is also a negligible increment in the density of GAGNPs aqueous suspensions when the weight concentration of GAGNPs increases. The higher density of nanofluids can be attributed to the density of GAGNPs which is higher than that of the base fluid.

Table 4.3: Density of GA-treated GNPs and DI water as a function of temperature and concentration

Concentration/temperature (°C)	Density (kg/m ³)				
	20	25	30	35	40
DI water	998.00	996.85	995.50	993.90	992.00
0.025 wt%	998.10	997.00	995.65	994.05	992.10
0.075 wt%	998.40	997.25	995.90	994.35	992.35
0.1 wt%	998.55	997.30	996.00	994.45	992.50

The specific heat capacity of the GAGNP aqueous nano-coolants and DI water are also presented in Figure 4.11. It is apparent that the specific heat capacity increases slightly when the temperature is increased for all samples. The slope is similar for the specific heat capacity curves, which agrees well with the findings of Pak and Cho (Amiri, Sadri, Shanbedi, Ahmadi, Kazi, et al., 2015; Pak & Cho, 1998). It can be seen that the specific heat capacity of the GAGNPs aqueous nanofluids decreases insignificantly with an increase in the GAGNPs mass fraction, whereby the average reduction in specific heat capacity is within a range of 0.5–1.88% compared to that of the DI water. This decrease is due to the fact that the CGNPs nanoparticles have a lower specific heat capacity than that of the base fluid.

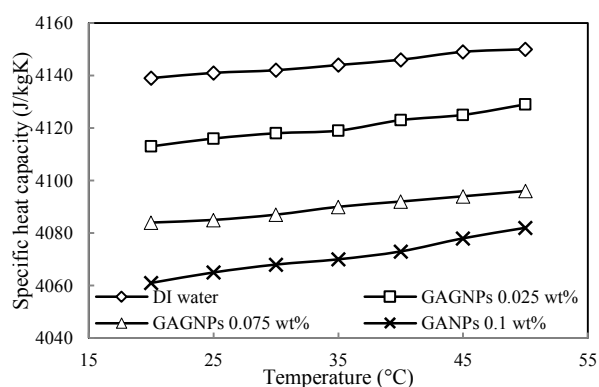


Figure 4.11: Variation of Specific heat capacity of Gallic acid-treated GNPs aqueous suspensions versus temperature at different weight concentrations

4.3 Heat transfer and hydrodynamic properties

4.3.1 Validation of the experimental results

In order to validate the reliability and accuracy of our closed conduit heat transfer system, a series of experiments are performed using DI water at constant heat flux boundary conditions prior to running the experiments using GAGNP-water nanofluids. The local Nu is determined using Eq. 3.3 based on our experimental data. The local Nu is plotted versus the axial distance of the horizontal stainless steel tube for various Re, as shown in Figure 4.12 (a). The fully developed thermal entry length for turbulent flows is given by $x > 10 D$ (E. B. Haghghi et al., 2014). It is seen from Figure 4.12 (a) that the local Nu is practically invariant for the fully developed thermal boundary layer region at various points along the closed conduit, which is in line with the theory described by Cengel (Cengel, 2003). This can be explained by considering the constant heat flux boundary condition and fully developed thermal boundary layer. In general, the temperature gradient is invariant along the axial distance, which results in a relatively constant local heat transfer coefficient and consequently, constant local Nu. Besides, the average Nu is plotted as (Figure 4.12 (b)) and compared with the values determined from empirical correlations proposed by Gnielinski (Volker Gnielinski, 1975), Petukhov (Petukhov, 1970) and Dittus-Boelter (Duangthongsuk & Wongwises, 2008). These empirical correlations are given by Equations (3.5), (3.6) and (3.7), and are applicable for turbulent flow. It is apparent from Figure 4.12 (b) that the Nu increases with an increase in Re. More importantly, the Nu values determined from experiments show good agreement with those calculated from empirical correlations. The average error between the experimental values and the values determined from Gnielinski's (Volker Gnielinski, 1975), Petukhov's (Petukhov, 1970) and Dittus-Boelter's (Duangthongsuk & Wongwises, 2008) empirical correlation is 7.11, 2.01 and 7.96%, respectively. Hence, it can be deduced that the experimental results conform

well to those from empirical correlations for the range of Re investigated in this study, indicating the reliability of our experimental set-up for heat transfer measurements. Hence, our experimental set-up can be employed to assess the heat transfer properties of the GAGNP-water nanofluids. In order to determine the pressure drop in the test section, the friction factor for the DI water is calculated using Eq.3.9 and compared with those determined from Petukhov's (Petukhov, 1970) and Blasius's (Blasius, 1907) empirical correlation given by Equation (3.8) and (3.10), respectively. The friction factor results are presented in Figure 4.12 (a). Our results are indeed encouraging since the maximum difference in the friction factor between experiments and those obtained from Petukhov's (Petukhov, 1970) and Blasius's (Blasius, 1907) empirical correlation is Eqs. 3.8 and 3.10, respectively. The maximum difference is small (less than 5%), which indicates that our experimental set-up is reliable to measure the pressure drop over the range of Re investigated in this research.

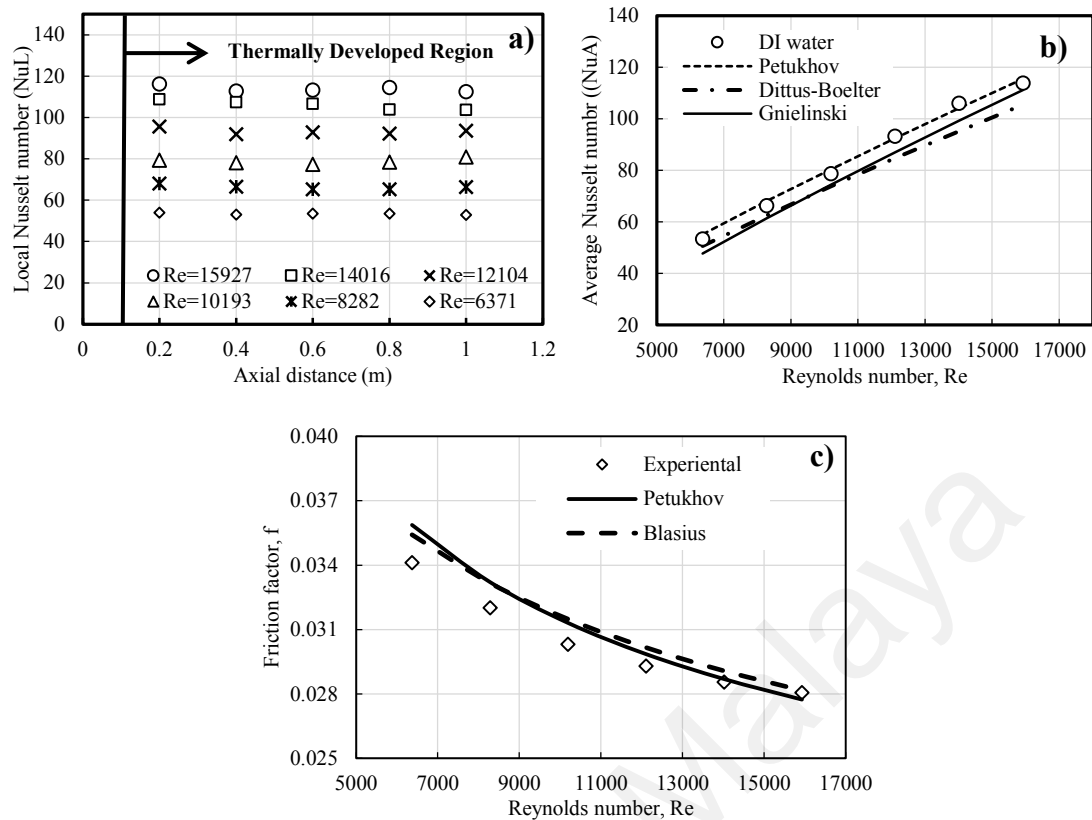


Figure 4.12: (a) Variation of local Nusselt number versus the conduit axial distance for DI water. (b) Comparison of measured Nusselt number of DI water with the empirical correlations. (c) Comparison of the measured friction factors for DI water with the empirical

4.3.2 GA-treated GNPs aqueous suspensions

To study the convective heat transfer of the nanofluids under turbulent flow regime, a series of experiments are performed for various weight concentrations of the GA-treated GNPs for different flow Reynolds numbers. The variations of the convective heat transfer coefficient as a function of Reynolds number for various concentrations of GA-GNPs are shown in Figure 4.13 (A) for the constant inlet temperature of 30°C. It is seen that the convective heat transfer coefficient of the nanofluids as well as base fluid, increases with the Reynolds number. Also it is clear that increase of nanoparticles concentration has a direct effect on heat transfer coefficient of aqueous suspensions. The significant improvement in convective heat transfer coefficient of GA-GNPs nanofluids was largely attributed to the thin thermal boundary layer at higher Reynolds number as a result of the enhancement of the thermal conductivity of nanofluids, and

the reduced thermal resistance between the inner wall surface of the tube and flowing nanofluids. Based on (S. J. Aravind et al., 2011; Yulong Ding et al., 2006), carbon nanostructures such as GNPs and CNTs have a trend to reduce the thickness of thermal boundary layer. In addition, improvement of convective heat transfer coefficient is strongly dependent on the specific surface area, Brownian motion of the nanoparticles. The presented data shows that the convective heat transfer coefficient increases by 9.89 %, 28.38% and 38.58%, respectively, for the nanoparticle weight concentrations of 0.025, 0.075 and 0.1wt.%. The average of experimental Nusselt numbers are evaluated from Eq. (3.3) and the data are plotted in Figure 4.13(B). It is seen that the Nusselt number increases markedly with an increase in Reynolds number and also with the increase in nanoparticles concentration. The higher Nusselt number for the GA-treated GNPs aqueous suspensions is attributed to the large surface area, Brownian motion and thermophysical properties of suspended nanoparticles and therefore the heat transport capability of nanofluid elevates further (Sundar et al., 2014). Also, it may be devoted to properties of nanofluid suspension in terms of lower specific heat and higher thermal conductivity compared to that of water. The maximum enhancement of Nusselt number for nanoparticle concentrations of 0.025, 0.075 and 0.1 wt.% are, respectively, 4.91, 13.85 and 18.75% for Reynolds number $Re=15925\pm 5$.

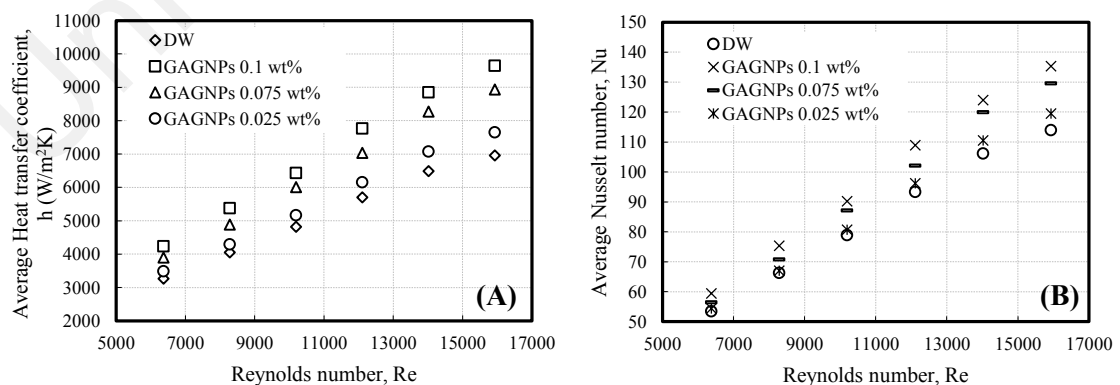


Figure 4.13: Variations of (A) average heat transfer coefficient and (B) Nusselt number of GA-treated GNPs aqueous suspensions as a function of Reynolds number at various concentrations

The pressure drop of the GAGNPs aqueous suspensions and DI water flowing through the experimental test section over a range of Reynolds number represented in Figure 4.14(A). The corresponding friction factor data were measured applying Eq. (3.9) and the results are shown in Figure 4.14(B). The data indicates that there is a slight enhancement with concentration in both friction factor and pressure drop for the GAGNPs aqueous suspensions compared to those for DI water. But the overall penalty in the friction factor is negligible. It is seen that the friction factor for GAGNP nanofluids show slight increase compared to that of DI water. The maximum increase in the friction factor of nanofluids for weight concentration of 0.025, 0.075 and 0.1% is, respectively, about 1.46, 3.35 and 3.9%. The enhancement in friction factor is largely attributed to the increase in the viscosity of nano-coolants. Note that for a constant Reynolds number, an increase in viscosity requires a small increase in fluid velocity. Therefore, the increase in the velocity of working fluid can be considered as the reason for increase of the friction factor of the nano-coolants in convective heat transfer systems.

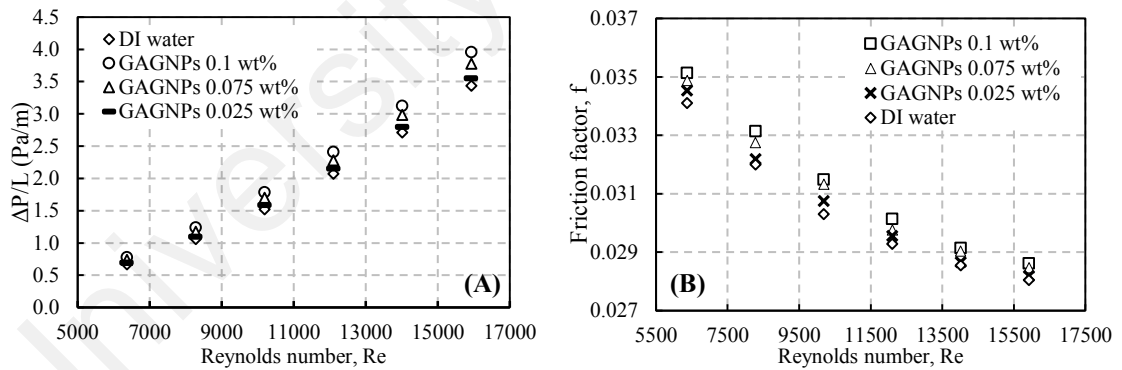


Figure 4.14: Variation of pressure drop (A) and friction factor of GA-treated GNPs (B) as a function of Reynolds number for various concentrations

The power consumption of a heat transfer set-up is a significant parameter in terms of economy and energy saving in various thermal applications. The pumping power for turbulent flow regime can be measured using following Equation (Mansour, Galanis, & Nguyen, 2007) :

$$\dot{W} = 0.158 \left(\frac{4}{\pi} \right)^{1.74} \left(\frac{L \dot{m}^{2.75} \mu^{0.25}}{\rho^2 D^{4.75}} \right) \quad (4.3)$$

Where, \dot{m} is mass flow rate. Using $\rho = \frac{\dot{m}}{\dot{V}}$ and $v = \frac{\dot{V}}{A}$ for a fixed $Re = \frac{\rho v D}{\mu}$ and substituting \dot{m} into the Eq. (4.3), the relative pumping power $\left(\frac{\dot{W}_{nf}}{\dot{W}_{bf}}\right)$ for constant Reynolds number is given as,

$$\frac{\dot{W}_{nf}}{\dot{W}_{bf}} = \left(\frac{\rho_{bf}}{\rho_{nf}}\right)^2 \left(\frac{\mu_{nf}}{\mu_{bf}}\right)^3 \quad (4.4)$$

Where \dot{W}_{bf} and \dot{W}_{nf} is the pumping power of the base fluid and GAGNP nano-coolants, respectively. The relative pumping power of the GAGNP nano-coolants is calculated employing the equation (4.4) and the results are presented in Figure 4.15 for various weight concentrations. This figure shows that the pumping power required for the nano-coolants with various GAGNPs nanoparticles loading is quite close to that of DI water.

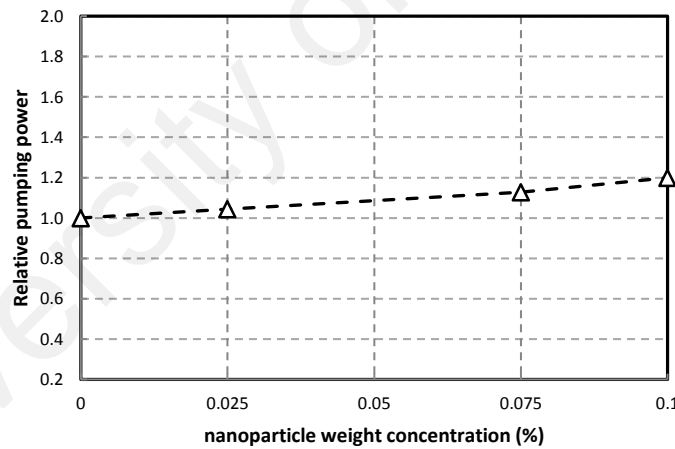


Figure 4.15: Relative pumping power of the GAGNP-water nanofluids and distilled water

To assess the economic performance of a new working fluid (GAGNPs) as a suitable alternative candidate for use in heat transfer equipment such as car radiators, heat exchangers and solar collectors, the performance index parameter (ε) is evaluated. The performance index is described as the ratio of the enhancement in convective heat

transfer coefficient (desired efficiency) to the enhancement in pressure drop (unpleasant efficiency) of nanofluid relative to the base fluid. The performance index is given as:

$$\varepsilon = \frac{h_{nf}/h_{bf}}{\Delta P_{nf}/\Delta P_{bf}} = \frac{R_h}{R_{\Delta P}} \quad (4.5)$$

Here, R_h is the ratio of the convective heat transfer enhancement, and $R_{\Delta P}$ is the ratio of pressure drop. The performance index of GAGNPs aqueous suspensions is determined for a range of Reynolds number and concentration and the results are presented in Figure 4.16. It is seen that the performance index for all concentrations is higher than 1. This shows the advantage of the new synthesized nanofluids for use in the heat transfer equipment. Figure 4.16 also indicates that as the weight concentration of the GAGNPs in base fluid increases, the performance index also increases, which is the proof of higher effectiveness of this new coolant at higher concentration. In addition, The Figure 4.16b shows a rising trend of performance index with Reynolds number for all concentrations. Thus, the results indicate that the GAGNPs nano-coolants could be as an appropriate alternative coolant for use in heat transfer applications for a range of Re.

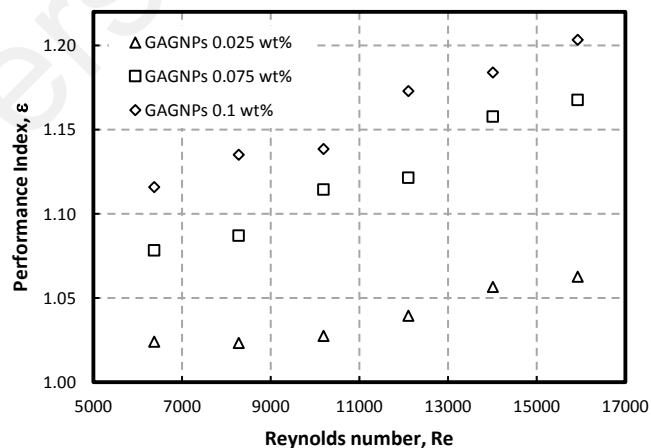


Figure 4.16: The performance index of the GA-treated GNPs versus Reynolds number at different concentrations

CHAPTER 5: CHARACTERIZATION, THERMO-PHYSICAL PROPERTIES, CONVECTIVE HEAT TRANSFER AND HYDRODYNAMIC PROPERTIES OF WATER-BASED CLOVE-TREATED GRAPHENE NANOPATELET NANO-COOLANT

5.1 Characterization of Clove functionalized GNPs

Figure 5.1(A) shows the FTIR spectra for the pristine GNPs and CGNPs, which are represented by the transmittance (%) *versus* the wavenumber (cm^{-1}). It can be observed from Figure 5.1 (A) that there are noticeable cues of the eugenol molecule in the CGNPs compared to the pristine GNPs. The broad peak at 3436.92 cm^{-1} is ascribed to O–H stretching vibrations, which may be caused by the reaction between the GNPs and hydroxyl groups of eugenol and/or hydrogen peroxide. The symmetric and asymmetric sharp vibrations of C–H bonds are observed within a wavenumber range of $2849.68\text{--}2917.09 \text{ cm}^{-1}$ for both GNPs and CGNPs.

A couple of peaks are observed within the wavenumber range of 1577.58 cm^{-1} , which arise from C=C stretching vibrations of GNPs after opening due to the addition of electrophilic reactions between the main structure of GNPs and the –OH band of eugenol. The functionalization of GNPs by eugenol is confirmed by the peaks at 1384.56 , and 1178 cm^{-1} , which are out-of-plane CH vibrations and C–O stretching vibrations, respectively. The peaks within the wavenumber range of 1715.75cm^{-1} and the peak centred at 1631 cm^{-1} are assigned to O–C=O stretching vibrations, indicating the formation of carboxyl groups at the main structure of GNPs.

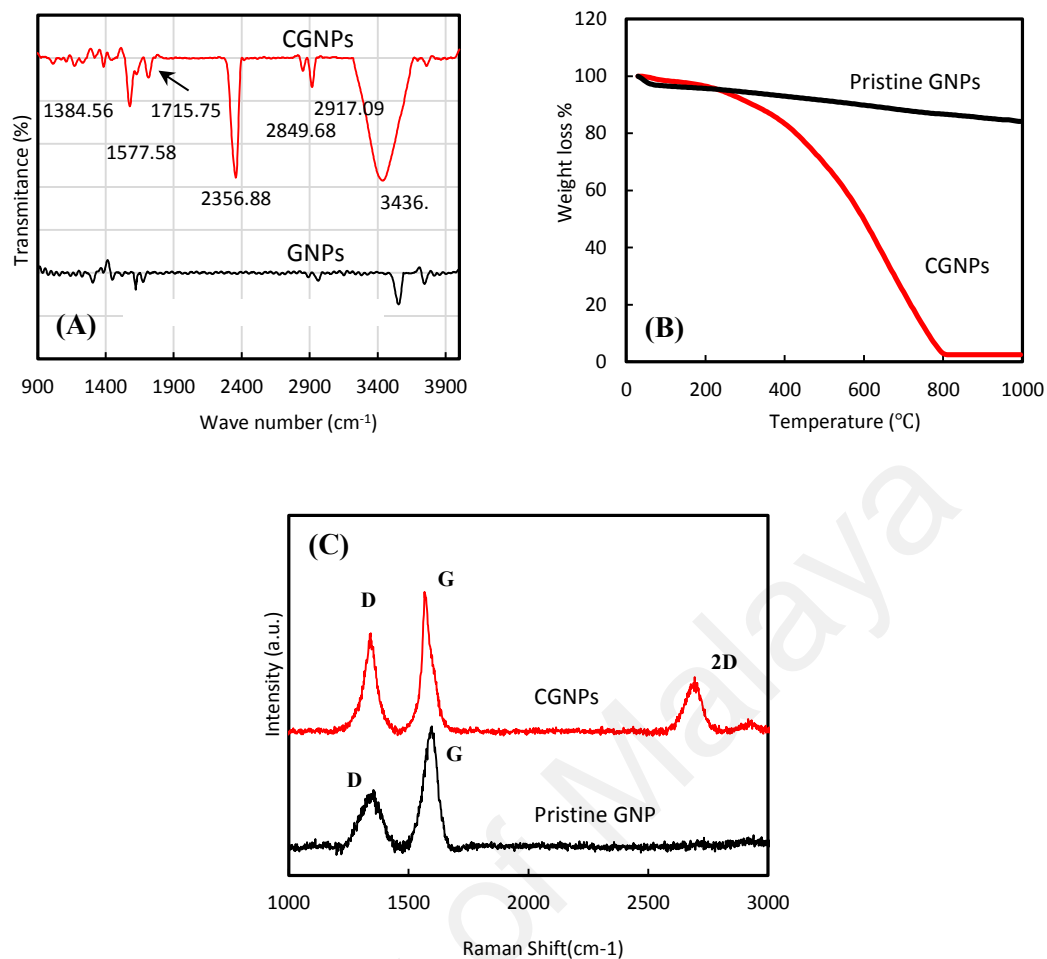


Figure 5.1: (A) FTIR spectra of pristine GNPs and C-GNPs, (B) TGA curves, and (C) Raman spectra of pristine GNPs and CGNPs

TGA provides information about the quantitative amount of each functional groups on the surface of GNPs, which were used to characterize the pristine GNPs and CGNPs. Figure 5.1(B) shows the TGA curves for pristine GNPs and CGNPs and it can be observed that there was feeble weight loss in the raw GNPs up to the temperature of ~800°C, which is the temperature at which the main graphitic structures began to decompose. However, there was a significant weight loss for the CGNPs, which confirms the decomposition of the functional groups. There are two distinctive steps of weight loss for the clove-treated GNPs within a temperature range of 0–800°C. The first weight loss occurred at ~100°C, which was attributed to water whereas the second weight loss happened between 160 and 800°C, which is due to the decomposition of the

functional group (*i.e.* eugenol) and the degradation of the graphitic structures in air (after 600°C). The results indicate the successful covalent functionalization of GNPs with eugenol, which is evidenced by the gradual weight loss observed in the TGA curve of CGNPs.

Raman spectroscopy provides fundamental information for us to examine the structure of sp^2 and sp^3 hybridized carbon atoms in carbon-based materials and therefore, Raman spectroscopy was chosen as the first characterization technique. In addition, Raman spectroscopy elicits essential information on the covalent functionalization of GNPs by following the variations in holes. Figure 5.1(C) shows the Raman spectra of the MWCNT and CGNPs. The enhancement in the Raman intensity ratio (I_D/I_G) indicates a change in hybridized carbon from sp^2 to sp^3 , which is a direct evidence of covalent functionalization (R. Das et al., 2015). The pristine GNPs have an I_D/I_G ratio of 0.57 whereas the CGNPs have an I_D/I_G ratio of 0.85. The larger I_D/I_G ratio obtained for the CGNPs indicates the presence of a higher number of sp^3 carbons and the occurrence of an electrophilic addition reaction, which confirms the successful covalent functionalization of GNPs. Raman spectra analysis data are presented in Table 5.1.

Table 5.1: Raman spectra analysis results for pristine and clove-treated GNPs

Sample	Peaks	Centre (cm ⁻¹)	Intensity (a.u.)	I_D/I_G
GNPs	D band	1353.94	593.47	0.57
	G band	1597.43	1036.38	
CGNPs	D band	1341.82	1682.44	0.85
	G band	1566.24	1970.01	

The elemental composition of the surface of the GNPs is examined before and after functionalization using XPS. Each peak was fitted to the binding energy of standard

carbon, *i.e.* 284.6 eV. It can be observed from the wide-scan XPS spectra for GNPs and CGNPs (Figure 5.2) that the C1s and O1s peaks are centred at ~284.6 and 532.8 eV, respectively. Unlike GNPs, the CGNPs have a higher O1s peak intensity since the oxygen-to-carbon (O/C) ratio increases from 0.029 (GNPs) to 0.247 (CGNPs). This proves the prospering oxidizing amorphous carbon impurities and free radical grafting of different oxygen functional groups onto the CGNPs. It is very likely that the oxygenated groups such as C–O (in hydroxyl and epoxy), C=O (in carbonyl derivatives) and COO (in carboxylic acids) are attached to the edge and surface of the GNPs after functionalization. The curve fitting of the high-resolution C1s and O1s spectra is performed in order to assess the contributions of these groups. Figure 5.2(b) and (c) shows the high-resolution XPS spectra of the C1s deconvoluted peak components for GNPs and CGNPs, respectively. Our results confirm the presence of sp²-hybridized graphitic structure (C=C) at 284.6 eV, aliphatic group (C–C) at 285.39 eV, hydroxyl and epoxy groups (C–O) at 286.27 eV, carbonyl group (C=O) at 287.61 eV, carboxyl group (O–C=O) at 289.02 eV as well as π - π interaction bonds at 290.13 eV. After oxidative treatment, the intensity of the C–O, C=O and O–C=O bonds increases from 5.75, 4.04 and 1.62% (pristine GNPs) to 13.04, 5.95 and 4.7% (CGNPs), respectively, while the π - π interaction bonds vanish completely. The higher peak intensities at 530.7 and 533 eV in the O1s spectrum (Figures 5.2 (d) and (e)) confirm the presence of large fractions of oxygen atoms in the form of C=O and C–O functional groups in the CGNPs. In contrast, the pristine GNPs show the presence of feeble and generic functional groups such as C–O and C=O (R. Das et al., 2015). These functional groups were generated unintentionally when the GNPs were exposed to the environment containing natural oxidizing agents such as ozone and hydroxyl radicals. The results of the XPS analysis are summarized in Table 5.2.

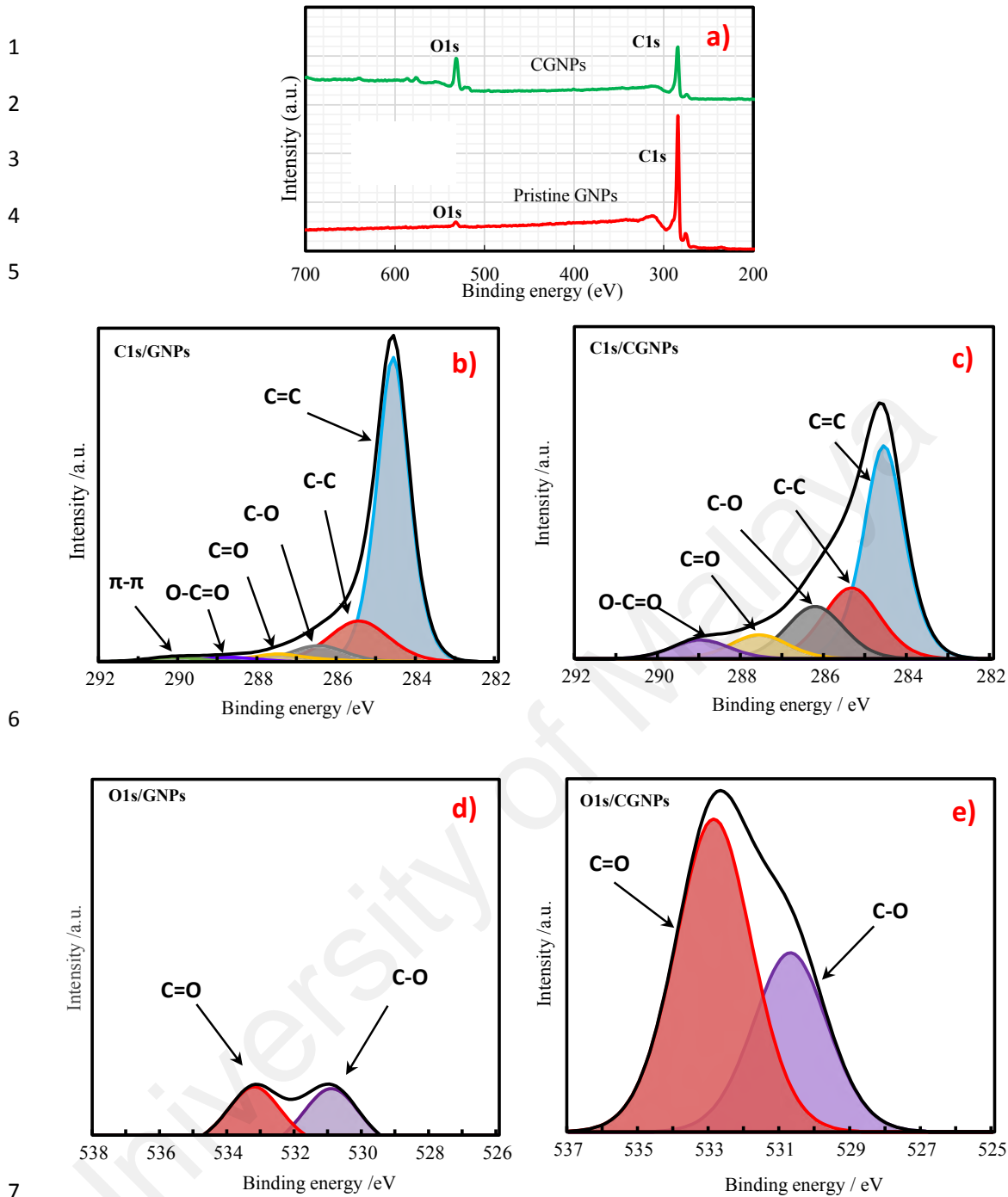


Figure 5.2: (a) Wide-scan XPS spectra for the GNPs and CGNPs; High-resolution XPS spectra of the deconvoluted peak components for C1s: (b) GNPs, (c) CGNPs; High-resolution XPS spectra of the deconvoluted peak components for O1s: (d) GNPs, (e) CGNPs

Table 5.2: XPS analysis results for GNPs and CGNPs

Sample	Elemental composition (atom %)									
	Overall percentage (atom %)		C1s						O1s	
	C1s	O1s	C = C	C - C	C - O	C = O	O - C = O	$\pi - \pi$	C - O	C = O
GNPs	97.09	2.91	68.15	16.19	5.75	4.04	1.62	1.52	1.32	1.41
CGNPs	80.15	19.85	39.63	17.63	13.04	5.95	4.7	0	6.84	12.21

Even though TEM highlights the surface deterioration (morphology) and wrinkling of GNPs, this technique does not provide any information on the functional groups. Figure 5.3(a) and (b) shows the TEM image of the GNPs and CGNPs, respectively. It can be observed from Figure 5.3(a) that the GNPs have a multi-layered structure with relatively smooth surface and edges (low edge defects) as well as higher presence of aggregation. In contrast, the surface of the CGNPs appears very rough with higher defects and wrinkles resulting from covalent functionalization. We attribute the presence of wrinkles and lines on the surface of the CGNPs to the inherent instability of the two-dimensional structures as well as improved flexibility of the GNPs after covalent functionalization with cloves.

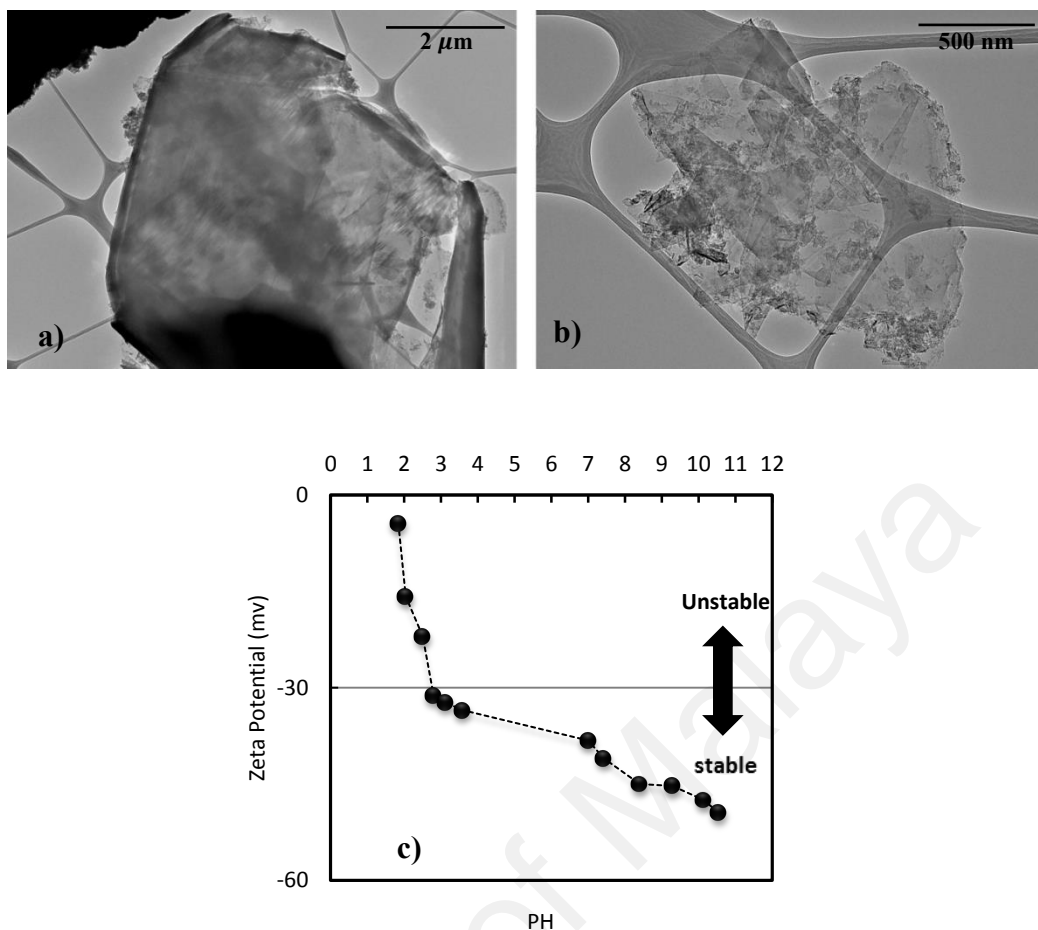


Figure 5.3: (a) TEM image of (a) pristine GNPs, (b) Clove-functionalized GNPs and (c) zeta potential values of the CGNP nanofluid as a function of PH

Figure 5.3(C) shows the measured zeta potential values as a function of pH for the CGNP aqueous suspension. It can be observed that the CGNP nanofluid has high negative values (-4.42 mV to -49.5 mV) within the pH variations from 1.84 to 10.55. More importantly, the zeta potential values for the CGNP nanofluids are far from the isoelectric point (*i.e.* point of zero charge), which indicates that this pH range (2.8–10.55) results in strong electric repulsion forces between the particles of CGNPs. This prevents aggregation of the CGNPs by non-covalent interactions such as π - π interactions or H-bonding. This phenomenon is attributed to the oxygen functionalities at the surface of the CGNPs. Hence, the CGNP aqueous suspension is stable when the pH is more than 2.8 (where the corresponding zeta potential is around -30.6 mV). In

this study it could be highlighted that the CGNP aqueous suspension is stable even in weak acidic conditions. In strong acidic solutions ($\text{pH} < 2.8$), the material tends to agglomerate and undergo intermolecular dehydration catalyzed by H^+ , leading to the coupling of CGNPs via ether linkages. It was identified that the CGNP nanofluid became more stable by adding alkali to the aqueous suspension, which lead to the generation of additional negatively charged in the nanoparticles.

UV-vis spectroscopy analysis is a common procedure used for evaluating stability of colloidal nanoparticles. Based on the Beer–Lambert’s law, there is a direct connection between the absorbance of a solution and the concentration of the absorbing species such as nanoparticles in the solution. Following this law, the absorption spectrum of the prepared nanofluids exhibited a maximum peak at around 265 nm corresponding to $\pi - \pi$ transition of conjugation system in the polyaromatic structures.

The UV–vis spectroscopy analysis for the DI water-based CGNPs nanofluids with different weight fractions were evaluated and the photometric analysis of the UV–vis spectroscopy was employed to pursue the variation of relative weight fraction of the samples versus times (day). The UV–vis spectrum for the water-based CGNPs nanofluids with different weight concentrations are presented in Figure 5.4 (a). It shows that the peak values of absorbance for all the samples were located in the wavelength of 265 nm that is due to the presence of CGNPs. Also it can be seen that the absorbance of CGNPs nanofluids declines from 0.1 to 0.025 wt.% that proves the enhancing amount of dispersed CGNPs will increase the value of absorbance. As shown in Figure 5.4(b), there is a good linear relationship between the concentration of GNPs and the absorbance, which conforms to the Beer's law and shows that graphene sheets were dispersed well into the base fluid.

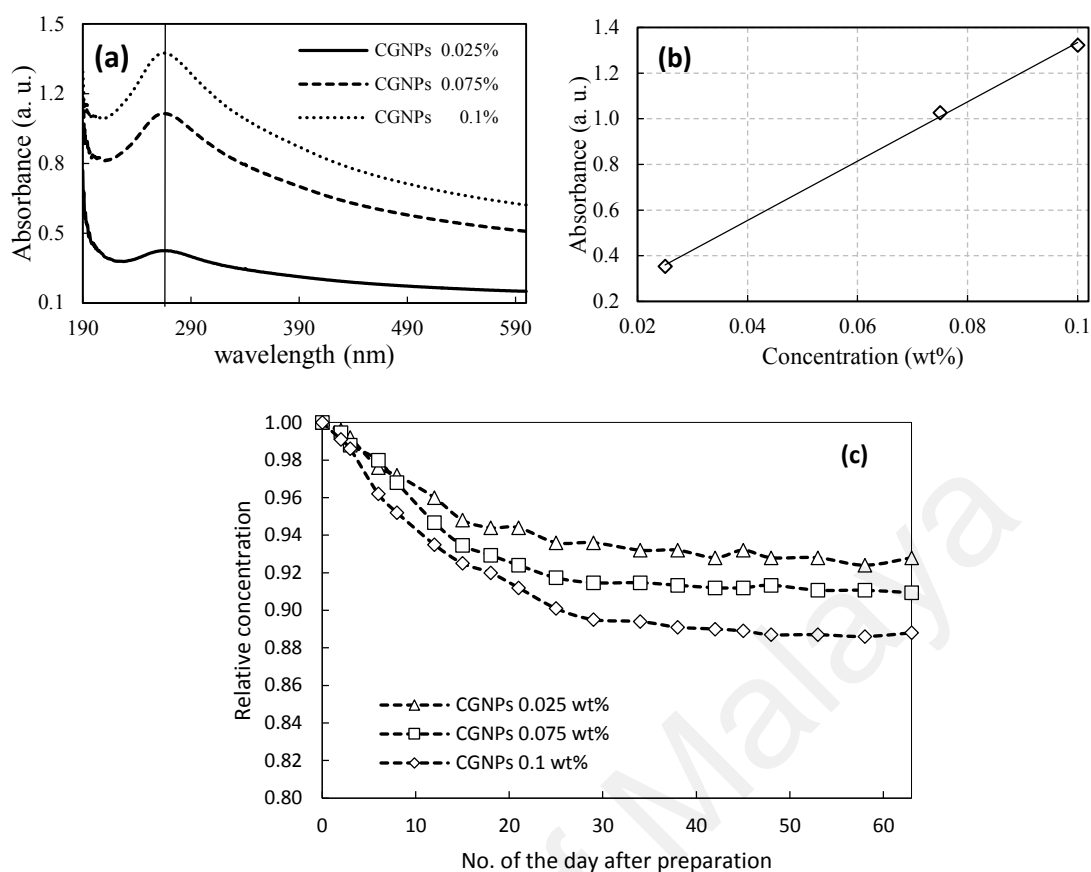


Figure 5.4: (a) UV–vis spectroscopy analyses of water-based CGNPs nanofluids at different concentrations and wavelengths, (b) absorption values of CGNPs dispersed in DI water at different concentrations and (c) colloidal stability of Clove-treated GNPs dispersed in DI water

UV-vis spectroscopy is a common technique employed to study the dispersibility of nanofluids as a function of the sedimentation time. Figure 5.4(c) indicates the stability of CGNP-water nanofluids with respect to the number of days after preparation. It is seen that the relative concentration of the nanofluids decreases by enhancing in the number of days after sample preparation. However, the relative concentration of the nanofluids is almost constant after Day 45 for all samples. The highest sedimentation magnitude is found to be 8.4, 10.4 and 11.8% for the sample containing 0.025, 0.075 and 0.1 wt% of CGNPs, respectively. This confirms the stability of our CGNP-water nanofluids.

5.2 Thermo-physical properties of water-based CGNPs nano-coolants

The effective dynamic viscosity, thermal conductivity and specific heat capacity of the CGNP-water nanofluids and DI water are measured in our experiments and we present the results as a function of temperature and particle concentration in Figure 5.5(a)–(c). The thermal conductivity of a coolant is one of the significant factors in raising the heat transfer rate (and thus, heat dissipation efficiency) of heat exchangers. The thermal conductivity of the DI water used as the base fluid in our study is similar to those in the NIST database (Ramires et al., 1995) with a maximum error of 1%. It is apparent from Figure 5.5(a) that the effective thermal conductivity is significantly higher for the CGNP-water nano-coolants compared to DI water. In addition, the thermal conductivity of CGNP-water nano-coolants increases when the temperature increases. Interestingly, the rate of increment in thermal conductivity for the CGNP-water nano-coolants is greater at higher particle concentrations. Temperature plays a pivotal pattern in enhancing the thermal conductivity of nanofluids, as evidenced from Figure 5.5(a). This is caused by the increment in Brownian motion of the CGNPs dispersed in the DI water. A maximum thermal conductivity enhancement of 5.65, 15.85 and 22.92% is attained for a particle weight concentration of 0.025, 0.075 and 0.1% at 45°C.

One of our goals is to prevent a radical increase in the viscosity of the coolant, since a higher viscosity will increase the pumping power. Here, the effective dynamic viscosity of the CGNP-water nanofluids (particle concentration: 0.025, 0.075 and 0.1 wt.%) and DI water are presented at a shear rate of 150 s^{-1} and temperature range of 20–50°C in Figure 5.5(b). It is clear that when the weight concentration of CGNPs is increased in DI water, there is only a slight increase in the dynamic viscosity of the nanofluids relative to that for DI water. This is indeed expected since only a low concentration of CGNPs used in our samples. Figure 5.5(b) also shows the benefit of covalent functionalization using cloves since the CGNPs remain suspended in the DI water. It

can also be observed that the dynamic viscosity of the CGNP-water nanofluids and DI water decreases when the temperature is increased, which is caused by the weakening of the intermolecular forces (S. J. Aravind et al., 2011). Interestingly, the samples in our study show the same declining trend for the dynamic viscosity. Our results conform well with those of Sadri et al. (Sadri, Hosseini, Kazi, Bagheri, Zubir, Solangi, et al., 2017) and Aravind et al. (S. J. Aravind et al., 2011). According to the results, it can be deduced that a pronounced increment in the dynamic viscosity of the working fluids can be prevented by devising an innovative and reliable synthesis route for nanofluids. Furthermore, it is important to consider the low weight concentration of the nanoparticles dispersed in the base fluid, especially if the nanofluid will be used as coolant in heat transfer systems. A higher particle concentration may increase the dynamic viscosity of the nanofluid which negates the positive impact of utilizing nanocoolants for heat transfer enhancement. This is due to the fact that a higher fluid viscosity will result in the pumping fluid penalty.

The specific heat capacity of the CGNP nano-coolants and DI water are presented in Figure 5.5(c). It is apparent that the specific heat capacity increases slightly when the temperature is increased for all samples. The slope is similar for the specific heat capacity curves, which agrees well with the findings of Pak and Cho (Amiri, Sadri, Shanbedi, Ahmadi, Kazi, et al., 2015; Pak & Cho, 1998). It can be seen that the specific heat capacity of the water-based CGNPs nanofluids decreases insignificantly with an increase in the CGNPs weight concentration, whereby the average reduction in specific heat capacity is within a range of 0.43–1.52% compared to that of the DI water. This decrease is due to the fact that the CGNPs nanoparticles have a lower specific heat capacity than that of the base fluid.

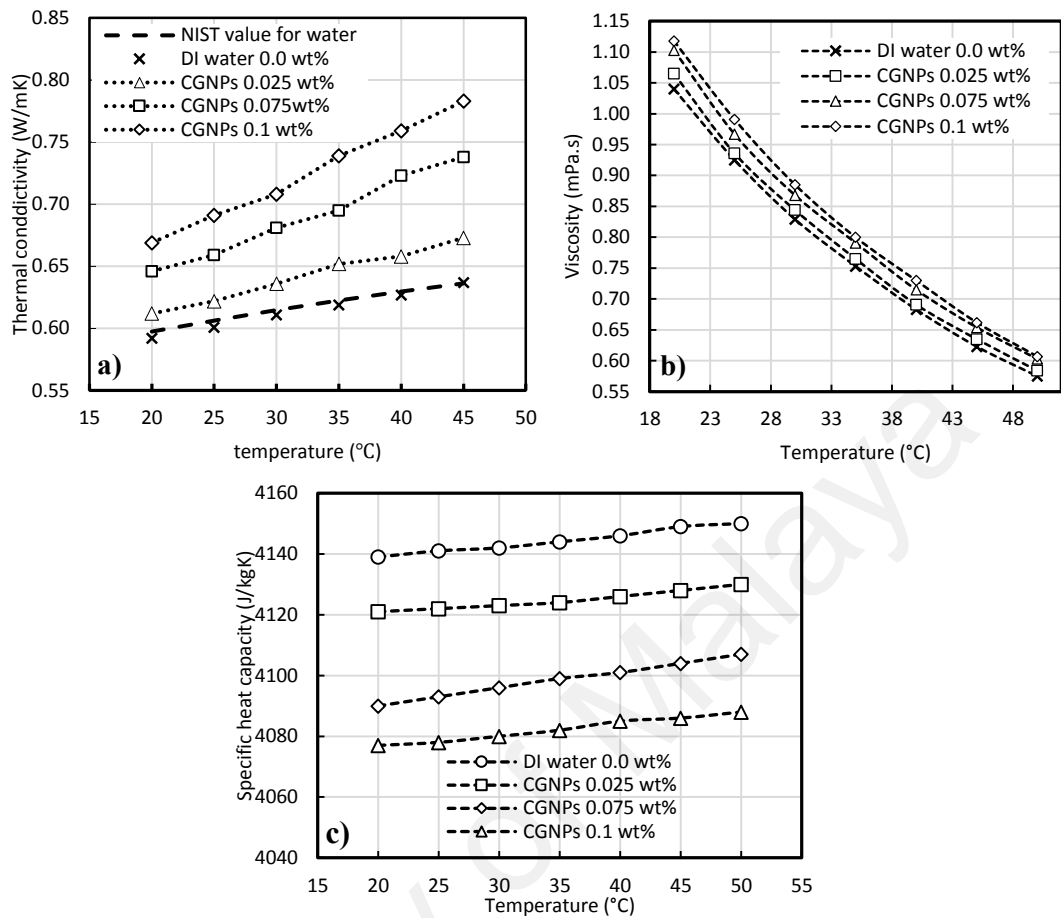


Figure 5.5: Variation of (a) thermal conductivity, (b) dynamic viscosity and (c) specific heat capacity of CGNP-water nano-coolants at different temperature and particle concentration

The Figure 5.6 shows the effective dynamic viscosity of the water-based CGNPs nanofluids and DI water as functions of shear rate, weight concentration and temperature. As it can be seen in Figures 5.6(c–e), the behavior of synthesized water-based CGNPs nanofluids in this study are quite Newtonian, whereby the viscosity of the nanofluids remains constant with an increase in the shear rate. The amount of variation in dynamic viscosity with increasing the weight concentration is insignificant and negligible. From a thermal transport perspective, this material is deemed suitable as an additive to enhance heat transfer performance.

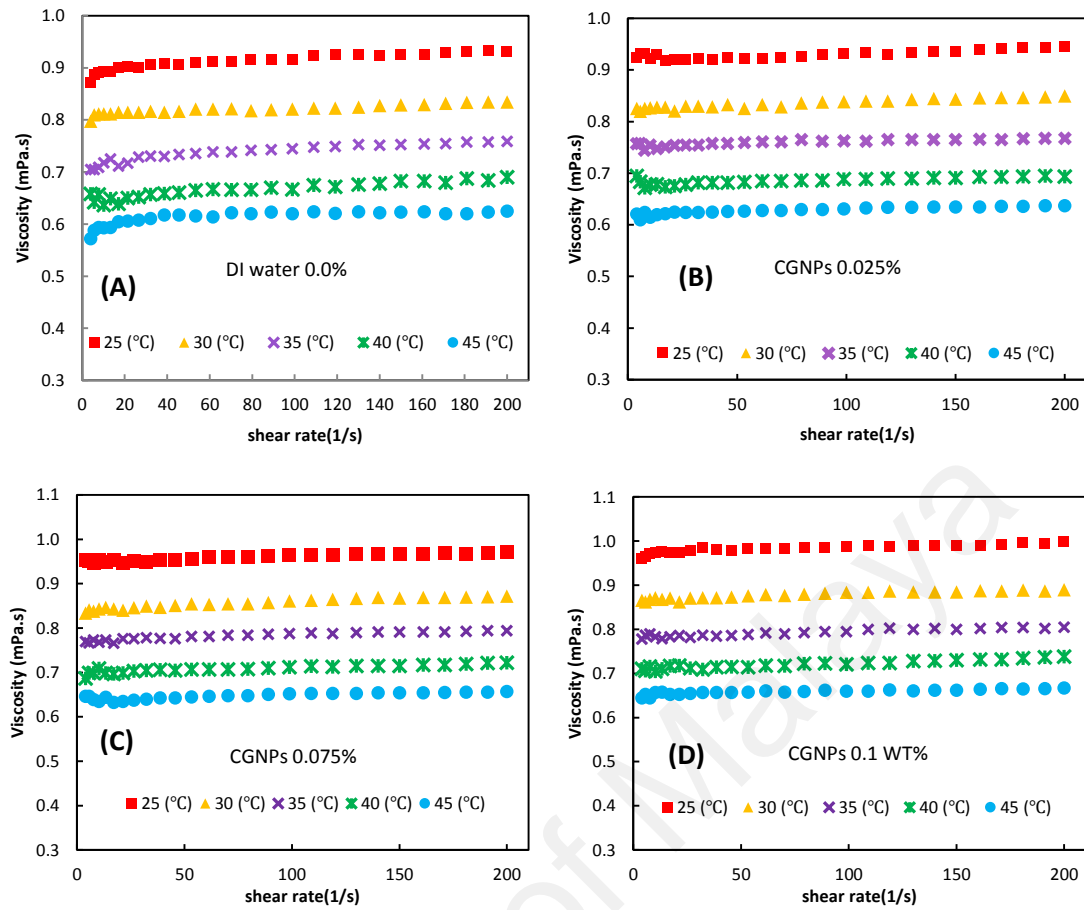


Figure 5.6: Plots of the measured values of dynamic viscosity versus shear rate for CGNPs aqueous nanofluids at various weight concentrations ((A) DI water, (B) 0.025 wt %, (C) 0.075 wt% and (D) 0.1 wt %) and temperatures

The experimentally measured values of viscosity for the water-based CGNPs suspension were compared with those calculated with the empirical correlations of Batchelor (Khanafar & Vafai, 2011) and Einstein (J.-H. Lee et al., 2008) using equations (4.1) and (4.2), respectively, and the results are depicted in the Figure 5.7. This indicates that the values calculated from experimental data are in good agreement with those determined from empirical correlations for water-based CGNPs nanofluid with a maximum error of $\sim 7\%$.

It is crucial to keep down the increment in viscosity of the heat transfer working fluids by using an appropriate synthesis method and considering low weight concentrations for the nano-coolants, particularly in heat transfer systems, in where the

overall positive impact in heat transfer is being undermined by pumping fluid penalty occurs with an increase in viscosity (Timofeeva et al., 2009; W Yu et al., 2010). Hence, in order to maximize the heat transfer performance of closed-loop systems in which nanofluids are used as the working fluids, it is imperative to maintain the resultant colloidal mixtures in Newtonian behavior since this will reduce the pumping power compared to non-Newtonian fluids.

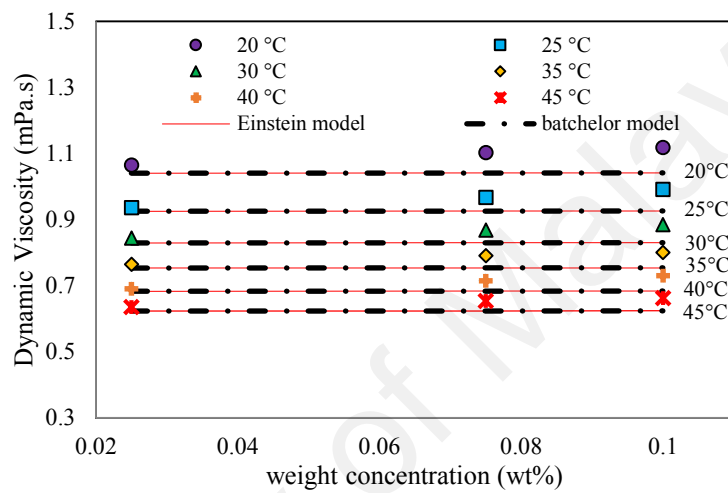


Figure 5.7: Dynamic Viscosity variation of water-based CGNPs nanofluids in comparison with those calculated with Batchelor and Einstein model as functions of concentration and temperature

Besides, the density of the CGNP-water nanofluids and DI water are measured from experiments within a temperature range of 20 to 40°C and the data are represented in Table 5.3. It can be noticed that the density for all samples decreases when the fluid temperature is increased, which we believe is due to the thermal expansion of the fluid. Furthermore, the density of the CGNP-water nano-coolant increases by increasing the particle concentration, though the increase is rather minor. The higher density of the CGNP-water nanofluids is attributed to the density of the CGNPs, which is greater than the density of water. The density of the CGNP-water nanofluid increases by only 0.045% for a particle concentration of 0.1 wt.% at 20°C. However, the density of this

nanofluid decreases by approximately 0.6% when the fluid temperature is increased from 20 to 40°C, indicating that temperature also plays a role.

Table 5.3: Density of CGNP-water nano-coolants and DI water as a function of temperature and particle concentration

Concentration/temperature (°C)	Density (kg/m ³)				
	20	25	30	35	40
DI water	998.00	996.85	995.50	993.90	992.00
0.025 wt%	998.10	997.00	995.60	994.00	992.05
0.075 wt%	998.35	997.20	995.80	994.30	992.30
0.1 wt%	998.45	997.30	995.90	994.40	992.40

5.3 Heat transfer and hydrodynamic properties

In order to investigate the convective heat transfer coefficient and Nu of the CGNP-water nanofluids, a series of experiments were conducted under the following conditions: (1) range of Re: 6371 to 15927, (2) input power: 600 W and (3) inlet temperature: 30°C. Only three particle concentrations have been considered in this study, *i.e.* 0.025, 0.075 and 0.1 wt.%. The convective heat transfer coefficient of the CGNP-water nanofluids and DI water are determined using Equation (3.1) and the results are presented as a function of the Re in Figure 5.8(a). It can be observed that there is an increment in the convective heat transfer coefficient when the Re is increased for the CGNP-water nanofluids and DI water. Moreover, the concentration of nanoparticles has a pronounced effect on the convective heat transfer coefficient of the CGNP-water nano-coolants. This effect can be attributed to the thin thermal boundary layer resulting from the enhanced thermal conductivity for the CGNP-water nano-coolants as well as the lower thermal resistance between the nanofluids and inner wall surface of the test section at higher Re. According to (S. J. Aravind et al., 2011; Yulong Ding et al., 2006), carbon-based materials such as carbon nanotubes and graphene nanoplatelets tend to reduce the thickness of thermal boundary layer. Furthermore, other factors such as the specific surface area and Brownian motion of the CGNPs play a key role in the convective heat transfer coefficient. Hereupon, the convective heat transfer

coefficient of the CGNP-water nanofluids increases by approximately 9.25, 26.6 and 37.53% for a particle concentration of 0.025, 0.075 and 0.1 wt%, respectively.

The average Nu are determined by inserting the average convective heat transfer coefficient values for the CGNP nano-coolants into Equation (3.3) and we present the results in Figure 5.8(b). It is seen that there is an obvious increase in the average Nu by increasing the Re and particle concentration. The higher average Nu for the CGNP-water nanofluids is due to the large surface area, Brownian motion and thermophysical properties of CGNPs nanoparticles suspended in the base fluid and therefore the heat transfer capability of nanofluid rises further (Sundar et al., 2014). A maximum average Nu enhancement of 4.96, 13.58 and 18.69% are obtained for a particle concentration of 0.05, 0.075 and 0.1 wt%, respectively, when $Re = 15927$.

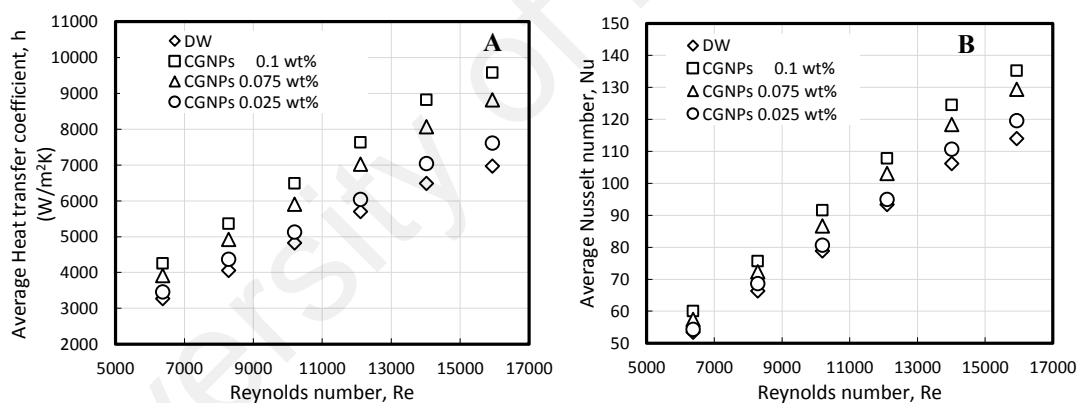


Figure 5.8: (a) average heat transfer coefficient and (b) average Nusselt number of the CGNP-water nano-coolants and distilled water at various Reynolds number

The pressure drop across the test section for the CGNP-water nanofluids and DI water is presented as a function of Re in Figure 5.6(a). The corresponding friction factor values are determined using Equation (3.9) and the data are represented in Figure 5.6 (b). It can be seen that there is a slight increase in the friction factor and pressure drop for the CGNP nano-coolants compared to those for DI water. Interestingly, the friction factor increases by approximately 1.76, 2.56, 3.79% for a particle concentration of

0.025, 0.075 and 0.1 wt.%. This is due to the slight increment in viscosity for all CGNP-water nanofluids (Figure 5.6 (b)) which requires negligible increment in fluid velocity since the Re is constant (Equation (3.4)). Hence, the velocity of the working fluid plays a vital pattern in increasing the friction factor and pressure drop in convective heat transfer systems.

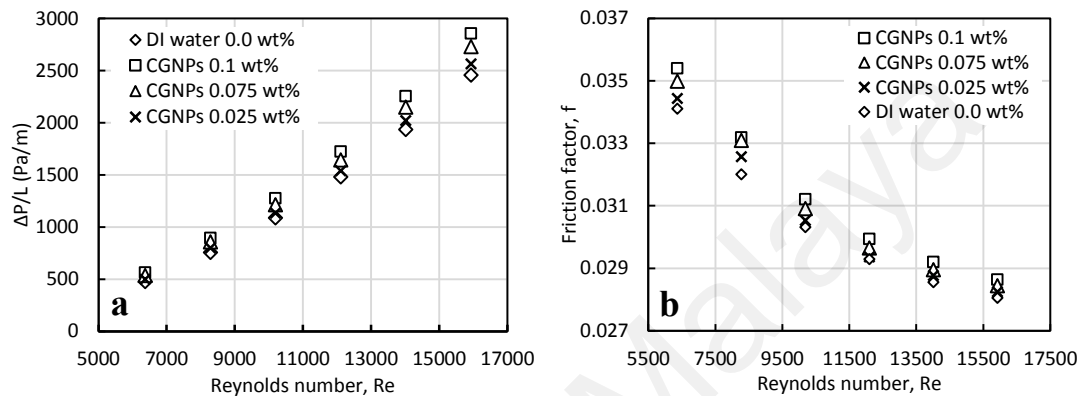


Figure 5.9: Variation of (a) pressure drop and (b) friction factor as a function of Re for the CGNP-water nanofluids in the test section

The power consumption of a heat transfer loop is important since both energy consumption and energy savings should be considered in order to optimize energy usage of thermal systems. In this study, the relative pumping power of CGNP-water nanofluids is determined using the following Eq.(4.4) (Mansour et al., 2007).

The relative pumping power of the CGNP-water nanofluids and DI water is represented in Figure 5.10. Our results appear promising since the relative pumping power increases insignificantly with respect to the particle concentration. More importantly, the relative pumping power of the CGNP-water nanofluids is close to that for DI water, *i.e.* the sample containing 0.0 wt% of CGNPs.

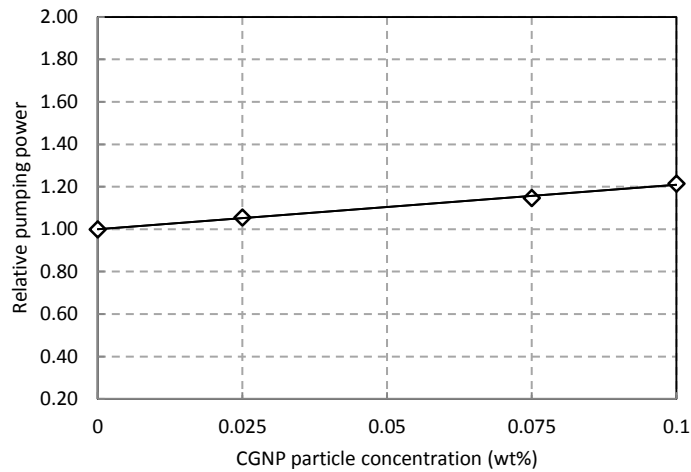


Figure 5.10: Relative pumping power of the CGNP-water nanofluids and distilled water

In general, the economic performance of a working fluid in heat transfer systems is assessed using the performance index (ϵ). The performance index is expressed as the ratio of the heat transfer enhancement (R_h) of the nanofluid to the ratio of the pressure drop ($R_{\Delta P}$) of the nanofluid relative to the base fluid. The performance index for the CGNP-water nanofluids is determined using Equation (4.5) and the corresponding results are represented in Figure 5.11 as a function of the Re.

It is apparent that the performance index is greater than 1 for all CGNP-water nanofluids. This indicates the benefit of using these environmentally friendly nanofluids in heat transfer systems. It is also apparent that the performance index increases when the CGNP particle concentration is increased in the base fluid. In addition, the performance index of the CGNP-water nanofluids increases when the Re is increased. Based on Figures 5.10 and 5.11, It can be concluded that our CGNP-water nanofluids are promising alternative coolants for heat transfer systems because of their thermal performance and energy-savings.

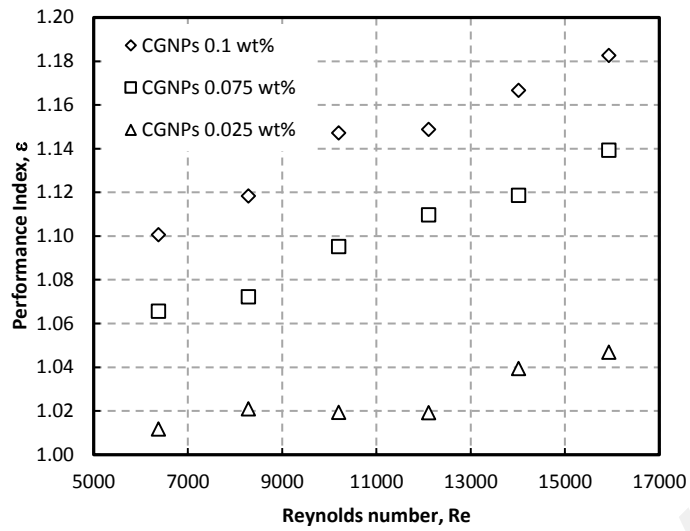


Figure 5.11: Performance index of CGNP-water aqueous suspensions as a function of Reynolds number

University of Malaya

CHAPTER 6: CHARACTERIZATION, THERMO-PHYSICAL PROPERTIES, CONVECTIVE HEAT TRANSFER AND HYDRODYNAMIC PROPERTIES OF WATER-BASED SRGO NANO-COOLANTS

6.1 Characterization of SrGO

The removal of the oxygen-containing groups of GO is clearly reflected by the FTIR spectra of GO and SrGO sample. Figure 6.1(A) depicts the Fourier transform infrared (FTIR) spectra of GO and SrGO sample. The GO shows couple of peaks in the range of 3424 cm^{-1} which can be attributed to the O–H stretching vibrations, whereas the peaks at 1731 , 1626 , and 1383 cm^{-1} are assigned, respectively, to the C=O stretching, sp^2 - hybridized C=C group and O–H bending (Cheng et al., 2013). Meanwhile, the peaks at 1062 cm^{-1} can be attributed to the C–O vibration of the epoxy or alkoxy groups in GO, respectively (Pham et al., 2011). The presence of new symmetric and asymmetric sharp peaks vibrations of C–H bonds are observed within a wavenumber range of $2850\text{--}3000\text{ cm}^{-1}$ for both SrGO. Other outstanding differences are observed in the appearance of the two peaks at 1574 and 1162 cm^{-1} attributed to N–H bending and C–N stretching, appears in the spectra of the reduced GO samples. These observations confirm that most of the oxygen functionalities have been removed from the GOs. Although the reduction of functional groups in the SrGO is obvious, also variety of functional groups remained in the final product that maintains the stability of the SrGO in water.

TGA characterization was also performed, to assess the thermal stability of the materials. TGA plots of GO and SrGO are shown in Figure 6.1(B). There were three distinctive steps of weight losses for both GO and SrGO within the temperature range of $0\text{--}800^\circ\text{C}$. Both samples showed a little mass loss around 100°C , which is mostly attributed to the removal of the trapped water molecules and epoxy oxygen functional

groups. whereas the second weight loss occurred between 200 and 400-500°C, which can be attributed to the removal of phenolic groups and decomposition of sp^3 hybridized carbon atoms located at the defect site of GO. This result indicates the high degree of oxidation of graphite after chemical exfoliation. However, for SrGO, there is less amount of weight loss below 525 °C, demonstrating the effective reduction and removal of oxygen functional groups. Comparing to GO, after functionalization and reduction with saffron, the thermal stability decrease and a large mass loss appears after 600 °C. This can be attributed to the decomposition of nitrogen containing functional group in reported results for saffron reduced GO. The last weight loss occurred after 550°C, caused by the degradation of the graphitic structures in air.

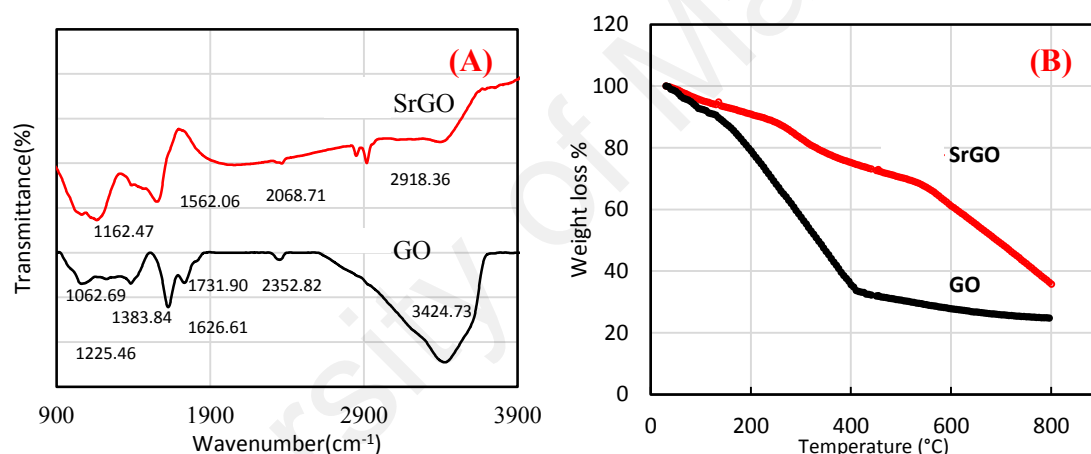


Figure 6.1: (A) FTIR spectra of graphene oxide (GO) and SrGO, (B) TGA curves of GO and SrGO

Raman spectroscopy is one of the most widely used techniques to characterize the structural and electronic properties of graphene including disorder and defect structures and, defect density. This technique is able to identify graphene from graphite and few layers graphene. Figure 6.2 (A) shows Raman spectra of graphene oxide (GO) before and after reduction and functionalization with saffron. The Raman spectra show significant structural changes occurring during the chemical processing from GO to SrGO. Both GO and SrGO have a couple of Raman-active bands in the spectra, with the D band at 1350 cm^{-1} corresponding to defects or edge areas and G band at 1598 cm^{-1}

related to the vibration of sp^2 hybridized carbon. The Raman spectra show an increase in the D/G ratio, from 1.313 for GO to 1.261 for SrGO, indicating the increased defects or edge areas by reduction of GO. These defects might be due to the smaller size of graphene sheets as well as the remaining functionalities (Ginic-Markovic, Matison, Cervini, Simon, & Fredericks, 2006; H. Wang, Hao, Yang, Lu, & Wang, 2010). For SrGO, two new peaks at 1484 cm^{-1} were attributed to C=N stretching vibration of quinonoid ring. The stretching band assigned to C-N appeared at 1331 and 1210 cm^{-1} . A band at 1016 cm^{-1} was attributed to N-H bending in-plane of the benzenoid ring. The peaks at 1162 cm^{-1} were attributed to C-H bending vibration of the benzenoid ring. (Ginic-Markovic et al., 2006). All evidences supported that the functional group have been grafted onto the surface of rGO. Generally, a peak for the 2D band of the monolayer graphene sheets is observed at 2676 cm^{-1} whereas this peak is broaden and shifted to higher wavenumber in case of multi-layer graphene. In this investigation 2D bands were observed at 2696 and 2709 cm^{-1} for GO and RGO respectively. This Figure indicates that both GO and RGO have multilayer structure. It is also cleared that after reduction of GO, the 2D band is shifted toward higher value which suggested about stacking of graphene layers. As GO has different types of functional groups which may prevent stacking of graphene layers but after reduction due to decrease of such functional groups a few graphene layers are stacking and formed multilayer RGO.

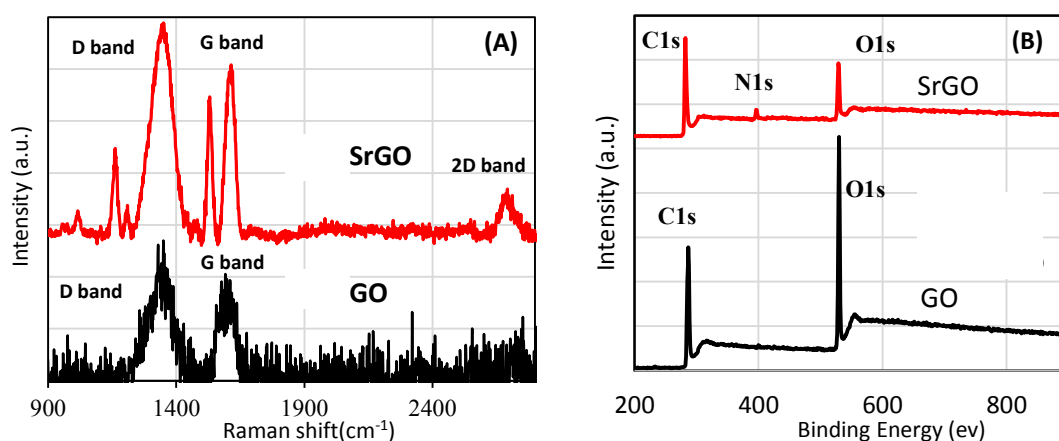


Figure 6.2: (A) Raman spectra and (B) wide-scan O1s and C1s XPS spectra for Graphene oxide and SrGO

To further illustrate the formation of graphene, XPS was performed to characterize the removal of the oxygen groups. Figure 6.2(B) shows the XPS spectra of graphite oxide and graphene reduced saffron. As can be seen from the wide-scan XPS spectra of GNPs and CGNPs (Figure 6.2 (B)), each peak was fitted to the binding energy of standard carbon, 284.6 eV. The C 1s, O 1s and N 1s peaks centered at ~284.6 eV, 532.8 eV and 400 eV, respectively. The GO sample includes high amount of oxygenated functional groups, and the O atomic percent is obviously higher than that of the SrGO, as the oxygen-to-carbon (O/C) ratio drops from 0.74 (GO) to 0.218 (SrGO). Four different peaks centered at 284.6, 286.78, 287.708, and 288.905 eV are observed, corresponding to C-C/C=C in aromatic rings, C-O, C (epoxy and alkoxy), C=O and O-C=O groups in GO, respectively (Figure 6.3). The peak intensities of these components (C-O and C=O) in saffron reduced GO are considerably smaller than those in GO, indicating considerable deoxygenation during the reduction process. It seems that the degree of reduction derived from the C/O ratio is not as high as expected. The C1s spectra of SrGO deconvoluted into C=C at 284.6, C-O/C-N at 285.917, C=O at 286.799, O-C=O/N-C=O at 288.146 and π - π at 289.178 which is confirmed reduction and functionalization of SrGO. The results of the XPS analysis are summarized in Table 6.1.

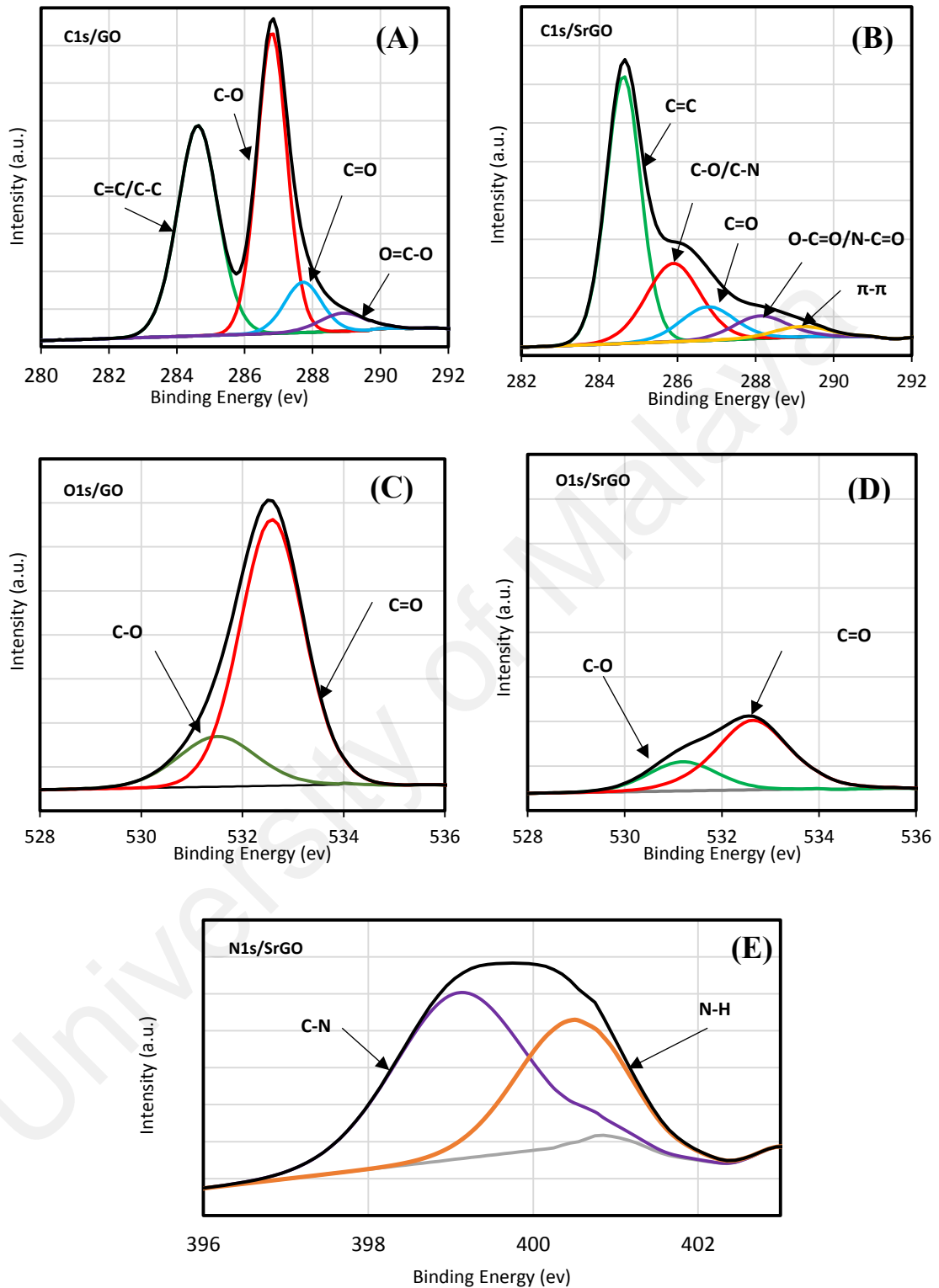


Figure 6.3: C1s XPS spectra for (A) graphene oxide and (B) saffron reduced graphene oxides, O1s XPS spectra for (C) GO and (D) SrGO, and N1s XPS spectra for (E) SrGO

This may be because some components of saffron such as protein and vitamin were bound to the rGO sheets and thus the high oxygen and nitrogen content of saffron (proteins and vitamins) contributed to the low O/C ratio of SrGO. In the high resolution spectrum of N 1s, the peaks at 398.938 and 400.362 eV correspond to the N-C and N-H, respectively (Figure 6.3(E)). The higher peak intensities at 531.482 and 532.572 eV in the O1s spectrum confirms the presence of large fractions of oxygen atoms in the form of C=O and C–O functional groups in the GO (Figure 6.3(C and D)). The O1s peaks intensities decreased significantly after reduction with saffron.

Table 6.1: XPS analysis results for GO and SrGO

Elemental composition (atom %)												
Sample	Overall percentage (Atom %)			C1s					O1s		N1s	
	C1s	N1s	O1s	C=C/C-C	C-O	C=O	O-C=O	π - π	C=O	C-O	C-N	N-H
GO	63.67	0	36.33	26.97	28.53	5.84	2.68	0	6.76	29.21	0	0
SrGO	72.37	6.09	21.55	39.65	18.17	7.82	5.22	2.44	5.69	15.10	3.34	2.56

Figure 6.4(A) illustrates the transmission electron microscopy (TEM) images of SrGO nanosheets. It can be seen from the figure that the rGO mostly consists of individual planar structure wrapped together to form a much crumpled morphology. Further, as shown in Figure 6.4(A), a close-up observation on the surface and edge structures of the rGO sheet reveals an elaborated roughness based on color intensity variation, which consists of a combination of dark and gray spots. Dark areas indicate the thick stacking nanostructure of several graphene oxide and/or graphene layers with some amount of oxygen functional groups. The higher transparency areas indicate much thinner films of a few layers graphene oxide and/or reduced graphene oxide resulting from stacking nanostructure exfoliation. Significantly larger surface area of high transparency of delaminated graphene layers (of about one to few layer thickness) is shown by the reduced graphene oxide sample (SrGO) contrary to graphene oxide

sample (SrGO), indicating layer delamination due to reduction. According to Navarro et al. (Gómez-Navarro et al., 2010) the light gray domain represents the defect free crystalline graphene layer having identical atomic configuration as to graphite. The wrinkles in SrGO, particularly at the edge can be associated with the structural damage of the sp^2 carbon arrangement, which occur during oxidation process, solution processing and drying.

Zeta potential measurement is one of the common characterization technique for determining the level of stability of colloids by providing a measure of the magnitude and sign of the effective surface charge associated with the double layer around the colloid particles (Konkena & Vasudevan, 2012). Highly dispersed nanofluids could be attributed to the suspensions with high surface charge density so that it can produce considerable electrostatic repulsive forces. The nanofluids that possess a zeta potential value stronger than $\sim +30$ mV or more negative than 30 mV are considered as a stable suspension due to interparticle electrostatic repulsion (Konkena & Vasudevan, 2012; H.-K. Lee, Lee, & Jeon, 2007). Close to the isoelectric point (point of zero charge), the particles could no longer be repelled strongly, and therefore start to aggregate and sediment over time (S. W. Lee, Park, Kang, Bang, & Kim, 2011). Figure 6.4(B) shows the measured zeta potentials values as a function of pH for the SrGO nanofluids. The results show that SrGO sheets are highly negatively charged in the range of -33.4 mV to -52 mV for the pH range of 6.45 to 10.73. Therefore, the SrGO in the investigated pHs has strong electrostatic repulsion force which avoids the SrGO sheets to aggregate by noncovalent interactions such as π - π interactions or H-bonding. On the other hand, zeta potential results of SrGO dispersion shows less negative values than that of the GO for the same pH range which was attributed to reduction and partial elimination of the oxygen functionalities at the surface of GO. In acidic solution ($\text{pH} < 6.45$), the material tends to agglomerate and undergo intermolecular dehydration catalyzed by H^+ , leading

to the coupling of SrGO via ether linkages. Figure 6.4(B) suggests that the SrGO aqueous suspensions is stable at pH more than 6 (the zeta potential around 33 mV) and never exceed the isoelectric point for the range of pH of interest. The SrGO nanofluids became more stable by adding alkali to the aqueous suspension, which leads to generation of additional negative charge in nanoparticles. Generally the pH plays a critical role in dispersion of the nanofluids SrGO(Y. Zhou, Bao, Tang, Zhong, & Loh, 2009), herein in this work, the SrGO nanofluid is stable in even slightly acidic conditions.

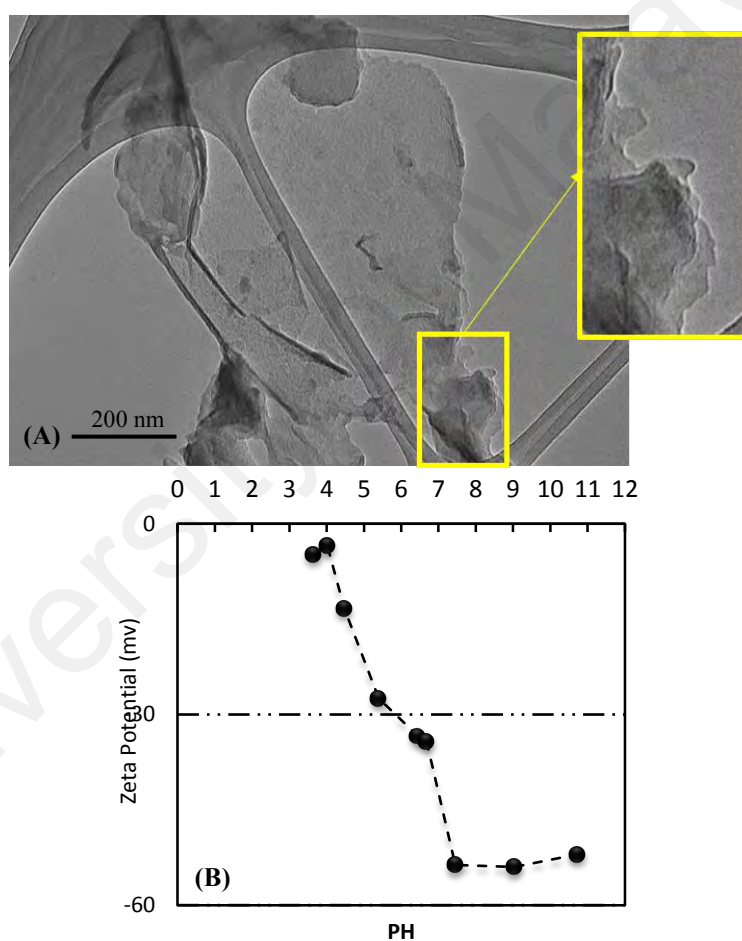


Figure 6.4: (A) TEM images of SrGO and (B) Zeta potential values of the SrGO nanofluid as a function of pH

UV-vis spectroscopy analysis is a common procedure used for investigating stability of nanoparticles aqueous suspensions. According to the Beer–Lambert’s law, there is a

direct connection between the absorbance of a solution and the concentration of the absorbing species such as particles in the solution. Following this law, the absorption spectrum of the prepared nanofluids exhibited a maximum peak at around 265 nm corresponding to $\pi - \pi$ transition of conjugation system in the polyaromatic structures.

The UV-vis spectroscopy analysis for the DI water-based SrGO nanofluids with different weight fractions were evaluated and the photometric analysis of the UV-vis spectroscopy was employed to pursue the variation of relative weight fraction of the samples versus times (day). The UV-vis spectrum for the water-based SrGO nanofluids with different weight concentrations are presented in Figure 6.5 (a). It shows that the peak values of absorbance for all the samples were located in the wavelength of 264 nm that is due to the presence of SrGO. Also it can be seen that the absorbance of SrGO reduces from 0.1 to 0.025 wt.% that illustrates the enhancing amount of dispersed SrGO will increase the value of absorbance. As shown in Figure 6.5(b), there is a good linear relationship between the concentration of SrGO and the absorbance, which conforms to the Beer's law and proves that SrGO sheets were dispersed well in the base fluid.

UV-vis spectroscopy is a common technique employed to study the dispersibility of nanofluids as a function of the sedimentation time. Figure 6.4(c) indicates the stability of SrGO -water nanofluids with respect to the number of days after preparation. It is seen that the relative concentration of the nanofluids decreases by enhancing in the number of days after sample preparation. However, the relative concentration of the nanofluids is almost constant after Day 42 for all samples. The highest sedimentation magnitude is found to be 7.2, 9.07 and 11.2% for the sample containing 0.025, 0.075 and 0.1 wt% of SrGOs, respectively. This confirms the stability of our SrGO -water nanofluids.

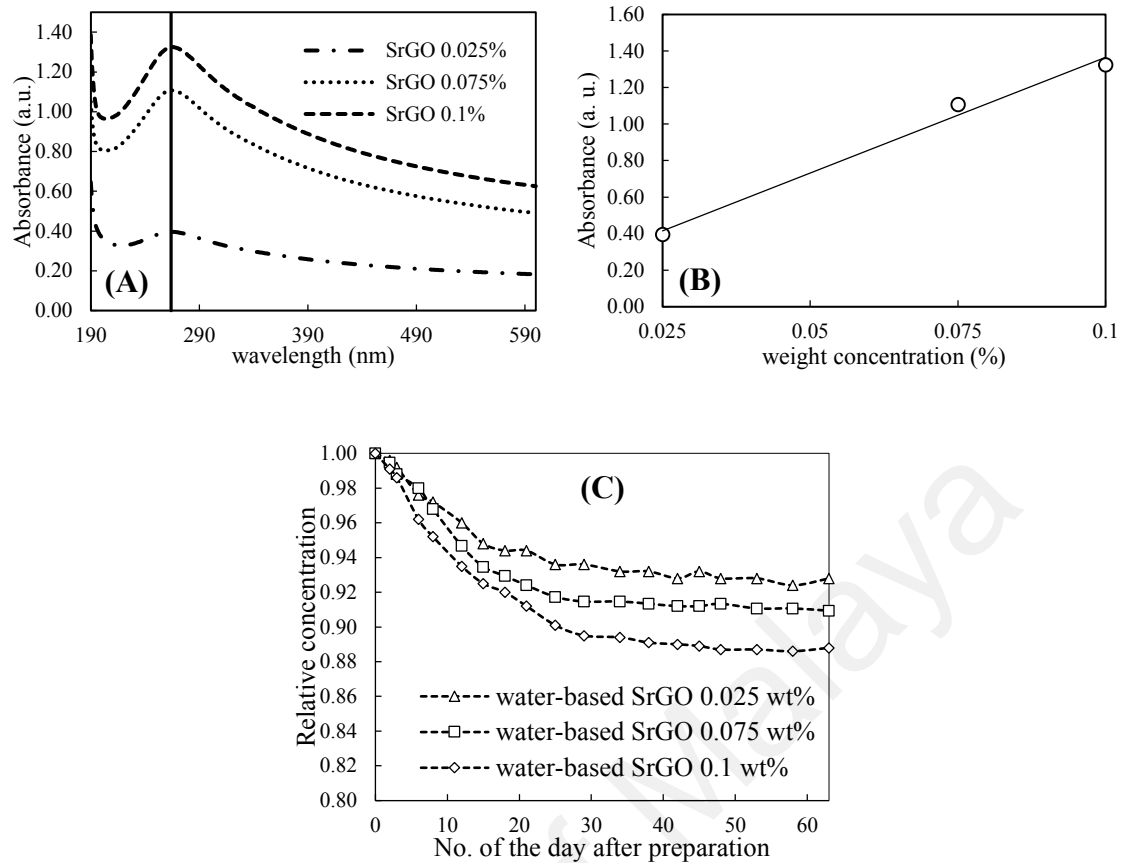


Figure 6.5: (A) UV–vis spectroscopy analyses of water-based SrGO nanofluids at different concentrations and wavelengths, (B) absorption values of SrGO dispersed in DI water at different concentrations and (C) colloidal stability of SrGO dispersed in DI water

6.2 Thermo-physical properties of SrGO nanofluids

The effective thermo-physical properties of the water-based Saffron-reduced Graphene Oxide (SrGO nanofluids) as well as DI water were experimentally measured for various range of temperature and weight concentration and the results are represented in Figure 6.6. The Figure 6.6 demonstrates the effective thermal conductivity as one the most principal thermo-physical properties, for the DI water and SrGO nanofluids at weight concentrations of 0.025, 0.075 and 0.1% and the temperature ranging from 20 to 45°C . It can shows that the thermal conductivity of DI water is in good agreement with the NIST database (Ramires et al., 1995) with a maximum error of

1%. The Figure 6.6 clearly displays the measured thermal conductivity of the SrGO nanofluids is much higher than that of the base fluid and it increases by loading nanoparticles. The reason for this discrepancy is associated with the liquid/particle interfacial nano-layers (nano-layer at the interface between nanoparticle and fluid) (S. J. Aravind et al., 2011; Murshed, Leong, & Yang, 2009), Brownian motion and specific surface area (SSA) of the nanoparticles (Amiri, Sadri, Shanbedi, Ahmadi, Chew, et al., 2015; S. J. Aravind et al., 2011; Sadri, Hosseini, Kazi, Bagheri, Zubir, Solangi, et al., 2017; Sadri, Zangeneh Kamali, et al., 2017; H. Xie, Fujii, & Zhang, 2005), and consequently higher thermal conductivity of the SrGO nanoparticles compare to that of the DI water. In light of previous researches (Sarsam, Amiri, Zubir, et al., 2016), the graphene sheets with higher SSA loaded in base fluid leads to higher thermal conductivity of the corresponding nano-coolants. Furthermore, some fundamental parameters such as temperature, thermal conductivities of the base fluid and nanoparticles, weight concentration, shape or geometry of nanostructures play significant roles in determining the thermal conductivity of the nano-coolants. (Amiri, Shanbedi, & Dashti, 2017; Amiri, Shanbedi, Rafieerad, et al., 2017). Also, It can be obviously seen in Figure 6.6 that the measured thermal conductivity of nano-coolants as well as DI water enhanced by increasing fluid temperature, which is an expected phenomenon. This shows the temperature plays a significant role in enhancing the thermal conductivity of aqueous suspensions that it can be devoted to the increased Brownian motion of the SrGO nanoparticles dispersed in base liquid. The thermal conductivity of the SrGO nanofluids increased up to 8.95, 20.72 and 28.88%, respectively, for the weight concentration of 0.025, 0.075 and 0.1% at temperature of 45°C.

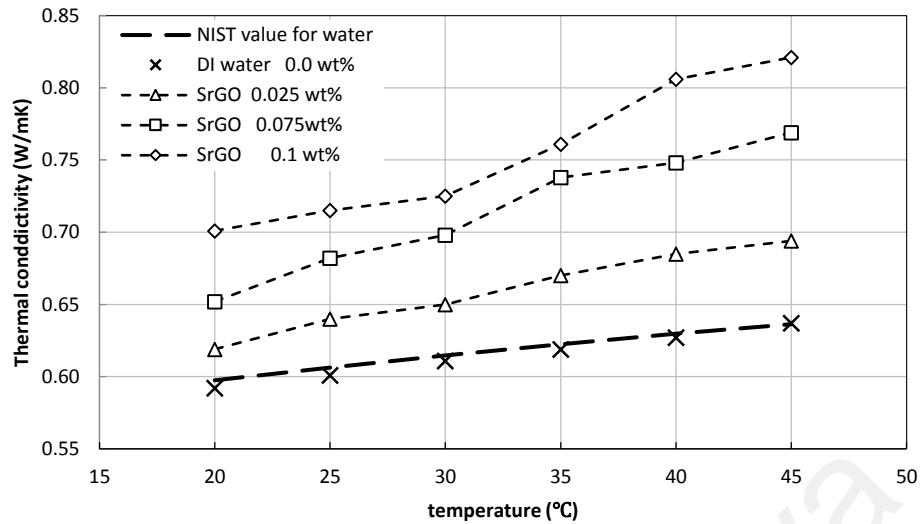


Figure 6.6: Thermal conductivity variation of water-based SrGO nano-coolants and DI water as a function of temperature and weight concentration

Figure 6.7 demonstrates the results of dynamic viscosity measurement for the DI water and water-based Saffron-reduced Graphene Oxide (SrGO nanofluids) at the shear rate of 150 s^{-1} , weight concentrations of 0.025, 0.05 and 0.1% and the temperature ranging from 20 to 45°C. It can be observed that the viscosity plots of the SrGO nanofluids resemble the viscosity plot for distilled water, whereby there is an insignificant and negligible increase in the viscosity of SrGO nanofluids compared to that of the DI water with an increase in SrGO weight concentration, as shown in Figure 6.7. The reason behind this phenomenon can be attributed to the low weight concentrations considered for the nanofluids in addition to the successfully implementation of covalent functionalization which leads to the well dispersing of the SrGO nanoparticles into the base fluid. It can be seen from the Figure 6.7 that the viscosity decreases when the temperature is increased, which is in tandem to the water behaviour, and this trend is caused by the weakening of the intermolecular adhesion forces (S. J. Aravind et al., 2011; Tian, He, Xu, Fang, & Zhang, 2016). This phenomenon is in agreement with Sadri et al. (Sadri, Hosseini, Kazi, Bagheri, Zubir, Ahmadi, et al., 2017) and Aravind et al. (S. J. Aravind et al., 2011).

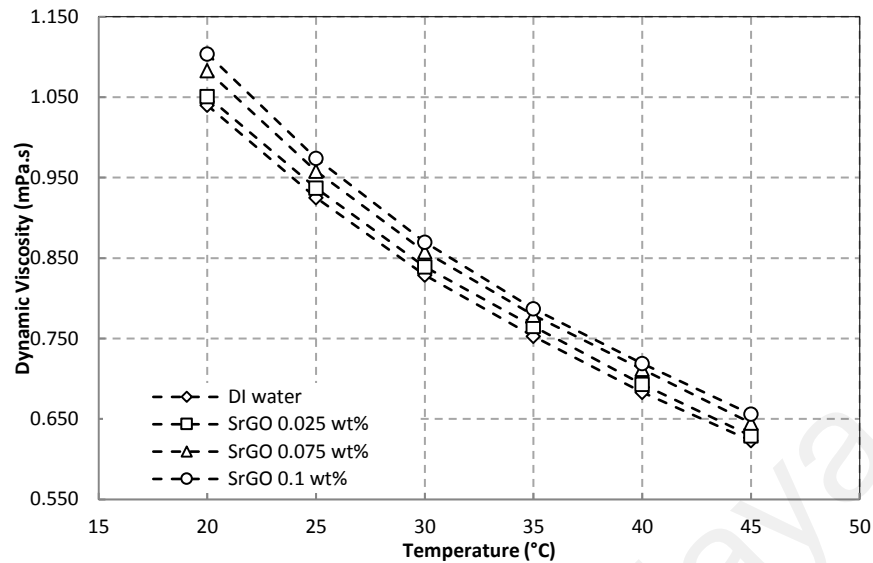


Figure 6.7: Dynamic viscosity of water-based SrGO nanofluids and DI water as a function of temperature and weight concentration at shear rate of 150 s^{-1}

The experimentally measured values of viscosity for the water-based SrGO suspension were compared with those calculated with the empirical correlations of Batchelor (Khanafar & Vafai, 2011) and Einstein (J.-H. Lee et al., 2008) using equations (4.1) and (4.2), respectively, and the results are depicted in the Figure 6.8. This indicates that the values calculated from experimental data are in good agreement with those determined from empirical correlations for water-based SrGO nanofluid with a maximum error of $\sim 6\%$.

It is crucial to keep down the increment in viscosity of the heat transfer working fluids by using an appropriate synthesis method and considering low weight concentrations for the nano-coolants, particularly in heat transfer systems, in where the overall positive impact in heat transfer is being undermined by pumping fluid penalty occurs with an increase in viscosity (Timofeeva et al., 2009; W Yu et al., 2010). Hence, in order to maximize the heat transfer performance of closed-loop systems in which nanofluids are used as the working fluids, it is imperative to maintain the resultant

colloidal mixtures in Newtonian behavior since this will reduce the pumping power compared to non-Newtonian fluids.

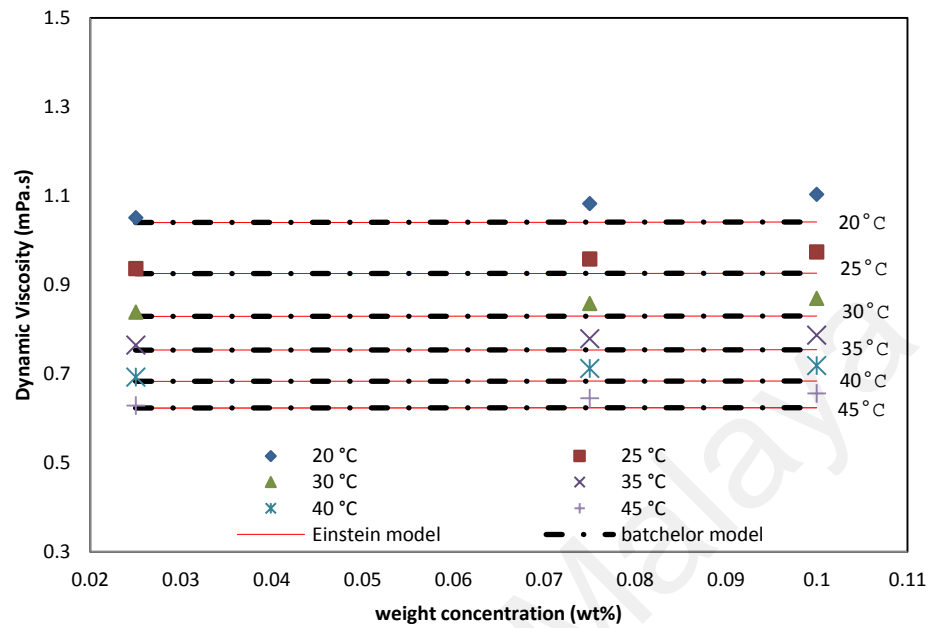


Figure 6.8: Viscosity of water-based SrGO nanofluids compared with those calculated by theoretical models as function of concentration and temperature at the shear rate of 150 s^{-1}

The Figure 6.9 represented the dynamic viscosity of nano-coolants as a function of shear rate at different temperatures. As shown in Figures 6.9(a–d), the water-based SrGO nanofluids synthesized in this research exhibit Newtonian behavior, whereby the viscosity of the nanofluids remains constant with an increase in the shear rate. From a thermal transport perspective, this material is deemed suitable as an additive to enhance heat transfer performance.

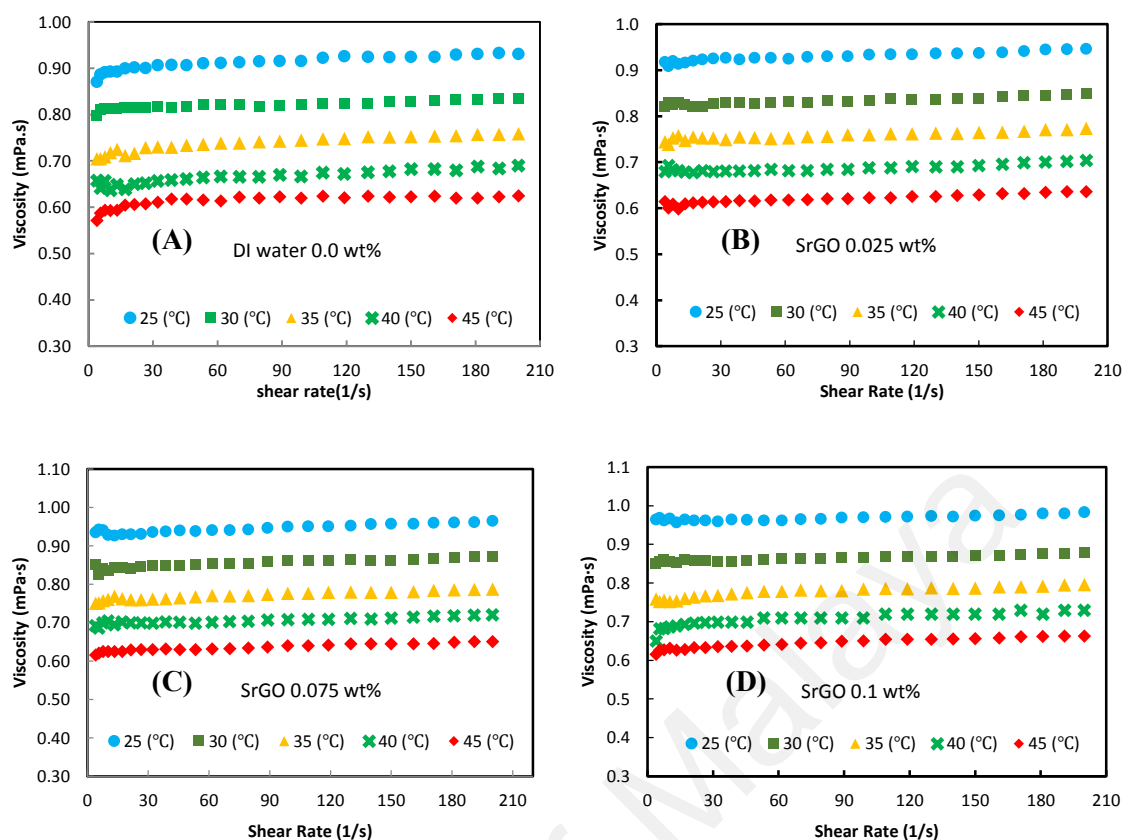


Figure 6.9: Plots of the measured values of dynamic viscosity versus shear rate for SrGO aqueous nanofluids at various weight concentrations((A) DI water,(B) 0.025 wt%,(C) 0.075 wt% and (D) 0.1 wt %) and temperatures

As another effective thermo-physical property, the specific heat capacity of the water-based SrGO nanofluids as a function of weight concentration and temperature is represented in Figure 6.10. The specific heat capacity for distilled water is also plotted in the same graph for comparison. It can be seen that the specific heat capacity of the water-based SrGO nanofluids decreases with an increase in the SrGO weight concentration, whereby the average reduction in specific heat capacity is within a range of 0.72–2.36% compared to that of the DI water, exhibiting insignificant decrease. This decrease is due to the fact that the SrGO nanoparticles have a lower specific heat capacity than that of the base fluid.

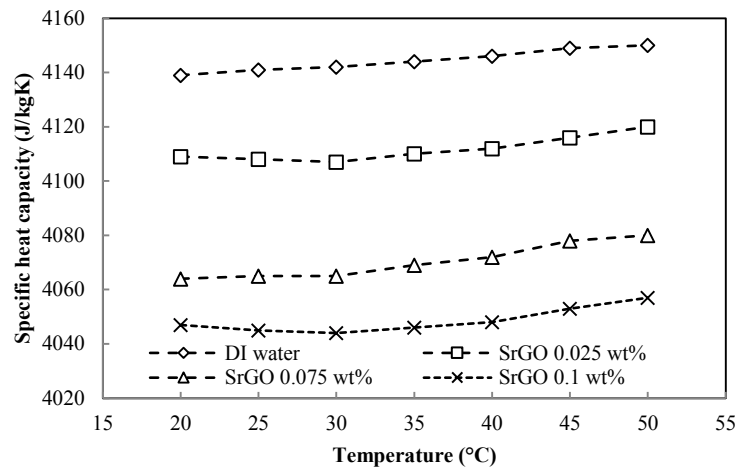


Figure 6.10: Variation of specific heat capacity of water-based SrGO nanofluids at different temperature and particle concentration

The densities of the water-based SrGO nanofluids and distilled water (base fluid) are determined with respect to the changes in the SrGO weight concentration and temperature and the results are summarized in Table 6.2. It can be seen that the density of the SrGO nanofluids and base fluid decreases by approximately 0.6% when the temperature is increased from 20 to 40°C. A plausible explanation for this is that the volume of the liquids increases when the temperature is increased and it is known that density is inversely proportional to the volume of liquid. Also, it is also apparent that the density of the SrGO nanofluids increases when the concentration of SrGO is increased, which can be a reasonable issue. However, the difference in the density values is rather minor.

Table 6.2: Density of water-based SrGO nanofluid and DI water as a function of temperature and concentration

Concentration/temperature (°C)	Density (kg/m ³)				
	20	25	30	35	40
DI water 0 wt%	998.00	996.85	995.50	993.90	992.00
SrGO 0.025 wt%	998.15	997.05	995.65	994.05	992.15
SrGO 0.075 wt%	998.40	997.35	995.95	994.35	992.40
SrGO 0.1 wt%	998.55	997.45	996.10	994.50	992.50

6.3 Heat Transfer and hydrodynamic properties

To study the convective heat transfer coefficient of water-based SrGO nanofluids, a series of experiments have been performed at the Reynolds number range of 6370 ± 5 to 15925 ± 5 , input power of 600 W and inlet temperature of 30°C under turbulent boundary condition. Three SrGO weight concentrations of 0.025, 0.075 and 0.1 % are considered in this research. The convective heat transfer coefficient of water-based SrGO nanofluids and DI water are evaluated using Equation (3.1) and the corresponding results are demonstrated in Figure 6.11(a) as a function of the Reynolds number. It can be seen clearly from Figure 6.11(a) that there is an increment in the convective heat transfer coefficient when the Reynolds number is elevated for the SrGO water-based SrGO nanofluids and DI water. Furthermore, the SrGO weight concentration has a noticeable effect on convective heat transfer coefficient enhancement of the water-based SrGO nano-coolants, which can be assigned to the thin thermal boundary layer and the enhanced thermal conductivity for the water-based SrGO nanofluids as well as the lower thermal resistance between the nanofluids and inner wall surface of the test section at higher Reynolds number. Based on the previous researches (S. J. Aravind et al., 2011; Yulong Ding et al., 2006), carbon allotropes such as carbon nanotubes and graphene nanoplatelets tend to reduce the thickness of thermal boundary layer. Moreover, other parameters such as the specific surface area and Brownian motion of the SrGO nanoparticles in base fluid play a key role in the convective heat transfer coefficient. The convective heat transfer coefficient of the SrGO-water nano-coolants rises by approximately 12.95, 31.59 and 41.79% for a weight concentration of 0.025, 0.075 and 0.1 wt%, respectively.

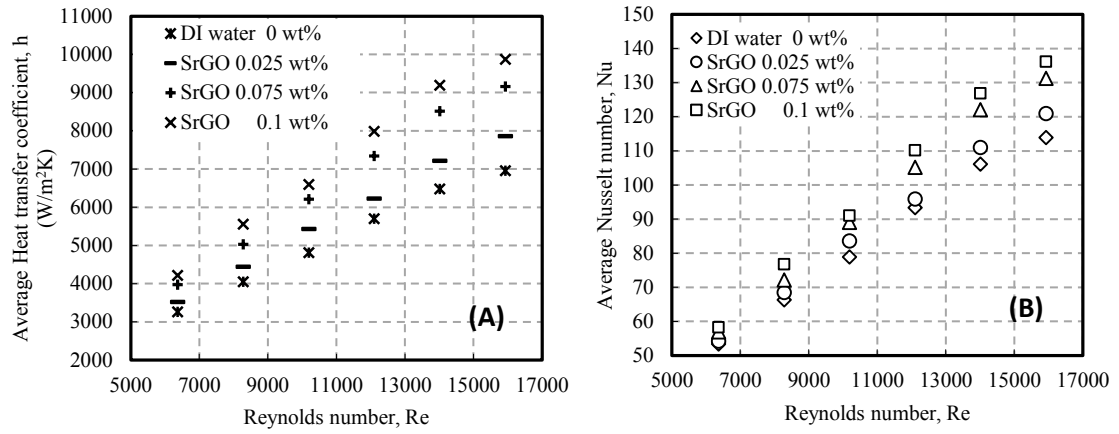


Figure 6.11: (a) Average heat transfer coefficient of the water-based SrGO nanofluid and distilled water at various Reynolds number and (b) Average Nusselt number of the water-based SrGO nanofluid and distilled water at various Reynolds number

The ratio of convective to conductive heat transfer of water-based SrGO nanofluids is determined by inserting the corresponding average convective heat transfer coefficient values into Equation (3.3) and the results are illustrated in Figure 6.11(b) with respect to the nanoparticle weight concentration and Reynolds numbers. It can be observed from Figure 6.11(b) that there is a clear increment in the average Nusselt number with an increase in the Reynolds number and SrGO weight concentration. The greater average Nusselt number for the water-based SrGO nano-coolants is attributed to the to the large surface area, Brownian motion and thermophysical properties of suspended SrGO and therefore the heat transport capability of nanofluid rises further (Sundar et al., 2014). A maximum average Nusselt number enhancement of 6.17, 15.2 and 19.5% achieved, respectively, for a weight concentration of 0.05, 0.075 and 0.1 wt% at Reynolds number of 15925 ± 5 .

The pressure drop across the experimental test section examined for various weight concentrations and Reynolds number of water-based SrGO nano-coolants and the results are depicted in Figure 6.12(a). The corresponding friction factor values are evaluated using Eq. (3.9) and the results are illustrated in Figure 6.12(b). It can be

observed clearly that pressure drop and friction factor increases slightly with an increase in weight concentration compared to that of DI water. The pressure drops for the SrGO nano-coolants at low concentration of 0.025 wt% is quite close to that for the DI water, which is assigned to the low weight concentration of SrGO. The enhancement in friction factor and pressure drop is due to the minor increment in the dynamic viscosity of nanofluids. It should be mentioned that for a constant Reynolds number, an increase in viscosity requires a small increase in fluid velocity. Accordingly, the increase in the velocity of working fluid can be considered as the main reason for increase in friction factor and pressure drop of the nanofluids in convective heat transfer systems. The maximum increase in the friction factor of nanofluids for weight concentration of 0.025, 0.075 and 0.1% is, respectively, about 1.17, 2.48 and 3.21%.

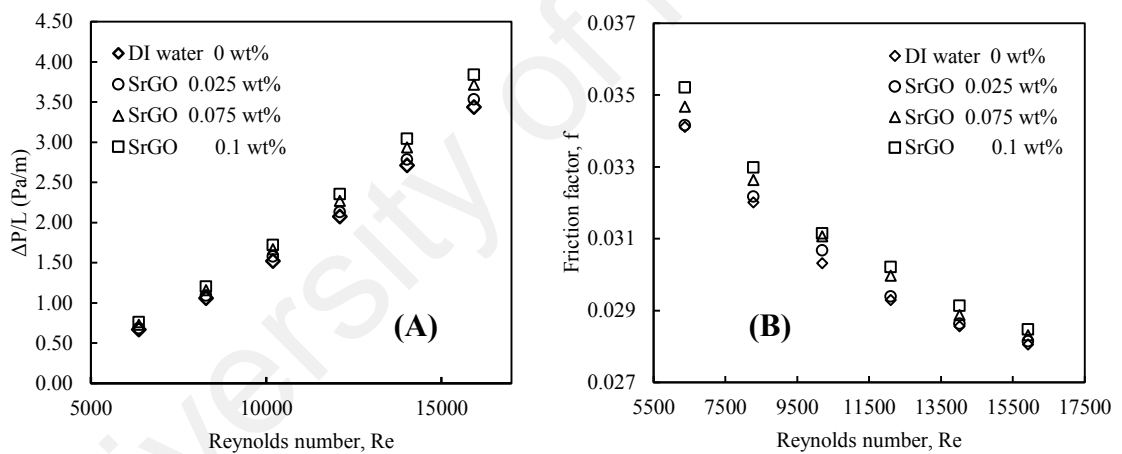


Figure 6.12: Variation of (a) Pressure drop and (b) friction factor of water-based SrGO nano-coolants as a function of Reynolds number for various concentrations

The pumping characteristics and power consumption of a heat transfer set-up is an important factor in respect of energy savings and energy consumption in order to evaluate the suitability of a working fluid and optimize energy usage of thermal equipment. The relative pumping power of water-based SrGO nano-coolants and DI water are calculated using the equation (4.4) and the results presented in Figure 6.13 as a function of weight concentration. It is noteworthy that the Figure 6.13 shows only a

small increase in relative pumping power with SrGO nanoparticles loading. The reason behind this phenomenon can be associated to the low weight concentrations considered for the nanofluids in this study.

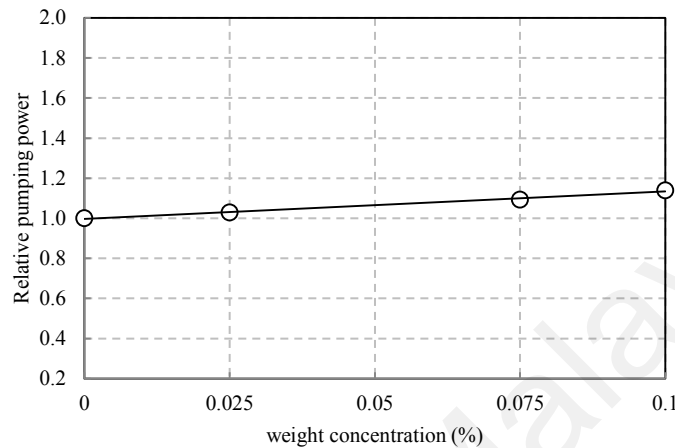


Figure 6.13: Relative pumping power of the water-based SrGO nano-coolants and distilled water

In this part the thermal and economic performance of the working fluids in heat transfer equipment is evaluated according to the performance index which is defined as the ratio of the enhancement in convective heat transfer coefficient to the enhancement in pressure drop of nanofluid relative to the base fluid. Based on the literature, adding high thermal conductive nanoparticles improves the convective heat transfer, however, the pressure drop across the test section also elevates which is undesirable. Evidently, when the performance index is greater than 1, it implies that the technique is more in the favor of heat transfer enhancement rather than in the favor of pressure drop increasing. Therefore, the heat transfer methods with performance indexes greater than 1 would be feasible choices in practical applications. The performance index for the water-based SrGO nanofluids is determined using Eq. (4.5) and the data is demonstrated in Figure 6.14 at various Reynolds number and weight concentration. It be clearly seen from the Figure 6.14 the values of performance index for all of the samples including SrGO is

greater than 1 and it rises with an increase in Reynolds number and weight concentration. Among the tested SrGO nanofluids, the with sample optimum volume concentration has the highest performance index ratio.

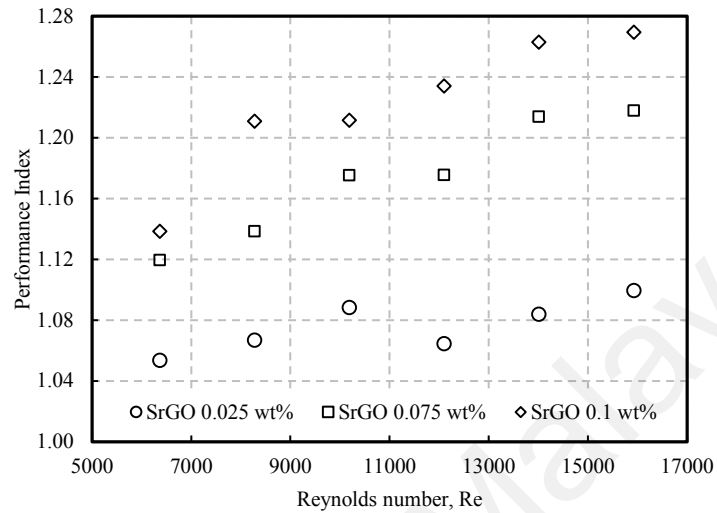


Figure 6.14: Performance index Variation of the water-based SrGO nanofluids versus Reynolds number at different concentrations

CHAPTER 7: CHARACTERIZATION, THERMO-PHYSICAL PROPERTIES, CONVECTIVE HEAT TRANSFER AND HYDRODYNAMIC PROPERTIES OF WATER-BASED GAMWCNT NANO-COOLANT

7.1 Characterization of GAMWCNT

The FTIR spectra of the pristine and GAMWCNT are shown in Figure 7.1. As can be seen, the GAMWCNT sample demonstrates clear cues of various functionality groups in contrast to the pristine MWCNT. The sharp and broad peaks at the range of 3446-3750 cm^{-1} is attributed to O–H stretching vibrations at the main structure of both MWCNTs and CMWCNTs with different intensity, which may be caused by the reaction between the MWCNTs and hydroxyl (O–H) groups of gallic acid and/or hydrogen peroxide(H_2O_2). Also the symmetric and asymmetric peaks in the range of 2850–3000 cm^{-1} in both GAMWCNT and MWCNT are signed with C–H bonds. It can be observed from Figure 7.1(a), a peak centered at the wavenumber range of 2360 cm^{-1} in the spectrum of GAMWCNT is corresponding to CO_2 (Rusu, Popa, Lisa, & Vereștiuc, 2015). Also a couple of peaks in the wavenumber of 1388 and 1562-1639 cm^{-1} are assigned to CH_2 bending vibrations and C=C stretching vibrations of MWCNTs after opening due to the addition of electrophilic reactions between the main structure of MWCNTs and the –OH band of gallic acid respectively. According to the FTIR results the gallic acid is successfully attached to the pristine multiwall carbon nanotube through free radical grafting reaction.

TGA is a thermal analysis technique, whereby modifications in the structure of materials are evaluated as a function of temperature. TGA trace of the GAMWCNTs shows evidence about functionalization by using thermal analysis of sample. Figure 7.1(b) shows the TGA curves for pristine MWCNTs and GAMWCNTs. It can be

figured out that there was no significant weight loss with raw MWCNTs, which was thermally stable when heated to 640 °C. Furthermore, GAMWCNTs indicates a mild weight loss in the temperature range of 30-220 °C and 220-580 °C, which can be due to the decomposition water and functional group respectively. The second phase of degradation 580-900 °C was related to the decomposition of the graphitic carbon. The obtained results indicate that the functionalization of MWCNT with gallic acid is successful.

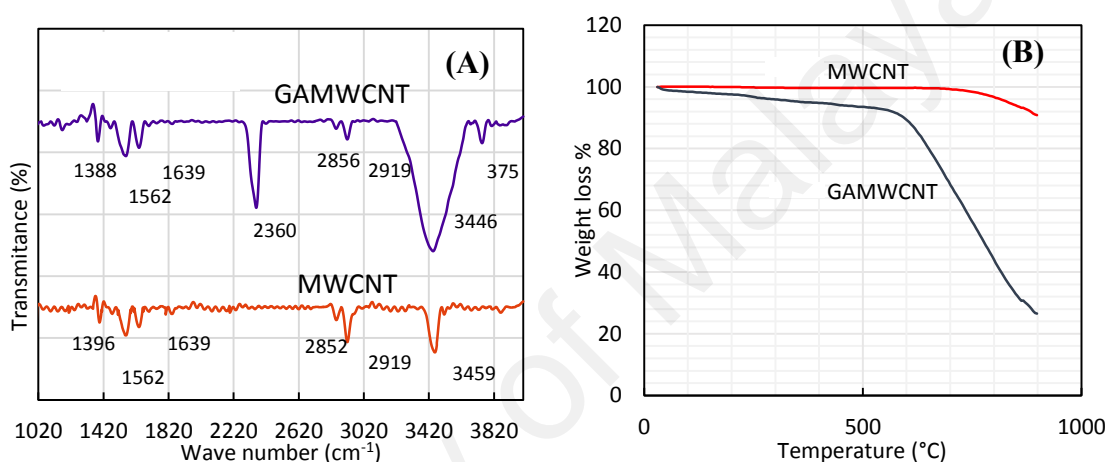


Figure 7.1: (A) FTIR spectra of pristine MWCNTs and GAMWCNTs, and (B) TGA curves of pristine MWCNTs and GAMWCNTs

Raman spectroscopy is becoming a technique of increasing relevance for the characterization of carbon materials. Apart from being non-destructive, it is simple and rather sensitive not only to the crystal structure (the long range order), but also to structural changes occurring at the molecular level (the short range order). Therefore, Raman spectroscopy has high potential to access chemical functionalization. The Raman spectrum of the GAMWCNTs and pristine MWCNTs are illustrated in Figure 7.2 (a). It can be observed from the Raman spectra that both pristine MWCNTs and GAMWCNTs have D and G band at a wavenumber of ~1350 and 1590 cm⁻¹, respectively. The D bands are related to the amorphous/disordered carbon (sp³) and G bands to the graphitic carbon (sp²). Increase in the ID/IG ratio means that number of

sp^2 hybridized carbons changed to sp^3 hybridization carbons because of the covalent functionalization. The I_D/I_G ratio is found to be 0.62 and 0.71 for the pristine CNTs and GAMWCNTs, respectively. The higher I_D/I_G ratio obtained for the GAMWCNTs is attributed to the higher number of sp^3 carbons present and the occurrence of electrophilic addition reaction. Full Raman spectra analysis data is given in Table 7.1.

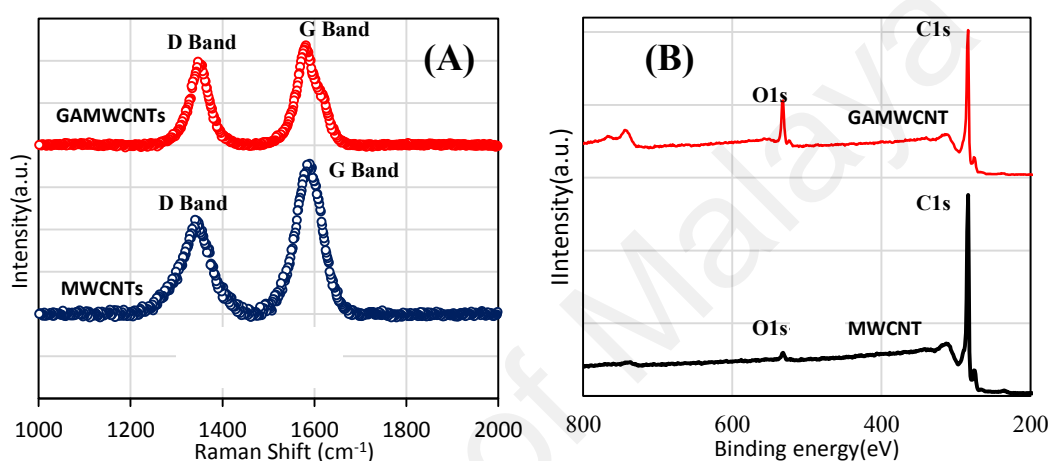


Figure 7.2: (A) Raman spectra and (B) wide-scan O1s and C1s XPS spectra for pristine MWCNTs and GAMWCNTs

Table 7.1: Raman spectra analysis results for pristine MWCNTs and GAMWCNTs

Sample	Peaks	Centre (cm ⁻¹)	Intensity(a.u.)	I_D/I_G
MWCNTs	D bond	1344.989	1117.054	0.63
	G bond	1594.618	1777.089	
GAMWCNTs	D bond	1352.577	1308.141	0.71
	G bond	1587.16	1836.491	

X-ray photoelectron spectroscopy (XPS) of the MWCNTs before and after covalent functionalization with cloves and the results are shown in Figure 7.2(b). Each peak was fitted to the binding energy of standard carbon, 284.6 eV. As can be seen from the wide-scan XPS spectra of MWCNTs and GAMWCNTs (Figure 7.2), C 1 s and O 1 s peaks

centered at ~ 284.6 eV and 532.8 eV, respectively. According to the results, pristine MWCNTs shows a very small amount of oxygen. Upon functionalization, the intensity of the O 1s peak increased considerably, while the carbon content in MWCNT is the opposite, as the oxygen to carbon (O/C) ratio increased from 0.024 of MWCNTs to 0.22 of GAMWCNTs. It confirms the successful free radical grafting of gallic acid on MWCNTs.

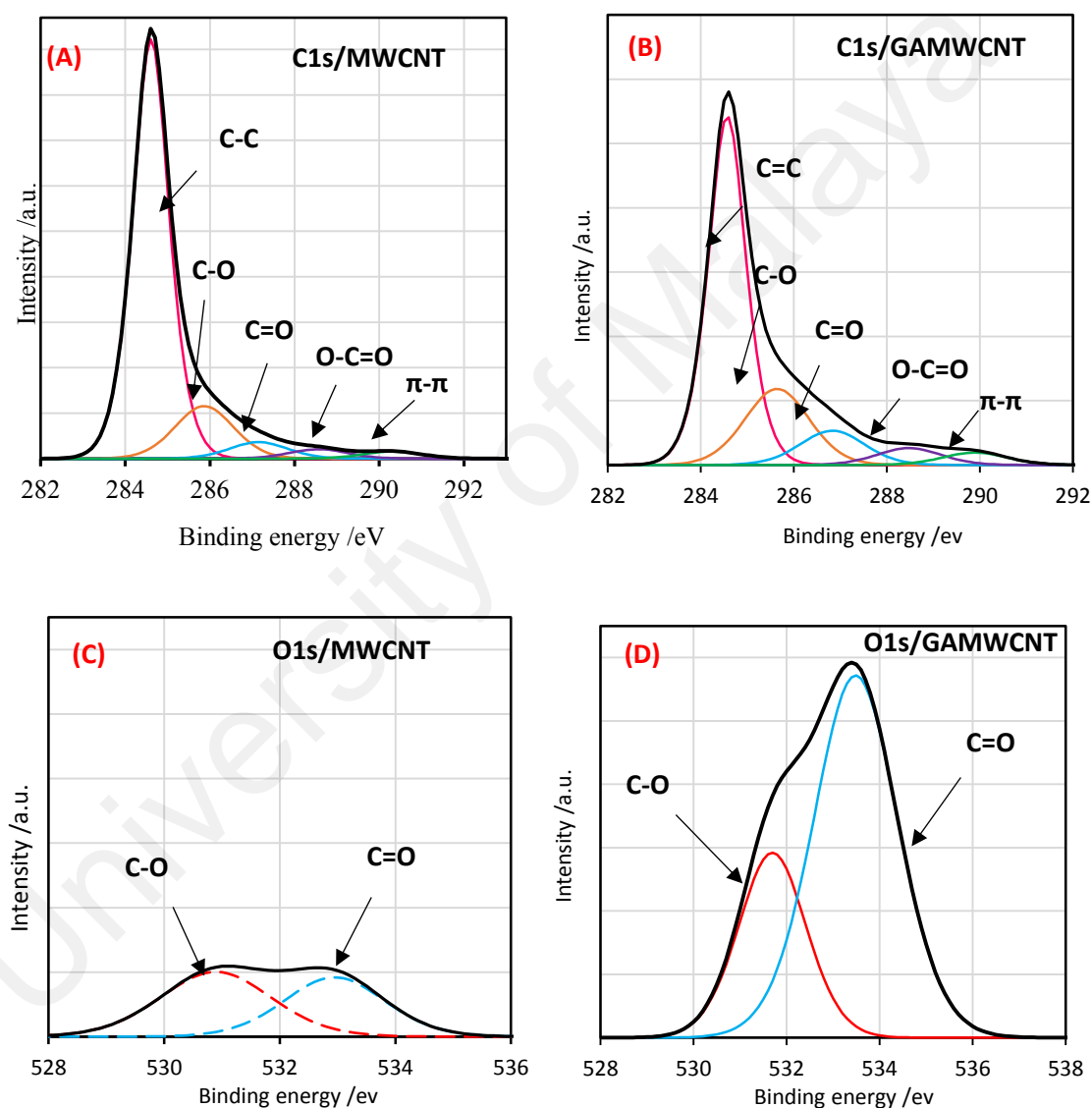


Figure 7.3: C1s XPS spectra for (a) pristine MWCNTs and (b) GAMWCNTs, and O1s XPS spectra for (c) pristine MWCNTs and (d) GAMWCNTs

Figure 7.3 shows the core level C1s spectra of pristine and functionalized MWCNTs. The C1s peaks were obtained in a binding energy range from 282 to 292 eV. The C1s spectra of all samples were deconvoluted into five components: the peak at 284.6 eV is attributed to the graphitic structure (C=C), the peak at 285.66 eV is attributed to C–O (hydroxyl and epoxy), and the peaks at 286.85 and 288.5 eV are attributed to C=O, and –COO–, respectively. The last peak at 289.9 eV is assigned to the π – π transition peak. The detailed elemental analysis and relative percentage of each peak fraction are illustrated in Table 7.2.

Table 7.2: XPS analysis results for pristine and GAMWCNTs

Elemental composition (atom %)									
Sample	Overall Percentage (atom%)		C1s					O1s	
	C1s	O1s	C = C	C – O	C = O	O – C = O	π – π	C = O	C – O
MWCNT	97.09	2.91	73.84	14.44	4.53	2.58	1.97	1.44	1.20
GAMWCNT	81.74	18.26	49.75	17.84	8.05	3.96	2.92	5.09	12.39

As can be seen from Table 7.2, the peak fractions of C=C decreased and those of C–O, C=O and –COO– increased after gallic acid treatment. This suggests that oxidation on the MWCNTs' surfaces occurred by the dissociation of the active p bonds in C=C bonds. The higher peak intensities at 531.7 and 533.47 eV in the O1s spectrum confirms the presence of large fractions of oxygen atoms in the form of C=O and C–O functional groups in the GAMWCNTs. In contrast, the pristine MWCNTs show the presence of feeble and generic functional groups such as C–O and C=O. These functional groups were generated unintentionally when the MWCNTs were exposed to the environment containing natural oxidizing agents such as ozone and hydroxyl radicals.

TEM images of the pristine MWCNTs and GAMWCNTs are illustrated in Figure 7.4. The pristine MWCNT shows smooth surface (Figure 7.4(a)) while, there is an increase in surface roughness for the modified GAMWCNTs (Figure 7.4(b)). The cut and open ends of the MWCNTs were separated completely, (which may be due to the partial damage of graphitic (sp^2) carbon after functionalization). This separation can be attributed to the carboxylation stages and replacement of carboxyl groups. The defects are the places for characterizing Gallic acid in the main structure of MWCNT. As the defects increased in the structure, the carboxylic groups (defects) in the structure of MWCNT increased the stability of MWCNT in the base fluid rose considerably.

Figure 7.4 (c) shows the measured zeta potentials values of GAMWCNTs as a function of pH. It can figure out that GAMWCNTs show high negative values in the range of -16 mV to -52.4 mv for the pH range of 2.7 to 9.56 and it's far from the isoelectric point. It can show that in the pH range of 3.1 to 9.56 the GAMWCNTs have strong electrostatic repulsion force which avoids the MWCNTs to aggregate by noncovalent interactions such as π - π interactions or H-bonding. This phenomenon can be attributed to the oxygen functional groups at the surface of MWCNTs. Therefore, the MWCNTs aqueous media is stable at pH more than 3.1 (the zeta potential around -32.1 mv). It is noteworthy to highlight that in this work, the GAMWCNTs aqueous suspensions is stable in even slightly acidic conditions. In more acidic solution (PH<3.1), the material tends to agglomerate and undergo intermolecular dehydration catalyzed by H^+ , leading to the coupling of MWCNTs via ether linkages. The GAMWCNTs nanofluids became more stable by adding alkali to the aqueous suspension, which leads to generation of additional negative charge in nanoparticles.

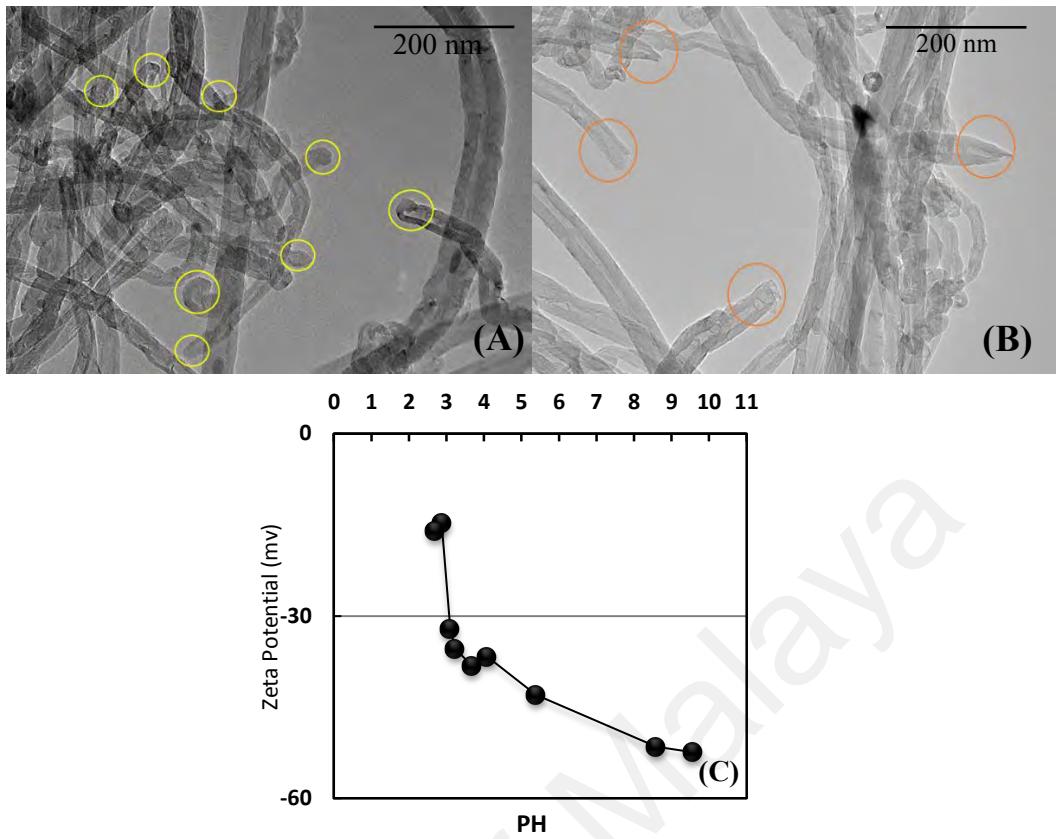


Figure 7.4: (A, B) TEM images of pristine MWCNTs and GAMWCNTs, and (C) zeta potential values of GAMWCNT-water nanofluid as a function of PH

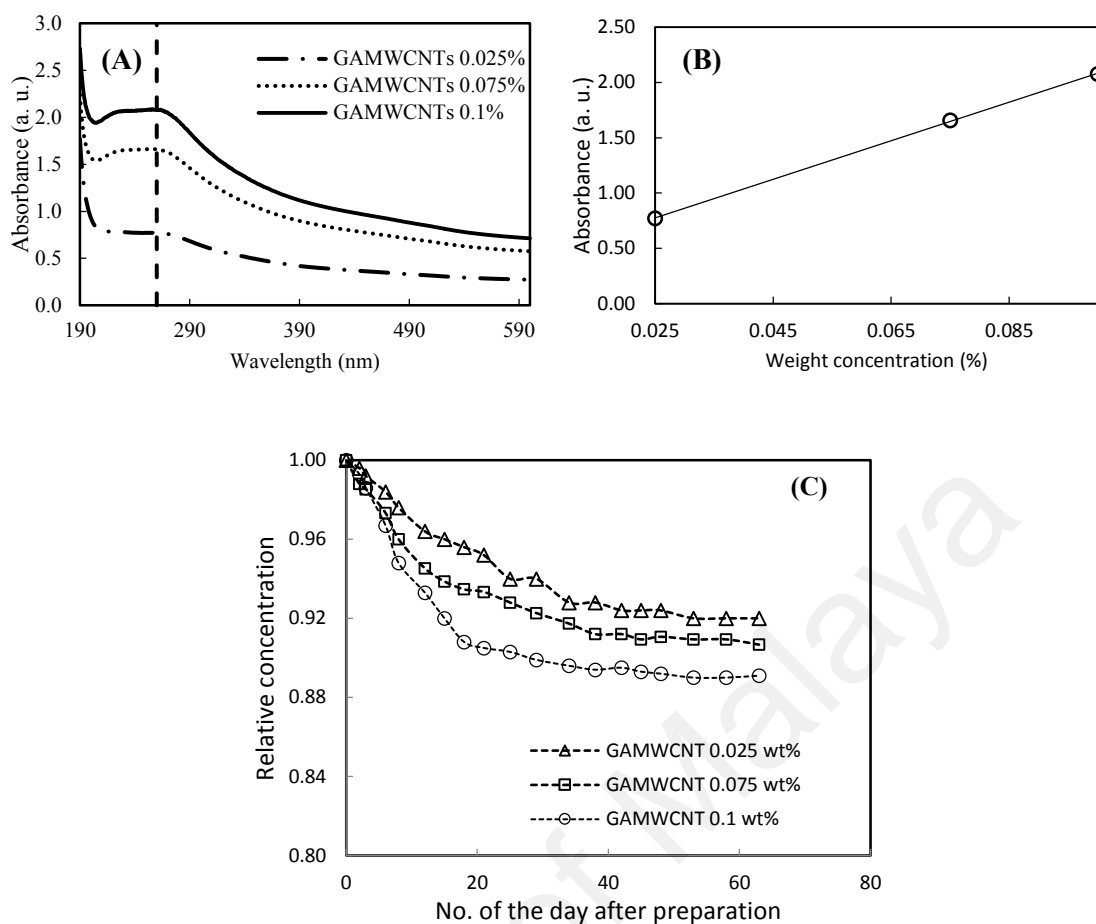


Figure 7.5: (A) UV–vis spectroscopy analyses of water-based GAMWCNTs nanofluids at various wavelengths and concentrations, (B) absorption values of GAMWCNTs dispersed in DI water at various concentrations and (C) colloidal stability of GAMWCNTs dispersed in DI

UV-vis spectra analysis is a typical procedure used for investigating stability of nanoparticles aqueous suspensions. In accordance with the Beer–Lambert’s law, there is a direct connection between the absorbance of a colloidal suspension and the mass fraction of the absorbing species such as particles in the solution. Following this law, the absorption spectrum of the prepared nanofluids exhibited a maximum peak at around 260 nm corresponding to $\pi - \pi$ transition of conjugation system in the polyaromatic structures.

The UV–vis spectroscopy analysis for the GAMWCNTs aqueous nanofluids with various weight fractions were evaluated and the photometric analysis of the UV–vis spectroscopy was employed to pursue the variation of relative weight fraction of the samples versus times (day). The UV–vis spectra for the GAMWCNT aqueous nanofluids with various mass fractions are illustrated in Figure 7.5 (a). It shows that the absorbance peak values for all the samples were located in the wavelength of 260 nm that is due to the presence of GAMWCNTs. Also it can be seen that the absorbance of MWCNTs decreases from 0.1 to 0.025 wt.% that indicates the increasing amount of dispersed MWCNTs will increase the value of absorbance. As shown in Figure 7.5, there is a good linear relationship between the concentration of MWCNTs and the absorbance, which conforms to the Beer's law and shows that MWCNT nanoparticles were dispersed well in the base fluid.

Figure 7.5 illustrates the variation of stability of water-based GAMWCNTs nanofluids as a function of the number of the days after preparation. It is seen that the relative concentration of GAMWCNTs suspensions decreases with the number of days after sample preparation. However, the relative concentration of the nanofluids is almost constant after Day 45 for all samples. The highest sedimentation magnitude of 8, 9.33 and 10.9% are found, respectively, for the weight concentration of 0.025, 0.075 and 0.1%. This verifies the stability of the GAMWCNTs-water nano-coolants. Digital image of gallic acid-functionalized MWCNTs (GAMWCNTs) dispersed in DI water after 90 days, is represented in Figure 7.5 (c).

7.2 Thermo-physical properties of GAMWCNTs nanofluids

The effective viscosity of nanofluids containing GAMWCNTs and DI water were measured experimentally and the data are shown in Figure 7.6. The effective dynamic viscosity is shown as a function of the nanoparticle concentration and temperature at a fixed shear rate of 150 S^{-1} . It can be observed that there is only a slight increase in the

dynamic viscosity of the samples by loading of the GAMWCNTs relative to that for DI water. This phenomenon is expected since a low weight concentration of GAMWCNTs is used in our samples. (Sadri et al., 2017) This slight increase in viscosity is also indicated the benefit of using covalent functionalization method rather than using non-covalent method including surfactants such as SDBS, triton X-100 and gum Arabic (GA), which lead to higher viscosity of corresponding nanofluids, moreover the GAMWCNTs remain more suspended in the DI water. According to the previous studies feeble dispersibility and consequently increasing agglomeration size will directly increase viscosity of nanofluids. (Azadeh Ghadimi & Metselaar, 2013) It can also be observed from Figure 7.6 that the dynamic viscosity of the GAMWCNTs nanofluids declines by increasing temperature, which may be attributed to weakening of intermolecular forces (S. J. Aravind et al., 2011). This observation corroborates well the findings of Aravind *et al.* (S. J. Aravind et al., 2011), Ko *et al.* (Ko et al., 2007) and Sadri *et al.* (Sadri et al., 2016), who observed that there is decrease in viscosity when the fluid temperature is increased. The rather mild increase in the effective viscosity with nanoparticle concentration is an important advantage, since the increase in viscosity could undermine the overall positive impact of enhanced thermal conductivity in heat transfer due to the pumping fluid penalty.

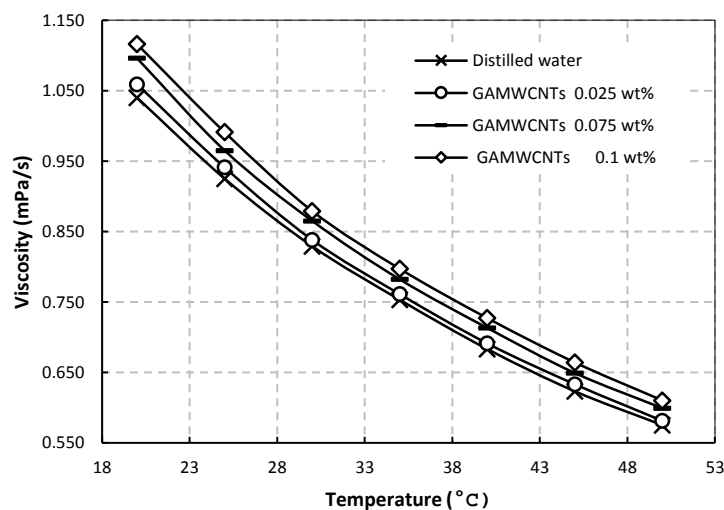


Figure 7.6: Dynamic viscosity of water-based GAMWCNT nanofluids as a function of temperature at various concentrations

The experimentally measured values of viscosity for the water-based GAMWCNTs suspension were compared with those calculated with the empirical correlations of Batchelor (Khanafar & Vafai, 2011) and Einstein (J.-H. Lee et al., 2008) using equations (4.1) and (4.2), respectively, and the results are depicted in the Figure 7.7. This indicates that the values calculated from experimental data are in good agreement with those determined from empirical correlations for water-based GAMWCNTs nanofluid with a maximum error of $\sim 7\%$. It is crucial to keep down the increment in viscosity of the heat transfer working fluids by using an appropriate synthesis method and considering low weight concentrations for the nano-coolants, particularly in heat transfer systems, in where the overall positive impact in heat transfer is being undermined by pumping fluid penalty occurs with an increase in viscosity (Timofeeva et al., 2009; W Yu et al., 2010). Hence, in order to maximize the heat transfer performance of closed-loop systems in which nanofluids are used as the working fluids, it is imperative to maintain the resultant colloidal mixtures in Newtonian behavior since this will reduce the pumping power compared to non-Newtonian fluids.

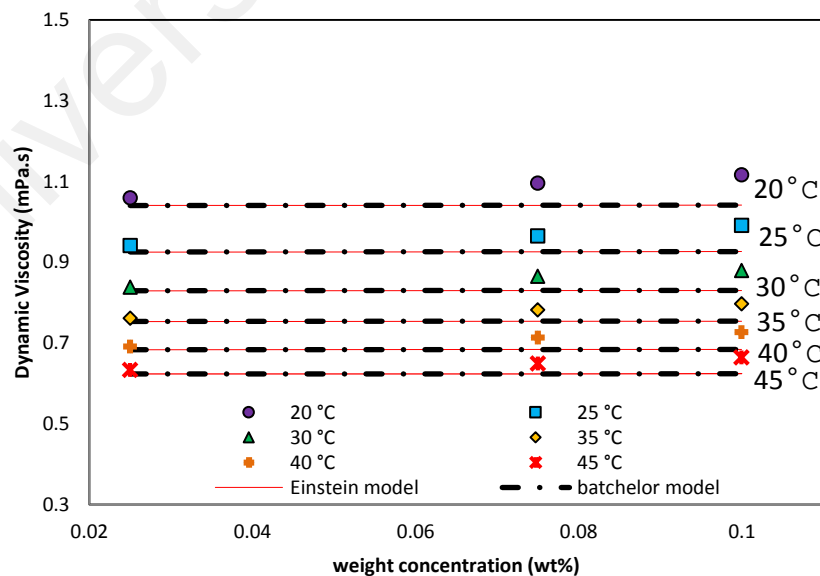


Figure 7.7: Viscosity of water-based GAMWCNTs nanofluids compared with those calculated by theoretical models as function of concentration and temperature at the shear rate of 150 s⁻¹

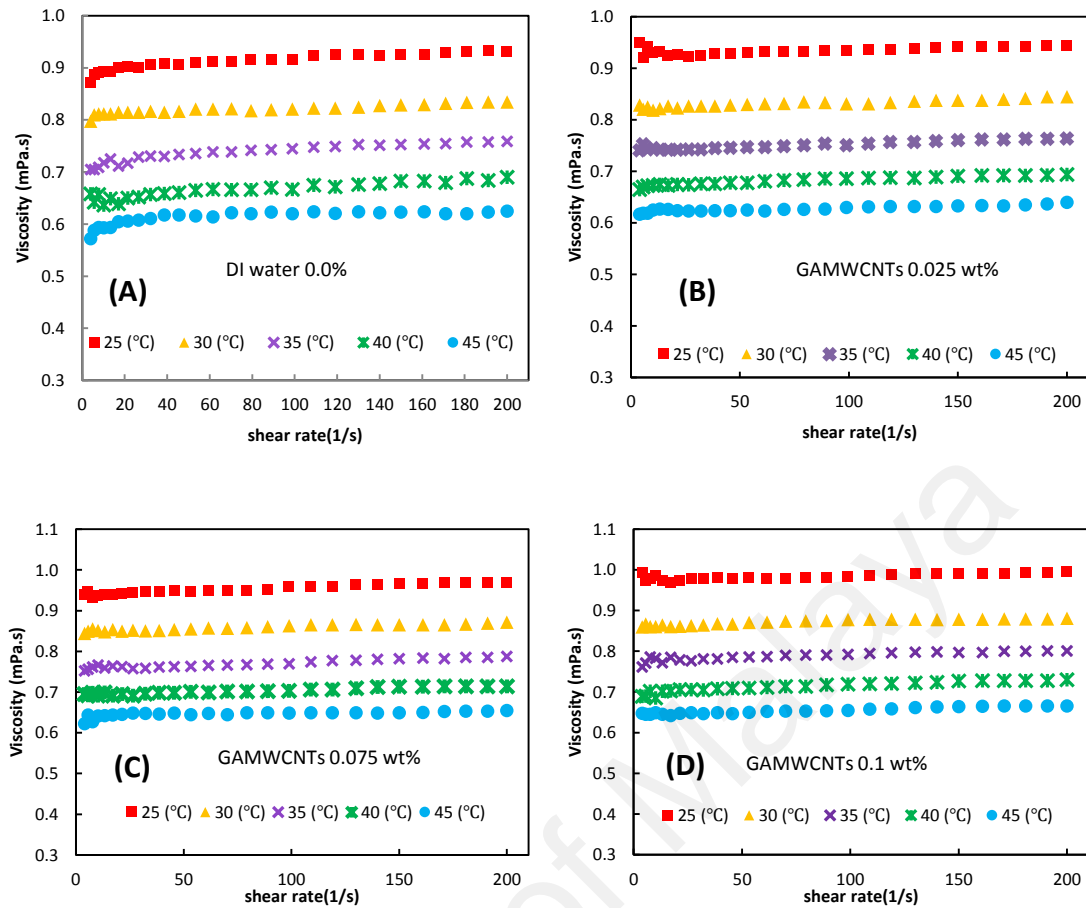


Figure 7.8: Plots of the measured values of dynamic viscosity versus shear rate for GAMWCNTs aqueous nanofluids at various mass fraction((A) DI water,(B) 0.025 wt%,(C) 0.075 wt% and (D) 0.1 wt %) and temperatures

The Figure 7.8 represented the dynamic viscosity of GAMWCNT nano-coolants as a function of shear rate at different temperatures. As shown in Figures 7.8(A-D), the water-based GAMWCNT nanofluids synthesized in this research exhibit Newtonian behavior, whereby the viscosity of the nanofluids remains constant with an increase in the shear rate. From a thermal transport perspective, this material is deemed suitable as an additive to enhance heat transfer performance.

The thermal conductivity of a coolant is one of the parameters that play a significant role in increasing the heat transfer rate of heat exchangers. Hence, the thermal conductivity of the GAMWCNT-DI aqueous suspensions was measured experimentally in this study and the data are represented in Figure 7.9. The thermal conductivity of the GAMWCNT-DI water nanofluids was plotted as functions of temperature and

nanoparticle concentration. It could be noted that only nanofluids with low concentrations of GAMWCNTs were considered in this study in order to prevent a drastic increase in viscosity. The thermal conductivity of the base fluid (DI water) was compared with that from the National Institute of Standards and Technology (NIST) database and there is good agreement between these values (Ramires et al., 1995), with an error less than 1%. It is evident from Figure 7.9 that the thermal conductivity of the GAMWCNT-DI water nanofluids is significantly greater than that for the base fluid. Moreover, it is evident that the thermal conductivity of the GAMWCNT aqueous suspensions and base fluid increases with an increase in fluid temperature. Nonetheless, the thermal conductivity enhancement is higher for the GAMWCNT aqueous nanofluids at higher nanoparticle concentrations. Based on Figure 7.9, it can be deduced that temperature plays a significant role on enhancing the effective thermal conductivity of nanofluids, which resulted in increase in Brownian motion of the GAMWCNTs dispersed in the base fluid (S. J. Aravind et al., 2011). The maximum thermal conductivity enhancement obtained is 5.024, 14.13 and 21.51% for nanoparticle concentration of 0.025, 0.075 and 0.1 wt.% at 45 °C.

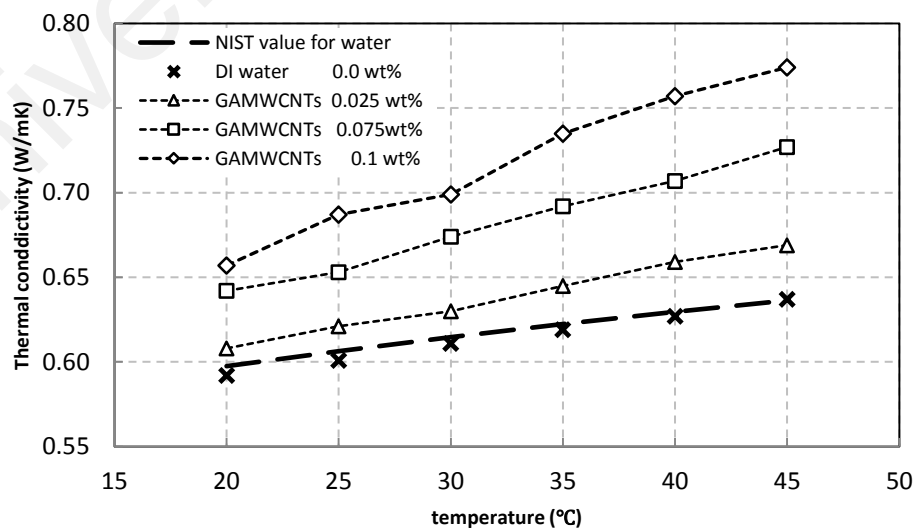


Figure 7.9: Effective thermal conductivity of water-based GAMWCNT nanofluids as a function of temperature at various concentrations

The specific heat capacity of the GAMWCNTs aqueous suspensions as functions of weight concentration and temperature is illustrated in Figure 7.10. The specific heat capacity for distilled water is also plotted in the same graph for comparison. It can be seen that the specific heat capacity of the nanofluids decreases with an increase in the GAMWCNTs mass fraction, whereby the average reduction in specific heat capacity is within a range of 0.33–1.42% compared to that of the DI water, exhibiting insignificant decrease. This decrease is due to the fact that the GAMWCNT nanoparticles have a lower specific heat capacity than that of the base fluid.

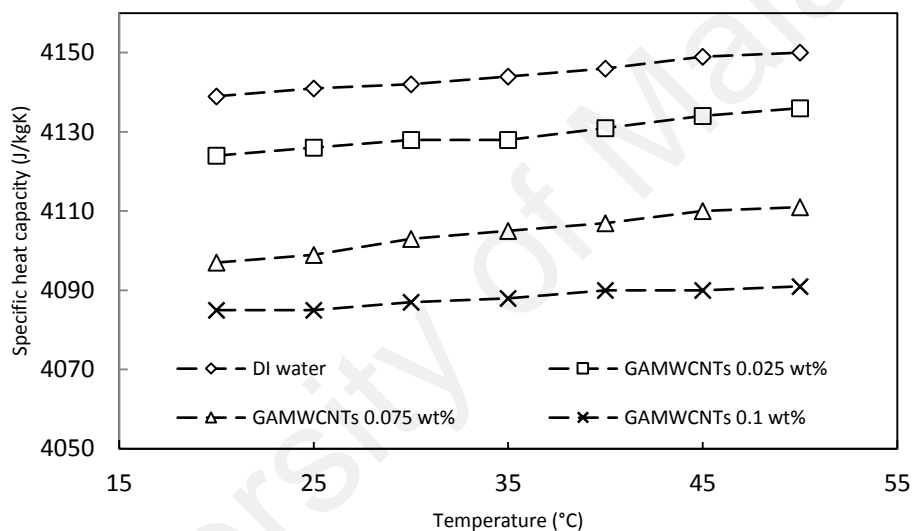


Figure 7.10: variation of Specific heat capacity of water-based GAMWCNT nanofluids as a function of temperature at various concentrations

The density was measured for the GAMWCNT aqueous suspensions and base fluid at various temperatures and the results are presented in Table 7.3. It can be seen that there is a decrease in the density of the water-based GAMWCNTs nanofluids and DI water with an increase in fluid temperature, which leads to the liquid thermal expansion. There is a slight increment in the density for the GAMWCNT-DI water nanofluids with an increase in nanoparticle concentration. The increase in density can be attributed to the density of the GAMWCNTs, which is higher than that of the base fluid. Hence, increasing the particle loading will increase the density of the nanofluid. The maximum

increase in density of the GAMWCNT-DI water nanofluid is 0.055% for a nanoparticle concentration of 0.1 wt.% at 30°C. However, the density decreases by approximately 0.6% when the temperature is increased from 20 to 40°C for the same nanoparticle concentration.

Table 7.3: Density of water-based GAMWCNT nano-coolants and DI water as a function of temperature and concentration

Concentration/temperature (°C)		Density (kg/m ³)				
		20	25	30	35	40
DI water	0 wt%	998.00	996.85	995.50	993.90	992.00
GAMWCNT	0.025 wt%	998.10	997.00	995.60	994.05	992.10
GAMWCNT	0.075 wt%	998.40	997.25	995.85	994.35	992.35
GAMWCNT	0.1 wt%	998.50	997.35	995.95	994.45	992.50

7.3 Heat Transfer and hydrodynamic properties

A series of experiments were conducted for the water-based GAMWCNT-DI nanofluids (nanoparticle weight concentration: 0.025, 0.075 and 0.1%) by varying the Reynolds number from 6371 to 15927 in order to determine the convective heat transfer of the aqueous suspensions in turbulent flow regime. The input power was kept fixed at 615 W. The results are shown in Figure 7.11 for a constant inlet temperature of 30°C. It can be observed that the convective heat transfer coefficient increases when the Reynolds number is increased for both the base fluid and GAMWCNT-DI water nanofluids. It can also be observed that the nanoparticle concentration affects the heat transfer coefficient of the nanofluids. The remarkable enhancement in convective heat transfer coefficient of the working fluids can be associated with the decreased thickness of thermal boundary layer and the increased thermal conductivity in the presence of GAGNPs aqueous suspensions, which result in a significant reduction in thermal resistance between the inner wall of tube and the working fluid as compared to that of the DI water (S. Z. Heris, M. N. Esfahany, & S. G. Etemad, 2007b; Qu & Wu, 2011; Tsai et al., 2004; Yarmand et al., 2016). According to (S. J. Aravind et al., 2011;

Yulong Ding et al., 2006), carbon nanomaterials (e.g. graphene nanoplatelets and carbon nanotubes) tend to reduce the thickness of the thermal boundary layer. The specific surface area and Brownian motion of the nanoparticles also play a role in enhancement of the convective heat transfer coefficient. In this study, the convective heat transfer coefficient of the nanofluids increases by 7.94, 22.37 and 33.05% for a nanoparticle concentration of 0.025, 0.075 and 0.1 wt.%, respectively.

To assess the convective-to-conductive heat transfer ratio of GAMWCNT aqueous suspensions, the average Nusselt number determined from Eq.3.3 was plotted as a function of Reynolds number and nanoparticle concentration. The results are shown in Figure 7.11 and it can be seen that there is a significant increase in the Nusselt number with an increase in the Reynolds number as well as concentration of GAMWCNTs relative to that for the base fluid. The greater Nusselt number for the GAMWCNT nanofluids is attributed to the large surface area, Brownian motion and thermophysical properties of suspended GAMWCNTs and therefore the heat transport capability of nanofluid elevates further (Sundar et al., 2014). Also, it may be devoted to properties of nanofluid suspension in terms of lower specific heat and higher thermal conductivity compared to that of water. The maximum increase in the Nusselt number of the GAMWCNT-DI water nanofluids is found to be 4.69, 10.93 and 16.30% for a nanoparticle concentration of 0.025, 0.075 and 0.1 wt.%, respectively. This maximum increase is achieved when $Re = 15927$.

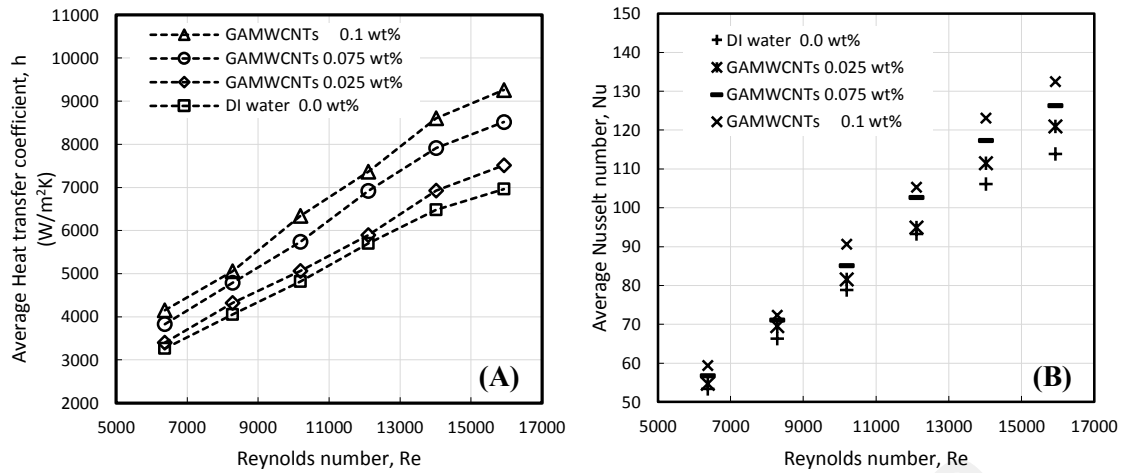


Figure 7.11: (a) average heat transfer coefficient and (b) average Nusselt number of the GAMWCNT-water nano-coolants and distilled water at various Reynolds number

The pressure drop of the GAMWCNT-DI water nanofluids flowing through the test section recorded over a range of Reynolds number is shown in Figure 7.12(a). The corresponding friction factor values were calculated using Eq. (3.9) and the results are shown in Figure 7.12(b). The results show that there is a small increment in both the pressure drop and friction factor for the GAMWCNT-DI water nanofluids relative to those for DI water. The maximum increase in the friction factor is found to be ~ 1.38 , 3 , 3.62% , respectively, for a nanoparticle concentration of 0.025 , 0.075 and 0.1 wt.%. This increment in friction factor is mainly due to the slight increment in viscosity for all GAMWCNT-DI water nanofluids (Figure 7.6) which required slight increment in fluid velocity since the corresponding Reynolds number is constant (Eq.3.4). Hence, it can be seen that the velocity of the working fluid plays a vital pattern in increasing the pressure drop and friction factor compared to DI water in convective heat transfer systems. This matter can be acknowledged by revisiting Eq. (3.9) for the pressure drop and friction factor, and Eq. (3.4) for the Reynolds number.

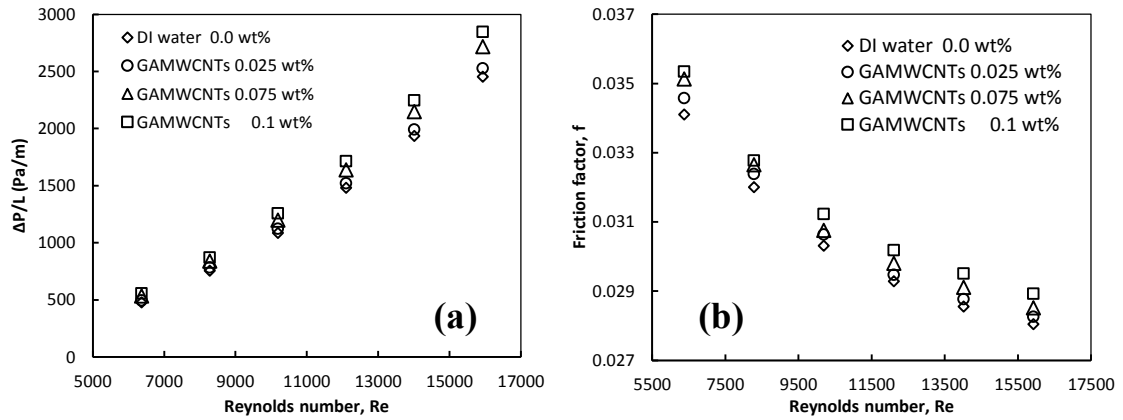


Figure 7.12: Variation of (a) pressure drop and (b) friction factor as a function of Re for the GAMWCNT-water nanofluids in the test section

The pumping characteristics and power consumption of a heat transfer set-up is an important factor in respect of energy savings and energy consumption in order to evaluate the suitability of a working fluid and optimize energy usage of thermal equipment. The relative pumping power of water-based GAMWCNT nano-coolants and DI water are calculated using the equation (4.4) and the results presented in Figure 7.13 as a function of mass fraction. It is noteworthy that the Figure 7.13 shows only a small increment in relative pumping power with GAMWCNT nanoparticles loading. The reason behind this phenomenon can be associated to the low mass concentrations considered for the nanofluids in this study.

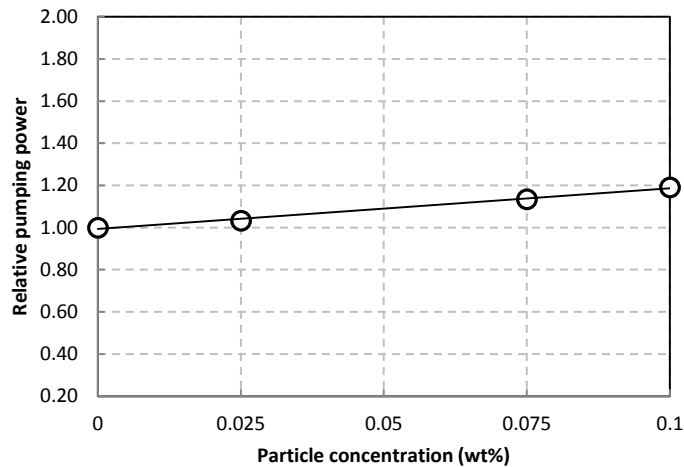


Figure 7.13: Relative pumping power of the GAMWCNT -water nanofluids and distilled water

The performance index (ε) was calculated using Eq. (4.5) in order to assess the economic performance of the novel, eco-friendly GAMWCNT-DI water nanofluids synthesized in this study as potential fluids in heat transfer systems such as solar collectors and heat exchangers (Amiri, Sadri, Shanbedi, Ahmadi, Kazi, et al., 2015).

Figure 7.14 indicates the performance index of the GAMWCNT aqueous suspensions over a range of Reynolds number and various nanoparticle concentrations. It can be observed that the performance index is higher than 1 for all samples, which shows the advantage of using these novel nanofluids in heat transfer systems. It is apparent that the performance index increases with increasing the concentration of GAMWCNTs in the base fluid. This implies that these eco-friendly nanofluids have higher effectiveness when the particle loading is increased. Figure 4.14 shows that the performance index of the GAMWCNT nanofluids tends to increase with an increase in the Reynolds number (regardless of the nanoparticle concentration), indicating that the GAMWCNT-DI water nanofluids are suitable alternative coolants for heat transfer applications.

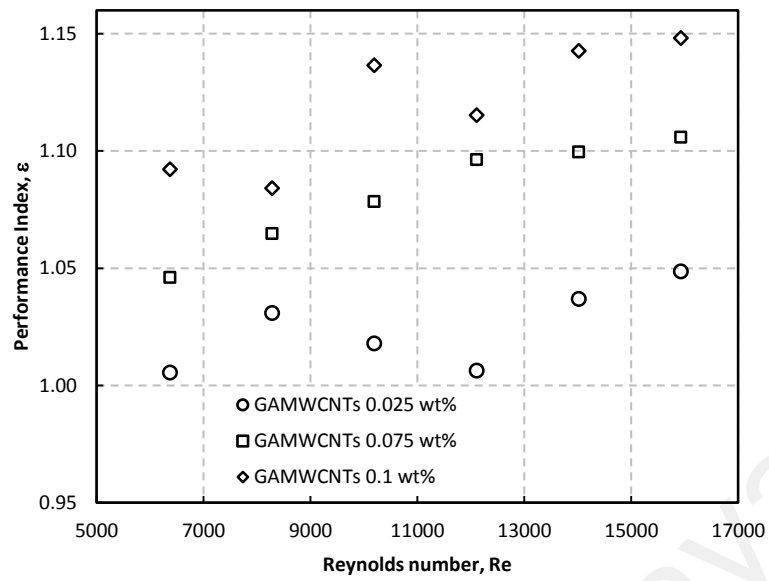


Figure 7.14: Performance index Variation of the water-based GAMWCNT nanofluids versus Reynolds number at different concentrations

University of Malaya

**CHAPTER 8: MODELING OF TURBULENT CONVECTIVE HEAT
TRANSFER OF NANOFLUIDS CONTAINING GREEN COVALENTLY
FUNCTIONALIZED GRAPHENE NANOPATELETS IN A HORIZONTAL
CIRCULAR HEATED TUBE**

CFD was used to investigate the thermal performance of clove-treated GNP nanofluids (CGNP) nanofluids flowing in a horizontal circular heated tube under steady-state fully developed turbulent flow condition. Figure 8.1 shows the geometry of the horizontal circular heated tube. The total length of the tube is 1.4 m, the heated section length is 1.2 m, and the inner diameter of the tube is 10 mm. The tube was subjected to a constant heat flux of 600 W. A commercial CFD software package, ANSYS Fluent v18 (double precision, 3D version), was installed in a computer with Intel® Core™ i7-4770 3.40 GHz processor and 16 GB of random access memory for these simulations. The grid was generated using meshing module provided in the software package. In this model, the pipe wall thickness was not considered and only the fluid control volume was modelled. A structured grid with 9 inflation layers was used to mesh the region near the surface (walls) of the control volume where large gradients of velocity and temperature exist. Unstructured grid was used for the interior volume cells. The grid of the solution domain, which includes the pipe fluid volume, is shown in Figure 8.2.

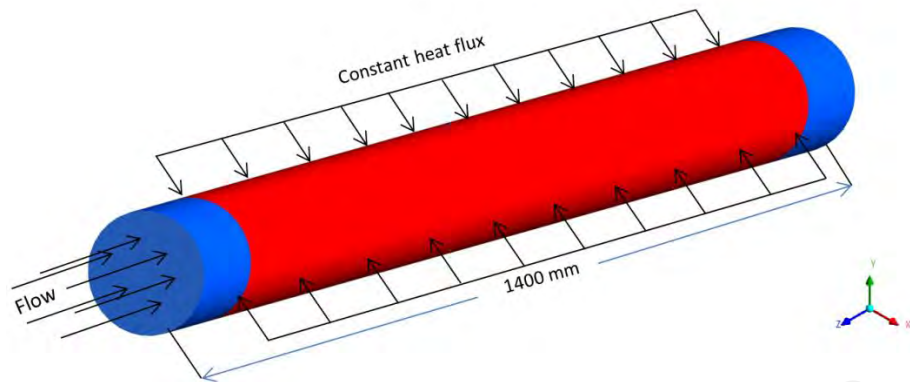


Figure 8.1: Geometry of the three-dimensional horizontal circular heated tube

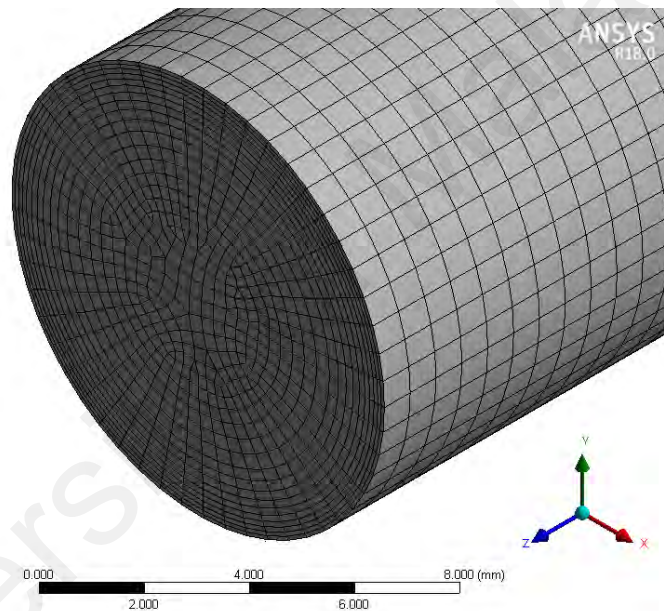


Figure 8.2: Grid of the solution domain

It was assumed that the nanofluid is homogeneous single-phase fluid, which means that the CGNPs and base fluid (DI water) have the same temperature and velocity. Since the properties of the nanofluid were obtained empirically, the single-phase flow model is more suitable for the analysis compared with the two-phase flow model. It was also assumed that the nanofluid is a Newtonian fluid.

The steady-state governing equations of mass, momentum, and energy for single-phase flows are presented as follows (Blazek, 2015; Chung, 2010):

Conservation of mass:

$$\nabla(\rho\vec{V}) = 0 \quad (6.1)$$

Conservation of momentum:

$$\nabla \cdot (\rho\vec{V}\vec{V}) = -\nabla P + \mu \nabla^2 \vec{V} + \rho\vec{g} \quad (6.2)$$

Conservation of energy:

$$\nabla \cdot (\rho C_p \vec{V}T) = K_{eff} \nabla^2 T + \nabla(\tau_{eff}\vec{V}) \quad (6.3)$$

where K_{eff} is the effective thermal conductivity of a homogeneous single-phase fluid. In order to solve the governing equations, the thermo-physical properties of the nanofluid such as density (ρ), viscosity (μ), specific heat capacity (C_p), and thermal conductivity (K) were determined from experiments at an inlet temperature of 30°C, as presented in Table 8.1.

Table 8.1: Thermo-physical properties of the CGNP nanofluid at an inlet temperature of 30°C

Thermo-physical properties	DI water 0 wt. %	CGNPs 0.025 wt. %	CGNPs 0.075 wt. %	CGNPs 0.1 wt. %
Thermal conductivity (W/m.K)	0.611	0.642	0.667	0.691
Viscosity (mPa.s)	0.829	0.860	0.884	0.907
Specific heat capacity (J/kg.K)	4142	4114	4086	4057
Density (kg/m ³)	995.50	995.85	996.15	996.45

The boundary conditions are described as follows. Turbulent flow condition was used for the liquid phase. Uniform heat flux and no-slip boundary condition were used for the walls of the tube. The fluid enters the tube at a constant inlet temperature (T_{in}) of 303.15 K and uniform axial velocity (ϑ). The flow and temperature field were assumed to be fully developed at the outlet of the tube. It was assumed that the tube walls were perfectly smooth and the external surface of the tube walls was insulated. The fluid

velocity at the wall boundary was set as zero such that the boundary condition for the velocity is $v_{\text{wall}} = 0$. The flow and thermal fields were assumed to be symmetrical with respect to the axial plane. The acceleration of gravity was set as 9.8 m/s^2 . Three CGNP concentrations were considered for the simulations: 0.025, 0.075, and 0.1 wt%.

To solve the governing equations of the flow field, it is necessary to use experimental data or approximate models to account for turbulence phenomena. In this study, the nanofluid flow inside the horizontal tube was solved over a Re number range of 6,371–15,927. The two-equation SST k - ω turbulence model proposed by Menter (Menter, 1994) was used to simulate the turbulent flow in order to determine the convective heat transfer coefficient. The SST k - ω turbulent model is given by the following equations:

$$U_j \frac{\partial \rho k}{\partial x_j} = \tau_{ij} \frac{\partial u_i}{\partial x_j} - \beta^* k \rho \omega + \frac{\partial}{\partial x_j} \left[(\mu + \sigma_k \mu_t) \frac{\partial k}{\partial x_j} \right] \quad (6.4)$$

$$U_j \frac{\partial \rho \omega}{\partial x_j} = \frac{\gamma}{v_t} \tau_{ij} \frac{\partial u_i}{\partial x_j} - \beta \omega^2 + \frac{\partial}{\partial x_j} \left[(\mu + \sigma_\omega \mu_t) \frac{\partial \omega}{\partial x_j} \right] + 2(1 - F_1) \rho \sigma_{\omega 2} \frac{1}{\omega} \frac{\partial k}{\partial x_j} \frac{\partial \omega}{\partial x_j} \quad (6.5)$$

The default values for the SST k - ω model were used for the simulations (Menter, 1994):

$$\sigma_{k1} = 0.5, \sigma_{\omega 1} = 0.5, \beta_1 = 0.075, \beta^* = 0.09, \kappa = 0.41, \gamma_2 = \beta_2 / \beta^* - \sigma_{\omega 2}. K^2 / \sqrt{\beta^*} \text{ where}$$

$$v_t = \frac{k}{\omega} \quad (6.6)$$

$$\tau_{ij} = \mu_t \left(\frac{\partial u_i}{\partial x_j} + \frac{\partial u_j}{\partial x_i} - \frac{2}{3} \frac{\partial u_k}{\partial x_k} \delta_{ij} \right) - \frac{2}{3} \rho k \delta_{ij} \quad (6.7)$$

$$F_1 = \tanh(\text{arg} g_1^4) \quad (6.8)$$

$$arg_1 = \min \left[\max \left(\frac{\sqrt{k}}{0.09\omega y}, \frac{500\nu}{y^2\omega} \right); \frac{4\rho\sigma_{\omega 2}k}{CD_{k\omega}y^2} \right] \quad (6.9)$$

where y is the distance to the next solid surface and $CD_{k\omega}$ is the positive portion of the cross-diffusion term that can be determined from the following equation:

$$CD_{k\omega} = \max \left(2\rho\sigma_{\omega 2} \frac{1}{\omega} \frac{\partial k}{\partial x_j} \frac{\partial \omega}{\partial x_j}, 10^{-20} \right) \quad (6.10)$$

The set of differential equations (governing equations) was discretized using the finite volume technique and solved iteratively by using the line-by-line method. The second-order upwind scheme was used for the convective and diffusive terms whereas the well-known SIMPLEC algorithm was used for the velocity-pressure coupling. For the convergence criteria, the sum of the scaled absolute residuals for the mass and velocity parameters were restricted to less than 10^{-3} and temperature was restricted to less than 10^{-6} . In order to ensure that the simulations were independent of the grid size, grid independence test was carried out for three grid sizes. It can be seen from Figures 8.3(a) and (b) that ~2,000,000 elements provide satisfactory results for the Nu and pressure drop. Increasing the grid size beyond 2,000,000 elements does not significantly influence the accuracy of the results. Based on the results, the optimal number of elements (i.e. 2,000,000) was selected in order to reduce computational time. More details on the effect of grid size on the Nu number and pressure drop are presented in Table 8.2 and Table 8.3, respectively.

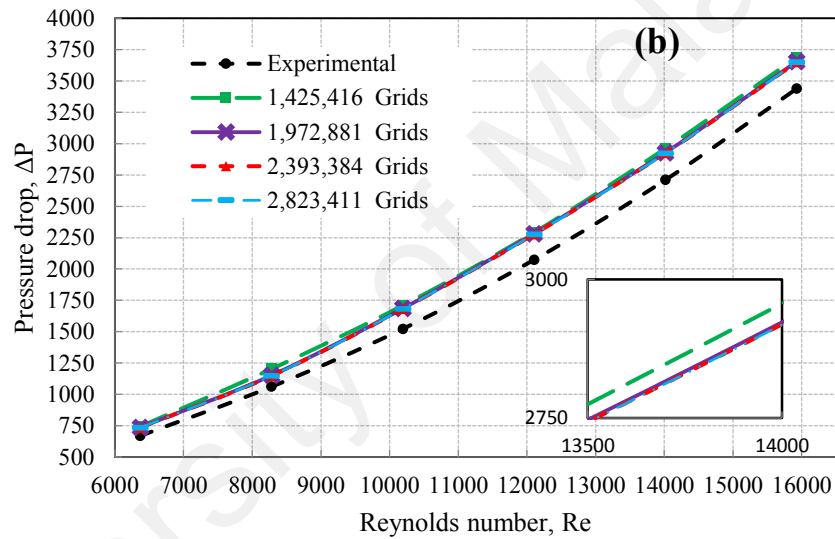
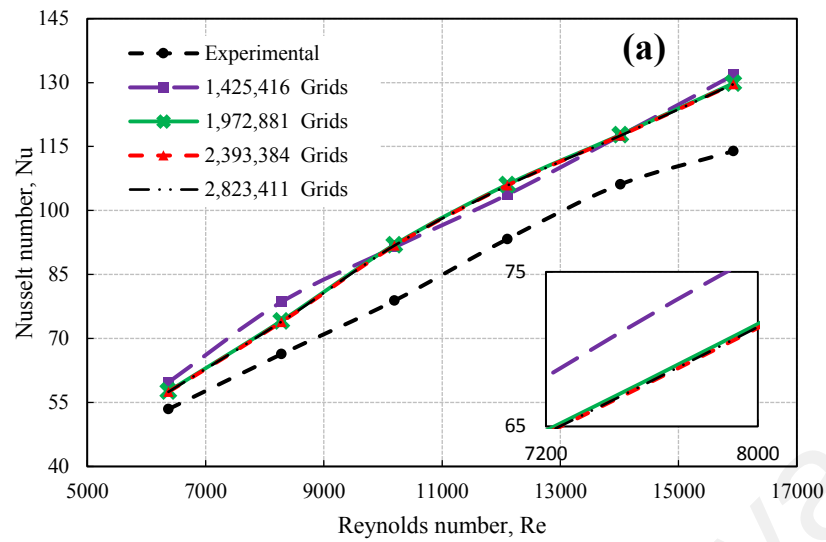


Figure 8.3: Grid independence test for the (a) Nu number and (b) pressure drop as a function of the Re number

Table 8.2: Effect of grid size on the Nu number for DI water

Reynolds number	Nusselt numbers, Nu					
	6371	8282	10193	12104	14015	15927
1,425,416 Grids	59.7213915	78.544463	91.3824366	103.726627	117.56892	131.76032
1,972,881 Grids	57.6303595	74.130975	91.9865781	106.09951	117.74801	129.826043
2,393,384 Grids	57.466916	73.865987	91.7359	105.89172	117.57621	129.62607
2,823,411 Grids	57.476412	73.926164	91.780276	105.86487	117.54243	129.62446
Experimental	53.41899	66.330881	78.857955	93.307219	106.13137	113.92504

Table 8.3: Effect of grid size on the pressure drop for DI water

Reynolds number	Pressure drop, ΔP					
	6371	8282	10193	12104	14015	15927
1,425,416 Grids	743.5361	1202.98584	1709.48568	2291.7849	2962.1777	3688.4428
1,972,881 Grids	736.4414	1151.11192	1685.1436	2282.0588	2928.3839	3655.4616
2,393,384 Grids	734.9233	1148.01736	1681.5624	2278.1842	2924.6347	3650.6411
2,823,411 Grids	734.8858	1148.56392	1682.12072	2277.8448	2923.9902	3650.5728
Experimental	669	1061	1522	2074	2711	3439

The results were obtained once convergence was achieved, as defined by the set of convergence criteria. The wall and bulk temperatures and the shear stress data along the heated tube were then collected. The friction factor (f), pressure drop (ΔP), local and average convective heat transfer coefficients (h), and Nusselt number (Nu) were then computed using the following equations based on the shear stress, wall and bulk temperature data along the heated tube obtained from CFD simulations.

$$f = \frac{8\tau_w}{\rho v^2} \quad (6.12)$$

$$\Delta p = \frac{4L\tau_w}{D} \quad (6.13)$$

$$\bar{h} = \frac{q}{T_w - T_b} \quad (6.14)$$

$$h_{(x)} = \frac{q}{T_{w(x)} - T_{b(x)}} \quad (6.15)$$

$$\overline{Nu} = \frac{\bar{h} \cdot D}{k} \quad (6.16)$$

$$Nu_{(x)} = \frac{h_x \cdot D}{k} \quad (6.17)$$

where, τ_w , v , ρ , h , q , D , k , T_b , and T_w represent the wall shear stress, flow velocity, fluid density, convective heat transfer coefficient, heat flux, inner tube diameter, thermal conductivity of the fluid, bulk temperature, and wall temperature, respectively.

8.1 Validation of simulation results

In order to ensure accuracy of the CFD model and the numerical procedure, the simulations were carried out using the same geometry and dimensions of the actual horizontal circular heated tube and the same operating conditions as those used in the experiments. The CFD model developed in this study includes all the components used in the experimental test section (see assembled the test section in Figure 3.10). The predicted average Nu for DI water inside the horizontal tube subjected to uniform heat flux were compared to those determined from experiments and empirical correlations proposed by Petukhov (Petukhov, 1970), Gnielinski (Volker Gnielinski, 1975), and Notter-Rouse (Khoshvaght-Aliabadi, Akbari, & Hormozi, 2016; Notter & Sleicher, 1972) and the results are plotted in Figure 8.4(a).

$$Nu = \frac{\left(\frac{f}{8}\right) Re Pr}{1.07 + 12.7 \left(\frac{f}{8}\right)^{0.5} (Pr^{2/3} - 1)} \quad (6.18)$$

Eq. (6.18) was used if $3000 < Re < 5 \times 10^6$ and $0.5 \leq Pr \leq 2000$.

$$Nu = \frac{\left(\frac{f}{8}\right) (Re - 1000) Pr}{1 + 12.7 \left(\frac{f}{8}\right)^{0.5} \left(Pr^{2/3} - 1\right)} \quad (6.19)$$

Here, Pr is the Prandtl number and f is the friction factor. Eq. (6.19) was used if $3 \times 10^3 < Re < 5 \times 10^6$ and $0.5 \leq Pr \leq 2000$.

$$Nu = 5 + 0.015 Re^{0.856} Pr^{0.347} \quad (6.20)$$

The friction factor (f) in Equations (6.18) and (6.19) were determined using the relationship proposed by Petukhov (Petukhov, 1970):

$$f = (0.79 \ln Re - 1.64)^{-2} \quad (6.21)$$

It is found that there is good agreement between the simulation data and those obtained from experiments and Notter-Rouse's and Petukhov's empirical correlations, with an

average relative deviation of 12.48, 13.72, and 11.31%, respectively. This may be due to the existence of conduction resistance in the experimental test section, which was not considered in the CFD model. Based on the results, it can be deduced that the CFD model is capable of simulating the heat transfer characteristics of the CGNP-DI water nanofluids.

The predicted friction factors for DI water were compared with those determined from experimental data and empirical correlations proposed by Petukhov (Petukhov, 1970) and Blasius (Blasius, 1907) (which are given by Equations (6.21) and (6.22), respectively) and the results are plotted in Figure 8.4(b).

$$f = 0.3164 Re^{-0.25} \quad (6.22)$$

This equation is valid for $3000 < Re < 10^5$.

The results are indeed encouraging since the average relative deviations in the friction factor between the simulations and those obtained from experiments and Petukhov's (Petukhov, 1970) and Blasius's (Blasius, 1907) empirical correlations are 8.94, 6.024, and 6.56%, respectively. This indicates that the CFD model is reliable to measure the hydrodynamic properties of CGNP-DI water nanofluids within the range of Re number investigated in this study.

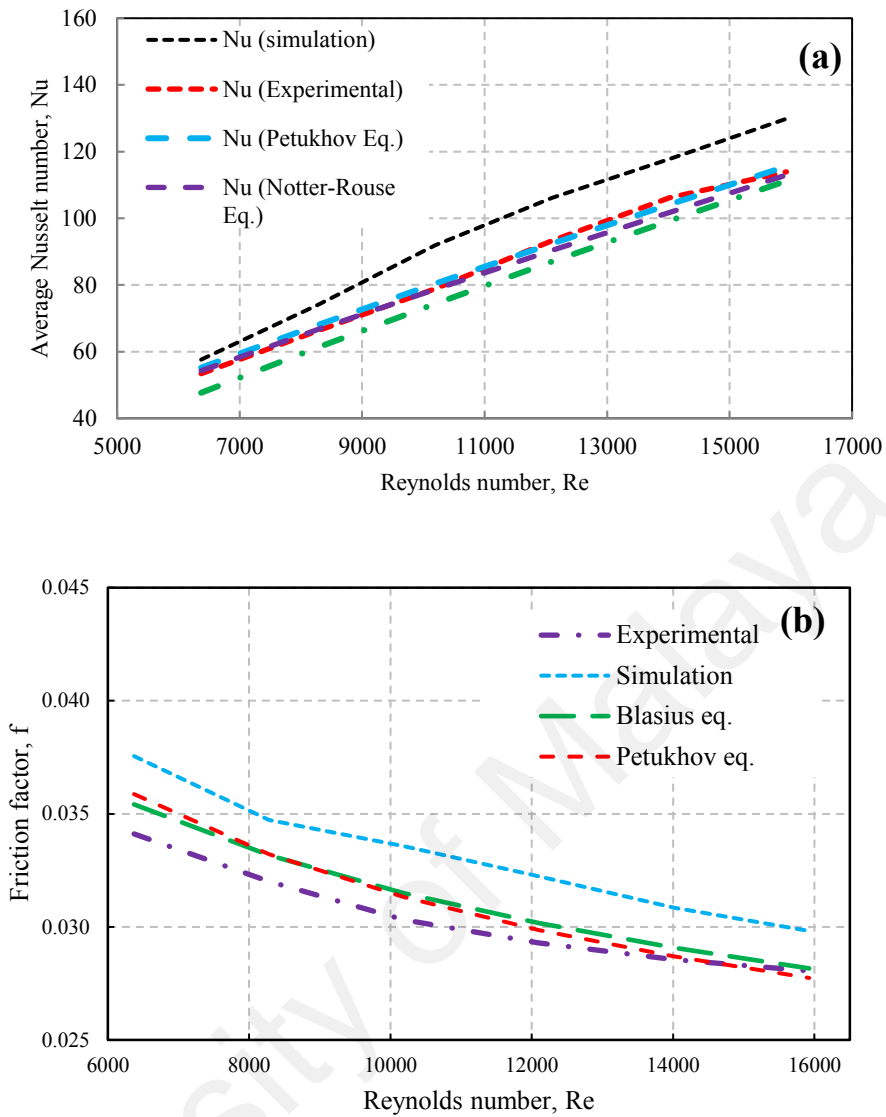


Figure 8.4: Comparison of the (a) average Nu number and (b) friction factor between simulation, experiment, and empirical correlations for DI water

Figure 8.5 shows the axial local Nu number for DI water as a function the Re number. It can be observed that the local Nu decreases with an increase in the axial distance along the horizontal tube, though the local Nu seems to be invariant when X/D is more than 15. It is apparent that there is a significant drop in the local Nu number when X/D is within a range of 0–15. The local Nu number remains relatively constant thereafter due to the fully developed turbulent flow. In addition, it is evident that increasing the Reynolds number reduces the temperature difference between the wall and bulk temperature which results in higher convective heat transfer and thus, higher Nu number.

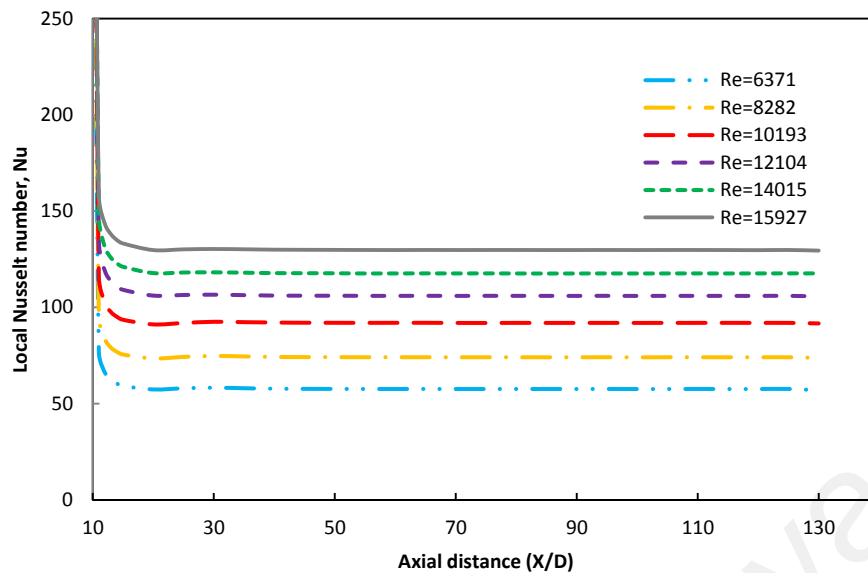


Figure 8.5: Variation of local Nusselt number along the horizontal tube for DI water in the turbulent flow regime at different Re numbers

A series of CFD simulations using the single-phase model were performed in order to predict the convective heat transfer coefficient and pressure drop of the CGNP-DI water nanofluids flowing in the horizontal tube with an input power of 600 W. The Re number was varied from 6,371 to 15,927, indicating that the simulations were conducted for turbulent flow condition. Likewise, three CGNP concentrations were considered in this study: 0.025, 0.075, and 0.1 wt%. Finally, the average heat transfer coefficient was determined by inserting the average wall temperature and bulk temperature determined from simulations into Eq. (6.15).

Figure 8.6(a) shows the comparison between numerical and experimental data for the average heat transfer coefficient as a function of the Re number for nanofluids with different CGNP concentrations. It can be seen that the average heat transfer coefficient significantly increases with an increase in the CGNP concentration. This is likely due to the thermal conductivity enhancement resulting from the Brownian motion of CGNPs suspended in DI water. Moreover, increasing the Re number leads to higher average heat transfer coefficient. The greater Re number results in higher fluid velocity and a steeper temperature gradient, which in turn, increases the heat transfer coefficient. In

general, there is good agreement between the simulation and experimental data, where the average relative deviations are 8.11, 1.87, and 6.02% when the CGNP concentrations are 0.025, 0.075, and 0.1 wt%, respectively.

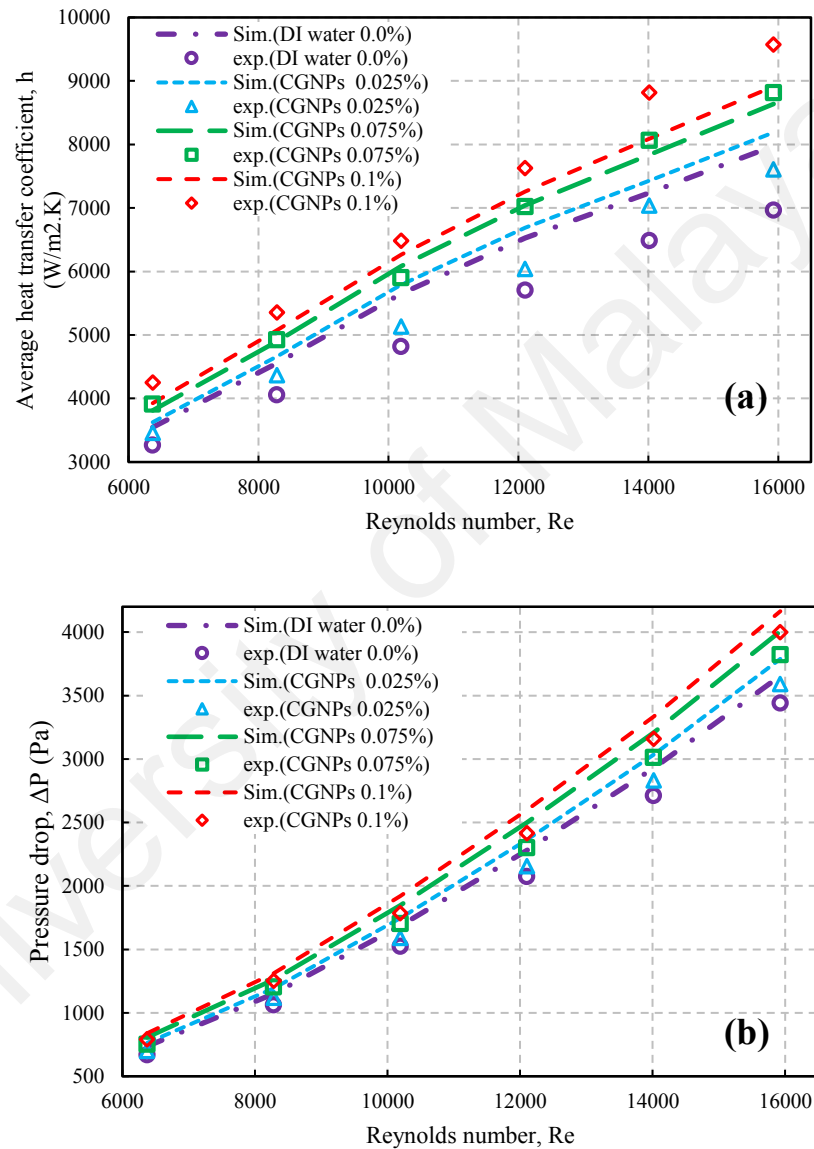


Figure 8.6: Comparison of the (a) average heat transfer coefficient and (b) pressure drop of the CGNP-water nanofluids between simulations and experiments

The pressure drop across the test section was determined by inserting the wall shear stress values obtained from simulations and the results are shown in Figure 8.6(b) for various concentrations of CGNPs and Re numbers.

It can be seen that there is a slight increase in the pressure drop for the CGNP-DI water nanofluids compared with those for DI water. It can be seen that the pressure drop increases slightly when the concentration of CNGPs in DI water is increased. It is believed that this is due to the slight increase in viscosity for all CGNP-DI water nanofluids, considering that there is negligible increase in the fluid velocity since the Re is constant (Equation (3.4)). Hence, it can be deduced that the velocity of the heat transfer liquids plays a vital role in enhancing the pressure drop in convective heat transfer systems. In general, there is a good agreement between the simulation and experimental results for both pressure drop where the average relative deviations are 8.02, 6.82, and 5.94% for CGNP concentration of 0.025, 0.075, and 0.1 wt%, respectively.

Figures 8.7(a) and (b) show the temperature distribution contours for the CGNP-DI water nanofluid (1 wt %) and DI water at $Re = 6,371$, respectively, in the horizontal tube subjected to a constant heat flux of $12,752 \text{ W/m}^2$. The color bar showing a range of colors in the visible spectrum from blue to red indicates the temperature range from minimum to maximum in the tube. It can be observed that the inner wall temperature decreases when the CNGPs/DI water nanofluids are used as the working fluids instead of DI water. In general, this reduction is due to the transport properties of the nanofluids (particularly, the higher thermal conductivity of CNGPs) and the role of Brownian motion of nanoparticles on the thermal conductivity enhancement. This in turn, leads to higher convective heat transfer enhancement, which promotes heat transfer from the higher-temperature surface (i.e. inner wall of the tube) to the fluid.

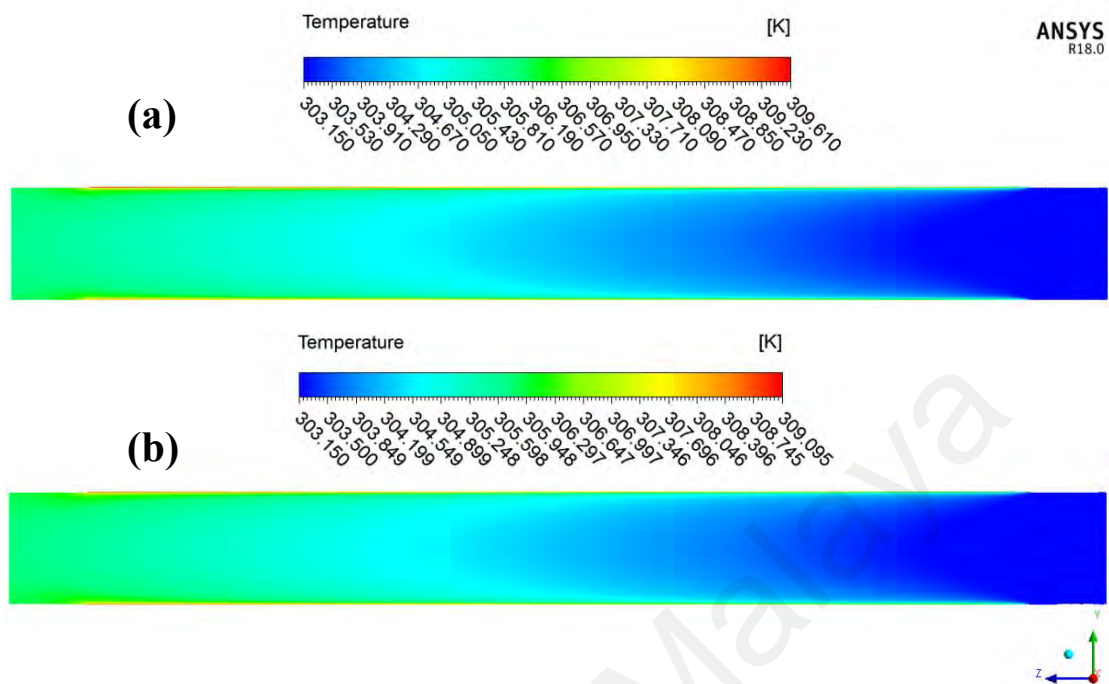


Figure 8.7: Temperature distribution contours of the horizontal tube for (a) DI water and (b) CGNP nanofluid at $Re = 6,371$ and uniform heat flux of $12,752 \text{ W/m}^2$

CHAPTER 9: CONCLUSIONS

In this study, a novel, environmentally friendly functionalization and reduction technique was successfully developed to synthesize well-dispersed water-based carbon nanostructure nanofluids for use as coolants in order to improve the convective heat transfer and hydrodynamic characteristics of a straight, stainless steel heat exchanger. The following conclusions are drawn based on the findings of this study:

The effectiveness covalent functionalization and reduction methods was determined using characterization techniques such as XPS, FTIR spectroscopy, TGA, UV-vis spectroscopy, Raman spectroscopy, and TEM. The nanofluids were prepared by dispersing the GAGNPs, CGNPs, GAMWCNTs and SrGO in DI water at different particle concentrations. The stability and solubility of the colloidal suspensions were verified by UV-vis spectroscopy. The dispersibility values are more than 89.3, 88.2, 89.1, and 88.8% for the water-based GAGNP, CGNP, GAMWCNT, and SrGO nanofluids, respectively, over the course of 63 days.

The thermal conductivity of the DI water shows excellent agreement with the NIST data (Ramires et al., 1995), with an error of less than 1%. The observed enhancement in thermo-physical characteristics of nanofluids compared with those for base fluid, indicating that the nanofluids are promising coolants for heat transfer applications. The maximum thermal conductivity enhancements are 24.17, 22.92, 21.51 and 28.88% for the GAGNP, CGNP, GAMWCNT, and SrGO nanofluids, respectively, at the lowest particle concentration (0.1 wt %) and fluid temperature of 45°C. In addition, the dynamic viscosity and density of all nanofluids are similar to those for DI water.

The reliability and accuracy of the closed conduit heat transfer system was validated by experiments where DI water was used as the working fluid. The results show that there is excellent agreement in the Nusselt number obtained from experiments with

those determined from Gnielinski's (Volker Gnielinski, 1975), Petukhov's (Petukhov, 1970), and Dittus-Boelter's (Duangthongsuk & Wongwises, 2008) empirical correlations with an average deviation of 7.11, 2.01, and 7.96%, respectively. There is also good agreement in the friction factor obtained from experiments and those determined from Petukhov's (Petukhov, 1970) and Blasius's (Blasius, 1907) empirical correlations, with an average deviation of 5 and 4%, respectively.

Detailed experiments were carried out to study the heat transfer and hydrodynamic characteristics of the nanofluids flowing in a heat exchanger under turbulent flow regime. The results show that there is pronounced increase in the heat transfer coefficient (~38.58, 37.53, 33.049 and 41.79%) of the water-based GAGNP, CGNP, GAMWCNT, and SrGO nanofluids, respectively, relative to that for the base fluid, at the low particle concentration (0.1 wt%) and Reynolds number of 15,927. More importantly, there is a negligible increase in the friction factor, with a maximum value of 3.896, 3.79, 3.62 and 3.21%, for the GAGNP, CGNP, GAMWCNT, and SrGO nanofluids, respectively. These results are obtained at a constant wall heat flux of 12,752 W/m². The significant enhancement on the heat transfer rate is associated with the loading and well-dispersion of the functionalized-carbon nanostructures in the base fluid.

The obtained results are very encouraging since the pumping power is close to that for DI water for all nanofluids synthesized in this study. In addition, the performance index for these nanofluids is greater than 1 and shows an increasing trend with increasing Re number, which indicates that these green water-based nanofluids have great potential for use as heat transfer fluids.

The thermo-physical properties obtained from experiments were used as the inputs for the CFD simulations. ANSYS Fluent commercial CFD software was used to predict the heat transfer and pressure loss of the heat exchanger with CGNP nanofluids as the

working fluid in single-phase turbulent flow. In general, there is good agreement between the numerical simulations and experimental results for pressure drop, with an average relative deviation of 8.02, 6.82 and 5.94% for a CGNP concentration of 0.025, 0.075, and 0.1 wt%, respectively. In addition, there is good agreement in the mean convective heat transfer coefficient with an average deviation of 8.11, 1.87 and 6.02% respectively, for a CGNP concentration of 0.025, 0.075, and 0.1 wt%, respectively.

In summary, the novel covalent functionalization technique developed in this study used to functionalize carbon nanostructures is eco-friendly, quick, cost-effective, and scalable. The results prove that the nanofluids prepared with the covalently functionalized carbon nanostructures result in a significant thermal enhancement with negligible pumping power penalty. The technique does not require the use of surfactants in synthesizing nanofluids and therefore, it is feasible means to synthesize a new generation of coolants for a wide range of industrial applications.

REFERENCES

- Abdolbaqi, M. K., Azmi, W., Mamat, R., Sharma, K., & Najafi, G. (2016). Experimental investigation of thermal conductivity and electrical conductivity of BioGlycol–water mixture based Al₂O₃ nanofluid. *Applied Thermal Engineering*, *102*, 932-941.
- Abdulagatov, I. M., & Azizov, N. D. (2006). Experimental study of the effect of temperature, pressure and concentration on the viscosity of aqueous NaBr solutions. *Journal of solution chemistry*, *35*(5), 705-738.
- Aberoumand, S., Jafarimoghaddam, A., Moravej, M., Aberoumand, H., & Javaherdeh, K. (2016). Experimental study on the rheological behavior of silver-heat transfer oil nanofluid and suggesting two empirical based correlations for thermal conductivity and viscosity of oil based nanofluids. *Applied Thermal Engineering*, *101*, 362-372.
- Abuilaiwi, F. A., Laoui, T., Al-Harhi, M., & Atieh, M. A. (2010). Modification and functionalization of multiwalled carbon nanotube (MWCNT) via fischer esterification. *The Arabian Journal for Science and Engineering*, *35*(1C), 37-48.
- Agarwal, R., Verma, K., Agrawal, N. K., Duchaniya, R. K., & Singh, R. (2016). Synthesis, characterization, thermal conductivity and sensitivity of CuO nanofluids. *Applied Thermal Engineering*, *102*, 1024-1036.
- Agharkar, M., Kochrekar, S., Hidouri, S., & Azeez, M. A. (2014). Trends in green reduction of graphene oxides, issues and challenges: a review. *Materials Research Bulletin*, *59*, 323-328.
- Ahuja, A. S. (1975a). Augmentation of heat transport in laminar flow of polystyrene suspensions. I. Experiments and results. *Journal of Applied Physics*, *46*(8), 3408-3416.
- Ahuja, A. S. (1975b). Augmentation of heat transport in laminar flow of polystyrene suspensions. II. Analysis of the data. *Journal of Applied Physics*, *46*(8), 3417-3425.
- Ajayan, P., Ebbesen, T., Ichihashi, T., Iijima, S., Tanigaki, K., & Hiura, H. (1993). Opening carbon nanotubes with oxygen and implications for filling. *Nature*, *362*(6420), 522-525.
- Akbari, M., Galanis, N., & Behzadmehr, A. (2012). Comparative assessment of single and two-phase models for numerical studies of nanofluid turbulent forced convection. *International Journal of Heat and Fluid Flow*, *37*, 136-146.
- Akbarinia, A., & Behzadmehr, A. (2007). Numerical study of laminar mixed convection of a nanofluid in horizontal curved tubes. *Applied Thermal Engineering*, *27*(8), 1327-1337.
- Akhavan-Zanjani, H., Saffar-Avval, M., Mansourkiaei, M., Ahadi, M., & Sharif, F. (2014). Turbulent convective heat transfer and pressure drop of graphene–water

nanofluid flowing inside a horizontal circular tube. *Journal of Dispersion Science and Technology*, 35(9), 1230-1240.

Alanyalıoğlu, M., Segura, J. J., Oró-Solè, J., & Casañ-Pastor, N. (2012). The synthesis of graphene sheets with controlled thickness and order using surfactant-assisted electrochemical processes. *Carbon*, 50(1), 142-152.

Allen, M. J., Tung, V. C., & Kaner, R. B. (2009). Honeycomb carbon: a review of graphene. *Chemical reviews*, 110(1), 132-145.

Aminfar, H., & Motallebzadeh, R. (2011). Numerical Investigation of the Effects of Nanoparticle Diameter on Velocity Field and Nanoparticle Distribution of Nanofluid Using Lagrangian-Eulerian Approach. *Journal of Dispersion Science and Technology*, 32(9), 1311-1317.

Amiri, A., Sadri, R., Shanbedi, M., Ahmadi, G., Chew, B., Kazi, S., & Dahari, M. (2015). Performance dependence of thermosyphon on the functionalization approaches: an experimental study on thermo-physical properties of graphene nanoplatelet-based water nanofluids. *Energy Conversion and Management*, 92, 322-330.

Amiri, A., Sadri, R., Shanbedi, M., Ahmadi, G., Kazi, S., Chew, B., & Zubir, M. N. M. (2015). Synthesis of ethylene glycol-treated graphene nanoplatelets with one-pot, microwave-assisted functionalization for use as a high performance engine coolant. *Energy Conversion and Management*, 101, 767-777.

Amiri, A., Shanbedi, M., Ahmadi, G., Eshghi, H., Chew, B., & Kazi, S. (2015). Microwave-assisted direct coupling of graphene nanoplatelets with poly ethylene glycol and 4-phenylazophenol molecules for preparing stable-colloidal system. *Colloids and Surfaces A: Physicochemical and Engineering Aspects*, 487, 131-141.

Amiri, A., Shanbedi, M., & Dashti, H. (2017). Thermophysical and rheological properties of water-based graphene quantum dots nanofluids. *Journal of the Taiwan Institute of Chemical Engineers*, 76, 132-140.

Amiri, A., Shanbedi, M., Eshghi, H., Heris, S. Z., & Baniadam, M. (2012). Highly dispersed multiwalled carbon nanotubes decorated with Ag nanoparticles in water and experimental investigation of the thermophysical properties. *The Journal of Physical Chemistry C*, 116(5), 3369-3375.

Amiri, A., Shanbedi, M., Rafieerad, A., Rashidi, M. M., Zaharinie, T., Zubir, M. N. M., . . . Chew, B. (2017). Functionalization and exfoliation of graphite into mono layer graphene for improved heat dissipation. *Journal of the Taiwan Institute of Chemical Engineers*, 71, 480-493.

Amrollahi, A., Hamidi, A., & Rashidi, A. (2008). The effects of temperature, volume fraction and vibration time on the thermo-physical properties of a carbon nanotube suspension (carbon nanofluid). *Nanotechnology*, 19(31), 315701.

Amrollahi, A., Rashidi, A., Lotfi, R., Meibodi, M. E., & Kashefi, K. (2010). Convection heat transfer of functionalized MWNT in aqueous fluids in laminar and turbulent

flow at the entrance region. *International Communications in Heat and Mass Transfer*, 37(6), 717-723.

An, X., Simmons, T., Shah, R., Wolfe, C., Lewis, K. M., Washington, M., . . . Kar, S. (2010). Stable aqueous dispersions of noncovalently functionalized graphene from graphite and their multifunctional high-performance applications. *Nano letters*, 10(11), 4295-4301.

Anastas, P. T., & Warner, J. C. (1998). Principles of green chemistry. *Green chemistry: Theory and practice*, 29-56.

Aravind, S. J., Baskar, P., Baby, T. T., Sabareesh, R. K., Das, S., & Ramaprabhu, S. (2011). Investigation of structural stability, dispersion, viscosity, and conductive heat transfer properties of functionalized carbon nanotube based nanofluids. *The Journal of Physical Chemistry C*, 115(34), 16737-16744.

Aravind, S. S. J., Eswaraiah, V., & Ramaprabhu, S. (2011). Facile and simultaneous production of metal/metal oxide dispersed graphene nano composites by solar exfoliation. *Journal of Materials Chemistry*, 21(43), 17094-17097.

Ashorynejad, H., Sheikholeslami, M., Pop, I., & Ganji, D. (2013). Nanofluid flow and heat transfer due to a stretching cylinder in the presence of magnetic field. *Heat and mass transfer*, 49(3), 427-436.

Assael, M., Chen, C.-F., Metaxa, I., & Wakeham, W. (2004). Thermal conductivity of suspensions of carbon nanotubes in water. *International Journal of Thermophysics*, 25(4), 971-985.

Assael, M., Metaxa, I., Arvanitidis, J., Christofilos, D., & Lioutas, C. (2005). Thermal conductivity enhancement in aqueous suspensions of carbon multi-walled and double-walled nanotubes in the presence of two different dispersants. *International Journal of Thermophysics*, 26(3), 647-664.

Aybar, H. Ş., Sharifpur, M., Azizian, M. R., Mehrabi, M., & Meyer, J. P. (2015). A review of thermal conductivity models for nanofluids. *Heat Transfer Engineering*, 36(13), 1085-1110.

Babu, K. J., Nahm, K. S., & Hwang, Y. J. (2014). A facile one-pot green synthesis of reduced graphene oxide and its composites for non-enzymatic hydrogen peroxide sensor applications. *RSC Advances*, 4(16), 7944-7951.

Baby, T. T., & Sundara, R. (2011). Synthesis and transport properties of metal oxide decorated graphene dispersed nanofluids. *The Journal of Physical Chemistry C*, 115(17), 8527-8533.

Bahiraeei, M. (2014). A comprehensive review on different numerical approaches for simulation in nanofluids: traditional and novel techniques. *Journal of Dispersion Science and Technology*, 35(7), 984-996.

Bala, H., Fu, W., Zhao, J., Ding, X., Jiang, Y., Yu, K., & Wang, Z. (2005). Preparation of BaSO₄ nanoparticles with self-dispersing properties. *Colloids and Surfaces A: Physicochemical and Engineering Aspects*, 252(2), 129-134.

- Bandow, S., Takizawa, M., Hirahara, K., Yudasaka, M., & Iijima, S. (2001). Raman scattering study of double-wall carbon nanotubes derived from the chains of fullerenes in single-wall carbon nanotubes. *Chemical Physics Letters*, 337(1), 48-54.
- Baskaran, D., Mays, J. W., & Bratcher, M. S. (2004). Polymer-grafted multiwalled carbon nanotubes through surface-initiated polymerization. *Angewandte Chemie International Edition*, 43(16), 2138-2142.
- Basu, J., Basu, J. K., & Bhattacharyya, T. K. (2010). The evolution of graphene-based electronic devices. *International Journal of Smart and Nano Materials*, 1(3), 201-223.
- Batchelor, G. (1977). The effect of Brownian motion on the bulk stress in a suspension of spherical particles. *Journal of Fluid Mechanics*, 83(01), 97-117.
- Beck, M. P., Yuan, Y., Warriar, P., & Teja, A. S. (2010a). The thermal conductivity of alumina nanofluids in water, ethylene glycol, and ethylene glycol+ water mixtures. *Journal of Nanoparticle Research*, 12(4), 1469-1477.
- Beck, M. P., Yuan, Y., Warriar, P., & Teja, A. S. (2010b). The thermal conductivity of aqueous nanofluids containing ceria nanoparticles. *Journal of Applied Physics*, 107(6), 066101.
- Behzadmehr, A., Saffar-Avval, M., & Galanis, N. (2007). Prediction of turbulent forced convection of a nanofluid in a tube with uniform heat flux using a two phase approach. *International Journal of Heat and Fluid Flow*, 28(2), 211-219.
- Benveniste, Y. (1987). Effective thermal conductivity of composites with a thermal contact resistance between the constituents: Nondilute case. *Journal of Applied Physics*, 61(8), 2840-2843.
- Bianco, V., Manca, O., & Nardini, S. (2014). Performance analysis of turbulent convection heat transfer of Al₂O₃ water-nanofluid in circular tubes at constant wall temperature. *Energy*, 77, 403-413.
- Blasius, H. (1907). *Grenzschichten in Flüssigkeiten mit kleiner Reibung*: Druck von BG Teubner.
- Blazek, J. (2015). *Computational fluid dynamics: principles and applications*: Butterworth-Heinemann.
- Bo, Z., Shuai, X., Mao, S., Yang, H., Qian, J., Chen, J., . . . Cen, K. (2014). Green preparation of reduced graphene oxide for sensing and energy storage applications. *Scientific reports*, 4.
- Bo, Z., Yu, K., Lu, G., Wang, P., Mao, S., & Chen, J. (2011). Understanding growth of carbon nanowalls at atmospheric pressure using normal glow discharge plasma-enhanced chemical vapor deposition. *Carbon*, 49(6), 1849-1858.

- Bobbo, S., Fedele, L., Benetti, A., Colla, L., Fabrizio, M., Pagura, C., & Barison, S. (2012). Viscosity of water based SWCNH and TiO₂ nanofluids. *Experimental Thermal and Fluid Science*, 36, 65-71.
- Bose, S., Kuila, T., Mishra, A. K., Kim, N. H., & Lee, J. H. (2012). Dual role of glycine as a chemical functionalizer and a reducing agent in the preparation of graphene: an environmentally friendly method. *Journal of Materials Chemistry*, 22(19), 9696-9703.
- Bostwick, A., Ohta, T., Seyller, T., Horn, K., & Rotenberg, E. (2007). Quasiparticle dynamics in graphene. *Nature Physics*, 3(1), 36-40.
- Böttcher, C. (1945). The dielectric constant of crystalline powders. *Recueil des travaux chimiques des Pays-Bas*, 64(2), 47-51.
- Brinkman, H. (1952). The viscosity of concentrated suspensions and solutions. *The Journal of Chemical Physics*, 20(4), 571-571.
- Britz, D. A., & Khlobystov, A. N. (2006). Noncovalent interactions of molecules with single walled carbon nanotubes. *Chemical Society Reviews*, 35(7), 637-659.
- Byl, O., Liu, J., & Yates, J. T. (2005). Etching of carbon nanotubes by ozone a surface area study. *Langmuir*, 21(9), 4200-4204.
- Carbon Nanotube TEM Image. (2017).
- Cengel, Y. A. (2003). Heat transfer a practical approach.
- Chang, C., & Powell, R. L. (1994). Effect of particle size distributions on the rheology of concentrated bimodal suspensions. *Journal of Rheology (1978-present)*, 38(1), 85-98.
- Chang, H., Jwo, C., Fan, P., & Pai, S. (2007). Process optimization and material properties for nanofluid manufacturing. *The International Journal of Advanced Manufacturing Technology*, 34(3-4), 300-306.
- Chang, H., Jwo, C., Lo, C., Tsung, T., Kao, M., & Lin, H. (2005). Rheology of CuO nanoparticle suspension prepared by ASNSS. *Rev. Adv. Mater. Sci*, 10(2), 128-132.
- Chen, J., Hamon, M. A., Hu, H., Chen, Y., Rao, A. M., Eklund, P. C., & Haddon, R. C. (1998). Solution properties of single-walled carbon nanotubes. *Science*, 282(5386), 95-98.
- Chen, J., Rao, A. M., Lyuksyutov, S., Itkis, M. E., Hamon, M. A., Hu, H., . . . Smalley, R. E. (2001). Dissolution of full-length single-walled carbon nanotubes. *The Journal of Physical Chemistry B*, 105(13), 2525-2528.
- Chen, L., & Xie, H. (2010). Properties of carbon nanotube nanofluids stabilized by cationic gemini surfactant. *Thermochimica Acta*, 506(1), 62-66.

- Chen, W., & Yan, L. (2010). Preparation of graphene by a low-temperature thermal reduction at atmosphere pressure. *Nanoscale*, 2(4), 559-563.
- Cheng, C., Nie, S., Li, S., Peng, H., Yang, H., Ma, L., . . . Zhao, C. (2013). Biopolymer functionalized reduced graphene oxide with enhanced biocompatibility via mussel inspired coatings/anchors. *Journal of Materials Chemistry B*, 1(3), 265-275.
- Choi, S., Zhang, Z., Yu, W., Lockwood, F., & Grulke, E. (2001). Anomalous thermal conductivity enhancement in nanotube suspensions. *Applied physics letters*, 79(14), 2252-2254.
- Choi, S. U., & Eastman, J. (1995). Enhancing thermal conductivity of fluids with nanoparticles: Argonne National Lab., IL (United States).
- Choi, S. U., & Eastman, J. A. (2001). Enhanced heat transfer using nanofluids: Google Patents.
- Chol, S. (1995). Enhancing thermal conductivity of fluids with nanoparticles. *ASME-Publications-Fed*, 231, 99-106.
- Chopkar, M., Sudarshan, S., Das, P., & Manna, I. (2008). Effect of particle size on thermal conductivity of nanofluid. *Metallurgical and Materials Transactions A*, 39(7), 1535-1542.
- Chung, T. (2010). *Computational fluid dynamics*: Cambridge university press.
- Colburn, A. P. (1933). A method of correlating forced convection heat transfer data and a comparison with fluid friction. *Trans Am Inst Chem Eng*, 29, 174-210.
- Colebrook, C. F. (1939). Turbulent Flow in Pipes, with particular reference to the Transition Region between the Smooth and Rough Pipe Laws. *Journal of the ICE*, 11(4), 133-156.
- Corcione, M., Cianfrini, M., & Quintino, A. (2012). Heat transfer of nanofluids in turbulent pipe flow. *International Journal of thermal sciences*, 56, 58-69.
- Das, R., Hamid, S. B. A., Ali, M., Annuar, M., Samsudin, E. M. B., & Bagheri, S. (2015). Covalent Functionalization Schemes for Tailoring Solubility of Multi-Walled Carbon Nanotubes in Water and Acetone Solvents. *Science of Advanced Materials*, 7(12), 2726-2737.
- Das, S. K., Choi, S. U., Yu, W., & Pradeep, T. (2007). *Nanofluids: science and technology*: John Wiley & Sons.
- Das, S. K., Putra, N., & Roetzel, W. (2003). Pool boiling characteristics of nano-fluids. *International Journal of Heat and Mass Transfer*, 46(5), 851-862.
- Das, S. K., Putra, N., Thiesen, P., & Roetzel, W. (2003). Temperature dependence of thermal conductivity enhancement for nanofluids. *Journal of Heat Transfer*, 125(4), 567-574.

- Davis, V. A., Ericson, L. M., Parra-Vasquez, A. N. G., Fan, H., Wang, Y., Prieto, V., . . . Kittrell, C. (2004). Phase behavior and rheology of SWNTs in superacids. *Macromolecules*, 37(1), 154-160.
- Del Rio-Castillo, A. E., Merino, C., Díez-Barra, E., & Vázquez, E. (2014). Selective suspension of single layer graphene mechanochemically exfoliated from carbon nanofibres. *Nano Research*, 7(7), 963-972.
- Ding, J., Liu, Y., Yuan, N., Ding, G., Fan, Y., & Yu, C. (2012). The influence of temperature, time and concentration on the dispersion of reduced graphene oxide prepared by hydrothermal reduction. *Diamond and Related Materials*, 21, 11-15.
- Ding, Y., Alias, H., Wen, D., & Williams, R. A. (2006). Heat transfer of aqueous suspensions of carbon nanotubes (CNT nanofluids). *International Journal of Heat and Mass Transfer*, 49(1), 240-250.
- Ding, Y., & Wen, D. (2005). Particle migration in a flow of nanoparticle suspensions. *Powder Technology*, 149(2), 84-92.
- Ding, Y., Zhang, P., Zhuo, Q., Ren, H., Yang, Z., & Jiang, Y. (2011). A green approach to the synthesis of reduced graphene oxide nanosheets under UV irradiation. *Nanotechnology*, 22(21), 215601.
- Dittus, F., & Boelter, L. (1930). Heat Transfer in Automobile Radiators of the Tubular Type. *University of California Publications in Engineering*, 2, 43.
- Doyle, C. D., Rocha, J.-D. R., Weisman, R. B., & Tour, J. M. (2008). Structure-dependent reactivity of semiconducting single-walled carbon nanotubes with benzenediazonium salts. *Journal of the American Chemical Society*, 130(21), 6795-6800.
- Dreyer, D. R., Murali, S., Zhu, Y., Ruoff, R. S., & Bielawski, C. W. (2011). Reduction of graphite oxide using alcohols. *Journal of Materials Chemistry*, 21(10), 3443-3447.
- Duangthongsuk, W., & Wongwises, S. (2008). Effect of thermophysical properties models on the predicting of the convective heat transfer coefficient for low concentration nanofluid. *International Communications in Heat and Mass Transfer*, 35(10), 1320-1326.
- Duangthongsuk, W., & Wongwises, S. (2009). Measurement of temperature-dependent thermal conductivity and viscosity of TiO₂-water nanofluids. *Experimental Thermal and Fluid Science*, 33(4), 706-714.
- Duangthongsuk, W., & Wongwises, S. (2010). An experimental study on the heat transfer performance and pressure drop of TiO₂-water nanofluids flowing under a turbulent flow regime. *International Journal of Heat and Mass Transfer*, 53(1), 334-344.
- Eastman, J. A., Choi, S., Li, S., Yu, W., & Thompson, L. (2001). Anomalously increased effective thermal conductivities of ethylene glycol-based nanofluids containing copper nanoparticles. *Applied physics letters*, 78(6), 718-720.

- Einstein, A. (1906). A new determination of molecular dimensions. *Ann. Phys*, 19(2), 289-306.
- Einstein, A. (1956). Investigations on the Theory of Brownian Motion. Reprint of the 1st English edition (1926): Dover, New-York.
- El-Batsh, H., Doheim, M., & Hassan, A. (2012). On the application of mixture model for two-phase flow induced corrosion in a complex pipeline configuration. *Applied Mathematical Modelling*, 36(11), 5686-5699.
- Esfe, M. H., Saedodin, S., Mahian, O., & Wongwises, S. (2014). Heat transfer characteristics and pressure drop of COOH-functionalized DWCNTs/water nanofluid in turbulent flow at low concentrations. *International Journal of Heat and Mass Transfer*, 73, 186-194.
- Eswaraiah, V., Aravind, S. S. J., & Ramaprabhu, S. (2011). Top down method for synthesis of highly conducting graphene by exfoliation of graphite oxide using focused solar radiation. *Journal of Materials Chemistry*, 21(19), 6800-6803.
- Eswaraiah, V., Sankaranarayanan, V., & Ramaprabhu, S. (2011). Graphene-based engine oil nanofluids for tribological applications. *ACS applied materials & interfaces*, 3(11), 4221-4227.
- Evans, W., Fish, J., & Keblinski, P. (2006). Role of Brownian motion hydrodynamics on nanofluid thermal conductivity. *Applied physics letters*, 88(9), 093116.
- Evans, W., Prasher, R., Fish, J., Meakin, P., Phelan, P., & Keblinski, P. (2008). Effect of aggregation and interfacial thermal resistance on thermal conductivity of nanocomposites and colloidal nanofluids. *International Journal of Heat and Mass Transfer*, 51(5), 1431-1438.
- Fan, X., Peng, W., Li, Y., Li, X., Wang, S., Zhang, G., & Zhang, F. (2008). Deoxygenation of exfoliated graphite oxide under alkaline conditions: a green route to graphene preparation. *Advanced Materials*, 20(23), 4490-4493.
- Fan, Z.-J., Kai, W., Yan, J., Wei, T., Zhi, L.-J., Feng, J., . . . Wei, F. (2010). Facile synthesis of graphene nanosheets via Fe reduction of exfoliated graphite oxide. *ACS nano*, 5(1), 191-198.
- Fan, Z., Wang, K., Wei, T., Yan, J., Song, L., & Shao, B. (2010). An environmentally friendly and efficient route for the reduction of graphene oxide by aluminum powder. *Carbon*, 48(5), 1686-1689.
- Faulkner, D. J., Rector, D. R., Davidson, J. J., & Shekarriz, R. (2004). *Enhanced heat transfer through the use of nanofluids in forced convection*. Paper presented at the ASME 2004 International Mechanical Engineering Congress and Exposition.
- Felten, A., Bittencourt, C., & Pireaux, J. (2006). Gold clusters on oxygen plasma functionalized carbon nanotubes: XPS and TEM studies. *Nanotechnology*, 17(8), 1954.

- Fernández-Merino, M. J., Guardia, L., Paredes, J., Villar-Rodil, S., Solís-Fernández, P., Martín z-Alonso, A., & Tascon, J. (2010). Vitamin C is an ideal substitute for hydrazine in the reduction of graphene oxide suspensions. *The Journal of Physical Chemistry C*, 114(14), 6426-6432.
- Fernandez-Seara, J., Uhía, F. J., Sieres, J., & Campo, A. (2007). A general review of the Wilson plot method and its modifications to determine convection coefficients in heat exchange devices. *Applied Thermal Engineering*, 27(17), 2745-2757.
- Ferrari, A., Meyer, J., Scardaci, V., Casiraghi, C., Lazzeri, M., Mauri, F., . . . Roth, S. (2006). Raman spectrum of graphene and graphene layers. *Physical review letters*, 97(18), 187401.
- Fluent, A. (2009). 12.0 Theory Guide. *Ansys Inc*, 5.
- Fricke, H. (1953). The Maxwell-Wagner dispersion in a suspension of ellipsoids. *The Journal of Physical Chemistry*, 57(9), 934-937.
- Fujigaya, T., & Nakashima, N. (2015). Non-covalent polymer wrapping of carbon nanotubes and the role of wrapped polymers as functional dispersants. *Science and technology of advanced materials*, 16(2), 024802.
- Fujitsuka, Y., & Oya, T. (2012). Fabrication of aligned-carbon-nanotube-composite paper with high and anisotropic conductivity. *Journal of Nanotechnology*, 2012.
- Gan, X., Zhou, H., Zhu, B., Yu, X., Jia, Y., Sun, B., . . . Luo, T. (2012). A simple method to synthesize graphene at 633K by dechlorination of hexachlorobenzene on Cu foils. *Carbon*, 50(1), 306-310.
- Garg, P., Alvarado, J. L., Marsh, C., Carlson, T. A., Kessler, D. A., & Annamalai, K. (2009). An experimental study on the effect of ultrasonication on viscosity and heat transfer performance of multi-wall carbon nanotube-based aqueous nanofluids. *International Journal of Heat and Mass Transfer*, 52(21), 5090-5101.
- Georgakilas, V., Otyepka, M., Bourlinos, A. B., Chandra, V., Kim, N., Kemp, K. C., . . . Kim, K. S. (2012). Functionalization of graphene: covalent and non-covalent approaches, derivatives and applications. *Chemical reviews*, 112(11), 6156-6214.
- Ghadimi, A., & Metselaar, I. H. (2013). The influence of surfactant and ultrasonic processing on improvement of stability, thermal conductivity and viscosity of titania nanofluid. *Experimental Thermal and Fluid Science*, 51, 1-9.
- Ghadimi, A., Saidur, R., & Metselaar, H. (2011). A review of nanofluid stability properties and characterization in stationary conditions. *International Journal of Heat and Mass Transfer*, 54(17), 4051-4068.
- Gherasim, I., Roy, G., Nguyen, C. T., & Vo-Ngoc, D. (2009). Experimental investigation of nanofluids in confined laminar radial flows. *International Journal of thermal sciences*, 48(8), 1486-1493.

- Ghozatloo, A., Shariaty-Niasar, M., & Rashidi, A. M. (2013). Preparation of nanofluids from functionalized graphene by new alkaline method and study on the thermal conductivity and stability. *International Communications in Heat and Mass Transfer*, 42, 89-94.
- Ginic-Markovic, M., Matisons, J. G., Cervini, R., Simon, G. P., & Fredericks, P. M. (2006). Synthesis of new polyaniline/nanotube composites using ultrasonically initiated emulsion polymerization. *Chemistry of materials*, 18(26), 6258-6265.
- Gnielinski, V. (1975). New equations for heat and mass transfer in the turbulent flow in pipes and channels. *NASA STI/recon technical report A*, 75, 22028.
- Gnielinski, V. (1976). New equations for heat and mass-transfer in turbulent pipe and channel flow. *International Chemical Engineering*, 16(2), 359-368.
- Gómez-Navarro, C., Meyer, J. C., Sundaram, R. S., Chuvilin, A., Kurasch, S., Burghard, M., . . . Kaiser, U. (2010). Atomic structure of reduced graphene oxide. *Nano letters*, 10(4), 1144-1148.
- Gómez, A. O. C., Hoffmann, A. R. K., & Bandarra Filho, E. P. (2015). Experimental evaluation of CNT nanofluids in single-phase flow. *International Journal of Heat and Mass Transfer*, 86, 277-287.
- Goodwin, J. W., & Hughes, R. W. (2008). *Rheology for chemists: an introduction*: Royal Society of Chemistry.
- Granqvist, C., & Hunderi, O. (1978). Conductivity of inhomogeneous materials: Effective-medium theory with dipole-dipole interaction. *Physical Review B*, 18(4), 1554.
- Guo, H.-L., Wang, X.-F., Qian, Q.-Y., Wang, F.-B., & Xia, X.-H. (2009). A green approach to the synthesis of graphene nanosheets. *ACS nano*, 3(9), 2653-2659.
- Gupta, M., Arora, N., Kumar, R., Kumar, S., & Dilbaghi, N. (2014). A comprehensive review of experimental investigations of forced convective heat transfer characteristics for various nanofluids. *International journal of mechanical and materials engineering*, 9(1), 11.
- Gurunathan, S., Han, J., & Kim, J. H. (2013). Humanin: a novel functional molecule for the green synthesis of graphene. *Colloids and Surfaces B: Biointerfaces*, 111, 376-383.
- Gurunathan, S., Han, J. W., Eppakayala, V., & Kim, J.-H. (2013). Green synthesis of graphene and its cytotoxic effects in human breast cancer cells. *International journal of nanomedicine*, 8, 1015.
- Hadjov, K. B. (2009). Modified self-consistent scheme to predict the thermal conductivity of nanofluids. *International Journal of thermal sciences*, 48(12), 2249-2254.

- Haghighi, B., & Tabrizi, M. A. (2013). Green-synthesis of reduced graphene oxide nanosheets using rose water and a survey on their characteristics and applications. *RSC Advances*, 3(32), 13365-13371.
- Haghighi, E. B., Saleemi, M., Nikkam, N., Khodabandeh, R., Toprak, M. S., Muhammed, M., & Palm, B. (2014). Accurate basis of comparison for convective heat transfer in nanofluids. *International Communications in Heat and Mass Transfer*, 52, 1-7.
- Hamilton, R., & Crosser, O. (1962). Thermal conductivity of heterogeneous two-component systems. *Industrial & Engineering chemistry fundamentals*, 1(3), 187-191.
- Hamon, M. A., Chen, J., Hu, H., Chen, Y., Itkis, M. E., Rao, A. M., . . . Haddon, R. C. (1999). Dissolution of single-walled carbon nanotubes. *Advanced Materials*, 11(10), 834-840.
- Hausen, H. (1959). Neue Gleichungen für die Wärmeübertragung bei freier oder erzwungener Stromung. *Allg. Wärmetech*, 9, 75-79.
- Heris, S. Z., Esfahany, M. N., & Etemad, G. (2007a). Numerical investigation of nanofluid laminar convective heat transfer through a circular tube. *Numerical Heat Transfer, Part A: Applications*, 52(11), 1043-1058.
- Heris, S. Z., Esfahany, M. N., & Etemad, S. G. (2007b). Experimental investigation of convective heat transfer of Al₂O₃/water nanofluid in circular tube. *International Journal of heat and fluid flow*, 28(2), 203-210.
- Hernandez, Y., Nicolosi, V., Lotya, M., Blighe, F. M., Sun, Z., De, S., . . . Gun'Ko, Y. K. (2008). High-yield production of graphene by liquid-phase exfoliation of graphite. *Nature nanotechnology*, 3(9), 563-568.
- Hetsroni, G., & Rozenblit, R. (1994). Heat transfer to a liquid—solid mixture in a flume. *International Journal of Multiphase Flow*, 20(4), 671-689.
- Hiemenz, P. C. (1986). *Principles of colloid and surface chemistry* (Vol. 188): M. Dekker New York.
- Hirsch, A. (2002). Functionalization of single-walled carbon nanotubes. *Angewandte Chemie International Edition*, 41(11), 1853-1859.
- Homenick, C. M., Lawson, G., & Adronov, A. (2007). Polymer grafting of carbon nanotubes using living free-radical polymerization. *Polymer Reviews*, 47(2), 265-290.
- Hong, K., Hong, T.-K., & Yang, H.-S. (2006). Thermal conductivity of Fe nanofluids depending on the cluster size of nanoparticles. *Applied physics letters*, 88(3), 031901.
- Hong, T.-K., Yang, H.-S., & Choi, C. (2005). Study of the enhanced thermal conductivity of Fe nanofluids. *Journal of Applied Physics*, 97(6), 064311.

- Hosseini, M., Sadri, R., Kazi, S. N., Bagheri, S., Zubir, N., Bee Teng, C., & Zaharinie, T. (2017). Experimental Study on Heat Transfer and Thermo-Physical Properties of Covalently Functionalized Carbon Nanotubes Nanofluids in an Annular Heat Exchanger: A Green and Novel Synthesis. *Energy & Fuels*, *31*(5), 5635-5644.
- Huang, L., Liu, Y., Ji, L.-C., Xie, Y.-Q., Wang, T., & Shi, W.-Z. (2011). Pulsed laser assisted reduction of graphene oxide. *Carbon*, *49*(7), 2431-2436.
- Huang, X., Qi, X., Boey, F., & Zhang, H. (2012). Graphene-based composites. *Chemical Society Reviews*, *41*(2), 666-686.
- Hudson, J. L., Casavant, M. J., & Tour, J. M. (2004). Water-soluble, exfoliated, nonroping single-wall carbon nanotubes. *Journal of the American Chemical Society*, *126*(36), 11158-11159.
- Huh, S., Park, J., Kim, K. S., Hong, B. H., & Kim, S. B. (2011). Selective n-type doping of graphene by photo-patterned gold nanoparticles. *ACS nano*, *5*(5), 3639-3644.
- Hummers Jr, W. S., & Offeman, R. E. (1958). Preparation of graphitic oxide. *Journal of the American Chemical Society*, *80*(6), 1339-1339.
- Hwang, K. S., Jang, S. P., & Choi, S. U. (2009). Flow and convective heat transfer characteristics of water-based Al₂O₃ nanofluids in fully developed laminar flow regime. *International Journal of Heat and Mass Transfer*, *52*(1), 193-199.
- Hwang, Y., Ahn, Y., Shin, H., Lee, C., Kim, G., Park, H., & Lee, J. (2006). Investigation on characteristics of thermal conductivity enhancement of nanofluids. *Current Applied Physics*, *6*(6), 1068-1071.
- Hwang, Y., Lee, J.-K., Lee, J.-K., Jeong, Y.-M., Cheong, S.-i., Ahn, Y.-C., & Kim, S. H. (2008). Production and dispersion stability of nanoparticles in nanofluids. *Powder Technology*, *186*(2), 145-153.
- Iijima, S. (1991). Helical microtubules of graphitic carbon. *Nature*, *354*(6348), 56-58.
- Iravani, S. (2011). Green synthesis of metal nanoparticles using plants. *Green Chemistry*, *13*(10), 2638-2650.
- Ishii, M. (1975). Thermo-Fluid Dynamic Theory of Two-Phase Flow., volume 22 of Direction des études et recherches d'électricité de France. Eyrolles, Paris.
- Izard, N., Kazaoui, S., Hata, K., Okazaki, T., Saito, T., Iijima, S., & Minami, N. (2008). Semiconductor-enriched single wall carbon nanotube networks applied to field effect transistors. *Applied physics letters*, *92*(24), 243112.
- Jang, S. P., & Choi, S. U. (2004). Role of Brownian motion in the enhanced thermal conductivity of nanofluids. *Applied physics letters*, *84*(21), 4316-4318.
- Jeng, E. S., Moll, A. E., Roy, A. C., Gastala, J. B., & Strano, M. S. (2006). Detection of DNA hybridization using the near-infrared band-gap fluorescence of single-walled carbon nanotubes. *Nano letters*, *6*(3), 371-375.

- Jiao, L., Zhang, L., Wang, X., Diankov, G., & Dai, H. (2009). Narrow graphene nanoribbons from carbon nanotubes. *Nature*, 458(7240), 877-880.
- Kakac, S., Yener, Y., & Pramuanjaroenkij, A. (2013). *Convective heat transfer*: CRC press.
- Kamyar, A., Saidur, R., & Hasanuzzaman, M. (2012). Application of computational fluid dynamics (CFD) for nanofluids. *International Journal of Heat and Mass Transfer*, 55(15), 4104-4115.
- Kartick, B., & Srivastava, S. (2013). Green synthesis of graphene. *Journal of nanoscience and nanotechnology*, 13(6), 4320-4324.
- Kazi, S. N. (2001). *Heat transfer to fibre suspensions : studies in fibre characterisation and fouling mitigation*. (PhD), University of Auckland. (THESIS 2001-K23)
- Keblinski, P., Eastman, J. A., & Cahill, D. G. (2005). Nanofluids for thermal transport. *Materials today*, 8(6), 36-44.
- Keblinski, P., Phillpot, S., Choi, S., & Eastman, J. (2002). Mechanisms of heat flow in suspensions of nano-sized particles (nanofluids). *International Journal of Heat and Mass Transfer*, 45(4), 855-863.
- Khan, M., Al-Marri, A. H., Khan, M., Shaik, M. R., Mohri, N., Adil, S. F., . . . Tremel, W. (2015). Green approach for the effective reduction of graphene oxide using salvadora persica l. root (miswak) extract. *Nanoscale research letters*, 10(1), 281.
- Khanafer, K., & Vafai, K. (2011). A critical synthesis of thermophysical characteristics of nanofluids. *International Journal of Heat and Mass Transfer*, 54(19), 4410-4428.
- Kharisov, B. I., Kharissova, O. V., & Ortiz-Mendez, U. (2016). *CRC Concise Encyclopedia of Nanotechnology*: CRC Press.
- Khoshvaght-Aliabadi, M., Akbari, M., & Hormozi, F. (2016). An empirical study on vortex-generator insert fitted in tubular heat exchangers with dilute Cu–water nanofluid flow. *Chinese Journal of Chemical Engineering*, 24(6), 728-736.
- Kim, S. H., Choi, S. R., & Kim, D. (2007). Thermal conductivity of metal-oxide nanofluids: particle size dependence and effect of laser irradiation. *Journal of Heat Transfer*, 129(3), 298-307.
- Kitagawa, M., & Tokiwa, Y. (2006). Polymerization of vinyl sugar ester using ascorbic acid and hydrogen peroxide as a redox reagent. *Carbohydrate polymers*, 64(2), 218-223.
- Ko, G. H., Heo, K., Lee, K., Kim, D. S., Kim, C., Sohn, Y., & Choi, M. (2007). An experimental study on the pressure drop of nanofluids containing carbon nanotubes in a horizontal tube. *International Journal of Heat and Mass Transfer*, 50(23), 4749-4753.

- Konkena, B., & Vasudevan, S. (2012). Understanding aqueous dispersibility of graphene oxide and reduced graphene oxide through p K a measurements. *The journal of physical chemistry letters*, 3(7), 867-872.
- Koo, J., & Kleinstreuer, C. (2005). Impact analysis of nanoparticle motion mechanisms on the thermal conductivity of nanofluids. *International Communications in Heat and Mass Transfer*, 32(9), 1111-1118.
- Koo, J., & Kleinstreuer, C. (2005). Laminar nanofluid flow in microheat-sinks. *International Journal of Heat and Mass Transfer*, 48(13), 2652-2661.
- Kosynkin, D. V., Higginbotham, A. L., Sinitskii, A., Lomeda, J. R., Dimiev, A., Price, B. K., & Tour, J. M. (2009). Longitudinal unzipping of carbon nanotubes to form graphene nanoribbons. *Nature*, 458(7240), 872-876.
- Krieger, I. M., & Dougherty, T. J. (1959). A mechanism for non-Newtonian flow in suspensions of rigid spheres. *Transactions of The Society of Rheology (1957-1977)*, 3(1), 137-152.
- Ksenevich, V., Gorbachuk, N., Ho, V., Shuba, M., Kuzhir, P., Maksimenko, S., . . . Zak, A. (2016). Electrical properties of carbon nanotubes/WS2 nanotubes (nanoparticles) hybrid films. *Наносистемы: физика, химия, математика*, 7(1).
- Kudin, K. N., Ozbas, B., Schniepp, H. C., Prud'Homme, R. K., Aksay, I. A., & Car, R. (2008). Raman spectra of graphite oxide and functionalized graphene sheets. *Nano letters*, 8(1), 36-41.
- Kuila, T., Bose, S., Hong, C. E., Uddin, M. E., Khanra, P., Kim, N. H., & Lee, J. H. (2011). Preparation of functionalized graphene/linear low density polyethylene composites by a solution mixing method. *Carbon*, 49(3), 1033-1037.
- Kuila, T., Mishra, A. K., Khanra, P., Kim, N. H., & Lee, J. H. (2013). Recent advances in the efficient reduction of graphene oxide and its application as energy storage electrode materials. *Nanoscale*, 5(1), 52-71.
- Kulkarni, D. P., Das, D. K., & Chukwu, G. A. (2006). Temperature dependent rheological property of copper oxide nanoparticles suspension (nanofluid). *Journal of nanoscience and nanotechnology*, 6(4), 1150-1154.
- Kumar, R., Tyagi, R., Parmar, V. S., Samuelson, L. A., Kumar, J., & Watterson, A. C. (2004). Biocatalytic "green" Synthesis of PEG-based aromatic polyesters: Optimization of the substrate and reaction conditions. *Green Chemistry*, 6(10), 516-520.
- Kumaresan, V., Khader, S. M. A., Karthikeyan, S., & Velraj, R. (2013). Convective heat transfer characteristics of CNT nanofluids in a tubular heat exchanger of various lengths for energy efficient cooling/heating system. *International Journal of Heat and Mass Transfer*, 60, 413-421.

- Kuznetsova, A., Mawhinney, D. B., Naumenko, V., Yates, J. T., Liu, J., & Smalley, R. (2000). Enhancement of adsorption inside of single-walled nanotubes: opening the entry ports. *Chemical Physics Letters*, 321(3), 292-296.
- Kwak, K., & Kim, C. (2005). Viscosity and thermal conductivity of copper oxide nanofluid dispersed in ethylene glycol. *Korea-Australia Rheology Journal*, 17(2), 35-40.
- Lam, C.-w., James, J. T., McCluskey, R., Arepalli, S., & Hunter, R. L. (2006). A review of carbon nanotube toxicity and assessment of potential occupational and environmental health risks. *Critical reviews in toxicology*, 36(3), 189-217.
- Larson, R. G. (2005). The rheology of dilute solutions of flexible polymers: Progress and problems. *Journal of Rheology (1978-present)*, 49(1), 1-70.
- Lauder, B. E., & Spalding, D. B. (1972). *Mathematical models of turbulence*: Academic press.
- Lauder, B. E., & Spalding, D. B. (1974). The numerical computation of turbulent flows. *Computer methods in applied mechanics and engineering*, 3(2), 269-289.
- Layek, R. K., & Nandi, A. K. (2013). A review on synthesis and properties of polymer functionalized graphene. *Polymer*, 54(19), 5087-5103.
- Lee, D., Kim, J.-W., & Kim, B. G. (2006). A new parameter to control heat transport in nanofluids: surface charge state of the particle in suspension. *The Journal of Physical Chemistry B*, 110(9), 4323-4328.
- Lee, G.-J., & Rhee, C. K. (2014). Enhanced thermal conductivity of nanofluids containing graphene nanoplatelets prepared by ultrasound irradiation. *Journal of materials science*, 49(4), 1506-1511.
- Lee, H.-K., Lee, H.-Y., & Jeon, J.-M. (2007). Codeposition of micro-and nano-sized SiC particles in the nickel matrix composite coatings obtained by electroplating. *Surface and Coatings Technology*, 201(8), 4711-4717.
- Lee, J.-H., Hwang, K. S., Jang, S. P., Lee, B. H., Kim, J. H., Choi, S. U., & Choi, C. J. (2008). Effective viscosities and thermal conductivities of aqueous nanofluids containing low volume concentrations of Al₂O₃ nanoparticles. *International Journal of Heat and Mass Transfer*, 51(11), 2651-2656.
- Lee, K., Hwang, Y., Cheong, S., Kwon, L., Kim, S., & Lee, J. (2009). Performance evaluation of nano-lubricants of fullerene nanoparticles in refrigeration mineral oil. *Current Applied Physics*, 9(2), e128-e131.
- Lee, S., Choi, S.-S., Li, S., and, & Eastman, J. (1999). Measuring thermal conductivity of fluids containing oxide nanoparticles. *Journal of Heat Transfer*, 121(2), 280-289.
- Lee, S., Choi, S. U., Li, S., and, & Eastman, J. (1999). Measuring thermal conductivity of fluids containing oxide nanoparticles. *Journal of heat transfer*, 121(2).

- Lee, S. W., Park, S. D., Kang, S., Bang, I. C., & Kim, J. H. (2011). Investigation of viscosity and thermal conductivity of SiC nanofluids for heat transfer applications. *International Journal of Heat and Mass Transfer*, 54(1), 433-438.
- Lei, Y., Tang, Z., Liao, R., & Guo, B. (2011). Hydrolysable tannin as environmentally friendly reducer and stabilizer for graphene oxide. *Green Chemistry*, 13(7), 1655-1658.
- Li, C., & Peterson, G. (2007). Mixing effect on the enhancement of the effective thermal conductivity of nanoparticle suspensions (nanofluids). *International Journal of Heat and Mass Transfer*, 50(23), 4668-4677.
- Li, C. C., Yu, H., Yan, Q., & Hng, H. H. (2015). Green synthesis of highly reduced graphene oxide by compressed hydrogen gas towards energy storage devices. *Journal of Power Sources*, 274, 310-317.
- Li, C. H., Williams, W., Buongiorno, J., Hu, L.-W., & Peterson, G. (2008). Transient and Steady-State Experimental Comparison Study of Effective Thermal Conductivity of Al₂O₃/ Water Nanofluids. *Journal of Heat Transfer*, 130(4), 042407.
- Li, J., & Grennberg, H. (2006). Microwave-Assisted Covalent Sidewall Functionalization of Multiwalled Carbon Nanotubes. *Chemistry-A European Journal*, 12(14), 3869-3875.
- Li, J., Li, Z., & Wang, B. (2002). Experimental viscosity measurements for copper oxide nanoparticle suspensions. *Tsinghua Science and Technology*, 7(2), 198-201.
- Li, Q., Xuan, Y., & Wang, J. (2003). Investigation on convective heat transfer and flow features of nanofluids. *Journal of Heat Transfer*, 125(2003), 151-155.
- Li, X., Zhu, D., Wang, X., Wang, N., Gao, J., & Li, H. (2008). Thermal conductivity enhancement dependent pH and chemical surfactant for Cu-H₂O nanofluids. *Thermochimica Acta*, 469(1), 98-103.
- Li, Y.-F., Liu, Y.-Z., Zhang, W.-K., Guo, C.-Y., & Chen, C.-M. (2015). Green synthesis of reduced graphene oxide paper using Zn powder for supercapacitors. *Materials Letters*, 157, 273-276.
- Li, Y., Tung, S., Schneider, E., & Xi, S. (2009). A review on development of nanofluid preparation and characterization. *Powder Technology*, 196(2), 89-101.
- Liao, L., & Liu, Z.-H. (2009). Forced convective flow drag and heat transfer characteristics of carbon nanotube suspensions in a horizontal small tube. *Heat and Mass Transfer*, 45(8), 1129-1136.
- Liao, R., Tang, Z., Lei, Y., & Guo, B. (2011). Polyphenol-reduced graphene oxide: mechanism and derivatization. *The Journal of Physical Chemistry C*, 115(42), 20740-20746.

- Lin, D., & Xing, B. (2008). Tannic acid adsorption and its role for stabilizing carbon nanotube suspensions. *Environmental science & technology*, 42(16), 5917-5923.
- Liu, C., Hu, G., & Gao, H. (2012). Preparation of few-layer and single-layer graphene by exfoliation of expandable graphite in supercritical N, N-dimethylformamide. *The Journal of Supercritical Fluids*, 63, 99-104.
- Liu, J., Zubiri, M. R., Vigolo, B., Dossot, M., Fort, Y., Ehrhardt, J.-J., & McRae, E. (2007). Efficient microwave-assisted radical functionalization of single-wall carbon nanotubes. *Carbon*, 45(4), 885-891.
- Liu, K., Zhang, J.-J., Cheng, F.-F., Zheng, T.-T., Wang, C., & Zhu, J.-J. (2011). Green and facile synthesis of highly biocompatible graphene nanosheets and its application for cellular imaging and drug delivery. *Journal of Materials Chemistry*, 21(32), 12034-12040.
- Liu, M.-S., Lin, M. C.-C., Huang, I.-T., & Wang, C.-C. (2005). Enhancement of thermal conductivity with carbon nanotube for nanofluids. *International Communications in Heat and Mass Transfer*, 32(9), 1202-1210.
- Liu, M.-S., Lin, M. C.-C., Tsai, C., & Wang, C.-C. (2006). Enhancement of thermal conductivity with Cu for nanofluids using chemical reduction method. *International Journal of Heat and Mass Transfer*, 49(17), 3028-3033.
- Liu, N., Zheng, Z., Yao, Y., Zhang, G., Lu, N., Li, P., . . . Ho, K. (2013). The organic functional group effect on the electronic structure of graphene nano-ribbon: A first-principles study. *arXiv preprint arXiv:1302.0097*.
- Liu, Y., Li, Y., Zhong, M., Yang, Y., Wen, Y., & Wang, M. (2011). A green and ultrafast approach to the synthesis of scalable graphene nanosheets with Zn powder for electrochemical energy storage. *Journal of Materials Chemistry*, 21(39), 15449-15455.
- Lo, C.-H., Tsung, T.-T., & Chen, L.-C. (2005). Shape-controlled synthesis of Cu-based nanofluid using submerged arc nanoparticle synthesis system (SANSS). *Journal of Crystal Growth*, 277(1), 636-642.
- Lo, C.-H., Tsung, T.-T., Chen, L.-C., Su, C.-H., & Lin, H.-M. (2005). Fabrication of copper oxide nanofluid using submerged arc nanoparticle synthesis system (SANSS). *Journal of Nanoparticle Research*, 7(2-3), 313-320.
- Loh, K. P., Bao, Q., Ang, P. K., & Yang, J. (2010). The chemistry of graphene. *Journal of Materials Chemistry*, 20(12), 2277-2289.
- Lomascolo, M., Colangelo, G., Milanese, M., & de Risi, A. (2015). Review of heat transfer in nanofluids: conductive, convective and radiative experimental results. *Renewable and Sustainable Energy Reviews*, 43, 1182-1198.
- Luckham, P. F., & Ukeje, M. A. (1999). Effect of particle size distribution on the rheology of dispersed systems. *Journal of colloid and interface science*, 220(2), 347-356.

- Maddinedi, S. B., Mandal, B. K., Vankayala, R., Kalluru, P., Tammina, S. K., & Kumar, H. K. (2014). Casein mediated green synthesis and decoration of reduced graphene oxide. *Spectrochimica Acta Part A: Molecular and Biomolecular Spectroscopy*, 126, 227-231.
- Maïga, S. E. B., Nguyen, C. T., Galanis, N., & Roy, G. (2004). Heat transfer behaviours of nanofluids in a uniformly heated tube. *Superlattices and Microstructures*, 35(3), 543-557.
- Maïga, S. E. B., Palm, S. J., Nguyen, C. T., Roy, G., & Galanis, N. (2005). Heat transfer enhancement by using nanofluids in forced convection flows. *International Journal of Heat and Fluid Flow*, 26(4), 530-546.
- Malvandi, A., & Ganji, D. (2014). Brownian motion and thermophoresis effects on slip flow of alumina/water nanofluid inside a circular microchannel in the presence of a magnetic field. *International Journal of thermal sciences*, 84, 196-206.
- Malvandi, A., & Ganji, D. (2015a). Effects of nanoparticle migration on hydromagnetic mixed convection of alumina/water nanofluid in vertical channels with asymmetric heating. *Physica E: Low-dimensional Systems and Nanostructures*, 66, 181-196.
- Malvandi, A., & Ganji, D. (2015b). Magnetic field and slip effects on free convection inside a vertical enclosure filled with alumina/water nanofluid. *Chemical Engineering Research and Design*, 94, 355-364.
- Malvandi, A., Ganji, D., & Kaffash, M. (2015). Magnetic field effects on nanoparticle migration and heat transfer of alumina/water nanofluid in a parallel-plate channel with asymmetric heating. *The European Physical Journal Plus*, 130(4), 63.
- Malvandi, A., Safaei, M., Kaffash, M., & Ganji, D. (2015). MHD mixed convection in a vertical annulus filled with Al₂O₃-water nanofluid considering nanoparticle migration. *Journal of Magnetism and Magnetic Materials*, 382, 296-306.
- Mansour, R. B., Galanis, N., & Nguyen, C. T. (2007). Effect of uncertainties in physical properties on forced convection heat transfer with nanofluids. *Applied Thermal Engineering*, 27(1), 240-249.
- Martinelli, R. C. (1947). Heat transfer to molten metals. *Trans. ASME*, 69(8), 947-959.
- Masuda, H., Ebata, A., & Teramae, K. (1993). Alteration of thermal conductivity and viscosity of liquid by dispersing ultra-fine particles. Dispersion of Al₂O₃, SiO₂ and TiO₂ ultra-fine particles.
- Masuda, H., Ebata, A., Teramae, K., & Hishinuma, N. (1993). Alteration of thermal conductivity and viscosity of liquid by dispersing ultra-fine particles. *Netsu Bussei*, 7(2), 227-233.
- Maxwell, J. C. (1881). *A treatise on electricity and magnetism* (Vol. 1): Clarendon press.

- Maxwell, J. C. (1904). *A Treatise on Electricity and Magnetism*, vol. II. Clarendon: Oxford.
- Mayer, C. R., Neveu, S., Secheresse, F., & Cabuil, V. (2004). Supramolecular assemblies of gold nanoparticles induced by hydrogen bond interactions. *Journal of colloid and interface science*, 273(2), 350-355.
- Mehrali, M., Sadeghinezhad, E., Rosen, M. A., Akhiani, A. R., Latibari, S. T., Mehrali, M., & Metselaar, H. S. C. (2015). Heat transfer and entropy generation for laminar forced convection flow of graphene nanoplatelets nanofluids in a horizontal tube. *International Communications in Heat and Mass Transfer*, 66, 23-31.
- Mehrali, M., Sadeghinezhad, E., Tahan Latibari, S., Mehrali, M., Togun, H., Zubir, M. N. M., . . . Metselaar, H. (2014). Preparation, characterization, viscosity, and thermal conductivity of nitrogen-doped graphene aqueous nanofluids. *Journal of materials science*, 49(20), 7156-7171.
- Menter, F. R. (1994). Two-equation eddy-viscosity turbulence models for engineering applications. *AIAA journal*, 32(8), 1598-1605.
- Michaelides, E. E. S. (2014). *Nanofluidics: thermodynamic and transport properties*: Springer.
- Mikkola, V. (2015). Impact of concentration, particle size and thermal conductivity on effective convective heat transfer performance of nanofluids.
- Mirmasoumi, S., & Behzadmehr, A. (2008). Effect of nanoparticles mean diameter on mixed convection heat transfer of a nanofluid in a horizontal tube. *International Journal of Heat and Fluid Flow*, 29(2), 557-566.
- Moghari, R. M., Akbarinia, A., Shariat, M., Talebi, F., & Laur, R. (2011). Two phase mixed convection Al₂O₃-water nanofluid flow in an annulus. *International journal of multiphase flow*, 37(6), 585-595.
- Mohammed, H., Bhaskaran, G., Shuaib, N., & Saidur, R. (2011). Heat transfer and fluid flow characteristics in microchannels heat exchanger using nanofluids: a review. *Renewable and Sustainable Energy Reviews*, 15(3), 1502-1512.
- Mohammed, K. A. K., Abdulkadhim, H. M., & Noori, S. I. (2016). Chemical Composition and Anti-bacterial Effects of Clove (*Syzygium aromaticum*) Flowers. *Int. J. Curr. Microbiol. App. Sci*, 5(2), 483-489.
- Mohd Zubir, M. N., Badarudin, A., Kazi, S., Nay Ming, H., Sadri, R., & Amiri, A. (2016). Investigation on the Use of Graphene Oxide as Novel Surfactant for Stabilizing Carbon Based Materials. *Journal of dispersion science and technology*, 37(10), 1395-1407.
- Mojarrad, M. S., Keshavarz, A., & Shokouhi, A. (2013). Nanofluids thermal behavior analysis using a new dispersion model along with single-phase. *Heat and mass transfer*, 49(9), 1333-1343.

- Mokmeli, A., & Saffar-Avval, M. (2010). Prediction of nanofluid convective heat transfer using the dispersion model. *International Journal of thermal sciences*, 49(3), 471-478.
- Moore, V. C., Strano, M. S., Haroz, E. H., Hauge, R. H., Smalley, R. E., Schmidt, J., & Talmon, Y. (2003). Individually suspended single-walled carbon nanotubes in various surfactants. *Nano letters*, 3(10), 1379-1382.
- Moraveji, M. K., & Ardehali, R. M. (2013). CFD modeling (comparing single and two-phase approaches) on thermal performance of Al₂O₃/water nanofluid in mini-channel heat sink. *International Communications in Heat and Mass Transfer*, 44, 157-164.
- Moraveji, M. K., Darabi, M., Haddad, S. M. H., & Davarnejad, R. (2011). Modeling of convective heat transfer of a nanofluid in the developing region of tube flow with computational fluid dynamics. *International Communications in Heat and Mass Transfer*, 38(9), 1291-1295.
- Moshizi, S., Malvandi, A., Ganji, D., & Pop, I. (2014). A two-phase theoretical study of Al₂O₃-water nanofluid flow inside a concentric pipe with heat generation/absorption. *International Journal of thermal sciences*, 84, 347-357.
- Murshed, S., Leong, K., & Yang, C. (2005a). Enhanced thermal conductivity of TiO₂-water based nanofluids. *International Journal of thermal sciences*, 44(4), 367-373.
- Murshed, S., Leong, K., & Yang, C. (2005b). Enhanced thermal conductivity of TiO₂-water based nanofluids. *International Journal of thermal sciences*, 44(4), 367-373.
- Murshed, S., Leong, K., & Yang, C. (2006). Determination of the effective thermal diffusivity of nanofluids by the double hot-wire technique. *Journal of Physics D: Applied Physics*, 39(24), 5316.
- Murshed, S., Leong, K., & Yang, C. (2009). A combined model for the effective thermal conductivity of nanofluids. *Applied Thermal Engineering*, 29(11), 2477-2483.
- Nakamura, G., Narimatsu, K., Niidome, Y., & Nakashima, N. (2007). Green tea solution individually solubilizes single-walled carbon nanotubes. *Chemistry Letters*, 36(9), 1140-1141.
- Namburu, P. K., Das, D. K., Tanguturi, K. M., & Vajjha, R. S. (2009). Numerical study of turbulent flow and heat transfer characteristics of nanofluids considering variable properties. *International Journal of Thermal Sciences*, 48(2), 290-302.
- Newaz, K., Duffy, G. G., & Chen, X. D. (1998). *Heat Transfer to Natural Fibre Suspensions*. Paper presented at the IPENZ Conference 98: The sustainable city; Volume 5; Chemical; engineering materials.
- Nguyen, C., Desgranges, F., Galanis, N., Roy, G., Maré, T., Boucher, S., & Mintsa, H. A. (2008). Viscosity data for Al₂O₃-water nanofluid—hysteresis: is heat

transfer enhancement using nanofluids reliable? *International Journal of thermal sciences*, 47(2), 103-111.

Nikuradse, J. (1933). Strömungsgesetze in Rauhen Rohren ForschHft. *Ver. Dt. Ing*, 361.

Nikuradse, V. (1932). gesetzmäßigkeiten der turbulent stromung in glatten rohren. *Forschungsheft*, 356.

Niu, J., Fu, C., & Tan, W. (2012). Slip-flow and heat transfer of a non-Newtonian nanofluid in a microtube. *PLoS One*, 7(5), e37274.

Noguchi, Y., Fujigaya, T., Niidome, Y., & Nakashima, N. (2008). Single-walled carbon nanotubes/DNA hybrids in water are highly stable. *Chemical Physics Letters*, 455(4), 249-251.

Notter, R. H., & Sleicher, C. A. (1972). A solution to the turbulent Graetz problem—III Fully developed and entry region heat transfer rates. *Chemical Engineering Science*, 27(11), 2073-2093.

Okamoto, M., Fujigaya, T., & Nakashima, N. (2009). Design of an Assembly of Poly (benzimidazole), Carbon Nanotubes, and Pt Nanoparticles for a Fuel-Cell Electrocatalyst with an Ideal Interfacial Nanostructure. *Small*, 5(6), 735-740.

Orozco, D. (2005). Hydrodynamic behavior of suspension of polar particles. *Encycl Surf Colloid Sci*, 4, 2375-2396.

Özerinç, S., Kakaç, S., & Yazıcıoğlu, A. G. (2010). Enhanced thermal conductivity of nanofluids: a state-of-the-art review. *Microfluidics and Nanofluidics*, 8(2), 145-170.

Pak, B. C., & Cho, Y. I. (1998). Hydrodynamic and heat transfer study of dispersed fluids with submicron metallic oxide particles. *Experimental Heat Transfer an International Journal*, 11(2), 151-170.

Pakdaman, M. F., Akhavan-Behabadi, M., & Razi, P. (2012). An experimental investigation on thermo-physical properties and overall performance of MWCNT/heat transfer oil nanofluid flow inside vertical helically coiled tubes. *Experimental Thermal and Fluid Science*, 40, 103-111.

Palm, S. J., Roy, G., & Nguyen, C. T. (2006). Heat transfer enhancement with the use of nanofluids in radial flow cooling systems considering temperature-dependent properties. *Applied Thermal Engineering*, 26(17), 2209-2218.

Pan, B., & Xing, B. (2008). Adsorption mechanisms of organic chemicals on carbon nanotubes. *Environmental science & technology*, 42(24), 9005-9013.

Park, Y., Hong, Y., Weyers, A., Kim, Y., & Linhardt, R. (2011). Polysaccharides and phytochemicals: a natural reservoir for the green synthesis of gold and silver nanoparticles. *IET nanobiotechnology*, 5(3), 69-78.

Parthasarathy, V. A., Chempakam, B., & Zachariah, T. J. (2008). *Chemistry of spices*: CABI.

- Patel, H. E., Das, S. K., Sundararajan, T., Nair, A. S., George, B., & Pradeep, T. (2003). Thermal conductivities of naked and monolayer protected metal nanoparticle based nanofluids: Manifestation of anomalous enhancement and chemical effects. *Applied physics letters*, 83(14), 2931-2933.
- Peng, H., Meng, L., Niu, L., & Lu, Q. (2012). Simultaneous reduction and surface functionalization of graphene oxide by natural cellulose with the assistance of the ionic liquid. *The Journal of Physical Chemistry C*, 116(30), 16294-16299.
- Peng, X., & Wong, S. S. (2009). Functional covalent chemistry of carbon nanotube surfaces. *Advanced Materials*, 21(6), 625-642.
- Pérez, E. M., & Martín, N. (2015). π - π interactions in carbon nanostructures. *Chemical Society Reviews*, 44(18), 6425-6433.
- Petukhov, B. (1970). Heat transfer and friction in turbulent pipe flow with variable physical properties. *Advances in heat transfer*, 6, 503-564.
- Petukhov, B., & Kirilov, V. (1958). The problem of heat exchange in the turbulent flow of liquids in tubes. *Teploenergetika*, 4(4), 63-68.
- Pham, V. H., Cuong, T. V., Hur, S. H., Oh, E., Kim, E. J., Shin, E. W., & Chung, J. S. (2011). Chemical functionalization of graphene sheets by solvothermal reduction of a graphene oxide suspension in N-methyl-2-pyrrolidone. *Journal of Materials Chemistry*, 21(10), 3371-3377.
- Philip, J., & Shima, P. (2012). Thermal properties of nanofluids. *Advances in colloid and interface science*, 183, 30-45.
- Phuoc, T. X., Massoudi, M., & Chen, R.-H. (2011). Viscosity and thermal conductivity of nanofluids containing multi-walled carbon nanotubes stabilized by chitosan. *International Journal of thermal sciences*, 50(1), 12-18.
- Prandtl, L. (1960). *Führer durch die Strömungslehre*: F. Vieweg.
- Prasher, R., Bhattacharya, P., & Phelan, P. E. (2006). Brownian-motion-based convective-conductive model for the effective thermal conductivity of nanofluids. *Journal of Heat Transfer*, 128(6), 588-595.
- Prasher, R., Evans, W., Meakin, P., Fish, J., Phelan, P., & Keblinski, P. (2006). Effect of aggregation on thermal conduction in colloidal nanofluids. *Applied physics letters*, 89(14), 143119.
- Prasher, R., Phelan, P. E., & Bhattacharya, P. (2006). Effect of aggregation kinetics on the thermal conductivity of nanoscale colloidal solutions (nanofluid). *Nano letters*, 6(7), 1529-1534.
- Putnam, S. A., Cahill, D. G., Braun, P. V., Ge, Z., & Shimmin, R. G. (2006). Thermal conductivity of nanoparticle suspensions. *Journal of Applied Physics*, 99(8), 084308.

- Putra, N., Roetzel, W., & Das, S. K. (2003). Natural convection of nano-fluids. *Heat and mass transfer*, 39(8-9), 775-784.
- Qingzhong, X. (2000). Effective-medium theory for two-phase random composites with an interfacial shell. *Cailiao Kexue Yu Jishu(Journal of Materials Science & Technology)(China)(USA)*, 16, 367-369.
- Qu, J., & Wu, H. (2011). Thermal performance comparison of oscillating heat pipes with SiO₂/water and Al₂O₃/water nanofluids. *International Journal of thermal sciences*, 50(10), 1954-1962.
- Ramires, M. L., de Castro, C. A. N., Nagasaka, Y., Nagashima, A., Assael, M. J., & Wakeham, W. A. (1995). Standard reference data for the thermal conductivity of water. *Journal of Physical and Chemical Reference Data*, 24(3), 1377-1381.
- Rashidi, M. M., Nasiri, M., Khezerloo, M., & Laraqi, N. (2016). Numerical investigation of magnetic field effect on mixed convection heat transfer of nanofluid in a channel with sinusoidal walls. *Journal of Magnetism and Magnetic Materials*, 401, 159-168.
- Rayleigh, L. (1892). LVI. On the influence of obstacles arranged in rectangular order upon the properties of a medium. *The London, Edinburgh, and Dublin Philosophical Magazine and Journal of Science*, 34(211), 481-502.
- Reina, A., Jia, X., Ho, J., Nezich, D., Son, H., Bulovic, V., . . . Kong, J. (2008). Large area, few-layer graphene films on arbitrary substrates by chemical vapor deposition. *Nano letters*, 9(1), 30-35.
- Rella, S., Giuri, A., Corcione, C. E., Acocella, M. R., Colella, S., Guerra, G., . . . Malitesta, C. (2015). X-ray photoelectron spectroscopy of reduced graphene oxide prepared by a novel green method. *Vacuum*, 119, 159-162.
- Ruan, B., & Jacobi, A. M. (2012). Ultrasonication effects on thermal and rheological properties of carbon nanotube suspensions. *Nanoscale research letters*, 7(1), 1-14.
- Rusu, A. G., Popa, M. I., Lisa, G., & Vereștiuc, L. (2015). Thermal behavior of hydrophobically modified hydrogels using TGA/FTIR/MS analysis technique. *Thermochimica Acta*, 613, 28-40.
- Sadri, R., Ahmadi, G., Togun, H., Dahari, M., Kazi, S. N., Sadeghinezhad, E., & Zubir, N. (2014a). An experimental study on thermal conductivity and viscosity of nanofluids containing carbon nanotubes. *Nanoscale research letters*, 9(1), 151.
- Sadri, R., Ahmadi, G., Togun, H., Dahari, M., Kazi, S. N., Sadeghinezhad, E., & Zubir, N. (2014b). An experimental study on thermal conductivity and viscosity of nanofluids containing carbon nanotubes. *Nanoscale research letters*, 9(1), 1-16.
- Sadri, R., Hosseini, M., Kazi, S., Bagheri, S., Abdelrazek, A. H., Ahmadi, G., . . . Abidin, N. (2017). A facile, bio-based, novel approach for synthesis of covalently functionalized graphene nanoplatelet nano-coolants toward improved

- thermo-physical and heat transfer properties. *Journal of colloid and interface science*, 509, 140-152.
- Sadri, R., Hosseini, M., Kazi, S., Bagheri, S., Abdelrazek, A. H., Ahmadi, G., . . . Abidin, N. (2018). A facile, bio-based, novel approach for synthesis of covalently functionalized graphene nanoplatelet nano-coolants toward improved thermo-physical and heat transfer properties. *Journal of colloid and interface science*, 509, 140-152.
- Sadri, R., Hosseini, M., Kazi, S., Bagheri, S., Ahmed, S., Ahmadi, G., . . . Dahari, M. (2017). Study of environmentally friendly and facile functionalization of graphene nanoplatelet and its application in convective heat transfer. *Energy Conversion and Management*, 150, 26-36.
- Sadri, R., Hosseini, M., Kazi, S., Bagheri, S., Zubir, N., Ahmadi, G., . . . Zaharinie, T. (2017). A novel, eco-friendly technique for covalent functionalization of graphene nanoplatelets and the potential of their nanofluids for heat transfer applications. *Chemical Physics Letters*, 675, 92-97.
- Sadri, R., Hosseini, M., Kazi, S., Bagheri, S., Zubir, N., Solangi, K., . . . Badarudin, A. (2017). A bio-based, facile approach for the preparation of covalently functionalized carbon nanotubes aqueous suspensions and their potential as heat transfer fluids. *Journal of colloid and interface science*, 504, 115-123.
- Sadri, R., Zangeneh Kamali, K., Hosseini, M., Zubir, N., Kazi, S., Ahmadi, G., . . . Golsheikh, A. (2017). Experimental study on thermo-physical and rheological properties of stable and green reduced graphene oxide nanofluids: Hydrothermal assisted technique. *Journal of Dispersion Science and Technology*, 38(9), 1302-1310.
- Sadri, R., Zangeneh Kamali, K., Hosseini, M., Zubir, N., Kazi, S., Ahmadi, G., . . . Moradi, A. (2016). Experimental Study on Thermo-Physical and Rheological Properties of Highly Stable and Green Reduced Graphene Oxide Nanofluids: Hydrothermal Assisted Technique. *Journal of dispersion science and technology*(just-accepted).
- Saini, A., Kaur, H., Sharma, S., & Gangacharyulu, D. (2016). Nanofluids: A Review Preparation, Stability, Properties and Applications. *Int. J. Eng. Res. Technol*, 5(07), 11-16.
- Sajadi, A., & Kazemi, M. (2011). Investigation of turbulent convective heat transfer and pressure drop of TiO₂/water nanofluid in circular tube. *International Communications in Heat and Mass Transfer*, 38(10), 1474-1478.
- Santra, A. K., Sen, S., & Chakraborty, N. (2009). Study of heat transfer due to laminar flow of copper–water nanofluid through two isothermally heated parallel plates. *International Journal of thermal sciences*, 48(2), 391-400.
- Sarkar, S., & Selvam, R. P. (2007). Molecular dynamics simulation of effective thermal conductivity and study of enhanced thermal transport mechanism in nanofluids. *Journal of Applied Physics*, 102(7), 074302.

- Sarsam, W. S., Amiri, A., Kazi, S., & Badarudin, A. (2016). Stability and thermophysical properties of non-covalently functionalized graphene nanoplatelets nanofluids. *Energy Conversion and Management*, 116, 101-111.
- Sarsam, W. S., Amiri, A., Zubir, M. N. M., Yarmand, H., Kazi, S., & Badarudin, A. (2016). Stability and thermophysical properties of water-based nanofluids containing triethanolamine-treated graphene nanoplatelets with different specific surface areas. *Colloids and Surfaces A: Physicochemical and Engineering Aspects*, 500, 17-31.
- Shanbedi, M., Heris, S. Z., Amiri, A., Hosseinipour, E., Eshghi, H., & Kazi, S. (2015). Synthesis of aspartic acid-treated multi-walled carbon nanotubes based water coolant and experimental investigation of thermal and hydrodynamic properties in circular tube. *Energy Conversion and Management*, 105, 1366-1376.
- Shaw, D. J., & Costello, B. (1993). Introduction to colloid and surface chemistry: Butterworth-Heinemann, Oxford, 1991, ISBN 0 7506 1182 0, 306 pp,£ 14.95: Elsevier.
- Sheikholeslami, M., Abelman, S., & Ganji, D. D. (2014). Numerical simulation of MHD nanofluid flow and heat transfer considering viscous dissipation. *International Journal of Heat and Mass Transfer*, 79, 212-222.
- Sheikholeslami, M., & Ganji, D. (2014). Heated Permeable Stretching Surface in a Porous Medium Using Nanofluids. *Journal of Applied Fluid Mechanics*, 7(3).
- Sheikholeslami, M., Gorji-Bandpy, M., & Soleimani, S. (2013). Two phase simulation of nanofluid flow and heat transfer using heatline analysis. *International Communications in Heat and Mass Transfer*, 47, 73-81.
- Shende, R., & Sundara, R. (2015). Nitrogen doped hybrid carbon based composite dispersed nanofluids as working fluid for low-temperature direct absorption solar collectors. *Solar Energy Materials and Solar Cells*, 140, 9-16.
- Shiral Fernando, K., Lin, Y., & Sun, Y.-P. (2004). High aqueous solubility of functionalized single-walled carbon nanotubes. *Langmuir*, 20(11), 4777-4778.
- Si, Y., & Samulski, E. T. (2008). Synthesis of water soluble graphene. *Nano letters*, 8(6), 1679-1682.
- Sieder, E. N., & Tate, G. E. (1936). Heat transfer and pressure drop of liquids in tubes. *Industrial & Engineering Chemistry*, 28(12), 1429-1435.
- Singh, N., Chand, G., & Kanagaraj, S. (2012). Investigation of Thermal Conductivity and Viscosity of Carbon Nanotubes–Ethylene Glycol Nanofluids. *Heat Transfer Engineering*, 33(9), 821-827.
- Singh, V., & Gupta, M. (2016). Heat transfer augmentation in a tube using nanofluids under constant heat flux boundary condition: A review. *Energy Conversion and Management*, 123, 290-307.

- Sohn, C., & Chen, M. (1981). Microconvective thermal conductivity in disperse two-phase mixtures as observed in a low velocity Couette flow experiment. *J. Heat Transfer;(United States)*, 103(1).
- Sommers, A. D., & Yerkes, K. L. (2010). Experimental investigation into the convective heat transfer and system-level effects of Al₂O₃-propanol nanofluid. *Journal of Nanoparticle Research*, 12(3), 1003-1014.
- Spitalsky, Z., Tasis, D., Papagelis, K., & Galiotis, C. (2010). Carbon nanotube–polymer composites: chemistry, processing, mechanical and electrical properties. *Progress in polymer science*, 35(3), 357-401.
- Stranks, S. D., Habisreutinger, S. N., Dirks, B., & Nicholas, R. J. (2013). Novel Carbon Nanotube-Conjugated Polymer Nanohybrids Produced By Multiple Polymer Processing. *Advanced Materials*, 25(31), 4365-4371.
- Sui, Z., Zhang, X., Lei, Y., & Luo, Y. (2011). Easy and green synthesis of reduced graphite oxide-based hydrogels. *Carbon*, 49(13), 4314-4321.
- Sun, Y.-P., Fu, K., Lin, Y., & Huang, W. (2002). Functionalized carbon nanotubes: properties and applications. *Accounts of Chemical Research*, 35(12), 1096-1104.
- Sun, Z., Yan, Z., Yao, J., Beitler, E., Zhu, Y., & Tour, J. M. (2010). Growth of graphene from solid carbon sources. *Nature*, 468(7323), 549-552.
- Sundar, L. S., Naik, M., Sharma, K., Singh, M., & Reddy, T. C. S. (2012). Experimental investigation of forced convection heat transfer and friction factor in a tube with Fe₃O₄ magnetic nanofluid. *Experimental Thermal and Fluid Science*, 37, 65-71.
- Sundar, L. S., Otero-Irurueta, G., Singh, M. K., & Sousa, A. C. (2016). Heat transfer and friction factor of multi-walled carbon nanotubes–Fe₃O₄ nanocomposite nanofluids flow in a tube with/without longitudinal strip inserts. *International Journal of Heat and Mass Transfer*, 100, 691-703.
- Sundar, L. S., Singh, M. K., & Sousa, A. C. (2013). Investigation of thermal conductivity and viscosity of Fe₃O₄ nanofluid for heat transfer applications. *International Communications in Heat and Mass Transfer*, 44, 7-14.
- Sundar, L. S., Singh, M. K., & Sousa, A. C. (2014). Enhanced heat transfer and friction factor of MWCNT–Fe₃O₄/water hybrid nanofluids. *International Communications in Heat and Mass Transfer*, 52, 73-83.
- Suresh, S., Chandrasekar, M., Selvakumar, P., & Page, T. (2012). Experimental studies on heat transfer and friction factor characteristics of Al₂O₃/water nanofluid under laminar flow with spiralled rod inserts. *International Journal of Nanoparticles*, 5(1), 37-55.
- Symon, K. (1971). *Mechanics* (Vol. 3rd Edition): Addison Wesley.
- Tanaka, H., Arima, R., Fukumori, M., Tanaka, D., Negishi, R., Kobayashi, Y., . . . Ogawa, T. (2015). Method for controlling electrical properties of single-layer

graphene nanoribbons via adsorbed planar molecular nanoparticles. *Scientific reports*, 5.

- Tasis, D., Papagelis, K., Prato, M., Kallitsis, I., & Galiotis, C. (2007). Water-Soluble Carbon Nanotubes by Redox Radical Polymerization. *Macromolecular rapid communications*, 28(15), 1553-1558.
- Tasis, D., Tagmatarchis, N., Bianco, A., & Prato, M. (2006). Chemistry of carbon nanotubes. *Chemical reviews*, 106(3), 1105-1136.
- Tavakoli, F., Salavati-Niasari, M., & Mohandes, F. (2015). Green synthesis and characterization of graphene nanosheets. *Materials Research Bulletin*, 63, 51-57.
- Tawfik, M. M. (2017). Experimental studies of nanofluid thermal conductivity enhancement and applications: A review. *Renewable and Sustainable Energy Reviews*, 75, 1239-1253.
- Teng, C.-C., Ma, C.-C. M., Lu, C.-H., Yang, S.-Y., Lee, S.-H., Hsiao, M.-C., . . . Lee, T.-M. (2011). Thermal conductivity and structure of non-covalent functionalized graphene/epoxy composites. *Carbon*, 49(15), 5107-5116.
- Teng, K., Amiri, A., Kazi, S., Bakar, M., & Chew, B. (2016). Fouling mitigation on heat exchanger surfaces by EDTA-treated MWCNT-based water nanofluids. *Journal of the Taiwan Institute of Chemical Engineers*, 60, 445-452.
- Thakur, S., & Karak, N. (2012). Green reduction of graphene oxide by aqueous phytoextracts. *Carbon*, 50(14), 5331-5339.
- Thompson, W. (1998). An introduction to error analysis: The study of uncertainties in physical measurements, by John R. Taylor. *Physics Today*, 51, 57-58.
- Tian, J., He, Z., Xu, T., Fang, X., & Zhang, Z. (2016). Rheological Property and Thermal Conductivity of Multi-walled Carbon Nano-tubes-dispersed Non-Newtonian Nano-fluids Based on an Aqueous Solution of Carboxymethyl Cellulose. *Experimental Heat Transfer*, 29(3), 378-391.
- Timofeeva, E. V., Routbort, J. L., & Singh, D. (2009). Particle shape effects on thermophysical properties of alumina nanofluids. *Journal of Applied Physics*, 106(1), 014304.
- Tran, D. N., Kabiri, S., & Losic, D. (2014). A green approach for the reduction of graphene oxide nanosheets using non-aromatic amino acids. *Carbon*, 76, 193-202.
- Tsai, C., Chien, H., Ding, P., Chan, B., Luh, T., & Chen, P. (2004). Effect of structural character of gold nanoparticles in nanofluid on heat pipe thermal performance. *Materials Letters*, 58(9), 1461-1465.
- Tsang, S., Chen, Y., Harris, P., & Green, M. (1994). A simple chemical method of opening and filling carbon nanotubes. *Nature*, 372(6502), 159-162.

- Uddin, A. J., Watanabe, A., Gotoh, Y., Saito, T., & Yumura, M. (2012). Green tea-aided dispersion of single-walled carbon nanotubes in non-water media: Application for extraordinary reinforcement of nanocomposite fibers. *Textile Research Journal*, 82(9), 911-919.
- Upadhyay, R. K., Soin, N., Bhattacharya, G., Saha, S., Barman, A., & Roy, S. S. (2015). Grape extract assisted green synthesis of reduced graphene oxide for water treatment application. *Materials Letters*, 160, 355-358.
- Usri, N., Azmi, W., Mamat, R., Hamid, K. A., & Najafi, G. (2015). Thermal Conductivity Enhancement of Al₂O₃ Nanofluid in Ethylene Glycol and Water Mixture. *Energy Procedia*, 79, 397-402.
- Vajjha, R., Das, D., & Mahagaonkar, B. (2009). Density measurement of different nanofluids and their comparison with theory. *Petroleum Science and Technology*, 27(6), 612-624.
- Vajjha, R. S., Das, D. K., & Kulkarni, D. P. (2010). Development of new correlations for convective heat transfer and friction factor in turbulent regime for nanofluids. *International Journal of Heat and Mass Transfer*, 53(21), 4607-4618.
- Van Noorden, R. (2011). The trials of new carbon. *Nature*, 469(7328), 14-16.
- Vanaki, S. M., Ganesan, P., & Mohammed, H. (2016). Numerical study of convective heat transfer of nanofluids: a review. *Renewable and Sustainable Energy Reviews*, 54, 1212-1239.
- Vigolo, B., Penicaud, A., Coulon, C., Sauder, C., Pailler, R., Journet, C., . . . Poulin, P. (2000). Macroscopic fibers and ribbons of oriented carbon nanotubes. *Science*, 290(5495), 1331-1334.
- Vij, V., Tiwari, J. N., & Kim, K. S. (2016). Covalent versus Charge Transfer Modification of Graphene/Carbon-Nanotubes with Vitamin B1: Co/N/S-C Catalyst toward Excellent Oxygen Reduction.
- Vilkhu, K., Mawson, R., Simons, L., & Bates, D. (2008). Applications and opportunities for ultrasound assisted extraction in the food industry—A review. *Innovative Food Science & Emerging Technologies*, 9(2), 161-169.
- Von Karman, T. (2012). Turbulence and skin friction. *Journal of the Aeronautical Sciences (Institute of the Aeronautical Sciences)*, 1(1).
- Vusa, C. S. R., Berchmans, S., & Alwarappan, S. (2014). Facile and green synthesis of graphene. *RSC Advances*, 4(43), 22470-22475.
- Wagener, M., & Günther, B. (1999). Sputtering on liquids—a versatile process for the production of magnetic suspensions? *Journal of Magnetism and Magnetic Materials*, 201(1), 41-44.
- Wang, G., Qian, F., Saltikov, C. W., Jiao, Y., & Li, Y. (2011). Microbial reduction of graphene oxide by *Shewanella*. *Nano Research*, 4(6), 563-570.

- Wang, H., Hao, Q., Yang, X., Lu, L., & Wang, X. (2010). A nanostructured graphene/polyaniline hybrid material for supercapacitors. *Nanoscale*, 2(10), 2164-2170.
- Wang, J., Zhu, J., Zhang, X., & Chen, Y. (2013). Heat transfer and pressure drop of nanofluids containing carbon nanotubes in laminar flows. *Experimental Thermal and Fluid Science*, 44, 716-721.
- Wang, Q. H., & Hersam, M. C. (2009). Room-temperature molecular-resolution characterization of self-assembled organic monolayers on epitaxial graphene. *Nature Chemistry*, 1(3), 206-211.
- Wang, X.-Q., & Mujumdar, A. S. (2007). Heat transfer characteristics of nanofluids: a review. *International Journal of thermal sciences*, 46(1), 1-19.
- Wang, X., Xu, X., & Choi, S. U. (1999). Thermal conductivity of nanoparticle-fluid mixture. *Journal of thermophysics and heat transfer*, 13(4), 474-480.
- Wang, X., Xu, X., & S. Choi, S. U. (1999). Thermal conductivity of nanoparticle-fluid mixture. *Journal of thermophysics and heat transfer*, 13(4), 474-480.
- Wang, Y., Iqbal, Z., & Mitra, S. (2005). Microwave-induced rapid chemical functionalization of single-walled carbon nanotubes. *Carbon*, 43(5), 1015-1020.
- Wang, Y., Iqbal, Z., & Mitra, S. (2006). Rapidly functionalized, water-dispersed carbon nanotubes at high concentration. *Journal of the American Chemical Society*, 128(1), 95-99.
- Wang, Y., Shi, Z., & Yin, J. (2011). Facile synthesis of soluble graphene via a green reduction of graphene oxide in tea solution and its biocomposites. *ACS applied materials & interfaces*, 3(4), 1127-1133.
- Wang, Y., Zhang, P., Liu, C. F., Zhan, L., Li, Y. F., & Huang, C. Z. (2012). Green and easy synthesis of biocompatible graphene for use as an anticoagulant. *RSC Advances*, 2(6), 2322-2328.
- Web of Science. (2017).
- Weydemeyer, E. J., Sawdon, A. J., & Peng, C.-A. (2015). Controlled cutting and hydroxyl functionalization of carbon nanotubes through autoclaving and sonication in hydrogen peroxide. *Chemical Communications*, 51(27), 5939-5942.
- WILCOX, D. (1988). Reassessment of the scale-determining equation for advanced turbulence models. *AIAA journal*, 26(11), 1299-1310.
- Wong, S. S., Woolley, A. T., Joselevich, E., Cheung, C. L., & Lieber, C. M. (1998). Covalently-functionalized single-walled carbon nanotube probe tips for chemical force microscopy. *Journal of the American Chemical Society*, 120(33), 8557-8558.

- Worsley, M. A., Pauzauskie, P. J., Olson, T. Y., Biener, J., Satcher Jr, J. H., & Baumann, T. F. (2010). Synthesis of graphene aerogel with high electrical conductivity. *Journal of the American Chemical Society*, 132(40), 14067-14069.
- Wu, D., Zhu, H., Wang, L., & Liu, L. (2009). Critical issues in nanofluids preparation, characterization and thermal conductivity. *Current Nanoscience*, 5(1), 103-112.
- Xie, H.-q., Wang, J.-c., Xi, T.-g., & Liu, Y. (2002). Thermal conductivity of suspensions containing nanosized SiC particles. *International Journal of Thermophysics*, 23(2), 571-580.
- Xie, H., Fujii, M., & Zhang, X. (2005). Effect of interfacial nanolayer on the effective thermal conductivity of nanoparticle-fluid mixture. *International Journal of Heat and Mass Transfer*, 48(14), 2926-2932.
- Xie, H., Lee, H., Youn, W., & Choi, M. (2003). Nanofluids containing multiwalled carbon nanotubes and their enhanced thermal conductivities. *Journal of Applied Physics*, 94(8), 4967-4971.
- Xie, H., Wang, J., Xi, T., Liu, Y., Ai, F., & Wu, Q. (2002). Thermal conductivity enhancement of suspensions containing nanosized alumina particles. *Journal of Applied Physics*, 91(7), 4568-4572.
- Xie, H., Yu, W., Li, Y., & Chen, L. (2011). Discussion on the thermal conductivity enhancement of nanofluids. *Nanoscale research letters*, 6(1), 1.
- Xu, J., Rouelle, A., Smith, K., Celik, D., Hussaini, M., & Van Sciver, S. (2004). Two-phase flow of solid hydrogen particles and liquid helium. *Cryogenics*, 44(6), 459-466.
- Xu, L. Q., Yang, W. J., Neoh, K.-G., Kang, E.-T., & Fu, G. D. (2010). Dopamine-induced reduction and functionalization of graphene oxide nanosheets. *Macromolecules*, 43(20), 8336-8339.
- Xu, Y., Wang, X., Tian, R., Li, S., Wan, L., Li, M., . . . Wang, S. (2008). Microwave-induced electrophilic addition of single-walled carbon nanotubes with alkylhalides. *Applied Surface Science*, 254(8), 2431-2435.
- Xuan, Y., & Li, Q. (2000). Heat transfer enhancement of nanofluids. *International Journal of Heat and Fluid Flow*, 21(1), 58-64.
- Xuan, Y., & Li, Q. (2003). Investigation on convective heat transfer and flow features of nanofluids. *Journal of Heat Transfer*, 125(1), 151-155.
- Xuan, Y., & Roetzel, W. (2000). Conceptions for heat transfer correlation of nanofluids. *International Journal of Heat and Mass Transfer*, 43(19), 3701-3707.
- Yan, Q.-L., Gozin, M., Zhao, F.-Q., Cohen, A., & Pang, S.-P. (2016). Highly energetic compositions based on functionalized carbon nanomaterials. *Nanoscale*, 8(9), 4799-4851.

- Yang, Q., Pan, X., Huang, F., & Li, K. (2010). Fabrication of high-concentration and stable aqueous suspensions of graphene nanosheets by noncovalent functionalization with lignin and cellulose derivatives. *The Journal of Physical Chemistry C*, 114(9), 3811-3816.
- Yang, S., Yue, W., Huang, D., Chen, C., Lin, H., & Yang, X. (2012). A facile green strategy for rapid reduction of graphene oxide by metallic zinc. *Rsc Advances*, 2(23), 8827-8832.
- Yang, Y., Qiu, S., He, C., He, W., Yu, L., & Xie, X. (2010). Green chemical functionalization of multiwalled carbon nanotubes with poly (ϵ -caprolactone) in ionic liquids. *Applied Surface Science*, 257(3), 1010-1014.
- Yang, Y., Qiu, S., Xie, X., Wang, X., & Li, R. K. Y. (2010). A facile, green, and tunable method to functionalize carbon nanotubes with water-soluble azo initiators by one-step free radical addition. *Applied Surface Science*, 256(10), 3286-3292.
- Yarmand, H., Gharekhani, S., Shirazi, S. F. S., Amiri, A., Alehashem, M. S., Dahari, M., & Kazi, S. (2016). Experimental investigation of thermo-physical properties, convective heat transfer and pressure drop of functionalized graphene nanoplatelets aqueous nanofluid in a square heated pipe. *Energy Conversion and Management*, 114, 38-49.
- Yoo, D.-H., Hong, K., & Yang, H.-S. (2007). Study of thermal conductivity of nanofluids for the application of heat transfer fluids. *Thermochimica Acta*, 455(1), 66-69.
- Youssef, M. S., Aly, A. A., & Zeidan, E.-S. B. (2012). Computing the pressure drop of nanofluid turbulent flows in a pipe using an artificial neural network model.
- Yu, D., Yang, Y., Durstock, M., Baek, J.-B., & Dai, L. (2010). Soluble P3HT-grafted graphene for efficient bilayer– heterojunction photovoltaic devices. *ACS nano*, 4(10), 5633-5640.
- Yu, L., Yasuda, S., & Murakoshi, K. (2012). Synthesis of Nanometer Size Single Layer Graphene by Moderate Electrochemical Exfoliation. *Transactions of the Materials Research Society of Japan*, 37(2), 209-212.
- Yu, W., & Choi, S. (2003). The role of interfacial layers in the enhanced thermal conductivity of nanofluids: a renovated Maxwell model. *Journal of Nanoparticle Research*, 5(1-2), 167-171.
- Yu, W., France, D., Timofeeva, E., Singh, D., & Routbort, J. (2010). Thermophysical property-related comparison criteria for nanofluid heat transfer enhancement in turbulent flow. *Applied physics letters*, 96(21), 213109.
- Yu, W., France, D. M., Routbort, J. L., & Choi, S. U. (2008). Review and comparison of nanofluid thermal conductivity and heat transfer enhancements. *Heat Transfer Engineering*, 29(5), 432-460.

- Yu, W., Xie, H., & Chen, W. (2010). Experimental investigation on thermal conductivity of nanofluids containing graphene oxide nanosheets. *Journal of Applied Physics*, 107(9), 094317.
- Yu, W., Xie, H., Wang, X., & Wang, X. (2011). Significant thermal conductivity enhancement for nanofluids containing graphene nanosheets. *Physics Letters A*, 375(10), 1323-1328.
- Yu, X., Hwang, C., Jozwiak, C. M., Köhl, A., Schmid, A. K., & Lanzara, A. (2011). New synthesis method for the growth of epitaxial graphene. *Journal of Electron Spectroscopy and Related Phenomena*, 184(3), 100-106.
- Zhang, J., Yang, H., Shen, G., Cheng, P., Zhang, J., & Guo, S. (2010). Reduction of graphene oxide via L-ascorbic acid. *Chemical Communications*, 46(7), 1112-1114.
- Zhang, J., Zou, H., Qing, Q., Yang, Y., Li, Q., Liu, Z., . . . Du, Z. (2003). Effect of chemical oxidation on the structure of single-walled carbon nanotubes. *The Journal of Physical Chemistry B*, 107(16), 3712-3718.
- Zhang, S., Shao, Y., Liao, H., Engelhard, M. H., Yin, G., & Lin, Y. (2011). Polyelectrolyte-induced reduction of exfoliated graphite oxide: a facile route to synthesis of soluble graphene nanosheets. *ACS nano*, 5(3), 1785-1791.
- Zhang, T., Liu, P., Sheng, C., Duan, Y., & Zhang, J. (2014). A green and facile approach for the synthesis of water-dispersible reduced graphene oxide based on ionic liquids. *Chemical Communications*, 50(22), 2889-2892.
- Zhang, W., Chen, C. H.-T., Lu, Y., & Nagashima, T. (2004). A highly efficient microwave-assisted Suzuki coupling reaction of aryl perfluorooctylsulfonates with boronic acids. *Organic letters*, 6(9), 1473-1476.
- Zhang, X., Gu, H., & Fujii, M. (2006). Experimental study on the effective thermal conductivity and thermal diffusivity of nanofluids. *International Journal of Thermophysics*, 27(2), 569-580.
- Zhang, X., Gu, H., & Fujii, M. (2007). Effective thermal conductivity and thermal diffusivity of nanofluids containing spherical and cylindrical nanoparticles. *Experimental Thermal and Fluid Science*, 31(6), 593-599.
- Zhengzong, S., Yan, Z., Yao, J., Beitler, E., Zhu, Y., & Tour, J. (2010). Growth of graphene from solid carbon source. *Nature*, 468, 549-552.
- Zhou, S., & Ni, R. (2008). Measurement of the specific heat capacity of water-based Al~ 2O~ 3 nanofluid. *Applied physics letters*, 92(9), 093123.
- Zhou, T., Chen, F., Liu, K., Deng, H., Zhang, Q., Feng, J., & Fu, Q. (2010). A simple and efficient method to prepare graphene by reduction of graphite oxide with sodium hydrosulfite. *Nanotechnology*, 22(4), 045704.
- Zhou, Y., Bao, Q., Tang, L. A. L., Zhong, Y., & Loh, K. P. (2009). Hydrothermal dehydration for the “green” reduction of exfoliated graphene oxide to graphene

and demonstration of tunable optical limiting properties. *Chemistry of materials*, 21(13), 2950-2956.

- Zhu, C., Guo, S., Fang, Y., & Dong, S. (2010). Reducing sugar: new functional molecules for the green synthesis of graphene nanosheets. *ACS nano*, 4(4), 2429-2437.
- Zhu, D., Li, X., Wang, N., Wang, X., Gao, J., & Li, H. (2009). Dispersion behavior and thermal conductivity characteristics of Al₂O₃-H₂O nanofluids. *Current Applied Physics*, 9(1), 131-139.
- Zhuo, Q., Zhang, Y., Du, Q., & Yan, C. (2015). Facile reduction of graphene oxide at room temperature by ammonia borane via salting out effect. *Journal of colloid and interface science*, 457, 243-247.
- Zubir, M. N. M., Badarudin, A., Kazi, S., Huang, N. M., Misran, M., Sadeghinezhad, E., . . . Gharehkhani, S. (2015). Experimental investigation on the use of reduced graphene oxide and its hybrid complexes in improving closed conduit turbulent forced convective heat transfer. *Experimental Thermal and Fluid Science*, 66, 290-303.
- Zubir, M. N. M., Badarudin, A., Kazi, S., Huang, N. M., Misran, M., Sadeghinezhad, E., . . . Yusoff, N. (2015). Highly dispersed reduced graphene oxide and its hybrid complexes as effective additives for improving thermophysical property of heat transfer fluid. *International Journal of Heat and Mass Transfer*, 87, 284-294.
- Zubir, M. N. M., Badarudin, A., Kazi, S. N., Misran, M., Ibrahim, R., Amiri, A., & Sadri, R. (2016). Exploration of the environmentally benign and highly effective approach for improving carbon nanotube homogeneity in aqueous system. *Journal of Thermal Analysis and Calorimetry*, 124(2), 815-825.

LIST OF PUBLICATIONS

1. R. Sadri, M. Hosseini, S. Kazi, S. Bagheri, S. Ahmed, G. Ahmadi, N. Zubir, M. Dahari, Study of environmentally friendly and facile functionalization of graphene nanoplatelet and its application in convective heat transfer, *Energy Conversion and Management* 150 (2017) 26-36. (ISI, Q1, Impact Factor 5.589)
2. R. Sadri, M. Hosseini, S. Kazi, S. Bagheri, N. Zubir, K. Solangi, T. Zaharinie, A. Badarudin, A. A bio-based, facile approach for the preparation of covalently functionalized carbon nanotubes aqueous suspensions and their potential as heat transfer fluids, *Journal of colloid and interface science* 504 (2017) 115-123. (ISI, Q1, Impact Factor 4.233)
3. R. Sadri, K. Zangeneh Kamali, M. Hosseini, N. Zubir, S. Kazi, G. Ahmadi, M. Dahari, N. Huang, A. Golsheikh, Experimental study on thermo-physical and rheological properties of stable and green reduced graphene oxide nanofluids: Hydrothermal assisted technique, *Journal of Dispersion Science and Technology* 38(9) (2017) 1302-1310. (ISI, Q3, Impact Factor 1.59)
4. R. Sadri, M. Hosseini, S. Kazi, S. Bagheri, G. Ahmadi, N. Zubir, R. Ahmad, N. Abidin, A facile, bio-based, novel approach for synthesis of covalently functionalized graphene nanoplatelet nano-coolants toward improved thermo-physical and heat transfer properties, *Journal of colloid and interface science* 509 (2018) 140-152 (ISI, Q1, Impact Factor 4.233)
5. R. Sadri, M. Hosseini, S. Kazi, S. Bagheri, N. Zubir, G. Ahmadi, M. Dahari, T. Zaharinie, A novel, eco-friendly technique for covalent functionalization of graphene nanoplatelets and the potential of their nanofluids for heat transfer applications, *Chemical Physics Letters* 675 (2017) 92-97. (ISI, Q3, Impact Factor 1.8)

6. R. Sadri, A. Mallah, M. Hosseini, G. Ahmadi, S. Kazi, A. Dabbagh, C. Yeong, CFD modeling of turbulent convection heat transfer of nanofluids containing green functionalized graphene nanoplatelets flowing in a horizontal tube: Comparison with experimental data, *Journal of Molecular Liquids* 269 (2018) 152-159. (*ISI, Q1, Impact Factor 4.513*)

University of Malaya